Image Reconstruction from Fan-Beam and Cone-Beam Projections

Bildrekonstruktion aus Fächerstrahl- und Kegelstrahlprojektionen

Submitted to

Technische Fakultät der
Universität Erlangen-Nürnberg

in partial fulfillment of the requirements for
the degree of

DOKTOR-INGENIEUR

of

Frank Dennerlein

Erlangen — 2008

Meinen Eltern

Abstract

This thesis addresses the problem of reconstructing static objects in 2D and 3D transmission computed tomography (CT). After reviewing the classical CT reconstruction theory, we discuss and thoroughly evaluate various novel reconstruction methods, two of which are original.

Our first original approach is for 2D CT reconstruction from full-scan fan-beam data, i.e., for 2D imaging in the geometry of diagnostic medical CT scanners. Compared to conventional methods, our approach is computationally more efficient and also yields results with an overall reduction of image noise at comparable spatial resolution, as demonstrated in detailed evaluations based on simulated fan-beam data and on data collected with a Siemens Somatom CT scanner. Part two of this thesis discusses the problem of 3D reconstruction in the short-scan circular cone-beam (CB) geometry, i.e., the geometry of medical C-arm systems. We first present a detailed comparative evaluation of innovative methods recently suggested in the literature for reconstruction in this geometry and of the approach applied on many existing systems. This evaluation involves various quantitative and qualitative figures-of-merit to assess image quality. We then derive an original short-scan CB reconstruction method that is based on a novel, theoretically-exact factorization of the 3D reconstruction problem into a set of independent 2D inversion problems, each of which is solved iteratively and yields the object density on a single plane. In contrast to the state-of-the-art methods discussed earlier in this thesis, our factorization approach does not involve any geometric approximations during its derivation and enforces all reconstructed values to be positive; it thus provides quantitatively very accurate results and effectively reduces CB artifacts in the reconstructions, as illustrated in the numerical evaluations based on computer-simulated CB data and also real CB data acquired with a Siemens Axiom Artis C-arm system.

Kurzfassung

Diese Arbeit behandelt das Problem der Rekonstruktion statischer Objekte in der 2D und 3D Transmissions-Computertomographie (CT). Wir geben einen Überblick der klassischen CT Rekonstruktionstheorie und diskutieren und evaluieren anschliessend mehrere neue CT Rekonstruktionsmethoden; zwei dieser Methoden sind originär.

Unser erstes originäres Verfahren ist für die 2D CT Rekonstruktion aus Vollkreis-Fächerstrahldaten, das heisst, für 2D Bildgebung in der Geometrie diagnositischer medizinischer CT Scanner. Unser Verfahren ist im Vergleich zu herkömmlichen Methoden recheneffizienter und liefert ausserdem Ergebnisse mit reduziertem Bildrauschen bei vergleichbarerer Ortsauflösung, was anhand ausführlicher Untersuchungen mit simulierten Daten und mit Daten eines Siemens Somatom CT Scanners demonstriert wird. Teil zwei dieser Arbeit behandelt das 3D Rekonstruktionsproblem in der Teilkreis-Kegelstrahlgeometrie, das heisst, in der Geometrie medizinischer C-Bogen Systeme. Wir präsentieren eine detaillierte Vergleichsstudie innovativer Methoden, die kürzlich in der Literatur für die Rekonstruktion in dieser Geometrie vorgeschlagen wurden, sowie des Verfahrens, das in vielen existierenden Systemen Anwendung findet. Unser Vergleich basiert auf quantitativen sowie qualitativen Bildqualitätskenngrössen. Wir leiten anschliessend eine originäre Teilkreis-Kegelstrahlrekonstruktionsmethode her, die auf einer neuen, theoretisch exakten Faktorisierung des 3D Rekonstruktionsproblems in eine Menge unabhängiger 2D Inversionsprobleme beruht. Jedes Inversionsproblem wird iterativ gelöst und liefert die Objektdichte auf einer einzelnen Ebene. Unser Faktorisierungsverfahren bezieht im Gegensatz zu den vorher untersuchten Methoden keinerlei geometrische Annäherungen während seiner Herleitung mit ein und erzwingt, dass alle rekonstruierten Werte positiv sind. Es liefert daher quantitativ sehr akkurate Ergebnisse und eine effektive Reduzierung von Kegelstrahlartefakten, was in den numerischen Auswertungen mit simulierten Daten und mit Daten eines Siemens Axiom Artis C-Bogen Systems veranschaulicht wird.

Acknowledgement

Contents

Chapter 1

Introduction

1.1 Computed Tomography

This thesis addresses specific research topics in the field of recovering human body structures from X-ray projection data in medical examination. The historical starting point to this examination method can be traced back into the 1890s, when the high-energetic electromagnetic rays that are nowadays known as X-rays were discovered [8]. One of the pioneers who carried out first experiments was the German physicist Wilhelm Conrad Roentgen, who was able to generate and measure X-rays and who managed to demonstrate, in 1895, that these rays, which are able to traverse most solid objects, can be used to create photographic impressions of interior object structures that are otherwise hidden to the human eye [77]. This was an exciting discovery [8], and over the years, examination of objects using X-rays has found its way into various fields of application, including the field of security systems, the field of non-destructive evaluation of industrial objects and – in particular – the field of medical imaging [71].

In the early days of X-ray examination and also in the contemporary application, the fundamental design of systems used for X-ray examination is based on the following concept: X-rays are generated in a ray source, sent through the object under investigation, so that they project the object structure onto some X-ray sensitive material, such as chemical film, that transforms incoming X-radiation into an image. Hence, the natural capability of X-ray systems is to acquire projection images of the investigated object and these projections can be collected from one or more viewing directions, as desired. The individual images may then be interpreted by a specialist and for a long time, this described examination method, known as projection radiography, was the method commonly used in the practical application [30, 85].

Over the last few decades, however, X-ray examination systems have become more and more sophisticated [30, 48]. Electronic control, for instance, allows the user to approach different viewing directions quickly, automatically and with high precision. Nowadays, projection images can be acquired using high-resolution digital detectors that involve semiconductor technology instead of using chemical film [71]. These and other refinements in the mechanical design and the acquisition process naturally created a desire for more complex imaging applications [30, 71, 70], such as

i) **quantitative measurements,** for instance, precise determination of the density, the length or the volume of structures within the investigated object,

ii) volumetric visualization, for instance, graphically illustrating the 3D surface of the object or of parts of the object, possibly using specific color schemes to encode additional information, or

iii) computer-aided image interpretation, for instance, assisting the user in detecting or locating specific features in the investigated object.

These applications significantly increase the practical benefit of X-ray examination systems, but they require information about the actual structure of the object; pure knowledge about individual projection images, as can be collected with an X-ray system, is not sufficient. Hence there is some discrepancy between the information that can be naturally obtained during examination and the information needed to carry out the desired applications listed above. This discrepancy is effectively tackled by the concepts of transmission computed tomography (CT) .

The objective of CT is to convert a set of projection images of an object, obtained from various viewing directions, into a representation of object structure [39]. This conversion, which is illustrated in Figure 1.1, is a highly non-trivial task. First, a data model is required that formally describes the physical data acquisition and therefore establishes a link between the object structure on one side and the X-ray measurements on the other side. The data model that became the standard for X-ray CT relates each sample of the acquired data to the integral density of the object along one geometric measurement line. This model is approximate in a sense that it disregards some second-order physical effects occurring during X-ray acquisition, such as X-ray scatter, but it relates the reconstruction problem to the task of inverting a system of integral equations and thus to a mathematical theory that may provide potential solutions to the reconstruction task.

Figure 1.1: The principle of computed tomography. (A) An X-ray system acquires projection data from the investigated object that is shown on the left (3D illustration from [3]). (B) The sequence of projection images is then converted into a structural representation of the initial object using a CT reconstruction algorithm.

The key challenge in the pursuit of recovering object structure from projection data is thus to invert this system of integral equations. The algorithms used to accomplish this inversion play a core role in the design of a CT X-ray system [21], since they directly influence whether or not the X-ray system is capable of carrying out the complex imaging applications, as desired.

1.2 CT Image Reconstruction in the Medical Environment

The concepts of CT have been applied on medical imaging systems for more than 30 years. One of the first prototype systems for CT imaging was developed by Godfrey Hounsfield and first commercially-available systems were introduced by the British company EMI [12]. Since then, the CT technology contributed to significant advancements in medical diagnosis and intervention by providing improved or entirely new imaging techniques; examples of these techniques are given, for instance, in [48, 70, 71, 59].

We here focus on CT imaging with two popular medical X-ray systems, namely the CT scanner and the medical C-arm system. These systems are used in almost complementary fields of application and they show distinct capabilities in the way projection data can be acquired.

Figure 1.2: Examples of X-ray CT systems commonly used in the clinical environment. (Left) A diagnostic CT scanner from the Siemens SOMATOM Sensation family [5]. (Right) A medical C-arm device from the Siemens AXIOM Artis family [2].

The CT scanner (one state-of-the-art system is shown in the left side of Figure 1.2) has been primarily designed for diagnostic applications [47]. In CT scanners of the 3rd generation, which is the generation most widely used nowadays, the X-ray source is mounted, together with the detector, on a ring-shaped rail. The detector is typically of curved shape and consists of many X-ray sensitive elements. In previous scanner generations, these elements were aligned in a single row; detectors of modern scanners, however, possess several rows (some of them for instance up to 256 or more, dependent on the clinical use) each of them consisting of up to 1000 detector elements. The CT scanner is capable of acquiring X-ray projections with the source-detector assembly performing one or more full rotations around the patient. Dependent on the medical application, the patient bed may be in fixed position or also shifted with respect to the source-detector rail during the scan. The CT scanner can provide 3D reconstruction results or also one or more individual 2D cross-sections through the patient, as desired [48].

The medical C-arm system, on the other hand, is designed to support interventional procedures, for instance, by providing image-based guidance in minimal-invasive surgery. On these systems, X-ray source and detector are mounted on opposite sides of a C-shaped

arm and the mechanical design of this arm is focussed on providing very flexible motion around the patient bed. The C-arm system differs in some aspects fundamentally from the diagnostic CT scanner. C-arm systems, for instance, do not in general allow X-ray projections to be acquired along a full rotation around the patient. Also, modern C-arm systems possess a large, digital flat-panel detector that, e.g., consists of several million X-ray sensitive elements arranged in a 2D grid that covers an area of about $30\,\text{cm} \times 40\,\text{cm}$ [2]. Another important fact is that C-arm systems were initially designed exclusively for acquiring 2D projections from various points of view [60] – the concepts of 3D CT were introduced as a standard feature of C-arm systems in the late 1990s [88].

The practical benefit of these two medical CT systems depends on the quality of the image reconstruction. For a long time, image quality issues were dominated not by the reconstruction algorithm but by the fact that the physical processes during data acquisition deviate to some respect from the data assumptions of the reconstruction algorithm – this inconsistency yields reconstruction artifacts. However, due to improvements in hardware and data processing, this mismatch between the data model and physical reality was reduced successively so that nowadays, the performance of the reconstruction algorithm becomes increasingly decisive for the resulting image quality. Considering the fact that CT image reconstruction on many existing systems is carried out using methods that are variations of approaches introduced more than 20 years ago [71], the consideration of novel reconstruction approaches may be the key for improving the overall system performance.

1.3   Scope and Original Contribution of this Thesis

In this thesis, we present and thoroughly evaluate various novel approaches to achieve image reconstruction from static objects on medical X-ray CT systems. The new methods come with advantages in image quality and/or efficiency compared to the conventional approaches that are typically considered in existing CT systems. Two of these presented methods are original and some of their concepts have been published in peer-reviewed journals; see [27, 29].

In the first part of this thesis, we derive and evaluate a novel analytic method for 2D image reconstruction from projection data measured in the geometry of the diagnostic CT scanner. Our novel approach is primarily designed to be computationally more efficient compared to classical approaches, by avoiding the application of a specific weighting factor during computation. In addition to that, it also yields improvements in the noise characteristics of the resulting images without noticeably sacrificing resolution. In the second part of this thesis, we consider 3D image reconstruction in the geometry of medical C-arm systems and present, in a uniform way, three methods recently suggested in the literature to accomplish that task. We describe a methodology for detailed comparison of image quality in C-arm CT and use this methodology to compare these three reconstruction methods to each other, but also to the reconstruction method currently in use in many existing C-arm systems. We then derive a novel, original approach for image reconstruction from C-arm data that comes along without any geometric approximations during its derivation, in contrast to the methods described before. It thus aims at achieving higher accuracy in the reconstruction results, in particular compared to the method currently used in most C-arm systems. Our new method involves analytic steps and also a 2D iterative scheme to recover 3D object density, and is furthermore designed to naturally cope with some degree of truncation in the acquired projection images.

Each of the two original reconstruction methods that we present in this thesis is carefully derived from known theory, thoroughly numerically evaluated against other competitive methods using computer-simulated CB data and also tested for image reconstruction from projection data acquired with commercially-available X-ray CT systems.

1.4 Outline of this Thesis

This thesis is structured as follows. Chapter 2 describes the standard CT data model, which is a prerequisite for the considerations in the subsequent chapters. The main body of this thesis, which follows this introductory chapter, is divided into two parts that are about image reconstruction in the 2D scenario (chapters 3 and 4) and in the 3D scenario (chapters 5, 6 and 7), respectively. Each of these parts starts with a chapter that reviews the classical theory of image reconstruction in the respective scenario. In these review chapters, we give derivations of the fundamental concepts wherever appropriate, and also present numerical examples to illustrate the corresponding theory. In the subsequent chapters of each part we thoroughly present our original contributions, in the following sequence:

Chapter 4 presents our novel, original filtered-backprojection method for 2D image reconstruction in the geometry of the diagnostic CT-scanner. In sections 4.2 and 4.3, we derive our method and point out its differences from the conventional approaches. Our novel approach is thoroughly evaluated and compared to the analytic reconstruction method of Noo *et al.* [67] in section 4.4. The evaluation is based on computer-simulated data and carried out in terms of spatial resolution, image noise and computational efficiency. Section 4.5 presents an evaluation based on real projection data acquired with a commercially-available CT scanner. Final discussions and conclusions are given in section 4.6.

Chapter 6 is focussed on 3D image reconstruction in the circular short-scan cone-beam acquisition geometry with a flat detector, i.e., in the geometry of most modern C-arm systems, which is formally introduced in section 6.2. We then present four state-of-the-art methods suggested for image reconstruction from short-scan circular cone-beam data, in sections 6.3, 6.4 and 6.5, and compare the image quality achievable with these methods in section 6.6. Our comparative image quality study is based on a uniform evaluation framework and carried out in terms of spatial resolution (section 6.6.1), contrast-to-noise ratio (section 6.6.2), cone-beam artifacts (section 6.6.3) and axial truncation artifacts (section 6.6.4). Section 6.7 gives conclusions and discussions about our comparison study.

Chapter 7 presents our novel, original factorization approach for circular short-scan cone-beam reconstruction. The general theoretical background of our method is illustrated in section 7.2. We then suggest, in section 7.3, a numerical scheme to implement from this theory a practical cone-beam reconstruction algorithm. The performance of this factorization algorithm is then evaluated and compared to that of the methods described earlier in this thesis. Section 7.6 is about reconstruction from cone-beam data collected with a clinical C-arm system. It first describes specific aspects of the geometry of existing C-arm systems and presents modifications we considered in our algorithm to cope with these geometric aspects. Reconstruction results of a physical thorax phantom are shown in section 7.6.3 and final discussions on our factorization approach are given in section 7.7.

In the final chapters of this thesis, we present an overall conclusion about our research and give an outlook about possible future theoretical and algorithmic developments of the specific topics discussed in this thesis and of the field of CT image reconstruction in general. Note finally that we use a notation scheme where a symbol is in general restricted to the

chapter in which it is introduced. Some symbols are, however, used throughout various chapters; these symbols are summarized in the glossary at the end of this thesis.

Chapter 2

The Data Model in CT

This chapter briefly describes the standard data model of X-ray CT, i.e., the model used to establish a formal relation between the measured data and the object under investigation. This formal relation is essential for the development of reconstruction algorithms, and thus also forms the backbone of the algorithms discussed in the following chapters.

Projection data acquired with modern CT systems is the result of an X-ray source that emits X-ray photons and many X-ray sensitive detector elements with each element measuring incoming radiation. Clearly, source and detector elements need to be located on distinct sides of the investigated object; in medical CT devices, which are the focus of this thesis, the distance between these two entities is about 1 to 1.5 meters, thus providing enough space for the patient to be conveniently placed in between. Compared to this geometric scale, both the X-ray focal spot and each considered detector element are tiny objects with typically only about one millimeter width and length [71].

Let us focus on one arbitrary sample of the X-ray data set from now on, i.e., on the measurement obtained at one single detector element at one point in time; the formal description of this data sample is based on a simplification on the real physical processes. First, it is assumed that both, focal spot of the X-ray source and the considered detector element are punctiform. In other words, X-ray photons are assumed to diverge from an infinitessimately small area centered on the actual X-ray focal spot and all photons registered by the detector element are assumed to pass through the central point on that finite size detector region. The ray that connects the points representing X-ray source and detector element will be referred to as a measurement ray in the following and will be denoted using the symbol $\mathcal{L}$. It is furthermore assumed that the source emits monochromatic X-radiation and that the direction in which each X-ray photon advances in space remains unchanged after emission. The number of photons sent from the source point along the considered line $\mathcal{L}$ will be denoted by the integer N_S and the amount of photons eventually registered at the detector element as N_D. The ratio of these two photon counts, N_D and N_S, contains information about the attenuation characteristic of the material along $\mathcal{L}$ as will become clearer below.

Let the value $\mu \geq 0$ denote the linear X-ray attenuation coefficient of the investigated object. Values of μ are commonly expressed in a scale (the Hounsfield scale [71]) that is defined relative to the attenuation of water, for which we use the value $\mu_{water} = 0.01836 \, \text{mm}^{-1}$ throughout this thesis. The linear attenuation coefficient is converted into values of the Hounsfield scale as [47]

$$\frac{\mu - \mu_{water}}{\mu_{water}} \times 1000. \tag{2.1}$$

7

Consequently, the absence of attenuating material corresponds to a value of -1000 Hounsfield units (HU), while the attenuation of water is given, for instance, as $0\,\text{HU}$. The attenuation coefficients of important structures of the human body, such as those of bones or of different organs, are given in [71].

Beer's law [71] then introduces the following relation between the object attenuation coefficient and the X-ray photon measurements:

$$N_D = N_S\, e^{-\int_{t_S}^{t_D} \mu_{\mathcal{L}}(t)\, dt}. \tag{2.2}$$

In (2.2), $\mu_{\mathcal{L}}(t)$ denotes the attenuation coefficient of the object along the considered measurement ray $\mathcal{L}$, while t is here the coordinate that defines locations on $\mathcal{L}$. The values t_S and t_D denote the positions of the source and the detector element along $\mathcal{L}$, respectively; see Figure 2.1 for an illustration.
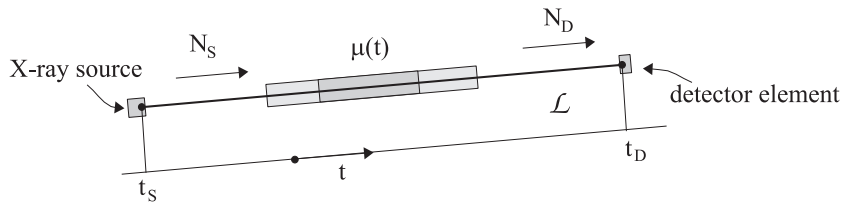
Figure 2.1: Illustration of one exemplary measurement ray $\mathcal{L}$. A total of N_S photons are emitted from the X-ray source along this ray; they are attenuated by the material along $\mathcal{L}$ so that only N_D photons are finally registered by the detector element.

In words, following the CT data model, each X-ray measurement contains information about the integral of the object X-ray attenuation coefficient[1] along the corresponding measurement ray, and this integral is obtained as

$$\int_{t_S}^{t_D} \mu_{\mathcal{L}}(t)\, dt = \ln\frac{N_S}{N_D}. \tag{2.3}$$

Note that (2.3) has to be understood in an approximate sense, since some subordinate physical effects are disregarded in the presented model. These effects include the impacts of finite size X-ray source and finite size detector elements on the measured data as well as the impacts of multi-energetic X-radiation and of photon scatter [71]. Equation (2.3), however, significantly supports the design of reconstruction algorithms, because it allows us to relate the task of image reconstruction to the task of inverting a system of integral equations of the object density function. The ray-integral data model thus establishes a link to a well-understood mathematical field that may provide practical solutions to the CT image reconstruction problem. This model is, however, only used for the design of reconstruction algorithms, whereas for numerical evaluation of the algorithmic performance, we involve in general projection data that contains several physical effects, as we will explain in the corresponding evaluation sections of this thesis. Note also that the geometric arrangement

---

[1]Throughout this thesis, we will frequently use the term object density instead of the expression linear X-ray attenuation coefficient. Technically, this is an abuse of the English language (these two entities are not necessarily identical), but it helps us to keep the terminology within this thesis less cumbersome.

of all measurement rays occurring during the X-ray CT data acquisition significantly determines both feasibility and difficulty of this reconstruction task [39], as will become clearer in the following chapters.

Chapter 3

Classical Theory for Image Reconstruction in Two Dimensions

This chapter introduces the classical theory about reconstruction of 2D objects from 1D projection data. The plane on which these objects are defined will be referred to as the image plane from now on. A Cartesian, right-handed world coordinate system with coordinates x and y is introduced on the image plane such that an arbitrary position can be addressed using the coordinate vector $\underline{x} = (x, y)^{\mathrm{T}}$. Note that here and throughout the rest of this thesis, the superscript T denotes the transpose of a matrix or vector.

The spatial density distribution of the investigated object on the 2D image plane will be described using the function $f(\underline{x})$. It is assumed that the object is of finite size and furthermore approximately centered on the origin of the world coordinate system. More specifically, the object is assumed to fit entirely into a circular region of radius R_o around the world coordinate origin; this region will be denoted as Ω_f from now on, so that

$$f(\underline{x}) = 0 \qquad \text{for all} \qquad \underline{x} \notin \Omega_f := \{\underline{x} \,|\, \sqrt{x^2 + y^2} \le R_o\}. \tag{3.1}$$

3.1 2D Radon Transform and Its Inversion

Section 3.1 deals with the problem of image reconstruction from integral data that is acquired with measurement lines aligned parallel to each other. This specific scenario corresponds to the least complex geometry discussed in this thesis and is referred to as the 2D parallel-beam geometry from now on. Note that direct data acquisition in this geometry is not very practical and has only be considered in CT scanners of the first generation [47]. However, this scenario is interesting from a theoretical perspective, because image reconstruction in the 2D parallel-beam geometry is a direct application of the theory of Radon integral transforms [46] that has been introduced by Johann Radon in 1917 [76].

3.1.1 2D Parallel-beam Geometry

Consider an arbitrary set of parallel lines in the image plane. This set may be specified, following the scheme used in [4], by the unit vector $\underline{\theta} = (\cos\theta, \sin\theta)^{\mathrm{T}}$ that is perpendicular to all lines in the set. In this notation, parameter θ corresponds to the angle that vector $\underline{\theta}$ describes with the x-axis, measured in counterclockwise direction. One specific element among all lines in the set defined by any $\underline{\theta}$ can be addressed by its signed distance $s \in \mathbb{R}$

from the origin $(0,0)^{\mathrm{T}}$ in the direction of $\underline{\theta}$. The selection of parameters θ and s then defines one specific line in the image plane that will be denoted as

$$\mathcal{L}(\theta, s) := \{\underline{x} \mid \underline{x} \cdot \underline{\theta} = s\}. \tag{3.2}$$
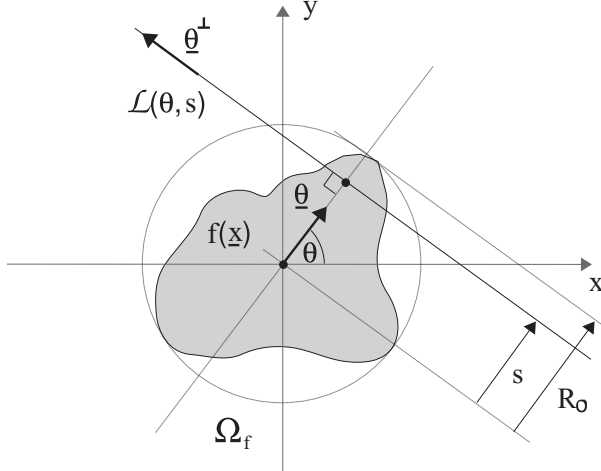
Figure 3.1: Illustration of the 2D parallel-beam geometry. The investigated object $f(\underline{x})$ (dark gray) is contained in the circular region Ω_f of radius R_o. One black, example line $\mathcal{L}(\theta, s)$ is shown, which is orthogonal to $\underline{\theta}$, parallel to $\underline{\theta}^\perp$ and has distance $|s|$ from the origin of the 2D image plane.

3.1.2 The 2D Radon Transform

The 2D Radon transform [46, 63] of a function f is defined as

$$
\begin{aligned}
\mathcal{R}f(\theta, s) &= \iint\limits_{\underline{x} \in \mathcal{L}(\theta, s)} f(\underline{x})\, d\underline{x} = \iint\limits_{\mathbb{R}^2} f(\underline{x})\, \delta(\underline{x} \cdot \underline{\theta} - s) d\underline{x} \\
&= \int\limits_{-\infty}^{\infty} f(s\underline{\theta} + t\underline{\theta}^\perp) dt.
\end{aligned}
\tag{3.3}
$$

In this definition, δ denotes the Dirac delta function and $\cdot$ the inner vector product [11]. Hence, the Radon transform operator delivers a function $\mathcal{R}f$ that contains information about integrals of f along lines, such that the value $\mathcal{R}f(\theta, s)$ corresponds to the integral of f along the line $\mathcal{L}(\theta, s)$. Following the data model described in section 2, this value of the 2D Radon transform directly corresponds to the X-ray measurement sample acquired with detector element and X-ray source both located on $\mathcal{L}(\theta, s)$; this measurement sample will be denoted as $p(\theta, s)$. Data acquisition in the 2D parallel-beam geometry thus yields direct access to values of the 2D Radon transform and we have

$$p(\theta, s) = \mathcal{R}f(\theta, s). \tag{3.4}$$

Function p will be denoted as 2D parallel-beam data in the following and 2D parallel-beam data at fixed θ will be called a 2D parallel-beam projection of the object at projection angle

θ. Clearly, any line $\mathcal{L}(\theta, s)$ with $|s| > R_o$ has no intersection with the object due to the initial assumption (3.1), and consequently

$$p(\theta, s) = 0 \qquad \text{for} \qquad |s| > R_o. \tag{3.5}$$

Therefore, if $p(\theta, s)$ is given for all $s \in [-R_o, R_o]$, the entire set of potentially non-zero values of the 2D Radon transform of f at parameter θ are known. The 2D parallel-beam projection at the corresponding projection angle will be called non-truncated from now on.

Consider the following example for an illustration of the 2D Radon transform operator [4]. Let

$$f_{circ}(\underline{x}) = \begin{cases} 1 & \text{if } \sqrt{x^2 + y^2} \leq R_{circ} \\ 0 & \text{otherwise} \end{cases} \tag{3.6}$$

define a circular object of homogeneous density 1 that is centered on the world coordinate origin and has radius $R_{circ} \leq R_o$. Substituting f_{circ} for f in the second line of (3.3) and computing the length of intersection between the circular object and measurement lines $\mathcal{L}$, as depicted in the left side of Figure 3.2, leads to the 2D Radon transform of f_{circ} as

$$\mathcal{R}f_{circ}(\theta, s) = \begin{cases} 2\sqrt{R_{circ}^2 - s^2} & \text{if } |s| \leq R_{circ} \\ 0 & \text{otherwise.} \end{cases} \tag{3.7}$$

In this example, $\mathcal{R}f_{circ}(\theta, s)$ is independent of θ; the parallel-beam projection of f_{circ} at an arbitrary projection angle is illustrated on the right side of Figure 3.2.
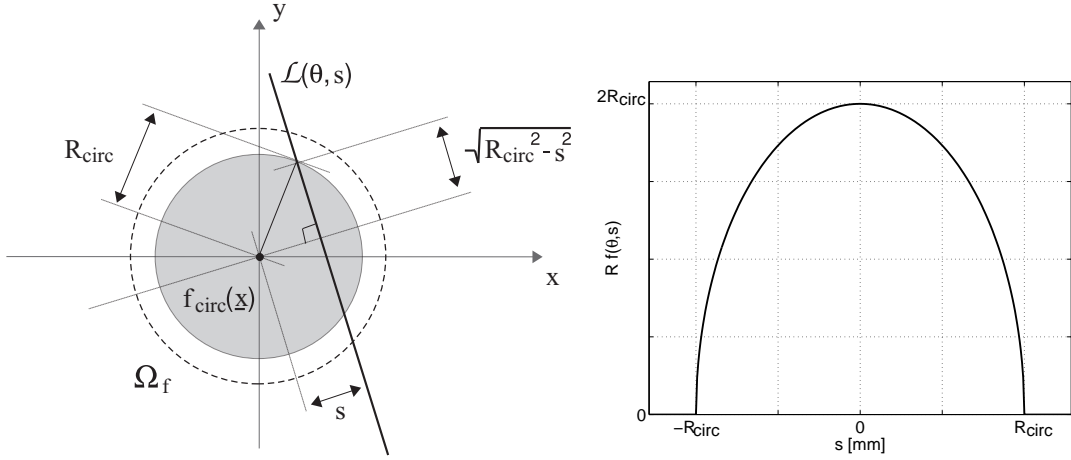
Figure 3.2: Illustration of the 2D Radon transform operator. (Left) The gray circle corresponds to the homogeneous object of radius R_{circ}, which is entirely contained in Ω_f. We illustrate for one example line $\mathcal{L}(\theta, s)$ how to obtain the length of its intersection with the object. (Right) 2D parallel-beam projection of f_{circ} at arbitrary projection angle $\theta \in [0, \pi]$.

The following list summarizes properties of the 2D Radon transform operator that are important for the derivations presented in the remainder of this chapter [4]. The interested reader may find further details about the 2D Radon transform, for instance, in [46, 63, 19].

Basic properties of the 2D Radon transform :

- Linearity:

$$\mathcal{R}\left(\sum_{i=1}^{N} c_i f_i\right)(\theta, s) = \sum_{i=1}^{N} c_i \,\mathcal{R} f_i(\theta, s) \tag{3.8}$$

- Periodicity:

$$\mathcal{R} f(\theta + 2\pi k, s) = \mathcal{R} f(\theta, s); \qquad k \in \mathbb{Z} \tag{3.9}$$

- Redundancy:

$$\mathcal{R} f(\theta + \pi, -s) = \mathcal{R} f(\theta, s) \tag{3.10}$$

The linearity of the operator $\mathcal{R}$ follows from its definition in (3.3) and from the linearity of the integral operation. The 2π periodicity in θ and the redundancy property, on the other hand, are a direct result from (3.3) and from the characteristics of the involved trigonometric functions.

2D Radon transform and object modification :

- Object translation:

  The 2D Radon transform of objects $f(\underline{x})$ and $f_0(\underline{x})$ that are related to each other through a translation with the translation vector $\underline{x}_0$, such that $f(\underline{x}) = f_0(\underline{x} - \underline{x}_0)$, satisfies the following relation [4]:

$$
\begin{aligned}
\mathcal{R} f(\theta, s) &= \iint\limits_{\mathbb{R}^2} f_0(\underline{x} - \underline{x}_0)\delta(\underline{x} \cdot \underline{\theta} - s)\, d\underline{x} \\
&= \iint\limits_{\mathbb{R}^2} f_0(\underline{x}')\delta(\underline{x}' \cdot \underline{\theta} + \underline{x}_0 \cdot \underline{\theta} - s)\, d\underline{x}' \\
&= \iint\limits_{\mathbb{R}^2} f_0(\underline{x}')\delta(\underline{x}' \cdot \underline{\theta} - (s - \underline{x}_0 \cdot \underline{\theta}))\, d\underline{x}' \\
&= \mathcal{R} f_0(\theta, s - \underline{x}_0 \cdot \underline{\theta}).
\end{aligned}
\tag{3.11}
$$

- Linear object distortion:

  If the object f can be related to a reference object f_0 through a non-singular linear transformation, such as a rotation or a dilation, i.e., if $f(\underline{x}) = f_0(A\underline{x})$ with $A \in \mathbb{R}^{2 \times 2}$ and $\det A \neq 0$, it can be shown that

$$
\begin{aligned}
\mathcal{R} f(\theta, s) &= \iint\limits_{\mathbb{R}^2} f_0(A\underline{x})\delta(\underline{x} \cdot \underline{\theta} - s) d\underline{x} \\
&= \frac{1}{\det A} \iint\limits_{\mathbb{R}^2} f_0(\underline{x}')\delta(A^{-1}\underline{x}' \cdot \underline{\theta} - s) d\underline{x}' \\
&= \frac{1}{\det A} \iint\limits_{\mathbb{R}^2} f_0(\underline{x}')\delta(\underline{x}' \cdot A^{-T}\underline{\theta} - s) d\underline{x}' \\
&= \frac{1}{\det A} \frac{1}{\|A^{-T}\underline{\theta}\|} \iint\limits_{\mathbb{R}^2} f_0(\underline{x}')\delta\left(\underline{x}' \cdot \underline{\psi} - \frac{s}{\|A^{-T}\underline{\theta}\|}\right) d\underline{x}' \\
&= \frac{1}{\det A} \frac{1}{\|A^{-T}\underline{\theta}\|} \mathcal{R} f_0\left(\psi, \frac{s}{\|A^{-T}\underline{\theta}\|}\right),
\end{aligned}
\tag{3.12}
$$

where $\underline{\psi} = (\cos\psi, \sin\psi)^{\mathrm{T}} = (A^{-T}\underline{\theta})/\|A^{-T}\underline{\theta}\|$. In (3.12), $\det A$ denotes the determinant of matrix A and $\|\cdot\|$ denotes the Euclidean vector norm.

From the properties (3.8), (3.11) and (3.12) of the 2D Radon transform and the result of (3.7), 2D parallel-beam data can be readily constructed for any object that consist of the superposition of an arbitrary number of ellipses with arbitrary sizes, positions, rotations and densities. An object that belongs to this category is the Shepp-Logan phantom [46], which consists of 10 ellipses that are arranged to coarsely represent a cross-section through a human head. The density function of the Shepp-Logan phantom is shown on the left side of Figure 3.3.

2D parallel-beam data are commonly presented in a sinogram, i.e., a 2D image based on a Cartesian $\theta - s$ coordinate system, which is composed by mapping each value of the function p onto a gray value and assigning this gray value to the corresponding point in the sinogram space. This thesis follows the convention that a sinogram column corresponds to one 2D parallel-beam projection, whereas one row of the sinogram visualizes 2D parallel-beam data at fixed s. The sinogram of the Shepp-Logan phantom for $\theta \in [0, \pi]$ and $s \in [-R_o, R_o]$ with $R_o = 90\,\mathrm{mm}$ is presented on the right side of Figure 3.3.
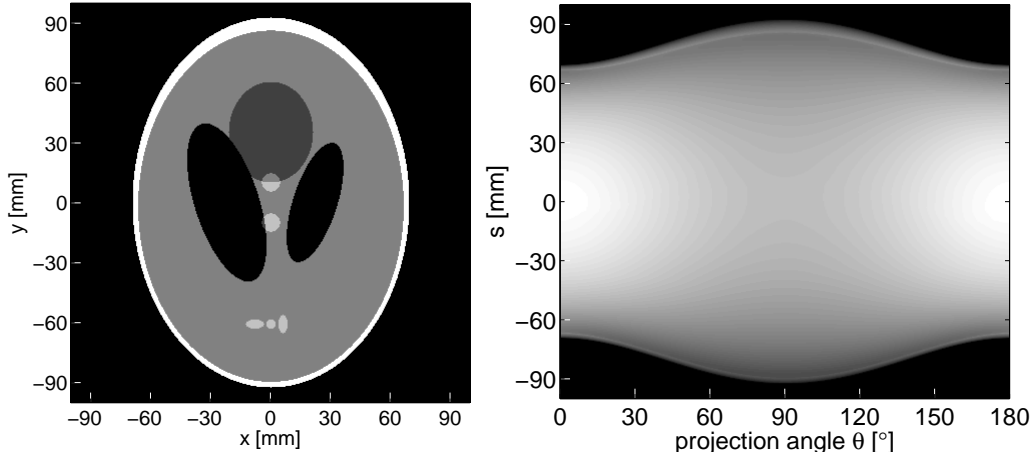
Figure 3.3: The 2D Shepp-Logan phantom. (Left) The object density function of the phantom in the grayscale window $[0\,\mathrm{HU}, 40\,\mathrm{HU}]$. (Right) Sinogram displaying the 2D parallel-beam data $p(\theta, s)$ of the Shepp-Logan phantom with $\theta \in [0, \pi]$ and $s \in [-90, 90]\,\mathrm{mm}$.

3.1.3 Concept of Backprojection

The backprojection operator $\mathcal{R}^{\#}$ transforms parallel-beam data $p(\theta, s)$ into the image $\mathcal{R}^{\#}p(\underline{x})$. This operator is defined implicitly by the relation [4]

$$< \mathcal{R}f, p > = < f, \mathcal{R}^{\#}p > \tag{3.13}$$

where $< \cdot, \cdot >$ denote scalar products that are in the 2D parallel-beam geometry given as

$$< \mathcal{R}f, p > = \int_{0}^{\pi} \int_{-\infty}^{\infty} \mathcal{R}f(\theta, s)p(\theta, s)\, ds\, d\theta \tag{3.14}$$

and

$$< f, \mathcal{R}^{\#} p > = \iint\limits_{\mathbb{R}^2} f(\underline{x}) \, \mathcal{R}^{\#} p(\underline{x}) \, d\underline{x}. \tag{3.15}$$

Using the definition of the 2D Radon transform (3.3) in (3.14) and applying the change of variable $\underline{x} = s\underline{\theta} + t\underline{\theta}^{\perp}$ of Jacobian 1 yields

$$< \mathcal{R}f, p > = \int\limits_{0}^{\pi} \int\limits_{-\infty}^{\infty} \int\limits_{-\infty}^{\infty} f(s\underline{\theta} + t\underline{\theta}^{\perp}) \, dt \, p(\theta, s) \, ds \, d\theta$$
$$= \int\limits_{0}^{\pi} \iint\limits_{\mathbb{R}^2} f(\underline{x}) p(\theta, \underline{x} \cdot \underline{\theta}) \, d\underline{x} \, d\theta. \tag{3.16}$$

Changing the order of integration in (3.16) and using the definitions (3.13) and (3.15) results in

$$\mathcal{R}^{\#} p(\underline{x}) = \int\limits_{0}^{\pi} p(\theta, \underline{\theta} \cdot \underline{x}) \, d\theta, \tag{3.17}$$

which is the wanted expression for the backprojection operator.

In order to obtain a valid backprojection result at a point $\underline{x}$ according to (3.17), 2D parallel-beam data need to be known for all $\theta \in [0, \pi)$ and within each parallel-beam projection at $s = \underline{x} \cdot \underline{\theta}$. The computation of $\mathcal{R}^{\#} p(\underline{x})$ thus requires integral data associated to all lines that contain $\underline{x}$. On the other hand, if 2D parallel-beam data are known for $\theta \in [0, \pi]$ and $s \in [-R_o, R_o]$, the function $\mathcal{R}^{\#} p$ can be computed everywhere in the image plane.
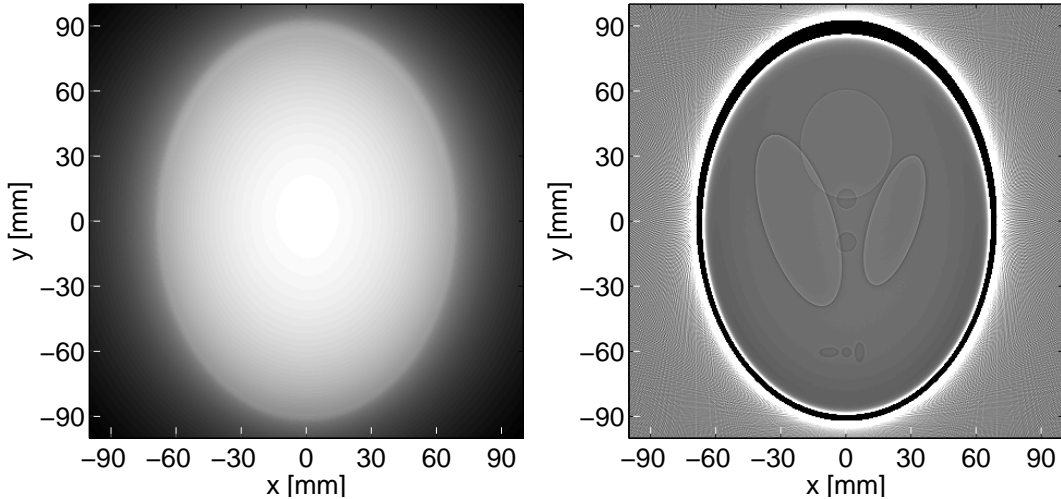
Figure 3.4: The effect of the backprojection operator $\mathcal{R}^{\#}$. (Left) Result of back-projecting the 2D parallel-beam data of the Shepp-Logan phantom. (Right) The outcome of applying the 2D Laplacian high-pass filter to the backprojection result shown in the left image, presented in a compressed grayscale window.

The left side of Figure 3.4 shows the result of backprojecting the 2D parallel-beam data of the Shepp-Logan phantom. As can be seen from this example, the resulting function does

not correspond to the object density f. However, the following relation can be established [46]:

$$
\begin{aligned}
\mathcal{R}^{\#}\mathcal{R}f(\underline{x}) &= \int_0^{\pi} \mathcal{R}f(\theta, \underline{\theta} \cdot \underline{x})\, d\theta = \int_0^{\pi} \int_{-\infty}^{\infty} f\left((\underline{\theta} \cdot \underline{x})\underline{\theta} + t\underline{\theta}^{\perp}\right) dt\, d\theta \\
&= \int_0^{\pi} \int_{-\infty}^{\infty} f(\underline{x} + t\underline{\theta}^{\perp})\, dt\, d\theta = \iint_{\mathbb{R}^2} \frac{1}{\|\underline{x} - \underline{x}'\|} f(\underline{x}')\, d\underline{x}'.
\end{aligned}
\tag{3.18}
$$

Hence, $\mathcal{R}^{\#}\mathcal{R}f$ corresponds to the result of convolving f with the 2D low-pass filter kernel $1/\|\underline{x}\|$. Discontinuities in the object density function f can be determined by applying the 2D Laplacian operator on $\mathcal{R}^{\#}\mathcal{R}f$ [4], see the right side of Figure 3.4. This approach, however, does not allow a quantitative recovery of the object density.

3.1.4 Classical Inversion Formula for the 2D Radon Transform

In the following, an inverse of the 2D Radon transform operator is derived. This result is based on a link between the 2D Fourier transform in $\underline{x}$ of the object density function and the 1D Fourier transform in s of the 2D parallel-beam data at projection angle θ. These Fourier transforms are given respectively as [46]

$$
\mathcal{F}_{\underline{x}}f(\underline{\xi}) = \iint_{\mathbb{R}^2} f(\underline{x})e^{-2\pi i \underline{\xi} \cdot \underline{x}}\, d\underline{x} \qquad \text{and} \qquad \mathcal{F}_s\mathcal{R}f(\theta, \sigma) = \int_{-\infty}^{\infty} \mathcal{R}f(\theta, s)e^{-2\pi i \sigma s}\, ds \tag{3.19}
$$

with the subscript parameter denoting the argument in which the transform is applied. The link between these two functions, which is known as the 2D Fourier slice theorem, is obtained as

$$
\begin{aligned}
\mathcal{F}_s\mathcal{R}f(\theta, \sigma) &= \int_{-\infty}^{\infty} \mathcal{R}f(\theta, s)e^{-2\pi i \sigma s}\, ds \\
&= \int_{-\infty}^{\infty} \int_{-\infty}^{\infty} f(s\underline{\theta} + t\underline{\theta}^{\perp})e^{-2\pi i \sigma s}\, dt\, ds \\
&= \iint_{\mathbb{R}^2} f(\underline{x})e^{-2\pi i \sigma \underline{\theta} \cdot \underline{x}}\, d\underline{x} \\
&= \mathcal{F}_{\underline{x}}f(\sigma\underline{\theta}).
\end{aligned}
\tag{3.20}
$$

The inversion formula for the 2D Radon transform is now derived in a similar fashion as in [4] by first expressing the object as the inverse 2D Fourier transform of $\mathcal{F}_{\underline{x}}f$, i.e., as

$$
f(\underline{x}) = \iint_{\mathbb{R}^2} \mathcal{F}_{\underline{x}}f(\underline{\xi})e^{2\pi i \underline{\xi} \cdot \underline{x}}\, d\underline{\xi} \tag{3.21}
$$

with $\underline{\xi} = (\xi_1, \xi_2)^{\mathrm{T}}$. The change of variable from Cartesian to polar coordinates

$$
\xi_1 = \sigma \cos\theta, \qquad \xi_2 = \sigma \sin\theta \tag{3.22}
$$

of Jacobian $|\sigma|$ and the use of the 2D Fourier slice theorem (3.20) transforms (3.21) into

$$
\begin{aligned}
f(\underline{x}) &= \int_0^\pi \int_{-\infty}^\infty |\sigma| \mathcal{F}_{\underline{x}} f(\sigma\underline{\theta}) e^{2\pi i \sigma \underline{\theta} \cdot \underline{x}} \, d\sigma \, d\theta \\
&= \int_0^\pi \int_{-\infty}^\infty |\sigma| \mathcal{F}_s \mathcal{R} f(\theta, \sigma) e^{2\pi i \sigma \underline{\theta} \cdot \underline{x}} \, d\sigma \, d\theta
\end{aligned}
\tag{3.23}
$$

and thus into an analytical inversion approach for the 2D Radon transform, which is based on the following steps:

Step 1 − **1D Filtering:** 2D parallel-beam data at fixed θ are filtered in s to obtain

$$
\begin{aligned}
p_F(\theta, s) &= \int_{-\infty}^\infty \mathcal{F}_s h_{ramp}(\sigma) \mathcal{F}_s p(\theta, \sigma) e^{2\pi i \sigma s} \, d\sigma \tag{3.24} \\
&= \int_{-R_o}^{R_o} h_{ramp}(s - s') p(\theta, s) \, ds' \tag{3.25}
\end{aligned}
$$

with the filter kernel h_{ramp} defined in frequency and spatial domain, respectively, as

$$
\mathcal{F}_s h_{ramp}(\sigma) = |\sigma| \qquad \text{and} \qquad h_{ramp}(s) = \lim_{b \to \infty} \int_{-b}^b |\sigma| e^{2\pi i \sigma s} d\sigma.
\tag{3.26}
$$

The function h_{ramp} is of infinite support and known as the ramp filter kernel [46]. Note that the limits of integration in (3.25) were adjusted to $-R_o$ and R_o, respectively, and that this adjustment became possible because of the bounded support of p.

Step 2 − **2D Backprojection:** Backprojection of the filtered parallel-beam projections onto the image plane using the operator $\mathcal{R}^\#$ yields the object density function as

$$
f(\underline{x}) = \int_0^\pi p_F(\theta, \underline{x} \cdot \underline{\theta}) \, d\theta.
\tag{3.27}
$$

The analytical filtered backprojection (FBP) inversion method presented in (3.25)-(3.27) is referred to as the classical 2D Radon inversion method from now on. For a valid recovery of the value of f at a single point $\underline{x}$, this method requires filtered parallel-beam data p_F to be known for all projection angles $\theta \in [0, \pi)$, using in every projection the sample at $\underline{x} \cdot \underline{\theta}$. On the other hand, the values p_F at any fixed angle θ can only be computed if the corresponding parallel-beam projection is non-truncated, because the convolution equation (3.25) corresponds to a global filter operation. In order to allow object density to be recovered at a single point, the 2D Radon inversion formula thus requires non-truncated projections for $\theta \in [0, \pi)$, or, in other words, the integral data associated to every line intersecting the object. Note that if recovery of f according to (3.25)-(3.27) can be achieved at some point $\underline{x}$, then it is achievable everywhere within Ω_f.

3.1.5 Parallel Beam Reconstruction Formula for Redundant Data

In the previous section, an inversion formula for the operator $\mathcal{R}$ was given that requires non-truncated parallel-beam data for $\theta \in [0, \pi]$. If p is, for instance, known over an interval $\theta \in [0, \theta_{max}]$ with $\pi < \theta_{max} < 2\pi$, however, the 2D parallel-beam data contains redundancies. That means that data samples at coordinates (θ, s) and at $(\theta + \pi, -s)$ are identical, which follows from (3.10); see Figure 3.5 for illustration.
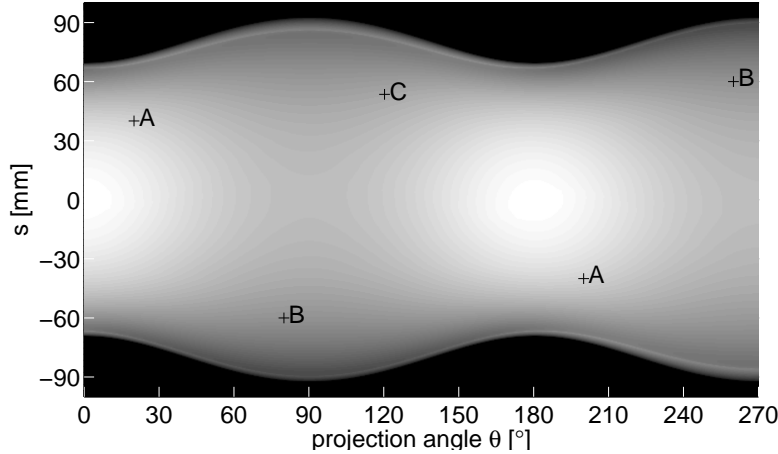
Figure 3.5: Sinogram illustrating the 2D parallel-beam data $p(\theta, s)$ of the Shepp Logan phantom for $\theta \in [0, 270°]$. The points marked with A correspond to redundant data samples, as do the points marked with B. The data sample at C, however, is contained only once in p.

A straight-forward extension of the classical 2D Radon inversion formula for recovery of f by simply adjusting the limits of integration in (3.27) to 0 and θ_{max} does not lead to valid results. This is, because 2D Radon data that are contained twice in the parallel-beam data set would contribute more to the final reconstruction than non-redundant data samples. For a valid reconstruction, these contributions have to be normalized, or in other words, the total contribution of each 2D Radon value to the final reconstruction has to be unity, independently of how often this 2D Radon value is contained in the parallel-beam data set. This normalization may be achieved by multiplying p prior to data filtering with a weighting function $m(\theta, s)$ that has to be smooth, 2π-periodic in the angular parameter θ and that needs to satisfy the condition

$$m(\theta, s) + m(\theta + \pi, -s) = 1 \tag{3.28}$$

while $m(\theta, s) = 0$ for parameter θ that describes sets of parallel lines for which no integral-data is known. In words, the weighting factors for pairs of parameters θ and s describing the same geometric line $\mathcal{L}$ have to add up to 1 and function m needs to vanish for parameters for which p is not known. The inversion formula that provides valid reconstruction from redundant 2D Radon data is then given as [4]

$$f(\underline{x}) = \int_{0}^{\theta_{max}} \int_{-\infty}^{\infty} h_{ramp}(\underline{x} \cdot \underline{\theta} - s) m(\theta, s) \mathcal{R}f(\theta, s) \, ds \, d\theta. \tag{3.29}$$

A common additional constraint in this context is to require that $m(\theta, s) \geq 0$ so that each measured data sample has positive contribution to the final reconstruction.

3.1.6   Numerical Reconstruction Algorithm

In the practical context of 2D CT, reconstruction of object density is usually carried out from sampled 2D parallel-beam data. CT scanners of the first generation [71, 48], for instance, consisted of an X-ray source and one detector element and therefore acquired one measurement ray, i.e. one sample of p, at a time. During the scan, the source-detector assembly was translated and rotated, which allowed function p to be determined within the desired intervals in θ and s, but only at a finite number of sampling positions depending on the increments of the scanner motion. This section presents a numerical FBP algorithm based on the results of Section 3.1.4 to compute from the discrete 2D parallel-beam data an estimate of the true object density. This estimate will be denoted as f^e where the superscript e emphasizes that the entity is computed from sampled data. For convenience, but without loss of generality, we assume that the sampling in both s and θ is uniform with discretization steps given as Δs and $\Delta \theta$, respectively.
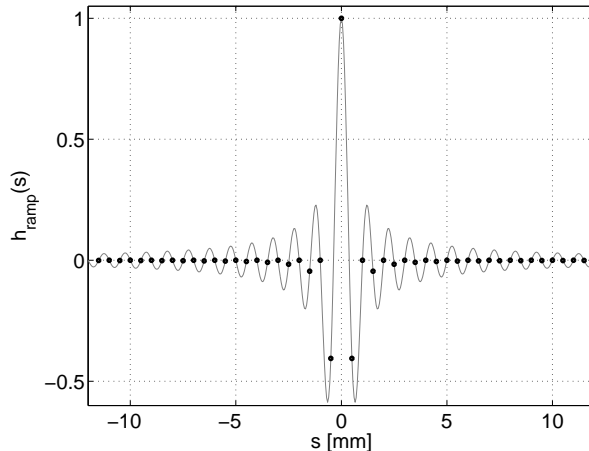
Figure 3.6: The ramp filter h^b_{ramp} with rectangular band-limitation, presented in spatial domain. The black markers illustrate the sampling positions at which the kernel is discretized using the discretization scheme explained in the text.

The suggested numerical reconstruction algorithm achieves data filtering through discretizing (3.25) at positions $k\Delta s$ with $k \in \mathbb{Z}$. Furthermore, the ramp filter kernel in (3.25) is replaced with the bandlimited ramp-filter kernel that has rectangular apodization

$$h^b_{ramp}(s) = \int_{-b}^{b} |\sigma| e^{2\pi i \sigma s} d\sigma = \frac{b}{\pi s} \sin 2\pi bs + \frac{\cos 2\pi bs - 1}{2\pi^2 s^2} \qquad (3.30)$$

in order to avoid aliasing in the filter result. In compliance with Shannon's sampling theorem [46] the bandwidth is set to $1/(2\Delta s)$, so that:

$$h^b_{ramp}(s) = \frac{1}{2\Delta s \pi s} \sin\left(\frac{\pi s}{\Delta s}\right) + \frac{1}{2\pi^2 s^2} \left(\cos\left(\frac{\pi s}{\Delta s}\right) - 1\right). \qquad (3.31)$$

Figure 3.6 shows the filter kernel h^b_{ramp} with the positions where this kernel is evaluated using the suggested discretization scheme. For improved computational efficiency, the 1D convolution in (3.25) is carried out using standard signal processing techniques, i.e., using multiplication in frequency domain and using the fast-Fourier transform (FFT) and the inverse FFT to convert between the domains.

The backprojection step of the reconstruction formula is here implemented by approximating the integral in equation (3.27) with a discrete sum according to the rectangular rule for numerical integration. We furthermore use linear interpolation in s in order to obtain for each projection angle the data sample at $\underline{x} \cdot \underline{\theta}$ from the filtered parallel-beam projection p_F, which is required for reconstruction at $\underline{x}$.
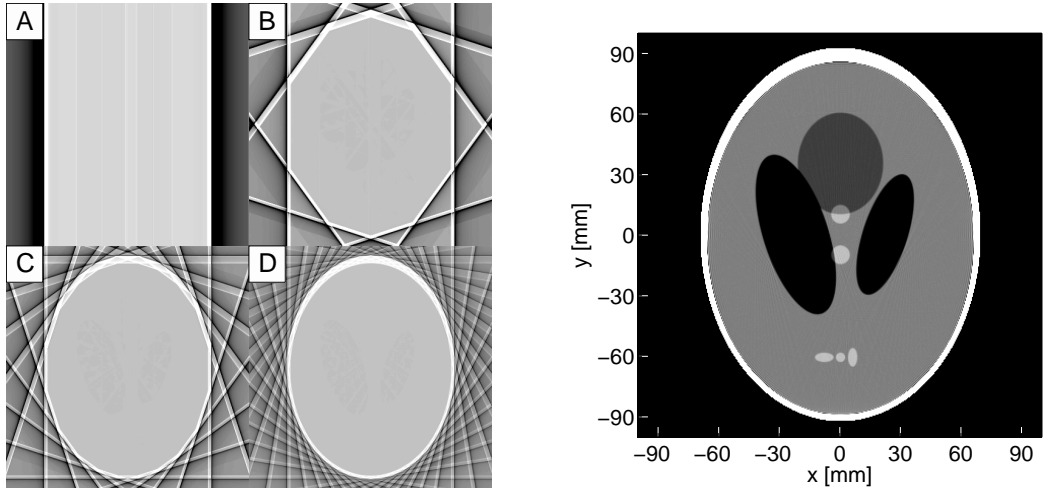
Figure 3.7: Illustration of the numerical algorithm for reconstruction from discretized 2D parallel-beam data. (Left) Intermediate reconstruction results obtained by backprojecting only data corresponding to (A) the first projection at $\theta = 0°$ and data corresponding to (B) 5, (C) 10 and (D) 20 projections with projection angles that are multiples of 36°, 18° and 9°, respectively. (Right) Final reconstruction result f^e obtained using all 360 projections in the grayscale window $[0\,\mathrm{HU}, 40\,\mathrm{HU}]$.

The steps of the numerical algorithm presented in this section are illustrated on the reconstruction of the Shepp-Logan phantom from its 2D parallel-beam data. Projection data was simulated for 360 projection angles with $\Delta\theta = 0.5°$ and using in each parallel-beam projection 400 samples in s with $\Delta s = 0.5\,\mathrm{mm}$. Reconstruction was obtained on a Cartesian grid in x and y with isotropic sampling $\Delta x = \Delta y = 0.5\,\mathrm{mm}$. Intermediate reconstruction results using only a subset of the parallel-beam projections are presented in the left of Figure 3.7, whereas the final reconstruction result $f^e(\underline{x})$ is shown on the right side of this figure.

3.2   2D Fan-Beam Transform and Its Classical Inversion Formula

The considerations in the previous section provided a general introduction into the concepts of analytical reconstruction theory. Most practical CT scanners used for 2D imaging, however, do not acquire data in the parallel-beam geometry. Data acquisition happens with measurement rays that occur in groups of fans on the image plane rather than in parallel sets [47]. This described scenario will here be referred to as the 2D fan-beam geometry, and image reconstruction in this geometry will be discussed below.

3.2.1   The 2D Fan-Beam Geometry

Diagnostic CT scanners may be used to acquire 1D projection data by sending X- rays from the X-ray focal spot through the image plane; these rays pass the object and eventually interact with an appropriately located X-ray detector [71, 47]. During the scan, X-ray source and detector typically rotate as a single assembly around the object under investigation, so that projections are acquired with the X-ray focal spot moving along a circular trajectory on the image plane. The radius of this trajectory will be denoted using the symbol R and since the source is necessarily located outside the object region Ω_f, we have $R > R_o$. Without loss of generality, it is here assumed that the circular trajectory is centered on the image plane origin $(0,0)^{\mathrm{T}}$ and that the source is located on the positive x-axis at the start of the scan. The function

$$\underline{a}(\lambda) = (R\cos\lambda, R\sin\lambda)^{\mathrm{T}} \tag{3.32}$$

then gives the source location during acquisition; the trajectory parameter λ corresponds to the source polar angle and may take values $\lambda \in [0, \lambda_{max}]$ in our geometric set-up.
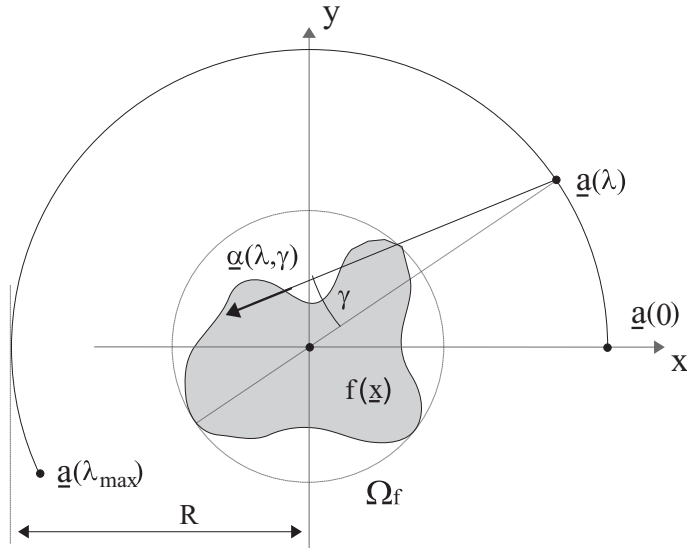
Figure 3.8: Illustration of the 2D fan-beam geometry, where a ray is described with parameters λ and γ. The quantity $\lambda \in [0, \lambda_{max}]$ corresponds to the polar angle of the ray source and γ denotes the ray fan-angle.

It is assumed that data acquisition is carried out with a curved detector [71], i.e., a detector where each element has fixed distance D from the point $\underline{a}(\lambda)$. The rays that

connect the source point with all detector elements form a fan and for each such fan, a central ray can be identified, i.e., the ray that passes through the origin of the image plane $(0, 0)^{\mathrm{T}}$. Each ray within one fan may then be addressed using the fan angle $\gamma \in [-\gamma_m, \gamma_m]$ that it describes with the central ray, where γ increases in the clockwise direction. The quantity γ_m denotes the absolute value of the fan-angle of the ray that intersects with the first or last element of the detector, respectively. We assume that the detector is large enough so that all rays that diverge from the source and intersect the region Ω_f also hit the detector and this condition will be met if $\gamma_m = \mathrm{asin}(R_o/R)$.

For a description of the 2D fan-beam data let us furthermore introduce the two unit vectors

$$
\begin{align}
\underline{e}_u(\lambda) &= (-\sin\lambda, \cos\lambda)^{\mathrm{T}} \tag{3.33} \\
\underline{e}_w(\lambda) &= (\cos\lambda, \sin\lambda)^{\mathrm{T}}. \tag{3.34}
\end{align}
$$

Note that the vector $\underline{e}_u(\lambda)$ is tangent to the source trajectory at $\underline{a}(\lambda)$ while $\underline{e}_w(\lambda)$ gives the direction from the origin $(0, 0)^{\mathrm{T}}$ towards the source $\underline{a}(\lambda)$. The unit vector along the ray described with parameters λ and γ is then given as

$$
\underline{\alpha}(\lambda, \gamma) = \sin\gamma \, \underline{e}_u(\lambda) - \cos\gamma \, \underline{e}_w(\lambda). \tag{3.35}
$$

3.2.2 The 2D Fan-Beam Transform

According to the data model of section 2, measurements in the fan-beam geometry then yields samples of the function

$$
g(\lambda, \gamma) = \int_0^\infty f\left(\underline{a}(\lambda) + t\underline{\alpha}(\lambda, \gamma)\right) dt. \tag{3.36}
$$

Function g will be referred to as fan-beam data from now on and fan-beam data at fixed λ will be called a fan-beam projection. Due to the geometric assumptions introduced in the previous section

$$
g(\lambda, \gamma) = 0 \qquad \text{for} \qquad |\gamma| > \gamma_m \tag{3.37}
$$

so that all acquired fan-beam projections are non-truncated.

Since $\underline{a}(\lambda)$ is always outside the region Ω_f, either the ray facing in direction $\underline{\alpha}$ or the one facing in direction $-\underline{\alpha}$ will never intersect the object. Consequently, the limits of integration in (3.36) can be modified to

$$
g(\lambda, \gamma) = \int_{-\infty}^\infty f\left(\underline{a}(\lambda) + t\underline{\alpha}(\lambda, \gamma)\right) dt \tag{3.38}
$$

without changing the fan-beam data function. This modification allows us to establish a link between samples of fan-beam data and 2D Radon data, as described below. A specific selection of parameters λ and γ defines one specific ray, and thus also one specific line $\mathcal{L}$ on the image plane. The unit vectors parallel and orthogonal to this line $\mathcal{L}$ are given, respectively, as

$$
\underline{\theta}^\perp(\lambda, \gamma) = \underline{\alpha}(\lambda, \gamma) \qquad \text{and} \qquad \underline{\theta}(\lambda, \gamma) = \cos\gamma\underline{e}_u(\lambda) + \sin\gamma\underline{e}_w(\lambda). \tag{3.39}
$$

Following this geometric property and the definition in (3.38), the fan-beam data sample $g(\lambda, \gamma)$ thus coincides with the value of the 2D Radon transform $\mathcal{R}f(\theta(\lambda, \gamma), s(\lambda, \gamma))$ with the arguments given as

$$\theta(\lambda, \gamma) = \lambda + \frac{\pi}{2} - \gamma \qquad \text{and} \qquad s(\lambda, \gamma) = \underline{a}(\lambda) \cdot \underline{\theta}(\lambda, \gamma) = R \sin \gamma. \qquad (3.40)$$
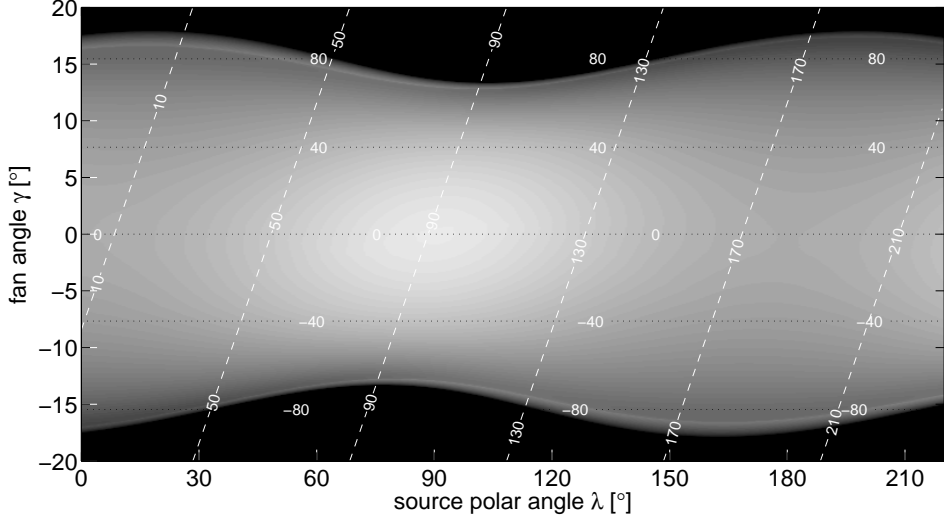
Figure 3.9: Fan-beam data of the Shepp-Logan phantom for $\lambda \in [0°, 220°]$ and $\gamma \in [-20°, 20°]$, while using $R = 30$ cm. The dotted lines indicate for some locations in the image the corresponding parallel-beam coordinate s (in mm) and the dashed lines similarly the corresponding values of θ (in degrees).

Fan-beam values and values of the 2D Radon transform are thus directly related to each other; the corresponding data functions p and g therefore possess similar properties, such as 2π periodicity in the first argument. One important characteristic of fan-beam data, which may be derived in a straight-forward way from the geometry defined in this section is the property

$$g(\lambda, \gamma) = g(\lambda + \pi - 2\gamma, -\gamma) \qquad (3.41)$$

that describes the distribution of redundancies in the function g [46].

Visualization of fan-beam data may be achieved using a concept similar to that of sinograms introduced in section 3.1.2. Values of g are mapped onto gray values and are visualized in a 2D image based on the Cartesian alignment of coordinates λ and γ. More specifically, a column of this 2D image corresponds to data at fixed λ, i.e., to one fan-beam projection, whereas one row contains fan-beam data at fixed γ. Figure 3.9 illustrates fan-beam data of the Shepp-Logan phantom for $\lambda \in [0°, 220°]$, $\gamma \in [-20°, 20°]$ and using the scan radius $R = 30$ cm.

3.2.3   Classical Inversion Formula for the 2D Fan-Beam Transform

The previous subsection demonstrated that measurements in the fan-beam geometry are directly related to samples of the 2D Radon transform. Fan-beam image reconstruction

may thus be achieved by a rather straight-forward application of techniques derived in section 3.1.4. It can be shown that using the 2D Radon inversion formula for redundant data (presented in section 3.1.5) and applying the change of variables $(\theta, s) \to (\lambda, \gamma)$, which has been defined in (3.40), directly leads to the following analytical inversion formula for the 2D fan-beam geometry [4, 46]:

$$f(\underline{x}) = \int\limits_{0}^{\lambda_{max}} \frac{R}{\|\underline{x} - \underline{a}(\lambda)\|^2} \int\limits_{-\pi/2}^{\pi/2} h_{ramp}\left(\sin(\gamma^*(\underline{x}) - \gamma)\right) \cos\gamma \, \tilde{m}(\lambda, \gamma) \, g(\lambda, \gamma) \, d\gamma \, d\lambda. \quad (3.42)$$

The quantity

$$\gamma^*(\underline{x}) = \mathrm{atan}\left(\frac{\underline{x} \cdot \underline{e}_u(\lambda)}{R - \underline{x} \cdot \underline{e}_w(\lambda)}\right) \quad (3.43)$$

in this formula denotes the fan angle of the measurement ray that diverges from $\underline{a}(\lambda)$ and contains $\underline{x}$, the function h_{ramp} is the ramp filter kernel and $\tilde{m}$ is a redundancy weighting function. Note that here and in the following, the superscript $*$ is used to denote a function that depends on λ, without explicitly listing this argument.

The redundancy weight $\tilde{m}$ in (3.42) is similar to the function m in the 2D parallel-beam geometry: it equalizes the contribution of every 2D Radon value contained in the set of fan-beam data for the final reconstruction. Function $\tilde{m}$ needs to be smooth in γ [46], 2π-periodic in λ and is assumed to be 0 at parameters λ for which no ray-integrals have been measured. Equalization will then be achieved if $\tilde{m}$ satisfies the normalization condition

$$\tilde{m}(\lambda, \gamma) + \tilde{m}(\lambda + \pi - 2\gamma, -\gamma) = 1, \quad (3.44)$$

which follows directly from the redundancy property (3.41) of the fan-beam data function.

Equation 3.42 will be referred to as the classical analytical fan-beam inversion formula throughout this thesis. It has FBP structure and may be decomposed into the following three steps:

Step 1 – **Data Weighting:** Fan-beam data are multiplied with the redundancy weighting function and a cosine term to yield weighted fan-beam projections

$$g_W(\lambda, \gamma) = \tilde{m}(\lambda, \gamma) \cos\gamma \, g(\lambda, \gamma). \quad (3.45)$$

Step 2 – **1D Filtering:** The weighted fan-beam projections are filtered in γ using the kernel of the ramp filter to obtain filtered projections

$$g_F(\lambda, \gamma) = \int\limits_{-\gamma_m}^{\gamma_m} h_{ramp}(\sin(\gamma - \gamma'))g_W(\lambda, \gamma')d\gamma'. \quad (3.46)$$

Step 3 – **2D Weighted Backprojection:** The function g_F is backprojected onto the image plane using a weighting factor that is inversely proportional to the square of the distance between the source position $\underline{a}(\lambda)$ and the point $\underline{x}$ where reconstruction is to be achieved to obtain

$$f(\underline{x}) = \int\limits_{0}^{\lambda_{max}} \frac{R}{\|\underline{x} - \underline{a}(\lambda)\|^2} g_F(\lambda, \gamma^*(\underline{x})) \, d\lambda \quad (3.47)$$

with the function γ^* defined in (3.43).

In order to obtain valid reconstruction of f at any point $\underline{x} \in \Omega_f$ using the classical scheme described above, we require filtered fan-beam projections for a scan with at least $\lambda_{max} = \pi + 2\gamma_m$ [46, 47], which is referred to as a short-scan. Note also that data filtering at any λ can only be achieved if the corresponding projection is non-truncated, which is guaranteed when $g(\lambda, \gamma)$ is known over the interval $\gamma \in [-\gamma_m, \gamma_m]$. The redundancy weight used for reconstruction can be selected somewhat flexibly within the constraints imposed by the normalization and the smoothness conditions. One possible explicit espression for function $\tilde{m}$ can, for instance, be given as [1]

$$
\tilde{m}(\lambda, \gamma) = \begin{cases} \sin^2\left(\frac{\pi}{4} \cdot \frac{\lambda}{\gamma_{thres}+\gamma}\right) & \text{if } 0 \le \lambda < 2(\gamma_{thres}+\gamma), \\ 1 & \text{if } 2(\gamma_{thres}+\gamma) \le \lambda < \pi + 2\gamma, \\ \sin^2\left(\frac{\pi}{4} \cdot \frac{\pi+2\gamma_{thres}-\lambda}{\gamma_{thres}+\gamma}\right) & \text{if } \pi + 2\gamma \le \lambda < \pi + 2\gamma_{thres}, \\ 0 & \text{if } \pi + 2\gamma_{thres} \le \lambda < 2\pi. \end{cases}
\tag{3.48}
$$

The weighting function defined in this equation gives a contribution of 1 to each ray integral that is measured only once and nicely balances the contributions of redundant data samples, using the property of the trigonometric functions, so that the weights corresponding to data samples considered twice for reconstruction sum up to unity.
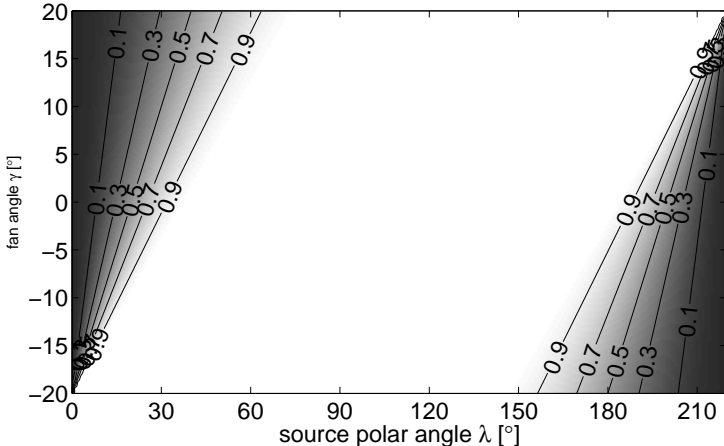
Figure 3.10: Illustration of the Parker weighting function which is used to account for data redundancies in fan-beam data g.

The parameter γ_{thres} in (3.48), which may here take values $\gamma_m \le \gamma_{thres} \le \pi/2$, provides some control about the amount of data used for reconstruction. For $\gamma_{thres} = \gamma_m$, equation (3.48) corresponds to the redundancy weighting function suggested by Parker [75], which is widely used for fan-beam reconstruction from a short-scan trajectory, i.e., for $\lambda_{max} = \pi + 2\gamma_m$. Figure 3.10 illustrates the Parker weighting function for $\gamma_m = 20°$. For the case that fan-beam projections are acquired over an interval in λ exceeding a short-scan, the use of $\gamma_{thres} = (\lambda_{max} - \pi)/2$ was suggested [79], so that all known values of g receive a non-zero contribution to the final reconstruction; the resulting weighting function will be referred to as the generalized Parker weight from now on.

---

[1]Note that in the equation, we only define one period of the redundancy weighting function, which is 2π periodic in λ.

3.2.4 Numerical Reconstruction Algorithm

From the results of section 3.2.3, a numerical algorithm may be given for image reconstruction from fan-beam data in practical CT applications. CT data acquisition allows in general the function g to be determined only at a finite number of sampling positions. Here it is assumed that the polar angles λ of the source of two adjacent fan-beam projections differ by the fixed increment $\Delta\lambda$ and that furthermore the rays within one fan-beam projection are uniformly sampled in γ; the angular sample spacing between two adjacent rays is denoted as $\Delta\gamma$. This section presents a numerical algorithm to compute from this sampled fan-beam data function an estimate of the object density. This estimate will be denoted as f^e.
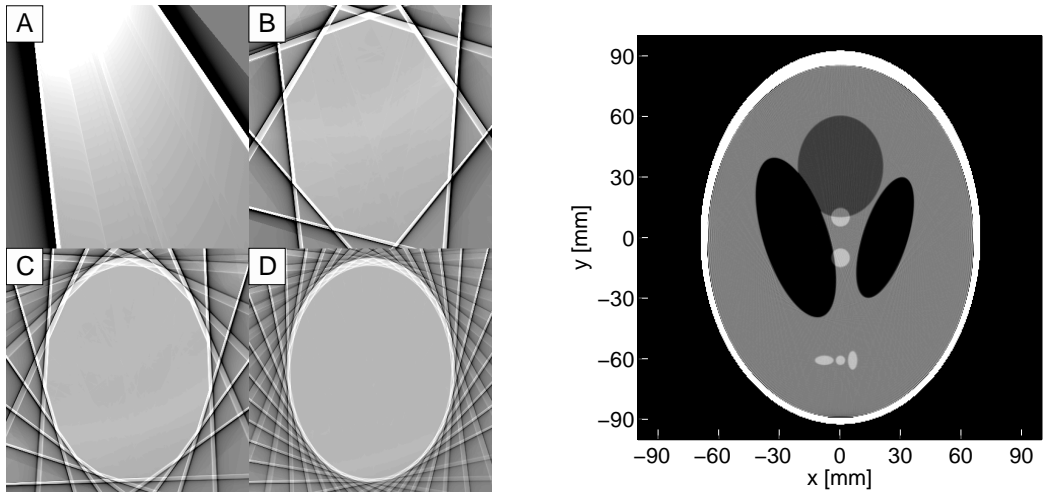
Figure 3.11: Illustration of the numerical 2D fan-beam reconstruction algorithm. (Left) Intermediate results obtained by backprojecting only (A) 1 (B) 5 (C) 10 or (D) 20 filtered fan-beam projections, respectively, which are evenly distributed over the known interval $[0, 220°]$. (Right) Final reconstruction result f^e obtained using 440 fan-beam projections, presented in the grayscale window $[0\,\text{HU}, 40\,\text{HU}]$.

The numerical algorithm achieves data filtering by first modifying (3.46) using the identity [46]

$$
\begin{aligned}
h_{ramp}\left(\sin(\gamma^*(\underline{x}) - \gamma)\right) &= h_{ramp}\left(\frac{\gamma^*(\underline{x}) - \gamma}{\gamma^*(\underline{x}) - \gamma}\sin(\gamma^*(\underline{x}) - \gamma))\right) \\
&= \left(\frac{\gamma^*(\underline{x}) - \gamma}{\sin(\gamma^*(\underline{x}) - \gamma)}\right)^2 h_{ramp}(\gamma^*(\underline{x}) - \gamma) \\
&= \tilde{h}_{ramp}(\gamma^*(\underline{x}) - \gamma)
\end{aligned}
\tag{3.49}
$$

that can be derived using the scaling property of the ramp filter kernel:

$$
\begin{aligned}
h_{ramp}(as) &= \int_{-\infty}^{\infty} |\sigma| e^{2\pi i \sigma a s}\, d\sigma = \int_{-\infty}^{\infty} \frac{1}{a^2}|\sigma'| e^{2\pi i \sigma' s}\, d\sigma' \\
&= \frac{1}{a^2}\, h_{ramp}(s)
\end{aligned}
\tag{3.50}
$$

that holds for any $a \neq 0$. Equation (3.49) then enables us to express the data filtering equation as a 1D convolution in γ of the weighted fan-beam data with the modified ramp filter

$$h^{\gamma}_{ramp}(\gamma) = \left(\frac{\gamma}{\sin \gamma}\right)^2 h_{ramp}(\gamma) \tag{3.51}$$

In our implementation, the function $h_{ramp}(\gamma)$ in (3.51) was substituted with its band-limited version using bandwidth $1/(2\Delta\gamma)$; see section 3.1.6 for details. The resulting filter equation is discretized at the sampling positions $k\Delta\gamma$ with $k \in \mathbb{Z}$ and 1D convolution is again efficiently carried out by multiplication of the involved functions in frequency domain; see again section 3.1.6. Backprojection is achieved by discretizing (3.47) and using linear interpolation in γ to obtain in each filtered fan-beam projection the value at the required sampling position $\gamma^*(\underline{x})$.

The steps of the resulting numerical algorithm are illustrated by reconstruction of the Shepp-Logan phantom. Fan-beam data of the phantom were simulated over a short-scan of $\lambda \in [0°, 220°)$ using $\Delta\gamma = 0.1°$, $\Delta\lambda = 0.5°$ and $R = 300\,\text{mm}$. The estimate f^e of the object density was computed on an isotropic sampling grid on the image plane with $\Delta x = \Delta y = 0.5\,\text{mm}$. The left image in Figure 3.11 shows intermediate results of backprojecting this filtered data into the image plane while using only 1, 5, 10 or 20 filtered projections that are evenly distributed over the simulated interval in λ. The right side in this figure displays the reconstruction result f^e that was obtained using all 440 fan-beam projections in a compressed grayscale window.

Chapter 4

Fan-Beam Reconstruction without Backprojection Weight

4.1 Introduction

Filtered-backprojection is a common way to achieve image reconstruction in 2D X-ray CT, see, for instance, the classical inversion methods for the 2D parallel beam geometry and 2D fan beam geometry, as explained in sections 3.1.4 and 3.2.3, respectively.

This chapter addresses the issue of FBP image reconstruction from fan-beam data. Fan-beam reconstruction may be carried out directly, by applying the FBP in the measurement geometry, see chapter 3.2.3 or the methods in [7, 14, 46, 56, 66, 74], but also indirectly, by first rebinning the 2D fan-beam data into the 2D parallel-beam geometry and then using a 2D parallel- beam reconstruction method to recover the object density function [10, 46, 73].

Both approaches, direct and indirect, have their pros and cons, and are currently in use in medical CT scanners. One drawback of indirect approaches is that the rebinning step comes with additional computational cost. Furthermore, rebinning requires in general interpolation in order to yield 2D parallel-beam data with a sampling beneficial for the application of a 2D parallel-beam reconstruction method; this interpolation is expected to have negative impact on the spatial resolution achievable in the reconstruction result.

On the other hand, one disadvantage of the direct FBP approach is that the backprojection step includes a weighting factor that varies with both, the source polar angle λ and the point $\underline{x}$ where reconstruction is to be performed. This weighting factor is often seen as a source of noise increase [96], and also makes backprojection in the direct approach more computationally demanding and more difficult to code in hardware than the indirect approach [10, 73].

This chapter is focussed on the direct FBP approach and presents a novel FBP formula for image reconstruction from 2D fan-beam data collected over a full 2π scan, which is derived from the alternative inversion formula for fan-beam data suggested by Noo *et al.* [66]. Our novel formula operates directly in the fan-beam geometry, so that it does not require any data rebinning, and it also comes along without the spatially varying weighting factor during backprojection.

4.2 Alternative Inversion Formula for the 2D Fan-Beam Transform

In [66], Noo *et al.* suggested a direct fan-beam inversion formula that is different from the classical approach introduced in section 3.2.3. Noo's alternative formula is based on the classical 2D parallel beam inversion method

$$f(\underline{x}) = \int\limits_0^\pi p_F(\theta, \underline{\theta} \cdot \underline{x}) \, d\theta \qquad \text{with} \qquad p_F(\theta, s) = \int\limits_{-\infty}^\infty h_{ramp}(s - s')p(\theta, s') \, ds' \qquad (4.1)$$

and derived using the following two concepts:

Concept 1 - **Decomposition of the ramp filter** h_{ramp} :

In Fourier domain, the ramp filter may be developed into

$$\mathcal{F}_s h_{ramp}(\sigma) = |\sigma| = \sigma \operatorname{sign} \sigma = \frac{1}{2\pi} (-i)\operatorname{sign} \sigma \, 2\pi i \sigma$$
$$= \frac{1}{2\pi} \mathcal{F}_s h_{hilb}(\sigma) \, \mathcal{F}_s h_{der}(\sigma) \qquad (4.2)$$

where h_{der} and h_{hilb} denote the kernels of the differentiation operator and of the Hilbert transform, respectively, which are given as

$$h_{der}(s) = \int\limits_{-\infty}^\infty 2\pi i\sigma \, e^{2\pi i\sigma s} \, d\sigma \qquad (4.3)$$

and

$$h_{hilb}(s) = \int\limits_{-\infty}^\infty (-i) \operatorname{sign}\sigma \, e^{2\pi i\sigma s} d\sigma. \qquad (4.4)$$

Hence, ramp filtering of a 1D function may be alternatively achieved by applying subsequently but in arbitrary order the following operations: data differentiation, convolution with the kernel of the Hilbert transform and data weighting. The filtering in (4.1) can thus be expressed as

$$p_F(\theta, s) = \frac{1}{2\pi} \frac{\partial}{\partial s} p_H(\theta, s) \qquad (4.5)$$

with $p_H(\theta, s)$ denoting the Hilbert transform of 2D parallel beam data in the parameter s:

$$p_H(\theta, s) = \int\limits_{-\infty}^\infty h_{hilb}(s - s')p(\theta, s') \, ds'. \qquad (4.6)$$

Hence, an alternative expression of the 2D parallel beam inversion formula (4.1) is given as

$$f(\underline{x}) = \frac{1}{2\pi} \int\limits_0^\pi \frac{\partial}{\partial s} p_H(\theta, s)\Big|_{s=\underline{x}\cdot\underline{\theta}} \, d\theta. \qquad (4.7)$$

Concept 2 - **Hilbert transform in angular parameter** γ :

Image reconstruction according to (4.7) requires values of the function p_H, which may be obtained according to (4.6). However, as shown in [66], samples of p_H may also be obtained directly in the fan-beam geometry, namely by using the convolution

$$p_H(\theta, \underline{a}(\lambda) \cdot \underline{\theta}) = \int_{-\pi}^{\pi} h_{hilb}(\sin(\theta - \gamma)) \, g(\lambda, \gamma) \, d\gamma. \tag{4.8}$$

In order to proof the identity in (4.8), we use the fact that $\sin(\theta - \gamma) = -\underline{\alpha}(\lambda, \gamma) \cdot \underline{\theta}$ with $\underline{\alpha}(\lambda, \gamma)$ defined in (3.35), which follows directly from the theorems of trigonometric functions, and develop the right hand side in (4.8) as

$$
\begin{aligned}
\int_{-\pi}^{\pi} h_{hilb}(\sin(\theta - \gamma)) \, g(\lambda, \gamma) \, d\gamma &= \int_{-\pi}^{\pi} h_{hilb}(-\underline{\alpha}(\lambda, \gamma) \cdot \underline{\theta}) \, g(\lambda, \gamma) \, d\gamma \\
&= \int_{-\pi}^{\pi} h_{hilb}(-\underline{\alpha}(\lambda, \gamma) \cdot \underline{\theta}) \int_{0}^{\infty} f(\underline{a}(\lambda) + t\underline{\alpha}(\lambda, \gamma)) \, dt \, d\gamma \\
&= \int_{-\pi}^{\pi} \int_{0}^{\infty} t \, h_{hilb}(-t\underline{\alpha}(\lambda, \gamma) \cdot \underline{\theta}) f(\underline{a}(\lambda) + t\underline{\alpha}(\lambda, \gamma)) \, dt \, d\gamma \\
&= \iint_{\mathbb{R}^2} h_{hilb}((\underline{a}(\lambda) - \underline{x}) \cdot \underline{\theta}) f(\underline{x}) \, d\underline{x} \\
&= \iint_{\mathbb{R}^2} \int_{-\infty}^{\infty} \delta(s - \underline{x} \cdot \underline{\theta}) \, h_{hilb}(\underline{a}(\lambda) \cdot \underline{\theta} - s) f(\underline{x}) \, ds \, d\underline{x} \\
&= \int_{-\infty}^{\infty} h_{hilb}(\underline{a}(\lambda) \cdot \underline{\theta} - s) \, p(\theta, s) \, ds = p_H(\theta, \underline{a}(\lambda) \cdot \underline{\theta}).
\end{aligned}
\tag{4.9}
$$

The step from line 2 to line 3 in this derivation involves the scaling property of the Hilbert kernel, namely the identity $t \, h_{hilb}(ts) = h_{hilb}(s)$ for $t \neq 0$, which can be derived analog to the scheme in (3.50). Furthermore, to obtain line 4 from line 3, we use the change of variable $\underline{x} = \underline{a}(\lambda) + t\underline{\alpha}(\lambda, \gamma)$, which comes with a Jacobian that cancels out the factor t in front of the expression of the Hilbert kernel function. Note that the calculation of the value $p_H(\theta, s)$ according to (4.8) requires a non-truncated fan-beam projection with the source at polar angle λ that satisfies $\underline{a}(\lambda) \cdot \underline{\theta} = s$. Geometrically, we thus require integral data associated to all rays that diverge from $\underline{a}(\lambda)$ and that intersect Ω_f. Requirement on the data is therefore different from that of the conventional filter equation (4.6), which requires integral data to be known for all lines that are orthogonal to $\underline{\theta}$ and that intersect Ω_f.

Using the two concepts listed above, Noo *et al.* derived an alternative direct FBP formula for reconstruction from fan-beam data $g(\lambda, \gamma)$. For a full-length derivation of this formula, we direct the reader to [66]. Reconstruction from full-scan fan-beam data using Noo's alternative formula is achieved as

$$f(\underline{x}) = \frac{1}{2\pi} \int_{0}^{2\pi} \frac{w(\lambda, \underline{x})}{\|\underline{x} - \underline{a}(\lambda)\|} \int_{-\gamma_m}^{\gamma_m} h_{hilb}(\sin(\gamma^*(\underline{x}) - \gamma)) \, \hat{g}(\lambda, \gamma) \, d\gamma \, d\lambda \tag{4.10}$$

In this equation

$$\gamma^*(\underline{x}) = \text{atan}\,\frac{u^*(\underline{x})}{D} \qquad \text{with} \qquad u^*(\underline{x}) = \frac{D\,\underline{x}\cdot\underline{e}_u(\lambda)}{R - \underline{x}\cdot\underline{e}_w(\lambda)} \tag{4.11}$$

denotes again the fan-angle of the ray diverging from $\underline{a}(\lambda)$ and passing through $\underline{x}$. To understand the expression for $\gamma^*(\underline{x})$ we use here, picture a linear detector, parallel to $\underline{e}_u(\lambda)$ and at distance D from the source. The quantity $u^*(\underline{x})$ then describes the coordinate, measured along $\underline{e}_u(\lambda)$, where the ray through $\underline{x}$ intersects this detector, and the relation between $u^*(\underline{x})$ and D gives access to the fan-angle of this ray. Furthermore, the symbol $\hat{g}$ in (4.10) is defined as

$$\hat{g}(\lambda,\gamma) = \left(\frac{\partial}{\partial\lambda} + \frac{\partial}{\partial\gamma}\right)g(\lambda,\gamma) \tag{4.12}$$

and it can be shown that $\hat{g}(\lambda,\gamma)$ is the result of differentiating the fan-beam data with respect to λ while fixing the ray direction [66].

Function $w(\lambda,\underline{x})$ in (4.10) plays the same role as function $\tilde{m}(\lambda,\gamma)$ in (3.42), namely to allow for a proper, explicit handling of redundancies in the fan-beam data. In contrast with (3.42) however, the redundancy weighting in (4.10) applies after the convolution and can thus be carried out in the image domain as part of the backprojection step. This feature allows a definition of the redundancy weight individually for every point $\underline{x}$, which provides increased flexibility in the way data redundancies can be handled. In particular, points that are on the same backprojection ray can be assigned distinct weights without affecting the FBP structure of the reconstruction, which is not possible with the classical FBP inversion method presented in section 3.2.3.

As in the classical method, $w(\lambda,\underline{x})$ must satisfy a normalization condition for (4.10) to be valid: the total contribution to the final reconstruction of each line passing through $\underline{x}$ must be unity. A common choice for the full-scan is $w(\lambda,\underline{x}) = 1/2$ and this choice is referred to as the uniform weighting approach in the following. However, other choices are possible, as will be discussed in the next section.

4.3   Fan-Beam Reconstruction with No Backprojection Weight

Consider the redundancy weighting function

$$w(\lambda,\underline{x}) = \frac{\|\underline{x} - \underline{a}(\lambda)\|}{2R\cos\gamma^*} \tag{4.13}$$

as a candidate for reconstruction using the alternative fan-beam FBP formula (4.10). The idea is to let the contribution of a given ray to the reconstruction of $f(\underline{x})$ depend on the Euclidean distance between $\underline{x}$ and the source position during the backprojection. As will become clearer below, among all measured rays through $\underline{x}$, the suggested weight gives preference to the fan-beam rays emerging from the source positions that are most away from $\underline{x}$. This preference is accentuated with the distance of $\underline{x}$ from the origin. For reconstruction at $\underline{x} = (0,0)^{\mathrm{T}}$, however, all rays through $\underline{x}$ are treated equally.

To show that (4.13) defines a valid weighting function, it needs to be demonstrated that it normalizes the contribution from any line through any point $\underline{x}$ in Ω_f to one. Consider the reconstruction of f at such a point. Then, for any arbitrary source position $\underline{a}(\lambda)$, there
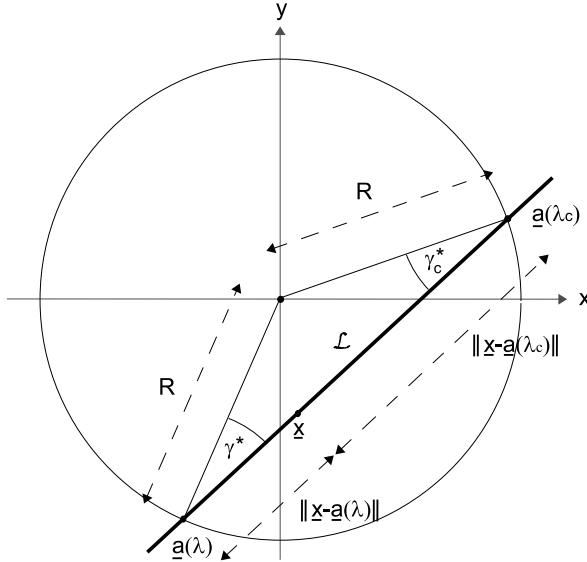
Figure 4.1: Geometric illustrations of the redundantly measured line $\mathcal{L}$. The line integral corresponding to $\mathcal{L}$ is obtained at source parameters λ and λ_c. The absolute value of the fan angle to the line $\mathcal{L}$ is identical in both views, λ and λ_c.

exists a complementary source parameter λ_c, such that $\underline{x}$, $\underline{a}(\lambda)$ and $\underline{a}(\lambda_c)$ are collinear and define a line $\mathcal{L}$ (see Figure 4.1). The integral along $\mathcal{L}$ is acquired twice, at source parameters λ and λ_c, respectively. From equation (4.13) which defines the weight that each measurement on $\mathcal{L}$ receives, and from the relation $\gamma_c^* = -\gamma^*$ (see Figure 4.1), it can be shown that

$$
\begin{aligned}
\frac{\|\underline{x} - \underline{a}(\lambda)\|}{2R\cos\gamma^*} + \frac{\|\underline{x} - \underline{a}(\lambda_c)\|}{2R\cos\gamma_c^*} &= \frac{\|\underline{x} - \underline{a}(\lambda)\| + \|\underline{x} - \underline{a}(\lambda_c)\|}{2R\cos\gamma^*} \\
&= \frac{\|\underline{a}(\lambda_c) - \underline{a}(\lambda)\|}{2R\cos\gamma^*} = 1 \,.
\end{aligned}
\tag{4.14}
$$

The result in (4.14) proves that the weighting scheme in (4.13) achieves the required normalization to unity of the contribution from each line through $\underline{x}$. Hence, the function w suggested in (4.13) defines a valid weighting scheme. Moreover, since w is proportional to $\|\underline{a}(\lambda) - \underline{x}\|$, it cancels out the backprojection weight $1/\|\underline{a}(\lambda) - \underline{x}\|$ in the alternative fan-beam FBP inversion formula (4.10). This means that the computationally costly step of applying the backprojection weight in a direct FBP reconstruction can be avoided. In compensation, the convolved fan-beam data just needs to be multiplied by $1/(2R\cos\gamma)$ prior to backprojection. Substituting the suggested weighting function (4.13) into (4.10) yields the novel direct FBP formula for reconstruction from full-scan fan-beam data:

$$
f(\underline{x}) = \frac{1}{4\pi R} \int\limits_{0}^{2\pi} g_F(\lambda, \gamma^*) \, d\lambda
\tag{4.15}
$$

where

$$
g_F(\lambda, \gamma) = \frac{1}{\cos\gamma} \int\limits_{-\gamma_m}^{\gamma_m} h_{hilb}(\sin(\gamma - \gamma')) \, \hat{g}(\lambda, \gamma') \, d\gamma'
\tag{4.16}
$$

with $\hat{g}$ given by equation (4.12). This formula has no backprojection weight.

4.4   Numerical Evaluation

This section presents a numerical evaluation of the suggested direct fan-beam FBP inversion formula with no backprojection weight, which we refer to as the efficient formula from now on. This evaluation is based on simulated fan-beam data and involves quantitative and qualitative figures-of-merit, such as spatial resolution, signal-to-noise ratio and computational efficiency.

    More specifically, the performance of the efficient formula is compared to that of the alternative fan-beam FBP formula (4.10) with uniform weights (namely, $w(\lambda, \underline{x}) = 1/2$). This selected candidate for comparison, which will be referred to as the uniform-weighting formula, has been shown to yield better image quality than the classical fan-beam inversion method [94].

    Many geometric factors can affect image quality in fan-beam tomography. These factors include the focal spot size, the anode angle, the size of detector elements, the type of X-ray emission (pulse or continuous), and the source-to-origin distance. This evaluation is based on fan-beam geometry parameters that are representative of current medical CT scanners; these parameters are summarized in table 4.1.

Table 4.1: Parameters of the fan-beam geometry considered for numerical evaluation of the reconstruction algorithm.

X-ray source	
dimensions (width×height)	$1.2 \, \mathrm{mm} \times 0.9 \, \mathrm{mm}$
anode angle	$7.0°$
X-ray emission	continuous
Detector	
# of pixels	672
pixel dimensions	$1.4083 \, \mathrm{mm} \times 1.4083 \, \mathrm{mm}$
detector offset	$0.352075 \, \mathrm{mm}$
source-to-detector distance	$D = 104 \, \mathrm{cm}$
Trajectory	
radius of the circle scan	$R = 57 \, \mathrm{cm}$
# of projections	1160

4.4.1   Implementation Details

The two formulae under comparison were implemented using the same discretization rules. The computation of $\hat{g}(\lambda, \alpha)$ in equation (4.12) was performed using the scheme described by equation (46) in [69]. Data filtering in both, the efficient and the uniform-weighting formula was achieved by using the identity

$$h_{hilb}\left(\sin(\gamma - \gamma')\right) = \frac{\gamma - \gamma'}{\sin(\gamma - \gamma')} h_{hilb}\left(\gamma - \gamma'\right) = h_{hilb}^{curved}\left(\gamma - \gamma'\right) \tag{4.17}$$

with

$$h_{hilb}^{curved}\left(\gamma\right) = \frac{\gamma}{\sin\gamma} h_{hilb}(\gamma). \tag{4.18}$$

This identity allows the filtering operation required in each reconstruction formula to be expressed as a 1D convolution and filtering can thus be carried out efficiently using FFTs, as explained before. Furthermore, the kernel h_{hilb} in (4.18) was substituted by a bandlimited Hilbert kernel h_{hilb}^b that involves rectangular apodization and bandwidth $1/(2\Delta\gamma)$. The expression of $h_{hilb}^b(\gamma)$ is given as

$$h_{hilb}^b(\gamma) = \int_{-b}^{b} (-i)\text{sign}\,\sigma\, e^{2\pi i\sigma\gamma}d\gamma = \frac{1}{\pi\gamma}(1 - \cos 2\pi b\gamma) = \frac{1}{\pi\gamma}\left(1 - \cos\left(\frac{\pi\gamma}{\Delta\gamma}\right)\right) \qquad (4.19)$$

Note that the discretization of the filter equation in both formulae at positions $k\Delta\gamma$ with $k \in \mathbb{Z}$ leads to a sampling where $h_{hilb}^b(m\Delta\gamma) = 0$ for $m = 2k$ because of the cosine term in (4.19). The computation of a sample of g_F thus involves only half of the samples of $\hat{g}$. To circumvent this issue and obtain an improved numerical scheme [32], we discretize at positions $k\Delta\gamma + \Delta\gamma/2$ with $k \in \mathbb{Z}$, so that all sampled values of the discrete filter kernel are non-zero [69]; see Figure 4.2. Note that doing so, we obtain the filtered fan-beam data on a sampling grid which is shifted along coordinate γ by $\Delta\gamma/2$ with respect to the sampling grid of $\hat{g}$.
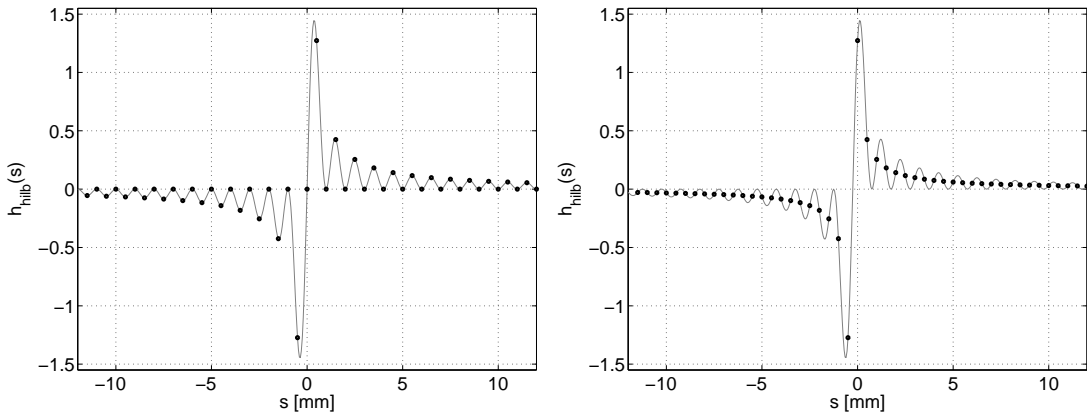
Figure 4.2: Two distinct sampling schemes for the bandlimited Hilbert kernel h_{hilb}^b with rectangular bandlimitation. (Left) Sampling at locations $k\Delta s$ with integer k, (right) sampling at locations $k\Delta s + \Delta s/2$. In each diagram, the gray curve corresponds to the function h_{hilb}^b and the black circles illustrate the used sampling positions.

Details on our implementation of the backprojection step are given in section 4.4.4.

4.4.2 Evaluation of Spatial Resolution

Predicting differences in spatial resolution performance between the efficient and the uniform-weighting formulas is not straightforward. By omitting the distance-dependent backprojection weight, the efficient formula gives more weight to fan-beam rays for which the source is further away from the point of interest $\underline{x}$. Using the rule of magnification, we could therefore predict a decrease in spatial resolution compared to the uniform-weighting formula, especially in regions far away from the origin of the image coordinate system. However, the efficient formula also favors fan-beam data for which the discretization in λ, i.e., the distance between two adjacent source positions, appears under a smaller angle. Hence, the

low-pass effects of continuous X-ray exposure could be less prominent for the efficient formula, and could overall make the efficient formula better in terms of resolution. Altogether, argumentation can thus be given in favor of each reconstruction formula. To clarify the issue, a thorough evaluation was performed of the two formulas in terms of spatial resolution by determining the point spread function (PSF) corresponding to each reconstruction formula at various locations within the region Ω_f.
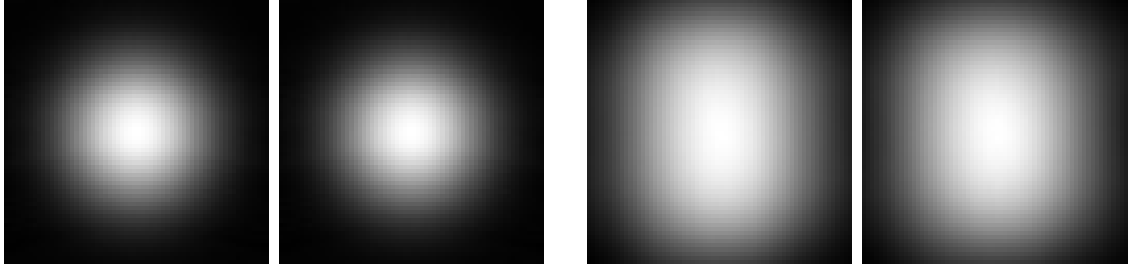
Figure 4.3: Point spread function (PSF) obtained at position $\underline{r} = (0.5\,\mathrm{cm}, 0\,\mathrm{cm})^{\mathrm{T}}$ (left two images) and at position $\underline{r} = (24.5\,\mathrm{cm}, 0\,\mathrm{cm})^{\mathrm{T}}$ (right two images). In each image pair, the PSF corresponding to the uniform-weighting formula is on the left side, while the PSF for the efficient formula is on the right side.

To obtain the PSF at a specific location $\underline{r} = (x, y)^{\mathrm{T}}$, a cylindrical object with a tiny circular base was placed at $\underline{r}$. Then, we simulated fan-beam data of this object and achieved from this data reconstruction on a fine Cartesian grid in x and y which was centered at $\underline{r}$. The cylindrical object is intended to be an approximation of the 2D Delta function (Dirac impulse). Its radius was selected as $0.15\,\mathrm{mm}$, which is almost 10 times smaller than the width of each detector pixel, and its attenuation coefficient was set to $12.2\,\mathrm{mm}^{-1}$. A ray passing through its center suffers an attenuation equivalent to the attenuation caused by a homogeneous water cylinder of $200\,\mathrm{mm}$ diameter. Due to discretization effects, the reconstruction of the cylindrical object looks like a blurred spot rather than a disk with a perfectly delineated boundary and this spot is here used as the estimate of the PSF at $\underline{r}$.
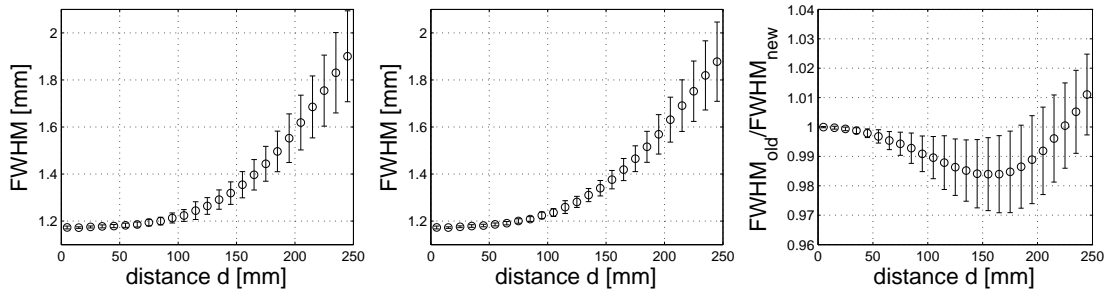
Figure 4.4: Mean value and standard deviation of FWHMs obtained from 256 radial profiles through the PSF. These quantities are shown as a function of d, the distance from the PSF to the origin. (left) Using the uniform-weighting approach. (center) Using the efficient formula. (right) Ratio of the FWHMs ('uniform-weighting' over 'efficient').

Let us denote by PSF data the fan-beam data of the tiny cylindrical object. To simulate PSF data, all finite-size geometric entities were represented by several points rather than

just by their midpoint. In other words, fan-beam data simulation was carried out in an upsampled scenario and the resulting data was subsequently binned to obtain PSF data corresponding to the desired sampling pattern and geometric dimensions. In the upsampling scenario, each detector pixel was divided into 14×14 square pieces uniformly covering its area, and similarly, the focal spot of the X-ray source was divided into a grid of 3×3 subspots. Furthermore, to account for the effect of continuous X-ray emission during data acquisition, 5 projections were simulated for each fan-beam projection, using 5 different positions for the focus-detector assembly. These positions were uniformly distributed over $2\pi/1160$ around the nominal position for the desired projection. In total, 8820 line integrals were computed to simulate each PSF data sample, and binning proceeded by first converting these line integrals into attenuation factors.

The PSF estimate at an arbitrary position of interest $\underline{r}$ was obtained on a Cartesian grid of 64×64 square pixels of side 0.04 mm. For a detailed analysis, profiles of the PSF were extracted along half-lines, with each half-line starting at $\underline{r}$ and describing some angle ω with the x-axis. Let p be the distance from $\underline{r}$ along each half-line; typically, the extracted profiles are monotonously decreasing functions of p with maximum value at $p = 0$ i.e., at point $\underline{r}$. Hence, a coordinate p_{half} may be defined where half the maximum value is reached. This coordinate, p_{half}, characterizes the spatial extent of the PSF as a function of angle ω and we call $2p_{half}$ the full-width at half maximum (FWHM) of the PSF in the direction given by ω. If the PSF were a radial function, the FWHM would be independent of ω. However, this is not the case in the presented evaluations. Hence, the FWHM was computed for 256 profiles corresponding to ω values uniformly sampled over the interval $[0, 2\pi)$. The mean value and the standard deviation of the obtained 256 FWHMs were then used as a characterization of the achievable spatial resolution at $\underline{r}$.

Due to the symmetry of the full-scan reconstruction problem, the spatial resolution is essentially a radial function i.e., a function of the distance d from the origin only. To compare the resolution given by the two formulas over the complete object region Ω_f, PSFs were generated and evaluated as explained above at 25 different distances d, starting at $d = 0.5$ cm and incrementing in steps of $\Delta d = 1.0$ cm. For convenience, all PSFs were located on the positive side of the x-axis.

Figure 4.3 shows the PSFs obtained with the uniform-weighting formula and the efficient formula at two locations, $d = 0.5$ cm and $d = 24.5$ cm. Variations in the PSF shape across Ω_f are presented in Figure 4.4, using the FWHM concept. This figure also includes a plot of the ratio between the FWHM given by each formula at each sampled ω; both, mean and standard deviation of this ratio are displayed.

The results show that both formulas yield a very similar resolution across the imaged region. Near the origin, a nearly radial PSF of FWHM smaller than 1.2 mm is obtained. As d increases, the mean of the FWHMs continuously increases to reach a value of approximately 1.9 mm at the edge of Ω_f. Furthermore, the standard deviation of the FWHMs over all profile angles gets larger, indicating a decrease in PSF symmetry. This decrease appears slightly worse when using the uniform-weighting formula. The ratio between the FWHMs shows there is less than 2% difference in resolution between the uniform-weighting formula and the efficient formula. This difference is in favor of the efficient formula in region $d < 200$ mm, and in favor of the uniform-weighting formula in region $d > 200$ mm. In length unit, the worst difference in FWHM is 0.025 mm.

4.4.3   Evaluation of Image Noise

Discretization errors and noise propagation were investigated using reconstructions from noisy fan-beam data of a slice through the FORBILD thorax phantom. For this investigation, the size of the phantom was enlarged using a bigger ellipse for the body contour; the new ellipse was of size $49\,\mathrm{cm}$ by $28\,\mathrm{cm}$, and was centered at $(0\,\mathrm{cm}, 2\,\mathrm{cm})^{\mathrm{T}}$. The reconstructions were performed from 800 distinct noise realizations, each on a Cartesian grid of square pixels of side $0.75\,\mathrm{mm}$. Thus, 800 images were obtained from each reconstruction formula. Variations in the intensities of each pixel across these 800 images give statistics on the uncertainty that can be expected in the reconstruction of the real, sought density function at each pixel location, due to data noise.

Data simulation for each noise realization was performed as in section 4.4.2, using upsampling and then binning to model all geometric factors. The upsampling parameters were the same as in section 4.4.2, except for the detector pixels which were represented each by a Cartesian grid of 3×3 subpixels (instead of 14×14), to speed up the simulation. Poisson noise was added to the noise-free fan-beam data after binning to the desired dimensions, assuming an emission of $150,000$ photons per ray. See [89] for a nice description about the noise model for CT measurements.

Figure 4.5 (left) shows the mean of the 800 reconstructions obtained from each formula. These means are displayed using a highly compressed grayscale to exhibit the discretization errors. Compared to the ground-truth, which is also displayed in Figure 4.5, we observe that both formulas perform very well. However, the uniform-weighting formula yields a bit more discretization errors away from the origin (see the regions within the dashed circles).

Figure 4.5 (right) shows the reconstructions obtained from each formula when using only a single set of noisy data. In each figure, differences in noise level that increase with the distance from the origin can be observed between the two reconstructions. To analyze further these differences, we computed on a pixelwise basis the standard deviation across the 800 reconstructions obtained from each formula. Figure 4.6 shows the resulting standard deviation images, and Figure 4.7 shows the ratio between these images, again computed pixelwise. These figures show that each formula delivers a similar standard deviation near the image plane origin, but away from this origin the efficient formula performs better. At a distance of $15\,\mathrm{cm}$ from the origin, reconstructions from the uniform-weighting formula show a 5% higher noise level compared to the efficient formula and this percentage increases rapidly with the distance from the origin; the percentage is 20% at $20\,\mathrm{cm}$ and as high as 40% at $25\,\mathrm{cm}$. Hence, the efficient formula is more robust to noise than the uniform-weighting formula, and the difference in robustness is not negligible off-center.

Technically, noise properties should be compared at equal spatial resolution, which is not achieved according to the results in section 4.4.2. However, these results show that resolution, if not equal, is at least very similar, so much that the gain observed in standard deviation may not be the cause of differences in resolution. In particular, note that if the difference in resolution was thought to be the cause of the difference in standard deviation, than this latter difference should follow the shape of the PSF plot in the right side of Figure 4.4. Nevertheless, we have investigated resolution matching through a modeling of the PSFs as Gaussian functions. As expected, this investigation yield no measurable difference in standard deviation.
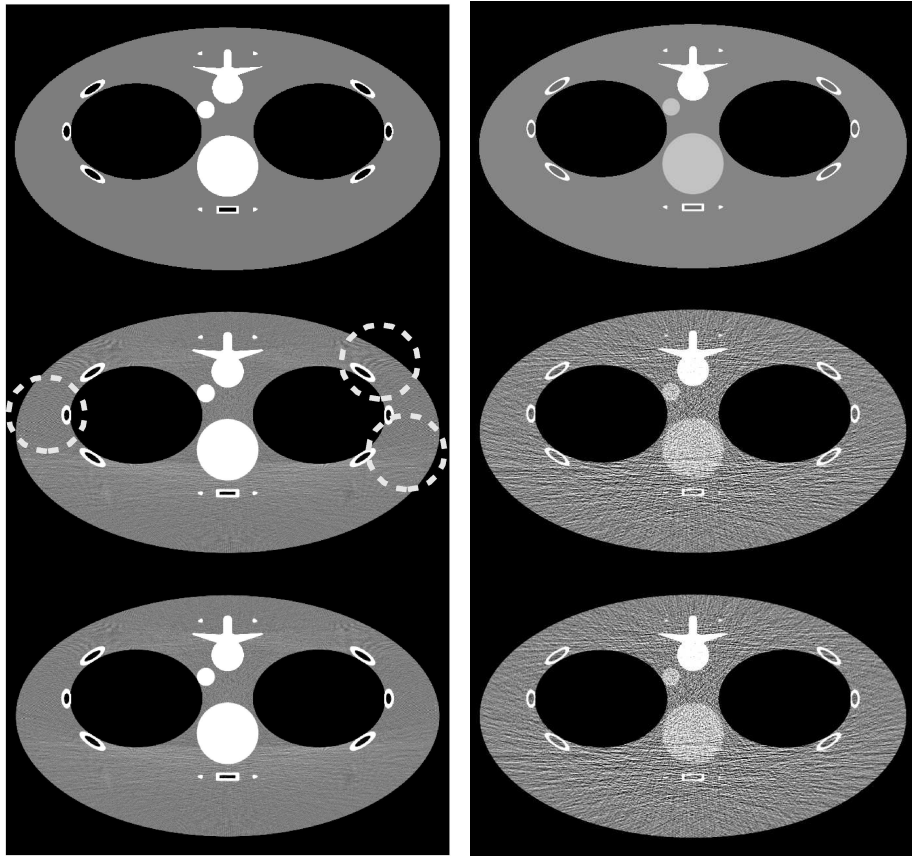
Figure 4.5: Reconstructions of the slice $z = 0\,\mathrm{mm}$ through the FORBILD thorax phantom with enlarged body contour. (left) Comparison between the ground truth and the mean over 800 reconstructions obtained from distinct noise realizations; grayscale: $[-20\,\mathrm{HU}, 20\,\mathrm{HU}]$. (right) Comparison between the ground truth and the reconstruction obtained from a single noisy data set; grayscale: $[-110\,\mathrm{HU}, 100\,\mathrm{HU}]$. In each case, left and right, the top image is the ground truth, the middle image is the result from the uniform-weighting formula, and the bottom image is the result from the efficient formula. The three dashed circles in the middle image of the left column indicate regions where the reconstruction with the uniform-weighting formula exhibits slight differences in discretization errors.

4.4.4   Evaluation of Computational Efficiency

The efficiency of the two reconstruction formulas was evaluated using direct counting of the number of required additions, multiplications and divisions, as well as using measurements of execution times on three different systems. We concentrated this evaluation on the backprojection step since this step is typically the most demanding one, and since the significant difference between the two reconstruction formulas lies in the backprojection step.

Clearly, any evaluation of efficiency depends on the amount of sophistication attached to the implementation of the reconstruction formulas. For example, a direct implementation of the uniform-weighting formula based on (4.10) is bound to be much slower than a direct implementation of the efficient formula because the backprojection weight in (4.10) requires
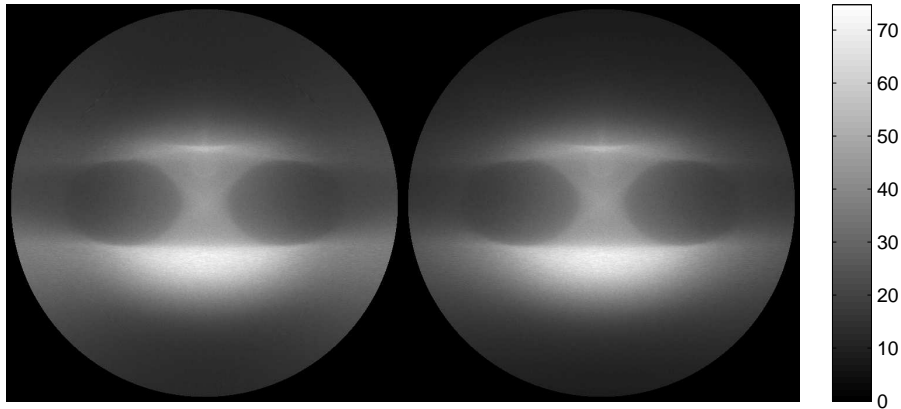
Figure 4.6: Standard-deviation images obtained from reconstructions of the FOR-BILD thorax phantom with enlarged body contour; 800 distinct Poisson noise realizations were considered with $150,000$ photons per ray. (left) Result for the uniform-weighting formula. (right) Result for the efficient formula.
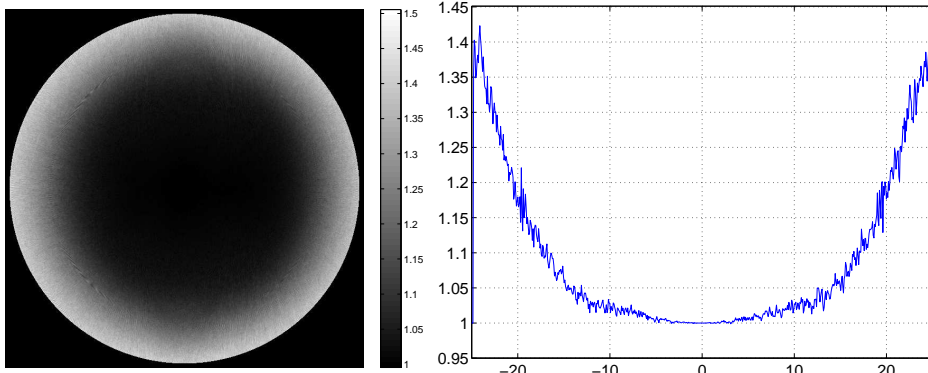
Figure 4.7: Close inspection of the standard-deviation images in Figure 4.6. (left) Noise behavior comparison using pixel-wise computation of the ratio between the standard deviation images ('uniform-weighting' over 'efficient'). (right) Profile along the line $y = 0\,\mathrm{mm}$ of the ratio image shown to the left.

the computation of a square root for each source position for each pixel. We aimed at a deeper comparison and decided to use the following relation in the implementation of the uniform-weighting formula [69]:

$$\|\underline{a}(\lambda) - \underline{x}\| = \frac{R - x\cos\lambda - y\sin\lambda}{\cos\gamma^*}. \tag{4.20}$$

Using this relation gives a much more efficient implementation of the uniform-weighting formula as the square root is avoided and the $\cos\gamma^*$ factor can be taken care of prior to backprojection by just multiplying the filtered data by $\cos\gamma$.

Now, note that a direct implementation of both formulas requires the computation of an inverse tangent to obtain γ^* from u^* in (4.11). When using (4.20), this requirement largely dominates the effort for the backprojection weight in the uniform-weighting formula, so that little difference could be observed between the two reconstruction formulas. This

issue was circumvented by resampling the filtered data on a fine grid in $u = \tan\gamma$ prior to backprojection. This resampling not only eliminates the need to compute the inverse tangent but also enables us to access data during backprojection using nearest-neighbor interpolation rather than the more costly linear interpolation.

Input: Filtered data: $g_F(\lambda, \gamma)$
Output: Reconstruction: $f(\underline{x})$
1   $g_1(\lambda, \gamma) = \cos\gamma \, g_F(\lambda, \gamma)$;
2   $g_2(\lambda, u) = g_1(\lambda, \tan^{-1}(u/D))$;
3   **foreach** *Projection* λ **do**
4     $T_1 = \Delta x \sin\lambda * (D/\Delta u)$;
5     $T_2 = \Delta x \cos\lambda$;
6   **foreach** *Row in the image* y **do**
7   Initialize NUM, DEN;
8   **foreach** *Column in the image* x **do**
9   **if** *(x,y)* $\in ROI$ **then**
10          $W = 1/DEN$;
11          $\hat{u} = NUM * W$;
12          $U_{idx} = \hat{u} + U_0$;
13          $f(x,y) += g_2(\lambda, U_{idx}) * W$;
14   **end**
15         $NUM = NUM - T_1$;
16         $DEN = DEN - T_2$;
17   **end**
18   **end**
19 **end**

Input: Filtered data: $g_F(\lambda, \gamma)$
Output: Reconstruction: $f(\underline{x})$
0.1 $g_1(\lambda, \gamma) = g_F(\lambda, \gamma)/\cos\gamma$;
0.2 $g_2(\lambda, u) = g_1(\lambda, \tan^{-1}(u/D))$;
0.3   **foreach** *Projection* λ **do**
0.4 $T_1 = \Delta x \sin\lambda * (D/\Delta u)$;
0.5 $T_2 = \Delta x \cos\lambda$;
0.6   **foreach** *Row in the image* y **do**
0.7   Initialize NUM, DEN;
0.8   **foreach** *Column in the image* x **do**
0.9   **if** *(x,y)* $\in ROI$ **then**
0.10 $\hat{u} = NUM/DEN$;
0.11 $U_{idx} = \hat{u} + U_0$;
0.12 $f(x,y) += g_2(\lambda, U_{idx})$;
0.13   **end**
0.14 $NUM = NUM - T_1$;
0.15 $DEN = DEN - T_2$;
0.16   **end**
0.17   **end**
0.18 **end**

Figure 4.8: Pseudo-code for the backprojection step corresponding to (left) the uniform-weighting formula and (right) the efficient formula. The resampled data $g_2(\lambda, u)$ is defined with a sampling distance Δu and the quantity $\hat{u} = u^*/\Delta u$ gives the detector coordinate where $\underline{x}$ is projected to, measured in multiples of Δu. The quantity NUM is the numerator of u^* in (4.11), divided by Δu; DEN stands for the denominator in (4.11). The increments that NUM and DEN experience when incrementing x at fixed y are defined by T_1 and T_2. Initialization of NUM and DEN refers to their calculation from the current value of y and the first sampled value in x. Finally, note that U_0 denotes in pixel units the location where the origin projects to, so that U_{idx} gives the index of the sample closest to $\hat{u}$.

A sketch of our implementation of the two reconstruction formulas is given in Figure 4.8. In addition to avoiding the square root and the inverse tangent, these sketches also show that we aimed at a minimization of the number of operations within the most inner loop, as this number has major impact on computation time. For the uniform-weighting formula, 1 division (line 10), 2 multiplications (lines 11 and 13) and 4 additions (lines 12, 13, 15 and 16) are required[1]. For the efficient formula, 1 division (line 0.10) and 4 additions (lines 0.11, 0.12, 0.14, 0.15) are required. Hence, in terms of operations, there is a gain of two multiplications out of 7 operations total in favor of the efficient formula.

How the gain observed in the number of operations converts into actual benefits on real systems is not trivial, as it highly depends on the system architecture, on the status of the

---

[1]The division plus the two multiplications could be replaced by two divisions, but the outcome was slower on the systems we used.

system at initialization time, on the compiler and on internal optimizations transparent to the software developer. For illustration, a C-implementation of both formulas was tested on three different platforms, called Vanda, Hailfire, and Anakin. These platforms all operated under Linux, and we compiled each code separately on each of them using the C compiler of the GNU library (gcc) while enabling code optimization using the compiler option -O4. After compilation, the code was executed 20 times for reconstruction on a Cartesian grid of 512×512 square pixels of side $1\,mm$, assuming a centered circular object region Ω_f and a water cylinder object of radius $24\,cm$. The mean CPU time of the 20 executions was recorded on each of the 3 systems, and is presented in table (4.4.4). Not surprisingly, significant differences were observed from one platform to the other, with the global gain in favor of the efficient formula being as high as 43% on Anakin. Note that Vanda has a 32-bit Intel Pentium 4 CPU with 3.40 GHz, 1 MB cache, and 2 GB RAM; Hailfire has a 64-bit AMD Opteron CPU with 2.00 GHz, 1 MB cache, and 7 GB RAM; and Anakin has a 64-bit Intel Pentium 4 CPU with 3.30 GHz, 2 MB cache, and 4 GB RAM.

Table 4.2: Execution times for the two algorithms ('unif.' and 'effic.' denote the uniform-weighting and the efficient formula, respectively) on 3 different systems as absolute values (in seconds) and as a ratio (uniform-weighting over efficient).

	Filtering			Backprojection			Total		
	unif.	effic.	ratio	unif.	effic.	ratio	unif.	effic.	ratio
Vanda	0.711	0.723	98.3%	4.483	3.873	115.7%	5.194	4.596	113.0%
Hailfire	0.655	0.661	99.1%	3.394	2.842	119.4%	4.048	3.503	115.5%
Anakin	0.707	0.713	99.2%	6.447	3.371	191.3%	7.154	4.084	175.2%
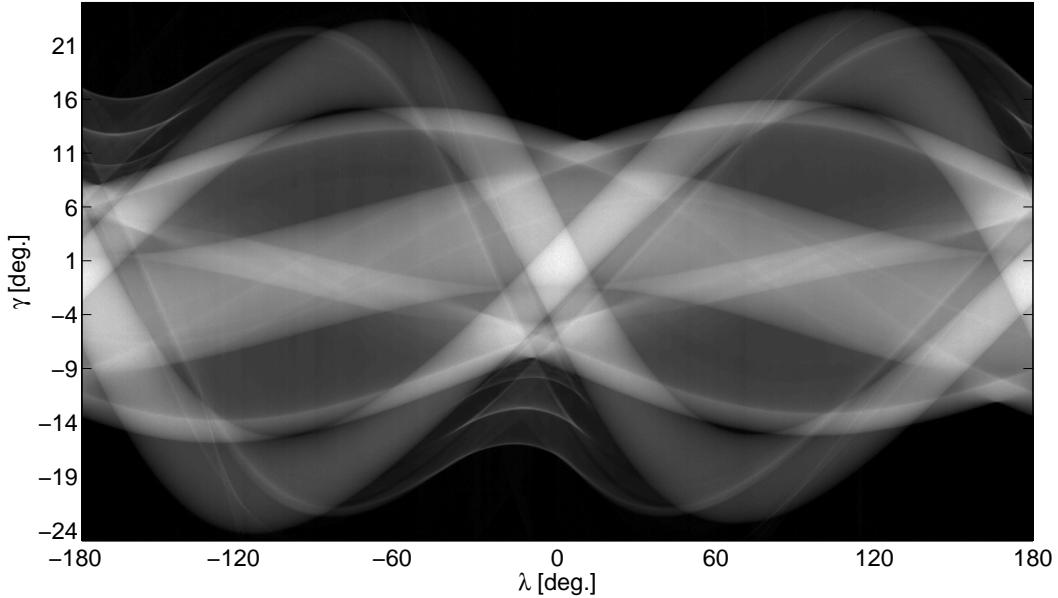
Figure 4.9: Fan-beam data $g(\lambda, \gamma)$ with $\lambda \in [0, 2\pi)$, $\gamma \in [-\gamma_m, \gamma_m]$ and $\gamma_m = 25°$, acquired from the QRM Antropomorphic Cardio CT Phantom using the commercially available Siemens SOMATOM Sensation 64 CT scanner.

4.5   Reconstruction from Real CT Data

This section demonstrates that the direct fan-beam FBP inversion method without back-projection weight, which has been introduced in section 4.3, can be readily applied for 2D image reconstruction on existing CT scanners. For this demonstration, we collected fan-beam data of a physical phantom using the commercially available Siemens SOMATOM Sensation 64 CT scanner [5], which is currently in use in the clinical environment.
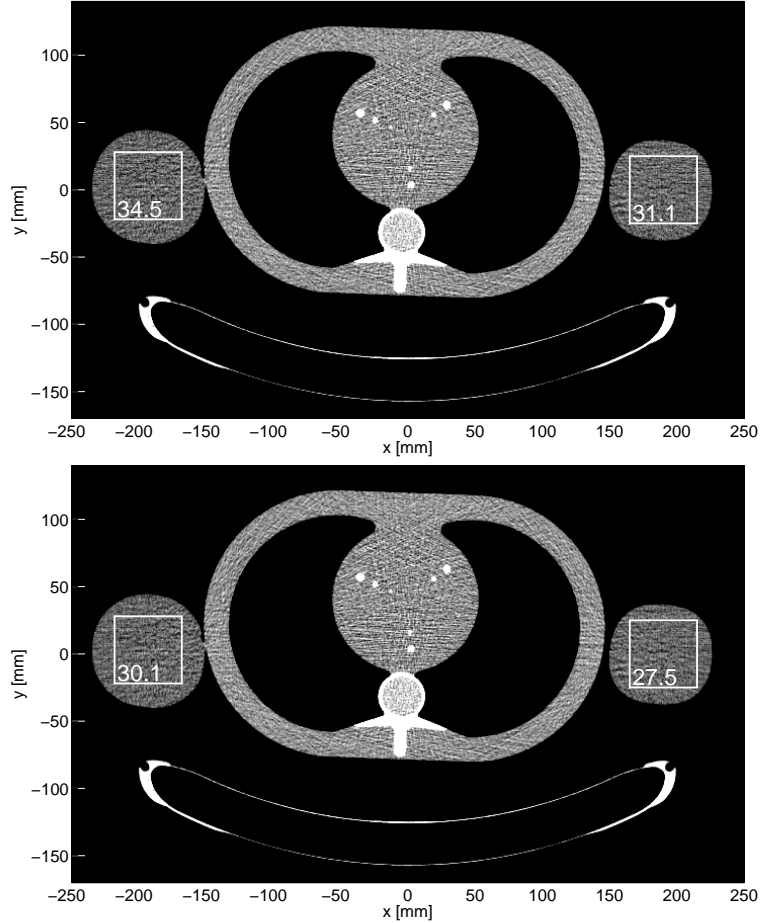
Figure 4.10: Reconstruction of the QRM phantom from the fan-beam data presented in Figure 4.9, presented in the grayscale window $[-100\,\mathrm{HU}, 150\,\mathrm{HU}]$. The reconstructions were obtained using (top) the uniform weighting formula and (bottom) the efficient formula. Image noise is estiamted using the two indicated square regions in each image, which are entirely located in the homogeneous water regions. The numers in each square correspond to the standard deviations of the reconstructed values within the corresponding region, in units of the HU scale.

The object used during this evaluation was the QRM Antropomorphic Cardio CT Phantom [1]. The QRM phantom has been designed to approximately represent the structure of a human thorax; it contains artificial lungs, a spine, soft tissue parts and furthermore a cardiac insert that consists of various cylindrical structures. The maximum width of this phantom is $15\,\mathrm{cm}$, but for the scan, two cylindrical objects of the density of water were attached to the phantom sides in order to represent the arms. The scanned region of the

QRM phantom including these two arm extensions fitted into a circular region of radius $R_o = 24\,\text{cm}$.

Fan-beam data acquisition was carried out for a full 2π-scan and according to the geometry parameters of the Siemens SOMATOM Sensation 64 CT scanner, which are summarized in [5]. The used scanning protocol involved a bowtie-filter [47] that was designed for a water-cylinder of radius $15\,\text{cm}$. Furthermore, the X-ray tube current was set to $25\,\text{mAs}$, which yielded a fairly low dose to the scanned object and consequently a high amount of noise in the fan-beam projections. See Figure 4.9 for an illustration of the acquired fan-beam data $g(\lambda, \gamma)$.

Image reconstruction from this fan-beam data was carried out on a Cartesian sampling grid in x and y with sample spacing $\Delta x = \Delta y = 0.5\,\text{mm}$ using the uniform-weighting and the efficient formula. The reconstruction results, which are illustrated in Figure 4.10, demonstrate that overall, both methods are fairly robust with respect to data noise and to other physical effects not consistent with the data model intrinsically assumed by the reconstruction formulae.
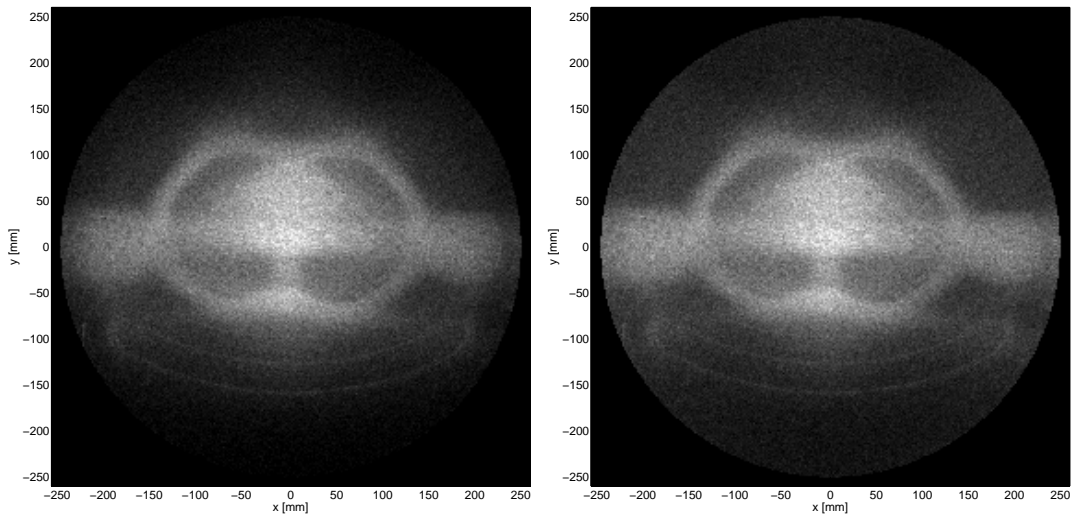
Figure 4.11: Illustration of the pixel-wise standard-deviation across the reconstructed values obtained from 100 fan-beam data sets of the QRM phantom. (Left) The efficient formula, (right) the uniform-weighting formula.

For a closer investigation of the noise level of the results in Figure 4.10, we defined two regions of square shape and side-length $50\,\text{mm}$ that are both located entirely inside the regions of the phantom that represent the arms. These regions are thus about $200\,\text{mm}$ away from the origin of the image plane and they comprise only homogeneous parts of the phantom. Because of noise in the fan-beam data, however, the estimates of f in these regions are not homogeneous, but rather distributed around the true density. The spatial standard deviation of the density values reconstructed with the efficient formula are 30.1 and 27.5 units on the HU scale in the left and right region, respectively; see Figure 4.10. The standard deviations achievable with the uniform-weighting formula measure 34.5 and 31.1 units on the HU scale, which corresponds to a noise increase of about 10% to 15% compared to the results of efficient formula.

For a more thorough investigation of image noise, we acquired 100 sets of fan-beam data of the QRM phantom using the experimental set-up described above and followed the
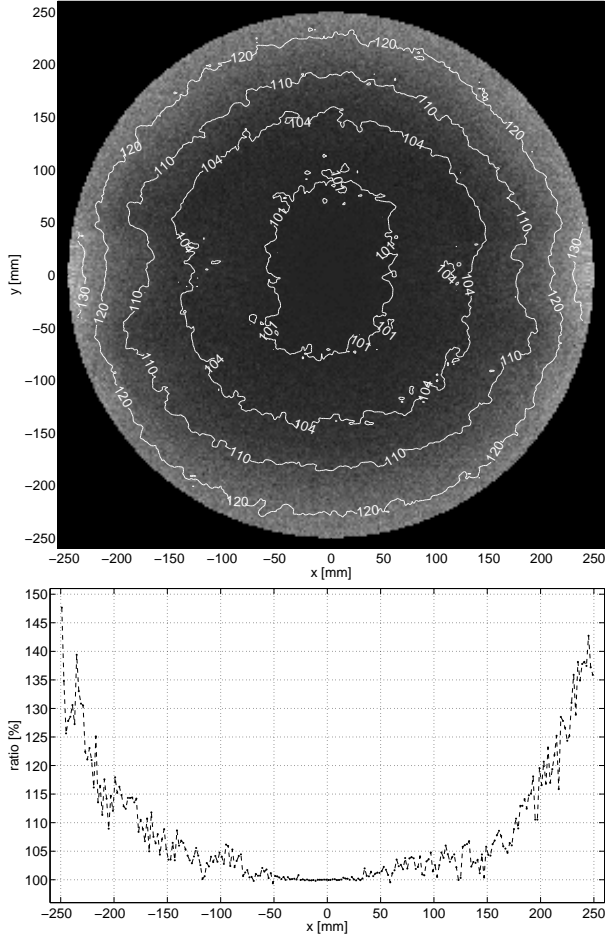
Figure 4.12: Comparison of noise propagation in the uniform-weighting and the efficient formula. (Top) The ratio (uniform-weighting over efficient) of the standard deviation images illustrated in Figure 4.11 on a pixel by pixel basis. The white isocurves illustrate the positions at which this ratio achieves values of 101%, 104%, 110%, 120% and 130%. (Bottom) Profile along the x-axis of this ratio of standard-deviations.

evaluation scheme of section 4.4.3. Obviously, each fan-beam data set contains a distinct realization of data noise so that reconstruction from these data sets yields 100 estimates of object density for each reconstruction method. The standard deviation on a pixel-wise basis across the 100 estimates obtained with the efficient formula are presented in the standard-deviation image on the left side of Figure 4.11. The result obtained for the uniform-weighting formula is presented in the right side of this figure. To emphasize the differences in noise propagation for the two methods, the ratio of the two standard-deviation images (uniform-weighting over efficient) was computed on a pixel-wise basis. This ratio is presented for the entire region Ω_f in the top of Figure 4.12, while the bottom of Figure 4.12 shows the profile of this ratio along the x-axis. These results illustrate that the two formulae under comparison behave similarly close to the image plane origin and that the efficient formula outperforms the uniform weighting formula in terms of image noise for increasing distance from this origin. The maximum gain in noise is about 45% and is obtained close to the edge of the region Ω_f. The differences in spatial resolution in the reconstructions ob-

tained with the two formulae under comparison, however, are not significant, as illustrated in Figure 4.13.
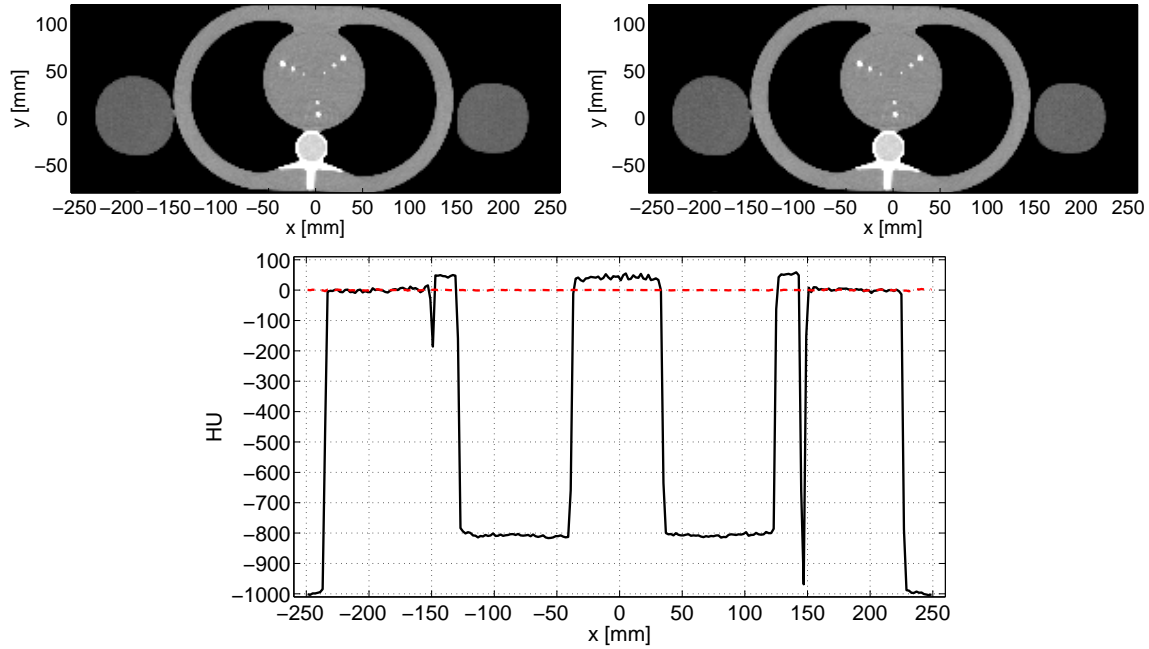
Figure 4.13: Comparison of spatial resolution in the real-data reconstruction. The top row shows in a grayscale window of $[-100\,\mathrm{HU}, 150\,\mathrm{HU}]$ the mean of the reconstructions from the 100 noisy fan-beam data sets for (left) the efficient formula and (right) the uniform-weighting formula. (Bottom) Profile through these mean reconstructions along the x-axis. The black curve shows the result of the efficient formula (in HU), the dashed, red curve the difference of the reconstructed values between the two formulae under comparison (a value of 0 means that there is no difference).

4.6   Discussion and Conclusions

In this chapter, we developed a novel direct FBP formula for full-scan fan-beam reconstruction with no backprojection weight. This formula was derived from the alternative fan-beam FBP inversion formula of Noo *et al.* [66]. We then evaluated the performance of our novel formula against the use of Noo's formula with uniform weighting of data redundancy. This evaluation was carried out using simulated fan-beam data but also data that has been acquired with a commercially-available diagnostic CT scanner.

First, a gain in terms of computation time was observed for our novel formula. In a software implementation this gain varied from 14% to 47% in backprojection effort, depending on the system used, with no significant difference in filtering time. A gain may also be expected in a hardware implementation, but quantification of this effect was not performed.

We then studied in high details various aspects of image quality achievable with our no-backprojection-weight formula from simulated data. We observed a gain in noise properties compared to Noo's formula: the standard deviation on the reconstructed values was reduced by a factor that rapidly increases from 0% at the origin of the image plane to 40% at the

edge of the region Ω_f; this improvement may be significant for large patients. On the other hand, spatial resolution and discretization errors appeared for both formulae very similar across the object support region Ω_f.

We also investigated image reconstruction from data collected with a clinical CT scanner and demonstrated that our novel formula is robust with respect to physical effects not contained in the underlying ray-integral data model. Moreover, improvements in image noise were observed compared to the uniform-weighting formula that are quantitatively almost identical to those determined previously, in the simulation studies. This advantage makes our formula an attractive candidate for reconstruction in 2D imaging applications on diagnostic CT scanners.

Note finally that the novel formula has not been compared against the classical fan-beam FBP method [46], which was described in section 3.2.3. However, a superior performance may be anticipated, both in computation time and in image quality. The gain in computation time is straightforward since our formula does not require any backprojection weight, while the effort in data filtering is essentially the same. For the gain in image quality, we refer the reader to [94], which shows that the classical formula is less robust to data noise and discretization errors than the uniform-weighting formula, which we compared the novel formula to. To achieve this superiority in image quality, it may however be needed to compute $\hat{g}(\lambda, \gamma)$ in equation (4.12) using the approach suggested in [94] rather than our discretization scheme.

Chapter 5

General Theory for Image Reconstruction in Three Dimensions

This chapter constitutes the beginning of part two of this thesis that is focussed on image reconstruction in the 3D scenario, i.e., on the reconstruction of 3D entities. The space where these entities are defined will be called the image volume in the following. To address locations in the image volume, a Cartesian, right-handed x-y-z coordinate system is introduced; an arbitrary position in the image volume may then be specified with the coordinate vector $\underline{x} = (x, y, z)^{\mathrm{T}}$.

The spatial distribution of object density is described with the function $f(\underline{x}) \in \mathbb{R}$. It is assumed that the object under investigation is entirely contained inside a specific region within the image volume and that an estimate of the convex hull of this region is known. This convex hull will be denoted using the symbol Ω_f and consequently,

$$f(\underline{x}) = 0 \qquad \text{for all} \qquad \underline{x} \notin \Omega_f. \tag{5.1}$$

5.1   3D Radon Transform and Its Inversion

The following briefly summarizes the theoretical background of the 3D Radon transform. Note that the concepts described in this review section will not necessarily all be involved in our original contributions; these concepts are, however, a prerequisite for a thorough understanding of the problem of 3D image reconstruction in CT that is addressed in the following chapters.

Generally spoken, the Radon transform maps a function defined in $\mathbb{R}^n$ onto its integrals on hyperplanes, i.e., on entities of dimension $n - 1$ [76, 19] (recall for instance that the 2D Radon operator discussed in chapter 3 yields line integrals of the function to which it is applied). Consequently, the Radon transform in 3D describes the mapping of a function $f(\underline{x})$ onto its plane integrals.

5.1.1   3D Radon Transform

Let $\Pi(\underline{\theta}, s)$ denote an arbitrary plane in the image volume. This plane is described by the unit vector $\underline{\theta} \in S^2$ that is normal to the plane and by the signed distance $s \in \mathbb{R}$ of the

plane from the origin $(0,0,0)^{\mathrm{T}}$, where s is measured along direction $\underline{\theta}$. The plane $\Pi(\underline{\theta}, s)$ will also be referred to as a Radon plane in the following and may be defined as

$$\Pi(\underline{\theta}, s) := \{\underline{x} \mid \underline{x} \cdot \underline{\theta} = s\}. \tag{5.2}$$

Note that the vector $\underline{\theta}$ may be expressed in terms of its polar and azimuthal angles φ and θ, respectively, as

$$\underline{\theta}(\varphi, \theta) = (\sin\theta \cos\varphi, \sin\theta \sin\varphi, \cos\theta)^{\mathrm{T}}. \tag{5.3}$$

See Figure 5.1 for an illustration of one example Radon plane and the geometric entities associated with it.
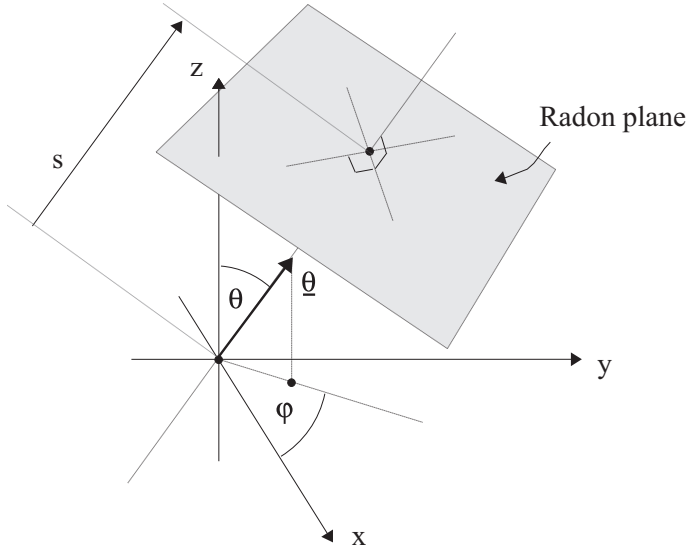
Figure 5.1: Illustration of the Radon plane $\Pi(\underline{\theta}, s)$. The unit vector $\underline{\theta}$, which is normal to this plane, has polar angle φ and azimuthal angle θ. The quantity s describes the signed distance of the Radon plane from the origin of the image volume.

The 3D Radon transform of a function f can then be defined as

$$\mathcal{R}f(\underline{\theta}, s) = \iiint\limits_{\underline{x} \in \Pi(\underline{\theta}, s)} f(\underline{x}) \, d\underline{x} = \iiint\limits_{\mathbb{R}^3} \delta(\underline{x} \cdot \underline{\theta} - s) f(\underline{x}) \, d\underline{x}. \tag{5.4}$$

In words, the operator $\mathcal{R}$ yields plane integrals of the function f to which it is applied, in a way that the value $\mathcal{R}f(\underline{\theta}, s)$ corresponds to the integral of f on the plane $\Pi(\underline{\theta}, s)$.

Visualization of the 3D function $\mathcal{R}f$ is more difficult than that of its 2D equivalent, because now the Radon data depends on three free parameters (here denoted as φ, θ and s). One option to present 3D Radon data is given in Figure 5.2: the 3D image in this figure[1] is based on the Cartesian x-y-z coordinate system and encodes values of the function $\mathcal{R}f$ using a specific color mapping within the image; the arrangement of values in this 3D domain (the 3D Radon domain) is such that the value $\mathcal{R}f(\underline{\theta}, s)$ is assigned to the point with coordinates $\underline{x} = s\,\underline{\theta}$.

---

[1]The 3D Radon data shown in Figure 5.2 is obtained from the 3D Shepp- Logan head phantom, which was introduced in [46] as a generalization of the 2D phantom that we have used throughout chapter 3.
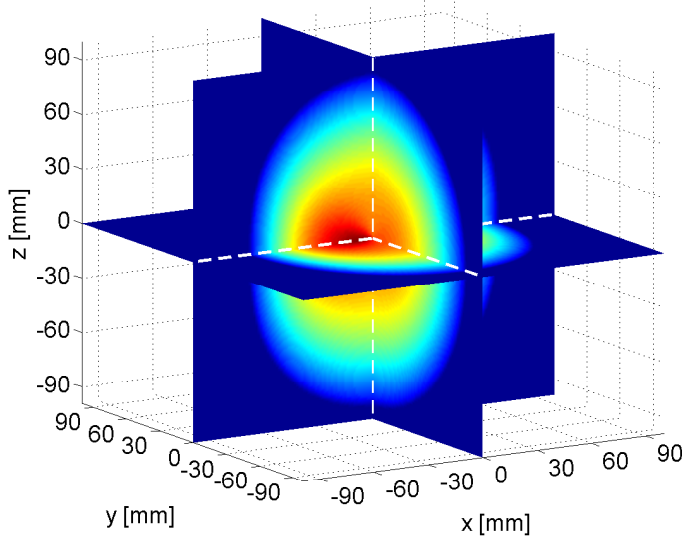
Figure 5.2: 3D Radon data of the 3D Shepp-Logan phantom. Note that the value at the origin of the presented 3D Radon domain is undefined.

5.1.2 Analytical 3D Radon Inversion Formula

We now present a derivation of an analytical formula to invert the 3D Radon transform, i.e., to recover a function f from its 3D Radon data $\mathcal{R}f$. This derivation is based on the 3D Fourier slice theorem [46]

$$\mathcal{F}_s\mathcal{R}f(\underline{\theta},\sigma) = \mathcal{F}_{\underline{x}}f(\sigma\underline{\theta}), \tag{5.5}$$

where the Fourier transforms on both sides of this equation are given as

$$\mathcal{F}_s\mathcal{R}f(\underline{\theta},\sigma) = \int\limits_{-\infty}^{\infty} \mathcal{R}f(\underline{\theta},s)e^{-2\pi i\sigma s}\,ds \qquad \text{and} \qquad \mathcal{F}_{\underline{x}}f(\underline{\xi}) = \iiint\limits_{\mathbb{R}^3} f(\underline{x})e^{-2\pi i\underline{\xi}\cdot\underline{x}}\,d\underline{x}, \tag{5.6}$$

respectively. Equation (5.5) states that the 1D Fourier transform in s of 3D Radon data at fixed $\underline{\theta}$ is identical to the profile along $\underline{\theta}$ through the 3D Fourier transform of f. This relation is obtained by using the definitions (5.4) and (5.6) together with (5.5) and developing

$$\begin{aligned}
\mathcal{F}_s\mathcal{R}f(\underline{\theta},\sigma) &= \int\limits_{-\infty}^{\infty} \mathcal{R}f(\underline{\theta},s)e^{-2\pi i\sigma s}\,ds \\
&= \int\limits_{-\infty}^{\infty} \iiint\limits_{\mathbb{R}^3} f(\underline{x})\delta(\underline{x}\cdot\underline{\theta}-s)e^{-2\pi i\sigma s}\,d\underline{x}\,ds \\
&= \iiint\limits_{\mathbb{R}^3} f(\underline{x})e^{-2\pi i\sigma\,\underline{\theta}\cdot\underline{x}}\,d\underline{x} = \mathcal{F}_{\underline{x}}f(\sigma\,\underline{\theta}).
\end{aligned} \tag{5.7}$$

An analytical inversion formula for the 3D Radon transform may then be given by expressing the object as

$$f(\underline{x}) = \iiint\limits_{\mathbb{R}^3} \mathcal{F}_{\underline{x}}f(\underline{\xi})e^{2\pi i\,\underline{\xi}\cdot\underline{x}}\,d\underline{\xi} \tag{5.8}$$

and changing variables from Cartesian to spherical coordinates $\underline{\xi} = \sigma\,\underline{\theta}$, where $\underline{\theta} \in S^2$ and $\sigma \in \mathbb{R}$. This change of variable has Jacobian $J(\underline{\theta}, \sigma) = \sigma^2/2$ and transforms (5.8) into

$$f(\underline{x}) = \frac{1}{2} \iint_{S^2} \int_{-\infty}^{\infty} \sigma^2 \mathcal{F}_{\underline{x}} f(\sigma\underline{\theta}) e^{2\pi i\,\sigma\underline{\theta}\cdot\underline{x}}\, d\sigma\, d\underline{\theta}. \tag{5.9}$$

Note that the factor $1/2$ accounts for the fact that the integration over σ and $\underline{\theta}$ considers every sample in $\underline{\xi}$ twice and therefore yields twice the quantity defined in (5.8). Inserting (5.5) into (5.9) yields the analytic 3D Radon inversion formula

$$f(\underline{x}) = \frac{1}{2} \iint_{S^2} \int_{-\infty}^{\infty} \sigma^2 \mathcal{F}_s \mathcal{R} f(\underline{\theta}, \sigma) e^{2\pi i\,\sigma\underline{\theta}\cdot\underline{x}}\, d\sigma\, d\underline{\theta} \tag{5.10}$$

from which the following two-step scheme for image reconstruction from 3D Radon data $\mathcal{R}f$ can be given:

***Step 1* - 1D Filtering:** 3D Radon data at fixed $\underline{\theta}$ is filtered in s to yield the function

$$p_F(\underline{\theta}, s) = \int_{-\infty}^{\infty} \mathcal{F}_s h_1(\sigma) \mathcal{F}_s \mathcal{R} f(\underline{\theta}, \sigma) e^{2\pi i\sigma s}\, d\sigma, \tag{5.11}$$

with the filter kernel h_1 defined as

$$\mathcal{F}_s h_1(\sigma) = \sigma^2 \tag{5.12}$$

Note that filtering according to (5.11) may be achieved using either of the two following approaches:

- Filtering with the ramp filter h_{ramp}: Since $\mathcal{F}_s h_1(\sigma) = (\mathcal{F}_s h_{ramp}(\sigma))^2$, filtering can be achieved by the two consecutive convolutions

$$p_F(\underline{\theta}, s) = \int_{-\infty}^{\infty} h_{ramp}(s - s') \int_{-\infty}^{\infty} h_{ramp}(s' - s'') \mathcal{R} f(\underline{\theta}, s'')\, ds''\, ds'. \tag{5.13}$$

- Filtering with data differentiation: In Fourier domain, the operator of the second-derivative is given as $-4\pi^2\sigma^2 = -4\pi^2 \mathcal{F}_s h_1(\sigma)$, so that data filtering can also be achieved as

$$p_F(\underline{\theta}, s) = -\frac{1}{4\pi^2} \left(\frac{\partial^2}{\partial s^2} \mathcal{R} f \right)(\underline{\theta}, s). \tag{5.14}$$

***Step 2* - Backprojection:** The function f is recovered by backprojecting filtered 3D Radon data into the image volume according to

$$f(\underline{x}) = \frac{1}{2} \iint_{S^2} p_F(\underline{\theta}, \underline{\theta} \cdot \underline{x})\, d\underline{\theta}. \tag{5.15}$$

Note that the convolution described in (5.13) corresponds to a global filtering operation and requires $\mathcal{R}f$ to be known over the entire support of s. Filtering using data differentiation according to (5.14), in contrast, is a local operation which requires only knowledge of values of $\mathcal{R}f$ in a neighborhood of the sample s at which p_F is desired. The latter filtering approach is thus preferable for practical implementation, and substituting (5.14) into (5.15) yields the well-known classical analytical 3D Radon inversion formula [46]:

$$f(\underline{x}) = -\frac{1}{8\pi^2} \iint\limits_{S^2} \left(\frac{\partial^2}{\partial s^2} \mathcal{R}f \right) (\underline{\theta}, s) \bigg|_{s=\underline{x} \cdot \underline{\theta}} d\underline{\theta}. \tag{5.16}$$

Equation (5.16) describes a stable analytical way of recovering the function f from its 3D Radon data; a practical and efficient algorithmic implementation of this formula has been suggested by [58]. Note that the reconstruction at $\underline{x}$ requires filtered 3D Radon data for all $\underline{\theta} \in S^2$, using for each $\underline{\theta}$ the sample of p_F at $(\underline{\theta}, \underline{x} \cdot \underline{\theta})$. Geometrically that means that image reconstruction at an arbitrary point $\underline{x}$ according to (5.16) requires the values of $\mathcal{R}f$ for all Radon planes through a neighborhood of $\underline{x}$. In other words, reconstruction of $f(\underline{x})$ based on equation (5.16) thus yields a valid result if the function $(\partial^2/\partial s^2)\mathcal{R}f$ is known over the entire surface of the smallest sphere in 3D Radon domain that contains the origin and the point $\underline{x}$.

5.2 Image Reconstruction in the Cone-Beam Geometry

In the following, we address the problem of 3D image reconstruction from 2D projections acquired in the geometry of state-of-the-art medical C-arm systems or multi-row diagnostic CT scanners.

5.2.1 General Cone-beam Acquisition Geometry

According to the model described in chapter 2, each 2D projection image acquired on X-ray CT systems provides access to integral values of the object density function along the rays that connect the elements of the 2D detector to the corresponding X-ray source point; each of these sets of rays thus forms geometrically a cone-beam (CB) in the image volume.

Here and in the following, we assume that projection data is acquired with the X-ray source point moving along a connected curve $\underline{a}(\lambda)$ in space, which we will call the source trajectory. The quantity λ corresponds to the curve parameter and is restricted to $\lambda \in [\lambda_{min}, \lambda_{max}]$. We assume that the source trajectory does not intersect with the convex region Ω_f that encloses the object.

X-ray measurements then yield samples of the function

$$g(\lambda, \underline{\alpha}) = \int\limits_0^\infty f(\underline{a}(\lambda) + t\underline{\alpha}) \, dt, \tag{5.17}$$

where $\underline{\alpha} \in S^2$ is used to describe the unit direction of the measurement ray. Note that (5.17) corresponds to a general definition of CB data; in practice, the set of potential realizations of the vector $\underline{\alpha}$ depends on the geometry of the detector that is used for data acquisition, as will be discussed in chapter 6. Values of g will be called CB data from now on, and CB

data at fixed λ will be referred to as a CB projection. If all non-zero values of the function g at fixed λ are known, the corresponding CB projection is called non-truncated.

5.2.2   Cone-Beam Reconstruction in General

This section briefly summarizes the fundamentals about 3D CB reconstruction theory. Our goal is not to provide a detailed topical review, but to describe the major theoretical developments as they occurred over the last about 30 years; for further information see [82, 62, 18, 21, 12] or others.

One of the major difficulties of the 3D CB reconstruction problem lies in the fact that CB data samples are not related to samples of the 3D Radon transform in a direct and straight-forward manner. In this respect, the reconstruction problem fundamentally differs from that in 2D fan-beam tomography: in the fan-beam scenario, data acquisition directly delivers 2D Radon values so that reconstruction can be easily accomplished by using 2D Radon inversion formulae with some minor modifications, as shown in chapter 3. In 3D, however, a direct generalization like that is not possible.

Some of the first methods suggested to achieve CB image reconstruction were based on approximate inversion formulae. Feldkamp *et al.*, for instance, suggested a practical reconstruction approach for CB data acquired along a full circular source trajectory [33]. Feldkamp's approach was derived as a heuristic generalization of the classical 2D fan-beam reconstruction method; it possesses an efficient FBP scheme and has therefore been considered in various clinical applications. Over the years, many variations of the Feldkamp algorithm have been suggested, some of which are described in [82], but these reconstruction approaches yield in general inexact results, and because they lack a thorough theoretical foundation, the degree of artifacts arising in the reconstruction results is in general not easy to predict.

The early 1980s brought some significant breakthroughs in the analytical CB reconstruction theory, as summarized, for instance, in the review papers [17, 81]. Advancements were mainly driven by the contributions of Tuy [83], Smith [80] and in particular by that of Grangeat [36], who found a link between CB data and the intermediate function $(\partial/\partial s)\mathcal{R}f(\underline{\theta}, s)$, which is related to the object density function through equation (5.16). For an illustration of Grangeat's approach, let us consider the function

$$g_G(\lambda, \underline{\theta}) = -\iint\limits_{S^2} h_{der}(\underline{\theta} \cdot \underline{\alpha}) g(\lambda, \underline{\alpha}) \, d\underline{\alpha}, \tag{5.18}$$

with $\underline{\theta} \in S_2$ and with $h_{der}(s)$ denoting the kernel of the first derivative, namely the inverse Fourier transform of $2\pi i\sigma$. The value of g_G at a given parameter λ can be computed, if the corresponding CB projection at λ is not truncated. Next, we substitute the function g by its definition (5.17) so that

$$g_G(\lambda, \underline{\theta}) = -\iint\limits_{S^2} \int\limits_{-\infty}^{+\infty} h_{der}(\underline{\theta} \cdot \underline{\alpha}) f(\underline{a}(\lambda) + t\underline{\alpha}) \, dt \, d\underline{\alpha}. \tag{5.19}$$
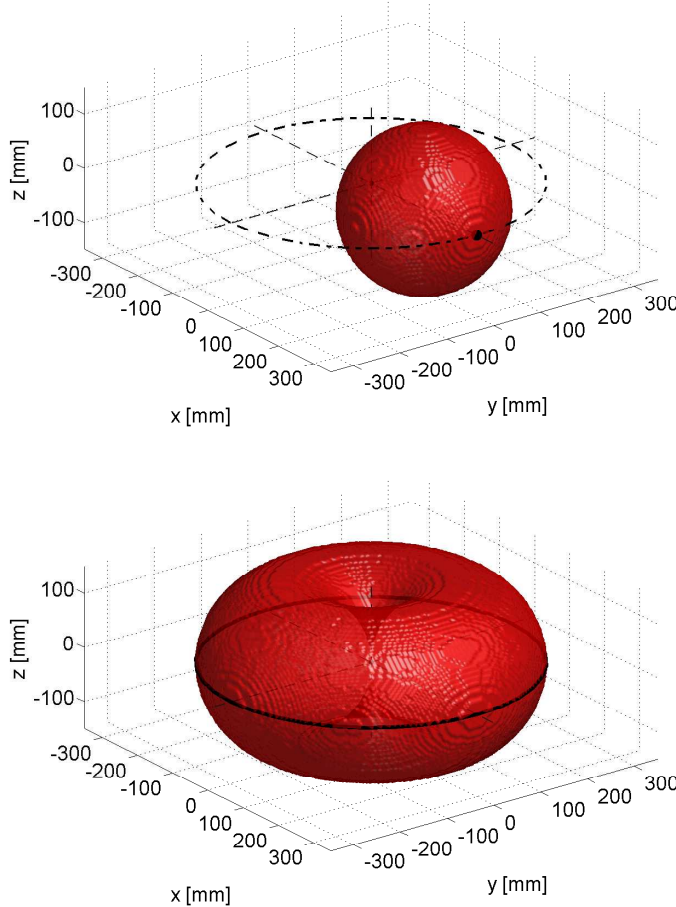
Figure 5.3: Intermediate 3D Radon values that can be obtained from CB data acquired along a circular scan with radius 300 mm. (Top) The surface of the illustrated sphere indicates the region in the 3D Radon domain where the intermediate function can be obtained from the single CB projection with the source at the black dot. The dashed circle shows the entire circular source trajectory. (Bottom) Region in the 3D Radon domain where the intermediate Radon function can be obtained using CB data from the entire circular scan. Obviously, the values of $(\partial/\partial s)\mathcal{R}f$ cannot be obtained at parameters $(\underline{\theta}, s)$ for which the points $s\,\underline{\theta}$ that are located in the gaps above and below the origin (with respect to the z-axis).

Applying the change of variables $\underline{x} = \underline{a}(\lambda) + t\underline{\alpha}$ with Jacobian $J(t, \underline{\alpha}) = t^2$ and using the scaling property $h_{der}(ts) = (1/t^2)\,h_{der}(s)$ (which holds for non-zero t) yields

$$
\begin{aligned}
g_G(\lambda, \underline{\theta}) &= - \iiint_{\mathbb{R}^3} h_{der}(\underline{\theta} \cdot (\underline{x} - \underline{a}(\lambda)))f(\underline{x})\,d\underline{x} \\
&= - \iiint_{\mathbb{R}^3} \int_{-\infty}^{+\infty} h_{der}(s' - \underline{\theta} \cdot \underline{a}(\lambda))\delta(\underline{x} \cdot \underline{\theta} - s')f(\underline{x})\,ds'\,d\underline{x} \\
&= \int_{-\infty}^{+\infty} h_{der}(\underline{\theta} \cdot \underline{a}(\lambda) - s')\mathcal{R}f(\underline{\theta}, s')\,ds'.
\end{aligned}
\tag{5.20}
$$

Finally we get

$$g_G(\lambda, \underline{\theta}) = \frac{\partial}{\partial s} \mathcal{R}f(\underline{\theta}, s) \bigg|_{s=\underline{a}(\lambda)\cdot\underline{\theta}} \tag{5.21}$$

and therefore a scheme to convert CB data $g(\lambda, \underline{\alpha})$ at a fixed λ into samples of the intermediate Radon function $(\partial/\partial s)\mathcal{R}f(\underline{\theta}, s)$, namely into all samples that belong to the surface of the smallest sphere in the 3D Radon domain that contains both, the origin and the source point $\underline{a}(\lambda)$, as illustrated, for instance, on the top of Figure 5.3. Applying (5.21) to all acquired CB projections yields $(\partial/\partial s)\mathcal{R}f(\underline{\theta}, s)$ within a specific region of the 3D Radon domain and this region depends on the realization of the source trajectory $\underline{a}(\lambda)$. The bottom of Figure 5.3, e.g., illustrates this region for the case that $\underline{a}(\lambda)$ describes a closed circle of radius 300 mm in the x-y plane around the origin of the image volume. In this case, the intermediate Radon function $(\partial/\partial s)\mathcal{R}f$ cannot be obtained in the regions of the 3D Radon domain that are attached the origin and are symmetric with respect to the z-axis; this data insufficiency is in general the cause for image artifacts, as will be addressed in more details in the following section. A similar illustration is given in Figure 5.4, for a partial circular source trajectory; in this case, the issue of data insufficiencies is even intensified compared to the full circular scan.
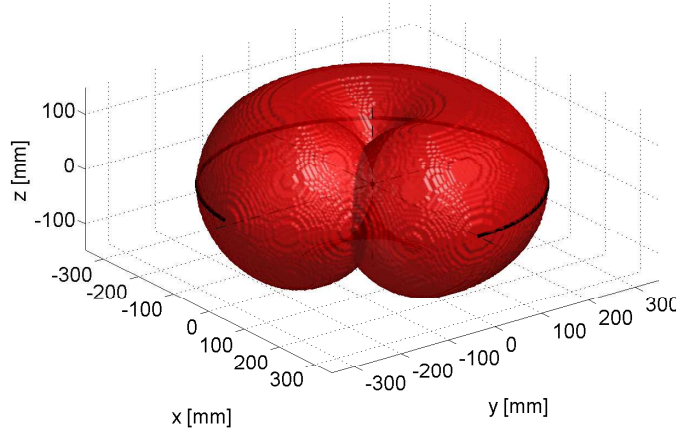
Figure 5.4: The red geometric object illustrates the region in the 3D Radon domain where the intermediate function can be obtained when the source moves along a partial circle in the x-y plane (marked as black).

5.2.3   The Issue of CB Data Sufficiency

One important issue in the context of 3D CB image reconstruction is the question under which circumstances an accurate reconstruction of the value $f(\underline{x})$ is possible. Among several contributions to this issue, which are briefly summarized in [31], Tuy's formulation of the CB data sufficiency criterion [83] has gained most attention. Tuy's sufficiency criterion states that theoretically-exact and stable CB reconstruction at a point $\underline{x}$ is only possible, if and only if almost every plane through $\underline{x}$ has at least one intersection with the source trajectory [83, 34]. CB reconstruction in regions in which Tuy's sufficiency condition is not satisfied corresponds in general to an ill-posed problem, which cannot be solved in a simultaneously stable and exact way [34]. The phrase 'in general' here denotes that reconstruction is to

be achieved for arbitrary objects f and that no a priori information about the function f is known.

To understand the criterion described in the previous paragraph, focus again on the scenario illustrated in Figure 5.3, where the source trajectory $\underline{a}(\lambda)$ corresponds to a closed circle in the x-y plane. Tuy's sufficiency condition is then satisfied only for points that belong to the plane of the trajectory. Accurate reconstruction outside this plane is in general impossible. Image quality is degraded by artifacts (CB artifacts) and the shape and structure of occurring CB artifacts may vary from one reconstruction algorithm to the other.

It is interesting to note that if the object density function f satisfies specific homogeneity criteria, accurate and stable CB reconstruction may be possible even if Tuy's criterion is not satisfied; for more details about this issue see e.g. [24].

5.2.4   Reconstruction via Filtered Backprojection

Numerical algorithms for accurate CB reconstruction from data that satisfies Tuy's sufficiency condition can be composed by a direct implementation of the theory presented in section 5.2.2 [78]. Applying (5.21) to each acquired CB projection successively delivers the intermediate Radon function throughout the 3D Radon domain. The application of a 3D Radon inversion algorithm on this intermediate result then simply yields, in a second step, the wanted object density function. The shortcomings of these straight-forward methods are that the second step can only be carried out after all CB projections have been processed, that interpolation steps in the 3D Radon domain are required and that all CB projections have to be non-truncated.

Subsequent research was thus focussed on deriving CB reconstruction algorithms that follow the practical FBP scheme, where every CB projection can be processed immediately after it has been measured. Clack and Defrise [20] and Kudo and Saito [57] suggested schemes to find such FBP-type CB reconstruction algorithms for a variety of source trajectories; one important ingredient in these schemes is a weighting function, which needs to be adapted to the considered source trajectory and accounts for redundancies in the intermediate Radon function that can be obtained from the given CB data set. The resulting numerical CB reconstruction algorithms are based on a shift-variant filtering step and a subsequent 3D weighted CB backprojection of the filtered data; these FBP methods allow accurate reconstruction, as long as the considered CB data is non-truncated and also satisfies Tuy's sufficiency condition. Interestingly, it was shown that the application of these schemes to a full circular source trajectory yields an algorithm that coincides with the one suggested by Feldkamp [44, 20], thus setting that heuristically derived method into a firm theoretical framework.

Another breakthrough in CB reconstruction theory was achieved by Katsevich, who suggested, in 2003, a novel general scheme to derive image reconstruction algorithms for theoretically-exact reconstruction from CB data that satisfies Tuy's sufficiency condition [50]. This scheme, which is also discussed in [53, 13], is related to the ones described in the previous paragraph [98]; it e.g. also requires a proper definition of a redundancy weighting function to find a practical algorithm for a given source trajectory. In contrast to the previously described scheme, however, Katsevich's method allows us to compose for many practically- relevant scenarios FBP algorithms that achieve data filtering by a shift-invariant 1D convolution along specific filter directions; these algorithms are therefore more efficient and in general more flexible with respect to truncation in the CB data, depending

on the required filter directions. In recent years, a variety of attractive reconstruction algorithms have been derived from Katsevich's general theory, such as for instance the ones for helical source trajectories [49], for circle-plus-arc trajectories [52] or for the ellipse-plus-oblique-line trajectory [25], to name only a few.

5.2.5   Reconstruction via Differentiated Backprojection

As illustrated in the previous section, various FBP methods exist to achieve 3D image reconstruction from CB data [87]. The common feature of FBP methods is that they require, at some point during CB data filtering, the convolution of data with a filter kernel that has infinite support. The filtering thus corresponds to a global operation which may yield inaccurate results in presence of truncation in one or more CB projections.

To tackle this sensitivity with respect to data truncation, novel approaches for CB image reconstruction have been suggested that avoid the global filtering operation on the projection data during the filtering step [99, 100, 72]. These approaches first differentiate CB data and then backproject the differentiated data into the image volume to obtain an intermediate function that is linked to the wanted object density function through some fundamental filter relation that involves the Hilbert transform. This relation has been derived in a general form e.g. in [72]. Reconstruction may then be achieved by transforming the intermediate function into the function f through additional filtering operations carried out in the image volume.

Approaches that are based on this scheme are in literature typically known under the term backprojection-filtration (BPF) or differentiated-backprojection (DBP); they can naturally cope with some scenarios of data truncation in which FBP methods fail. More details about these approaches will be given in the following chapters, in the context of circular CB CT.

Chapter 6

Comparative Evaluation of Four Circular Short-Scan Reconstruction Methods

6.1   Introduction

Over the past few years, cone-beam X-ray computed tomography has become a powerful imaging technology in the clinical arena [70, 59]. Among all possible scanning modes, circular motion of the X-ray scanning device relative to the interrogated object remains one of the most attractive ones. This is because a circular scan is easy to implement, mechanically robust and allows fast data acquisition.

Unfortunately, with the circular as well as with any planar source trajectory, Tuy's data sufficiency condition for exact and stable reconstruction [83] is not satisfied for the points that lie outside the plane of the X-ray source trajectory, as has been discussed in section 5.2.3. This means that CB image reconstruction is an ill-posed problem almost everywhere within the image volume [34]; a numerically stable recovery of the object density function in a 3D volume of interest from noisy data can thus only be achieved by sacrificing some accuracy in the reconstruction result. A reconstruction algorithm can only be useful for practical applications if it performs an efficacious trade-off between numerical stability and accuracy.

For the closed circular trajectory (full-scan), an attractive algorithm is given by the approach suggested in 1984 by Feldkamp *et al.* (FDK) [33]. However, not every X-ray CT system can acquire data along a full-scan. In particular, the mechanical design of medical C-arm systems typically prevents data acquisition over more than 330°. Moreover, for various physical reasons including dose and scanning time, most scanning protocols on C-arm systems are restricted to a short-scan of 210° to 240° [2]. Hence, FDK cannot be applied to C-arm systems.

Finding an efficacious algorithm for the short-scan geometry turns out to be a challenging task. A popular algorithm used to achieve image reconstruction in many state-of-the-art C-arm systems is a modification of FDK: short-scan FDK [86]. However, the short-scan FDK method uses geometric approximations to handle data redundancies in the CB data set and these approximations yield in general a significant amount of CB artifacts in the reconstruction results.

During the last few years, other methods to achieve reconstruction from circular short-scan CB data have been suggested [64, 56, 93, 67, 43, 37, 92]; some of them are based on novel reconstruction formulae that allow less severe geometric approximations, if any, and a more precise handling of data redundancies. In general, each of these methods comes with a different trade-off between accuracy and numerical stability and may thus respond differently to the data insufficiency and to data noise. Unfortunately, only few comparison studies have been published, see e.g. [84, 97], and these studies did not necessarily consider the most promising algorithmic developments in the field of circular CB reconstruction.

We here perform a detailed comparative evaluation of four analytical reconstruction methods for the circular short-scan CB geometry. Our study involves the short-scan FDK-method [33], which is widely used in practically-available X-ray CT systems, and three attractive, novel reconstruction methods, namely the ACE-method [64], the virtual PI-line BPF method [93] and the virtual PI-line BPF method with Parker weighting [93]. Our study is based on a uniform evaluation framework that includes quantitative figures of merit as well as a visual assessment of image quality.

6.2   Circular Short-Scan Geometry using a Planar Detector
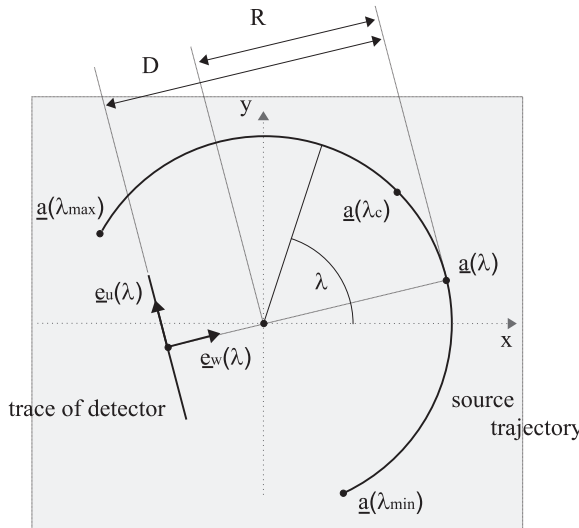
Figure 6.1: Illustration of the circular short-scan CB acquisition geometry, assuming a planar detector. Top view of the geometric entities in the plane of the scan: The curve $\underline{a}(\lambda)$ corresponds to the source trajectory, R denotes the scan radius and D the distance between source and detector.

In the following, we focus on image reconstruction in the circular short-scan CB geometry with planar detector. This geometry is a specific realization of the general 3D CB geometry introduced in section 5.2.1 and associated with the practical scenario where an assembly of X-ray source and flat-panel detector performs a partial rotation around the investigated object during the scan. The focal spot of the X-ray source thus moves along a circular trajectory and without loss of generality, it is assumed that this trajectory is contained in the plane $z = 0\,\mathrm{mm}$ and that the rotation axis of the scanning device coincides

with the z-axis; see Figure 6.1. Hence, we can here describe the source trajectory with the function

$$\underline{a}(\lambda) = (R\cos\lambda, R\sin\lambda, 0)^{\mathrm{T}}, \tag{6.1}$$

where R denotes the radius of the trajectory and λ corresponds to the polar angle of the source during the scan. We assume that CB projections are measured with λ varying in the interval $[\lambda_c - \lambda_s/2, \lambda_c + \lambda_s/2]$. The quantity λ_s then gives the scan-length of the short-scan and $\underline{a}(\lambda_c)$ defines the central point on the source trajectory, or, the short-scan center. The polar angle of the first source position is thus given as $\lambda_{min} = \lambda_c - \lambda_s/2$ and similarly, $\lambda_{max} = \lambda_c + \lambda_s/2$ will denote the polar angle of the source point at the end of the scan.

To describe the planar detector geometry, we introduce the orthonormal system of vectors

$$\underline{e}_u(\lambda) = (-\sin\lambda, \cos\lambda, 0)^{\mathrm{T}} \tag{6.2}$$
$$\underline{e}_v = (0,0,1)^{\mathrm{T}} \tag{6.3}$$
$$\underline{e}_w(\lambda) = (\cos\lambda, \sin\lambda, 0)^{\mathrm{T}}, \tag{6.4}$$

which is illustrated in Figure 6.2. Note that during the scan, this vector system rotates along with the source-detector assembly such that $\underline{e}_u(\lambda)$ is tangent to the source trajectory at $\underline{a}(\lambda)$ and such that $\underline{e}_w(\lambda)$ gives the direction from the image volume origin towards the source. We then assume that the plane of the detector is spanned by the vectors $\underline{e}_u(\lambda)$ and $\underline{e}_v$ and that this plane is at fixed distance D from the source during the scan. Locations on the detector plane are described using the vector $(u,v)^{\mathrm{T}}$, where u and v are coordinates measured along the axes $\underline{e}_u(\lambda)$ and $\underline{e}_v$, respectively; they are defined such that the value $(u,v)^{\mathrm{T}} = (0,0)^{\mathrm{T}}$ is obtained at the orthogonal projection of $\underline{a}(\lambda)$ onto the detector plane. We assume that the projection is measured with a detector that covers the area $u \in [u_{min}, u_{max}]$ and $v \in [v_{min}, v_{max}]$.

Let $\underline{\alpha}(\lambda, u, v)$ denote the unit vector along the ray diverging from $\underline{a}(\lambda)$ and intersecting the detector plane at coordinates $(u,v)^{\mathrm{T}}$; this vector may be written as

$$\underline{\alpha}(\lambda, u, v) = \frac{u\,\underline{e}_u(\lambda) + v\,\underline{e}_v - D\,\underline{e}_w(\lambda)}{\sqrt{u^2 + v^2 + D^2}}. \tag{6.5}$$

The CB data at $(u,v)^{\mathrm{T}}$ with the source at polar angle λ will be denoted as

$$g_m(\lambda, u, v) = g\left(\lambda, \underline{\alpha}(\lambda, u, v)\right), \tag{6.6}$$

where

$$g\left(\lambda, \underline{\alpha}\right) = \int_0^\infty f(\underline{a}(\lambda) + t\underline{\alpha})\,dt. \tag{6.7}$$

Furthermore, at a given λ, the coordinates of the CB projection of a point $\underline{x}$ onto the detector plane are given as

$$u^*(\underline{x}) = D\frac{\underline{x}\cdot\underline{e}_u(\lambda)}{R - \underline{x}\cdot\underline{e}_w(\lambda)} \qquad \text{and} \qquad v^*(\underline{x}) = D\frac{\underline{x}\cdot\underline{e}_v}{R - \underline{x}\cdot\underline{e}_w(\lambda)} \tag{6.8}$$

Note that in the definitions of (6.8) we use again, as in the previous chapters, the superscript $*$ to denote a function that depends on λ without explicitly listing this argument. Figure 6.2 presents the geometry of the detector as we picture it.
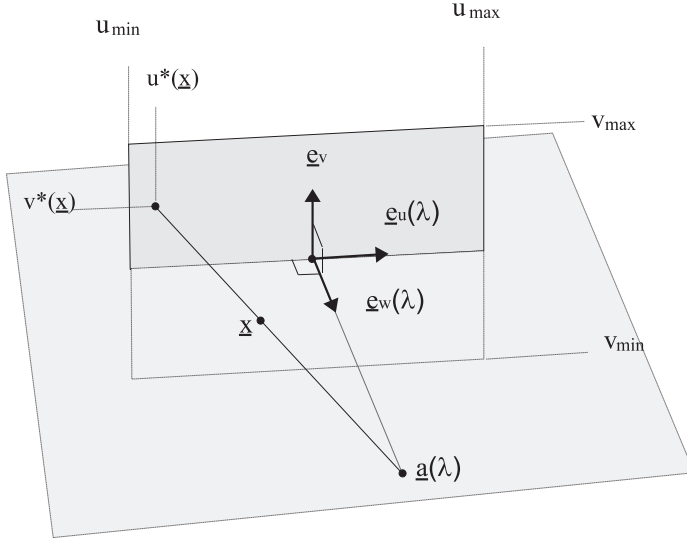
Figure 6.2: Geometric entities associated with the planar detector. The quantities u_{min}, u_{max}, v_{min} and v_{max} define the detector size, and $u^*(\underline{x})$ and $v^*(\underline{x})$ are the coordinates of the CB projection of $\underline{x}$ onto the detector plane.

If the CB projection of the object lies within the measured detector area for each λ, i.e., if $u^*(\underline{x}) \in [u_{min}, u_{max}]$ and $v^*(\underline{x}) \in [v_{min}, v_{max}]$ for all $\underline{x} \in \Omega_f$ and all $\lambda \in [\lambda_{min}, \lambda_{max}]$, CB data will be called non-truncated. If the projection of the object exceeds the measured interval in u for some λ, the CB data suffers from transaxial truncation. On the other hand, if this projection exceeds the measured interval in v, we say that the CB data set contains axial truncation.

Image reconstruction in the circular short-scan CB geometry then refers to the task of recovering the object density function $f(\underline{x})$ for $\underline{x} \in \Omega_f$ from the measured CB data $g_m(\lambda, u, v)$ with $\lambda \in [\lambda_{min}, \lambda_{max}]$, $u \in [u_{min}, u_{max}]$ and $v \in [v_{min}, v_{max}]$. Since this task cannot be simultaneously solved in a theoretically-exact and in a stable way and since discretization impacts the numerical computation, we can in general only compute an approximate estimate $f^e(\underline{x})$ of the true object density function. The following sections present four state-of-the-art methods that have been suggested in the literature to compute such an estimate.

6.3   The Short-Scan FDK Method

The short-scan FDK method is based on the algorithm introduced in 1984 by Feldkamp, Davis and Kress (FDK) [33] for approximate reconstruction from CB data acquired along a full circular scan (i.e., for a scan with $\lambda_s = 360°$). The full-scan FDK reconstruction algorithm is well-understood in terms of the 3D Radon theory [20, 57]. Almost all 3D Radon planes through Ω_f intersect the full circular source trajectory either twice or never. The full-scan FDK method uses for reconstruction the information associated with 3D Radon planes that have two such intersections. It weights each data sample with a factor of $1/2$ resulting in an equal contribution of every used 3D Radon value to the final reconstruction. Data associated to 3D Radon planes that do not intersect the source trajectory is never

measured and does not contribute to the FDK estimation of the object density; this lack of information causes CB artifacts in the reconstruction result.

In the short-scan geometry, the distribution of data redundancies is more complex - some 3D Radon planes intersect the source trajectory once, others twice, others never. Thus, the beneficial Radon-plane based weighting scheme intrinsically used for the full-scan trajectory that weights every measurement with $1/2$ cannot be applied. Wang *et al.* [86] suggested an heuristic modification of the full-scan FDK reconstruction approach to be able to apply that method for reconstruction from CB data corresponding to a circular short-scan. In this modification, which we will refer to as the short-scan FDK method from now on, CB data is multiplied with a v-independent weighing function prior to reconstruction to approximately account for data redundancies. A common selection for the weighting function, which we use within this comparison study, is the generalized Parker weighting function [79] that was introduced in chapter 3.2.3.

6.3.1 Reconstruction Method

The short-scan FDK method computes an estimate f^e of the object density function f from the circular CB data using the following steps:

Step 1 – **Weighting:** CB data is multiplied with a length correction weight and with the redundancy function to yield weighted CB projections

$$g_w(\lambda, u, v) = \frac{D}{\sqrt{u^2 + v^2 + D^2}} \, m_{gp}(\lambda, u) \, g_m(\lambda, u, v) \qquad (6.9)$$

where

$$m_{gp}(\lambda, u) = \tilde{m}\left(\lambda, \tan\frac{u}{D}\right) \qquad (6.10)$$

gives the generalized Parker weighting function [79] for the flat panel geometry; see (3.48) on page 26 for a definition.

Step 2 – **1D Filtering:** Convolution of the weighted CB projections in u with the kernel of the ramp filter yields filtered CB projections denoted as

$$g_F(\lambda, u, v) = \int\limits_{u_{min}}^{u_{max}} h_{ramp}(u - u') g_w(\lambda, u', v) \, du'. \qquad (6.11)$$

Step 3 – **3D Backprojection:** Filtered CB projections are backprojected into the image volume using the entire acquired interval in λ to yield the object estimate

$$f^e(\underline{x}) = RD \int\limits_{\lambda_{min}}^{\lambda_{max}} \frac{g_F\left(\lambda, u^*(\underline{x}), v^*(\underline{x})\right)}{(R - \underline{x} \cdot \underline{e}_w(\lambda))^2} \, d\lambda \qquad (6.12)$$

with functions u^* and v^* defined in (6.8).

6.3.2   Implementation Details

The short-scan FDK method follows the FBP scheme and involves only 1D filtering along lines that are in the direction of $\underline{e}_u(\lambda)$; it is thus relatively easy to implement and computationally efficient. The numerical algorithm considered in this evaluation study achieved data filtering and weighting by discretizing equations (6.9) and (6.11) at $k\Delta u$ with $k \in \mathbb{Z}$, and therefore yields the filter result on a sampling grid in u and v that is identical to that of the initial CB data function g_m. For implementation of (6.11) we used a band-limited version of the ramp filter kernel with bandwidth set to $1/(2\Delta u)$ and furthermore used sinc apodization on the kernel. To increase computation speed, the convolution in (6.11) was carried out in frequency domain, using standard signal-processing techniques. 3D CB backprojection according to (6.12) was implemented by approximating the integral in this equation with a discrete sum according to the rectangular rule of numerical integration and by using bilinear interpolation in u and v to obtain in each filtered CB projection the values required at $u^*(\underline{x})$ and $v^*(\underline{x})$.

6.4   The ACE Method

In 2003, Katsevich presented a novel, general framework to construct theoretically-exact inversion formulae for the 3D divergent beam transform for a large class of source trajectories [50]; see section 5.2.4. Reconstruction at a specific point $\underline{x}$ using such a formula can yield accurate results, dependent on the actual degree of data truncation, if the CB data set satisfies Tuy's sufficiency condition for exact and stable reconstruction at $\underline{x}$. The ACE method [64] (the acronym stands for arc based cone-beam reconstruction using an equal-weighting scheme) has been derived by applying Katsevich's framework to the short-scan circular source trajectory and by intrinsically using a uniform weighting of the measured 3D Radon data, following principles already applied in [67]. Hence, data redundancies in the CB data are handled accurately rather than by using a heuristic weighting scheme. However, CB data collected along the circular trajectory satisfies Tuy's sufficiency condition only for points inside the plane of the source motion. Hence, the ACE method will yield accurate results only within the slice $z = 0$ and will in general yield approximate results everywhere else throughout the image volume.

6.4.1   Reconstruction Method

The ACE method computes an estimate f^e of the object density function from the known CB data as follows:

Step 1 – **Differentiation:** Differentiation of CB data in λ at fixed ray direction yields differentiated CB projections denoted as

$$g_d(\lambda, u, v) = \lim_{\varepsilon \to 0} \frac{g\left(\lambda + \varepsilon, \underline{\alpha}(\lambda, u, v)\right) - g\left(\lambda - \varepsilon, \underline{\alpha}(\lambda, u, v)\right)}{2\varepsilon} \qquad (6.13)$$

Step 2 – **Weighting:** Cosine weighting of the differentiated CB data yields

$$g_w(\lambda, u, v) = \frac{D}{\sqrt{u^2 + v^2 + D^2}} g_d(\lambda, u, v). \qquad (6.14)$$

Step 3 – **1D Filtering:** The weighted and differentiated CB data is convolved with the
kernel of the Hilbert transform along 3 filtering lines to yield 3 filtered CB projections:

$$g_{F1}(\lambda, u, v) = \int_{u_{min}}^{u_{max}} h_{hilb}(u - u')g_w(\lambda, u', v)\, du', \tag{6.15}$$

$$g_{F2}(\lambda, u, v) = \int_{u_{min}}^{u_{max}} h_{hilb}(u - u')g_w(\lambda, u', v_1'(\lambda, u, u', v))\, du', \tag{6.16}$$

$$g_{F3}(\lambda, u, v) = \int_{u_{min}}^{u_{max}} h_{hilb}(u - u')g_w(\lambda, u', v_2'(\lambda, u, u', v))\, du', \tag{6.17}$$

with v_1' and v_2' denoting the equations of two lines on the detector plane:

$$v_1'(\lambda, u, u', v) = v + (u - u')\kappa_1, \qquad \kappa_1 = \frac{v - v^*(\underline{a}(\lambda_{min}))}{u - u^*(\underline{a}(\lambda_{min}))}, \tag{6.18}$$

$$v_2'(\lambda, u, u', v) = v + (u - u')\kappa_2, \qquad \kappa_2 = \frac{v - v^*(\underline{a}(\lambda_{max}))}{u - u^*(\underline{a}(\lambda_{max}))} \tag{6.19}$$

and κ_1 and κ_2 denoting their respective slopes.

The computation of one filter sample according to (6.15) requires function g_w at fixed
v; filtering is therefore geometrically carried out along filter lines on the detector that
are parallel to the u-axis, as in the FDK method. The convolutions in (6.16) and
(6.17), however, involve values of g_w on filter lines that vary with λ and are in general
oblique. More specifically, to obtain at a given λ the function g_{F2} at point $(u, v)^{\mathrm{T}}$,
consider the line that connects this point with the CB projection of the first source
position $\underline{a}(\lambda_{min})$ onto the detector plane; the equation of this line is given by (6.18).
The desired value of g_{F2} is then obtained by convolving values of g_w along this line
with the kernel of the Hilbert transform and evaluating the convolution result at
coordinate u. Data filtering for g_{F3} follows a similar scheme; it requires filter lines
that contain the CB projection of $\underline{a}(\lambda_{max})$ onto the detector plane, the equations of
which are given by (6.19).

Step 4 – **3D Backprojection:** The ACE estimate of the object density function is ob-
tained by 3D backprojection of the filtered CB projections using a non-squared back-
projection weight, according to

$$\begin{aligned}
f^e(\underline{x}) = -\frac{1}{4\pi^2} \int_{\lambda_{min}}^{\lambda_{max}} \frac{1}{R - \underline{x} \cdot \underline{e}_w(\lambda)} &\Bigg(g_{F1}(\lambda, u^*(\underline{x}), v^*(\underline{x})) \\
&+ \frac{\mathrm{sign}\,(u^*(\underline{x}) - u^*(\underline{a}(\lambda_{min})))}{2} g_{F2}\,(\lambda, u^*(\underline{x}), v^*(\underline{x})) \\
&+ \frac{\mathrm{sign}\,(u^*(\underline{a}(\lambda_{max})) - u^*(\underline{x}))}{2} g_{F3}\,(\lambda, u^*(\underline{x}), v^*(\underline{x})) \Bigg) d\lambda
\end{aligned} \tag{6.20}$$

6.4.2 Implementation Details

As the short-scan FDK method, the ACE algorithm also uses the FBP scheme, but ACE
involves a filtering step that is more complex than that of FDK: it requires CB data dif-
ferentiation, data weighting and three different 1D convolutions with the Hilbert kernel.

The differentiation of CB data according to (6.13) was here implemented following the view-differentiation scheme described in [68]. This scheme requires the selection of a differentiation parameter, which plays a similar role than ε in (6.13). We here fix this parameter to $\varepsilon = 0.01$, because this specific value was found to yield both, good spatial resolution in the differentiation result and good numerical stability [68].

Hilbert filtering was achieved by discretizing (6.15)-(6.17) at coordinates $k\Delta u$ [1] and by replacing the Hilbert kernel with its band-limited version, using rectangular apodization and bandwidth $1/(2\Delta u)$. Computationally efficient filtering along non-horizontal lines, which occur in (6.16) and (6.17), was achieved using an approach similar to that explained in [69]. First, the slope parameters κ_1 and κ_2 were discretized, which geometrically means that data filtering involved a fixed number of filtering lines. The discretization steps $\Delta\kappa_1$ and $\Delta\kappa_2$ were selected in a way that the v-coordinates of the intersection of the axis $u = 0$ with any two neighboring filter lines differed by $\Delta v/2$. Note that this scheme yielded a number of filter lines used for computation of g_2 or g_3 that is twice as high as the number of filter lines used for term g_1. Next, values of g_w along these filter lines were extracted, in a so called forward-rebinning step, using linear interpolation in v. These values were then convolved with the Hilbert kernel and subsequently, in a back-rebinning step, transformed back on a Cartesian sampling grid in u and v. This back-rebinning involved bilinear interpolation and was carried out on a sampling pattern with 8 times finer sampling along each dimension compared to the initial grid on which the function g_w is known.

3D CB backprojection was carried out by first combining the three filter contributions on the upsampled grid and then using nearest neighbor interpolation in u and v to obtain the required samples at $u^*(\underline{x})$ and $v^*(\underline{x})$ from this combined filter result.

6.5   The Virtual PI-Line BPF Methods

The third and forth reconstruction methods used in this comparison study are based on a theoretically exact reconstruction formula that has been proposed for image reconstruction from CB data acquired along a helical source trajectory [100]. The helical reconstruction formula described in this reference follows a scheme that the authors of [100] refer to as backprojection-filtration (BPF): Reconstruction is achieved by first backprojecting differentiated CB data into the image volume and then using 1D filtering along PI-lines to convert the backprojection result into the object density estimate; here, a PI-line is a line that connects two points on the source trajectory. An important feature of the BPF methods is that they naturally allow in some scenarios accurate reconstruction from transaxially-truncated CB data, in contrast to the FBP methods described earlier in this chapter [100, 99, 72].

In [93], the helical reconstruction formula has been modified to be useful for 3D reconstruction from a circular short-scan. Obviously, in this geometry, PI-lines only exist in the plane of the source motion; to allow reconstruction in other regions of the image volume, so called virtual PI-lines are heuristically introduced that are parallel to the plane $z = 0\,\mathrm{mm}$. The resulting reconstruction method will be denoted as the virtual PI-Line BPF method from now on.

---

[1]Note that filter lines with slopes of magnitude exceeding 1 were handled differently: equations (6.16) and (6.17) were then expressed as a convolution with respect to v instead of with respect to u. This yields a finer sampling on very oblique filter lines and thus less aliasing and better performance in the discrete scenario [64].

6.5.1 Reconstruction Method

We follow the notation of [93] and describe points in the image volume using the parameters $(\lambda_1, \lambda_2, z, t)$, where $[\lambda_1, \lambda_2] \subset [\lambda_{min}, \lambda_{max}]$. The first 3 parameters specify one (virtual) PI-line in the image volume, namely the line that is related to the line through the points $\underline{a}(\lambda_1)$ and $\underline{a}(\lambda_2)$ by a shift of z along the z-axis. Parameter t specifies locations along the virtual PI-line, increases when approaching $\underline{a}(\lambda_2)$ and takes value $t = 0$ at the orthogonal projection of the world coordinate origin onto the PI-line, as depicted in Figure 6.3. The Cartesian coordinates of the point described with $(\lambda_1, \lambda_2, z, t)$ are given as

$$\underline{x}(\lambda_1, \lambda_2, z, t) = \frac{\underline{a}(\lambda_1) + \underline{a}(\lambda_2)}{2} + t\frac{\underline{a}(\lambda_2) - \underline{a}(\lambda_1)}{\|\underline{a}(\lambda_2) - \underline{a}(\lambda_1)\|} + (0, 0, z)^{\mathrm{T}}. \tag{6.21}$$

In the following, we use the short-hand notation $\underline{x}_\pi$ to denote the function $\underline{x}(\lambda_1, \lambda_2, z, t)$.
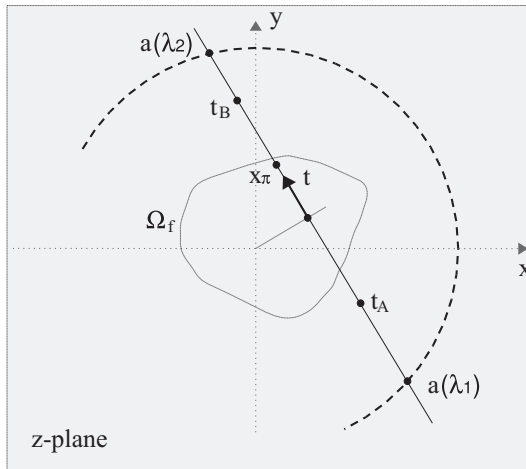

Figure 6.3: Illustration of the $(\lambda_1, \lambda_2, z, t)$ coordinate system used by the BPF methods to describe locations $\underline{x}_\pi$ in the image domain. The gray plane is parallel to the plane of the source trajectory and intersects the rotation axis at coordinate z. The points $\underline{a}(\lambda_1)$ and $\underline{a}(\lambda_2)$ are two positions along the source trajectory (illustrated as a dashed arc) that are used to define a line in that plane and parameter t describes locations on this line. The parameters t_A and t_B define arbitrary points that are, however, outside the region Ω_f.

The virtual PI-Line BPF method estimates the object density function from the known CB data using the following steps:

Step 1 – **Weighting:** Length-correction weighting of the CB projection data yields weighted CB projections denoted as

$$g_w(\lambda, u, v) = \frac{D}{\sqrt{u^2 + v^2 + D^2}} \, g_m(\lambda, u, v). \tag{6.22}$$

Step 2 – **Differentiation:** The weighted CB projections are differentiated in u to yield differentiated CB data

$$g_d(\lambda, u, v) = \frac{\partial}{\partial u} g_w(\lambda, u, v). \tag{6.23}$$

Step 3 – **3D Backprojection:** Backprojection of the differentiated CB projections using only the interval in $\lambda \in [\lambda_1, \lambda_2]$ and backprojection of boundary terms at λ_1 and λ_2 yields an intermediate function in the image domain

$$
\tilde{f}(\lambda_1, \lambda_2, z, t) = DR \int_{\lambda_1}^{\lambda_2} \frac{g_d(\lambda, u^*(\underline{x}_\pi), v^*(\underline{x}_\pi))}{(R - \underline{x}_\pi \cdot \underline{e}_w(\lambda))^2} \, d\lambda
$$
$$
+ \left. \frac{g_m(\lambda, u^*(\underline{x}_\pi), v^*(\underline{x}_\pi))}{\|\underline{x}_\pi - \underline{a}(\lambda)\|} \right|_{\lambda_1}^{\lambda_2}
\tag{6.24}
$$

with functions u^* and v^* defined in (6.8).

Step 4 – **1D Filtering:** The object density estimate is obtained from the intermediate function through 1D filtering

$$
f^e(\underline{x}_\pi) = \frac{1}{2\pi} \frac{1}{\sqrt{(t_B - t)(t - t_A)}}
$$
$$
\times \left(\int_{t_A}^{t_B} h_{hilb}(t - t') \sqrt{(t_B - t)(t - t_A)} \tilde{f}(\lambda_1, \lambda_2, z, t') dt' + 2P \right).
\tag{6.25}
$$

The quantities t_A and $t_B > t_A$ are coordinates along the virtual PI-Line containing $\underline{x}_\pi$ that describe points that are outside and on opposite sides of the object support region Ω_f. The term $2P$ in (6.25) stands for

$$
2P = g_m\left(\lambda, u^*(\underline{x}_\pi), v^*(\underline{x}_\pi)\right) \bigg|_{t=0, \lambda=\lambda_1} + g_m\left(\lambda, u^*(\underline{x}_\pi), v^*(\underline{x}_\pi)\right) \bigg|_{t=0, \lambda=\lambda_2}
\tag{6.26}
$$

i.e., $2P$ is the sum of the CB data samples corresponding to the rays that diverge from $\underline{a}(\lambda_1)$ or $\underline{a}(\lambda_2)$ and contain the central point on the virtual PI line, at coordinate $t = 0$, as suggested in [93].

6.5.2   The Virtual PI-Line BPF Method with Parker Weighting

The virtual PI-Line reconstruction method explained above uses for reconstruction only the CB data corresponding to $\lambda \in [\lambda_1, \lambda_2]$. To consider all acquired CB projections for reconstruction, a modification of the algorithm explained above has been suggested [93] that differs from that algorithm as follows:

Difference 1 – **Weighting:** CB data weighting now also involves a multiplication with a weighting function that is designed to approximately account for redundancies in the CB data for $\lambda \in [\lambda_1, \lambda_2]$. This approach is identical to that used in the short-scan FDK method; a popular choice is again to use the generalized Parker weighting function, defined in (6.10), so that altogether, we obtain weighted CB projections as

$$
g_w(\lambda, u, v) = \frac{D}{\sqrt{u^2 + v^2 + D^2}} \, m_{gp}(\lambda, u) \, g_m(\lambda, u, v).
\tag{6.27}
$$

Difference 2 – 3D Backprojection: CB backprojection considers now the interval $\lambda \in [\lambda_{min}, \lambda_{max}]$ and thus all acquired CB projections. This modification, however, introduces two additional boundary terms and requires the application of a signum weighting function prior to backprojection, so that the intermediate function is now obtained as

$$
\begin{aligned}
\tilde{f}(\lambda_1, \lambda_2, z, t) =& DR \int_{\lambda_{min}}^{\lambda_{max}} \operatorname{sign}\left(u^*(\underline{x}_\pi) - u^*(\underline{a}(\lambda_1))\right) \frac{g_d(\lambda, u^*(\underline{x}_\pi), v^*(\underline{x}_\pi))}{(R - \underline{x}_\pi \cdot \underline{e}_w(\lambda))^2} \, d\lambda \\
&+ \operatorname{sign}\left(u^*(\underline{x}_\pi) - u^*(\underline{a}(\lambda_1))\right) m_{gp}(\lambda, u^*(\underline{x}_\pi)) \frac{g_m(\lambda, u^*(\underline{x}_\pi), v^*(\underline{x}_\pi))}{\|\underline{x}_\pi - \underline{a}(\lambda)\|} \bigg|_{\lambda_{min}}^{\lambda_{max}} \\
&+ 2 m_{gp}(\lambda, u^*(\underline{x}_\pi)) \frac{g_m(\lambda, u^*(\underline{x}_\pi), v^*(\underline{x}_\pi))}{\|\underline{x}_\pi - \underline{a}(\lambda)\|} \bigg|_{\lambda_1}^{\lambda_2}.
\end{aligned}
\tag{6.28}
$$

6.5.3 Implementation Details

The numerical implementation of the virtual PI-Line BPF methods used for the comparison study uses PI-lines that are parallel to each other and orthogonal to the vector $(\cos \lambda_c, \sin \lambda_c, 0)^{\mathrm{T}}$.

To allow for the discrete scenario, the Hilbert kernel in filtering equation (6.25) has been replaced by its bandlimited version h_{hilb}^b with rectangular band-limitation and bandwidth $1/(2\Delta t)$. Equation (6.25) was furthermore discretized using $t = i\Delta t$ and $t' = j\Delta t + \Delta t/2$ with integers i and j. This discretization scheme yields a beneficial discretization of h_{hilb}^b that avoids sampling points at which the kernel becomes 0, but it also means that the sampling grids for functions f^e and $\tilde{f}$ are shifted with respect to each other by half a sampling step along the direction t [69].

Differentiation according to (6.23) was obtained by a finite difference between two neighboring samples in u and the differentiation result was assigned to the mid-point between the two samples. Backprojection used bilinear interpolation in u and v to obtain the values required at coordinates u^* and v^*, and furthermore linear interpolation in λ for the boundary terms from source locations λ that do not in general coincide with the known samples in λ. Moreover, backprojection according to (6.24) or (6.28) was carried out on a grid that was shifted in t by $\Delta t/2$ with respect to the grid on which the reconstruction result f^e is desired. This shifting accounts for the discretization scheme applied for (6.25) and allows the object density estimate to be obtained on the sampling grid initially defined.

6.6 Comparative Evaluation

This section presents the detailed comparative evaluation of the four reconstruction methods described above. In this study, which is based on simulated CB data, we assess spatial resolution and image noise, evaluate CB artifacts and investigate the impact of axial truncation on the reconstruction results.

Although the actual short-scan geometry may vary slightly from one experiment to the other, the general simulation parameters were fixed throughout this study and selected to approximate the acquisition geometry of real medical C-arm systems; these general

parameters are summarized in table 6.1. We did not consider physical effects so that the CB data were consistent with the data model intrinsically assumed by the evaluated reconstruction methods. However, we reduced aliasing in the CB data by subdividing each detector element during data simulation with a 2×2 Cartesian sampling grid with samples evenly distributed on the corresponding element. To obtain one CB data sample at $(u, v)^{\mathrm{T}}$, we then constructed 4 rays, each of which connects the vertex point with one of the 4 sub-sampling positions around $(u, v)^{\mathrm{T}}$. For each sub-ray, we computed the integral of the object density from the analytic phantom definition. The linear average of the 4 resulting values is then used as the CB datum finally assigned to the sampling position at $(u, v)^{\mathrm{T}}$.

Some of the algorithmic properties we investigate in the following are similar to those studied in chapter 4.4, while evaluating 2D full-scan fan- beam reconstruction methods. The evaluation presented here, however, is more complex because reconstruction results are now 3D entities and because the symmetry of the reconstruction problem occurring with the full-scan acquisition geometry is lost. Image quality may thus depend on the distance from the rotation axis, but also on the relative location with respect to the gap in the short-scan and on the distance from the plane of the source motion, $z = 0\,\mathrm{mm}$.

In our evaluation, we use figures-of-merit (FOMs) that are computed from only a few 3D reconstructions and we consider a specifically designed CB performance phantom. The main body of this phantom consists of a cylinder of radius $180\,\mathrm{mm}$ and height $130\,\mathrm{mm}$ that has density $0\,\mathrm{HU}$ (i.e., the density of water, here fixed as $\mu_{water} = 0.01836\mathrm{mm}^{-1}$). For the evaluation, the phantom is centered on the z-axis and placed such that its lower edge is below the plane of the scan, at $z = -20\,\mathrm{mm}$. We placed 58 small cylindrical inserts into the main phantom body and use these inserts to determine the algorithmic properties at various locations in the image volume, as will become clearer below. Each insert has density $40\,\mathrm{HU}$, diameter $12\,\mathrm{mm}$ and height $6\,\mathrm{mm}$ and is oriented such that its axis is parallel to the z-axis. Half of these inserts are centered on the plane $z = 0\,\mathrm{mm}$, i.e., on the plane of the source trajectory. The arrangement in x and y of these first 29 inserts is such that 20 of them are evenly distributed on a ring of radius $160\,\mathrm{mm}$ around the image volume origin, 8 inserts are located on a ring of radius $50\,\mathrm{mm}$ and one insert is centered on the origin; see Figure 6.4. The remaining 29 inserts have the same arrangement in the coordinates x and y, but they are centered at $z = 50\,\mathrm{mm}$.

6.6.1   Evaluation of Spatial Resolution

To determine spatial resolution, we simulated non-truncated CB data of the performance phantom in the C-arm geometry, using a short-scan that is centered at the polar angle $\lambda_c = 0°$ and that has a scan-range of $\lambda_s = 210°$. Hence, the source trajectory was symmetric

Table 6.1: Parameters of the C-arm geometry selected for our comparative evaluation

|	
radius of the source trajectory [mm]	$R = 750$
detector-source distance [mm]	$D = 1200$
discretization along trajectory [°]	$\Delta\lambda = 0.4$
detector pixel size [mm]	$\Delta u = 0.8, \quad \Delta v = 0.8$
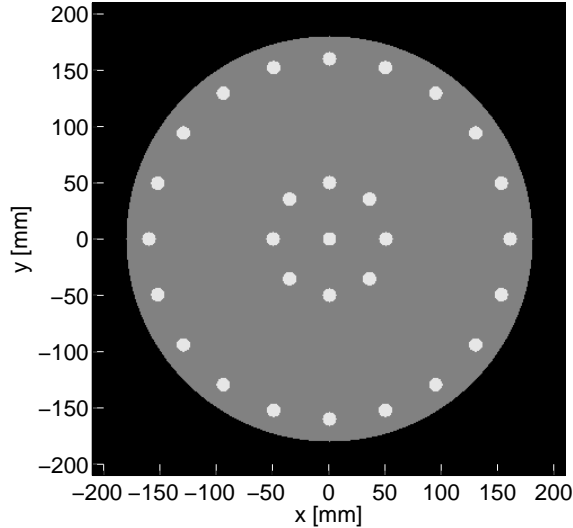
Figure 6.4: The slice $z = 0\,\text{mm}$ through the CB performance phantom in the grayscale window $[-50\,\text{HU}, 50\,\text{HU}]$.

with respect to the x-axis. Image reconstruction from these simulated CB projections was carried out on a Cartesian grid with sampling distance $\Delta x = \Delta y = \Delta z = 0.5\,\text{mm}$. [2]

We then estimated, as will become clearer below, at each insert location and individually for each reconstruction method, the mean (x,y)-resolution, the anisotropy of the (x,y)-resolution and resolution in the z-direction. These results allow us to determine for each method the homogeneity of the resolution within the entire image volume, but also to compare spatial resolution of the four algorithms at a specific location of interest.

The methodology to estimate (x,y)-resolution is now illustrated for an insert located at point $\underline{r}$. First, we create the following 1D profiles:

$$p_{xy}^e(\tau, \omega) = \frac{1}{9} \sum_{i_z=-4}^{4} f^e\left(\underline{r} + (0, 0, i_z\,\Delta z)^{\mathrm{T}} + \tau(\cos\omega, \sin\omega, 0)^{\mathrm{T}}\right), \qquad (6.29)$$

which are obtained along half-lines that are orthogonal to the z-axis and that diverge from $\underline{r}$. These profiles are extracted from the reconstructed f^e using bilinear interpolation in x and y. The parameter $\tau > 0$ denotes locations along the profile and $\omega \in [0, 2\pi)$ corresponds to the angle that the profile describes with the x-axis (measured in ccw direction); see the left side of Figure 6.5.

Ideally, these profiles would have a value of $40\,\text{HU}$ for regions inside the insert and a value of $0\,\text{HU}$ for regions in the phantom background, with a discontinuity occurring at the cylinder edge, i.e., at $\tau = 6\,\text{mm}$. In practice, however, profiles obtained according to (6.29) deviate from this ideal scenario. Deviations might include (i) a bias in the reconstructed densities, (ii) a slight offset of the location of the insert edge due to discretization and (iii) a smooth decay of density values in the transition between insert and background rather than an actual step. Here, effect (iii), i.e., the rate of decay of the reconstructed densities

---

[2]Note that in this geometry, the PI-lines using for the BPF methods were parallel to the y-axis and that we used the sampling $\Delta t = 0.5\,\text{mm}$ on these lines. The sampling grid on which the BPF estimate was determined therefore coincided with the Cartesian grid that was used for the FBP methods.

is used to characterize resolution. For a quantification of this effect, we compare thus each extracted profile p_{xy}^e to a reference profile defined as

$$p_{xy}(\tau, \omega) = \begin{cases} p_{in}(\omega) & \text{if } \tau < 6\,\text{mm} \\ p_{bg}(\omega) & \text{if } \tau \geq 6\,\text{mm} \end{cases} \tag{6.30}$$

where $p_{in}(\omega)$ and $p_{bg}(\omega)$ are the means of the values of $p_{xy}^e(\tau, \omega)$ for $\tau \in [3, 4.5]\,\text{mm}$ and $\tau \in [7.5, 9]\,\text{mm}$, respectively[3].
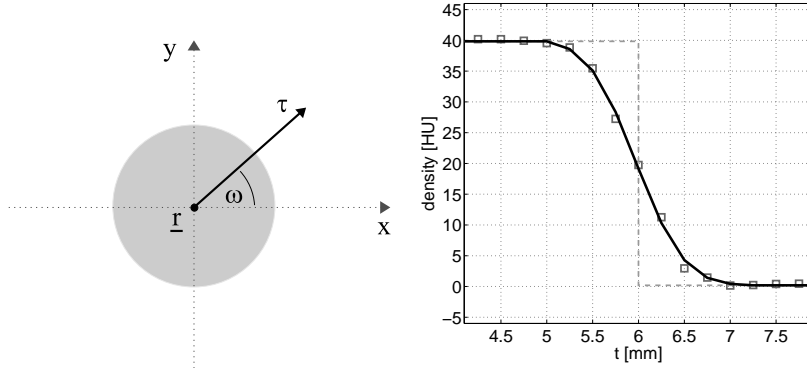

Figure 6.5: Illustration of the method used to estimate $x - y$ resolution from the insert at $\underline{r}$. (Left) An example ray that indicates the location of the profile p^e in the image domain. The angle ω defines the profile direction and τ gives the distance of points along the profile from $\underline{r}$. (Right) During profile matching, the reference profile p (dashed line) is convolved with a 1D Gaussian kernel to yield a blurred reference profile $\tilde{p}$ (black) that best matches the samples p^e obtained from the reconstruction result (squares), in a least-squares sense.

More specifically, let $\tilde{p}_{xy}(\tau, \omega, \sigma, o_\tau)$ denote a blurred reference profile, which is the result of the discrete convolution of p_{xy} from (6.30) with a 1D Gaussian of standard deviation $\sigma > 0$ and shift o_τ:

$$\tilde{p}_{xy}(\tau, \omega, \sigma, o_\tau) = \frac{1}{\sigma\sqrt{2\pi}} \int_{-\infty}^{\infty} p_{xy}(\tau', \omega) \exp\left(-\frac{(\tau - \tau' + o_\tau)^2}{2\sigma^2}\right) d\tau' \tag{6.31}$$

We determined parameters σ and o_τ that yield a blurred profile, $\tilde{p}_{xy}$, that best matches the profile p_{xy}^e in a least-squares sense within the interval $\tau \in [3, 9]\,\text{mm}$, i.e., around the location of the edge.

The value of σ that achieves that least-squares matching is used to quantify (x,y)-resolution in the direction ω; it is denoted using the symbol $\sigma_{xy}(\omega)$. Note that large values of $\sigma_{xy}(\omega)$ indicate a low resolution, since then, stronger low-pass filtering is required to match the desired profile to the profile extracted from the actual reconstruction. Note also that matching with $o_\tau \neq 0$ refers to a (slight) shift with respect to τ of the insert edge

---

[3]Note that the reference profiles are not generated from the ground truth, but from the reconstruction result in order to reduce the impact of the reconstruction bias on the resolution measurement [15]

in the reconstruction rather than to a resolution loss. Modeling this shift is similar to the concept of profile rectification in [15], and allows accurate estimation of spatial resolution.

At a given insert location, $\sigma_{xy}(\omega)$ was computed for 120 profiles with angles $\omega \in \mathcal{S}_\omega$ where $\mathcal{S}_\omega = \{i\pi/60 \mid i = 0 \ldots 119\}$. The (x-y)-resolution at $\underline{r}$ was then characterized using the mean and standard deviation of $\sigma_{xy}(\omega)$ over all 120 profiles, i.e., the values

$$\bar{\sigma}_{xy} = \frac{1}{|\mathcal{S}_\omega|} \sum_{\omega \in \mathcal{S}_\omega} \sigma_{xy}(\omega) \qquad \text{and} \qquad \sigma_{xy}^\sigma = \left(\frac{1}{|\mathcal{S}_\omega| - 1} \sum_{\omega \in \mathcal{S}_\omega} (\sigma_{xy}(\omega) - \bar{\sigma}_{xy})^2 \right)^{1/2} \qquad (6.32)$$

where $|\cdot|$ denotes the amount of elements in a given set. The quantity $\bar{\sigma}_{xy}$ gives the average (x,y)-resolution at $\underline{r}$, while σ_{xy}^σ indicates the degree of anisotropy in this resolution; a value $\sigma_{xy}^\sigma = 0$ means that the resolution is isotropic.

Spatial resolution in z at any insert location $\underline{r}$ was estimated using a methodology similar to that described previously in this section. However, instead of focussing on profiles parallel to the $x - y$ plane, we now investigate the profiles

$$p_z^e(\tau, \underline{s}) = f^e(\underline{r} + \underline{s} + (0, 0, \tau)^{\mathrm{T}}) \qquad (6.33)$$

that are parallel to the z-axis and that are obtained from the reconstruction f^e using linear interpolation in z and nearest-neighbor interpolation in x and y. The argument $\underline{s} \in \mathbb{R}^3$ is a translation vector that allows us to shift the profiles with respect to the point $\underline{r}$. Here, we restrict this translation vector to $\underline{s} \in \mathcal{S}_s$ with $\mathcal{S}_{\underline{s}} = \left\{ (i\Delta x, j\Delta y, 0)^{\mathrm{T}} \mid \sqrt{(i\Delta x)^2 + (j\Delta y)^2} \leq 3\,\mathrm{mm} \right\}$ and with integers i and j. All considered profiles are thus at least $3\,\mathrm{mm}$ away from the insert cylinder surface in x and y. Furthermore, we only allow values $\tau > 0$, such that all considered profiles face in positive z-direction.

The profiles constructed from the reconstruction are then compared to a reference profile that is defined as

$$p_z(\tau, \underline{s}) = \begin{cases} p_{in}(\underline{s}) & \text{if } \tau < 3\,\mathrm{mm} \\ p_{bg}(\underline{s}) & \text{if } \tau \geq 3\,\mathrm{mm}. \end{cases} \qquad (6.34)$$

where $p_{in}(\underline{s})$ and $p_{bg}(\underline{s})$ are the means of $p_z(\tau, \underline{s})$ within the intervals $\tau = [1, 2]\,\mathrm{mm}$ and $\tau = [4, 5]\,\mathrm{mm}$, respectively. Similarly as in evaluation of (x,y)-resolution, we convolve this reference profile with a (potentially shifted) 1D Gaussian kernel such that the convolution result best matches (in a least squares sense) the function p_z^e. The standard deviation of the kernel that achieves this matching will be denoted as $\sigma_z(\underline{s})$; the mean of this quantity over all considered profiles

$$\bar{\sigma}_z = \frac{1}{|\mathcal{S}_{\underline{s}}|} \sum_{\underline{s} \in \mathcal{S}_s} \sigma_z(\underline{s}) \qquad (6.35)$$

is then used as the estimate of the average z resolution at $\underline{r}$.

Figure 6.6 shows the resolution estimates in the plane $z = 0\,\mathrm{mm}$ for the inserts on the ring with radius $160\,\mathrm{mm}$. These estimates are plotted as functions of the angular position of the insert. As expected, the resolution behavior is for each method fairly symmetric with respect to the x-axis, i.e. the axis of symmetry of the short-scan. For short-scan FDK and the virtual PI-Line BPF methods, resolution in both, (x,y) and z is highest in the regions close to the short-scan center $\underline{a}(\lambda_c)$ and we note that the z-resolution follows closely the average (x,y)-resolution throughout the entire considered region. Slight deviations between these two properties can only be observed for the inserts at polar angles $0°$ and $180°$. The ACE method, in contrast, shows a different behavior. Its mean (x,y)-resolution is
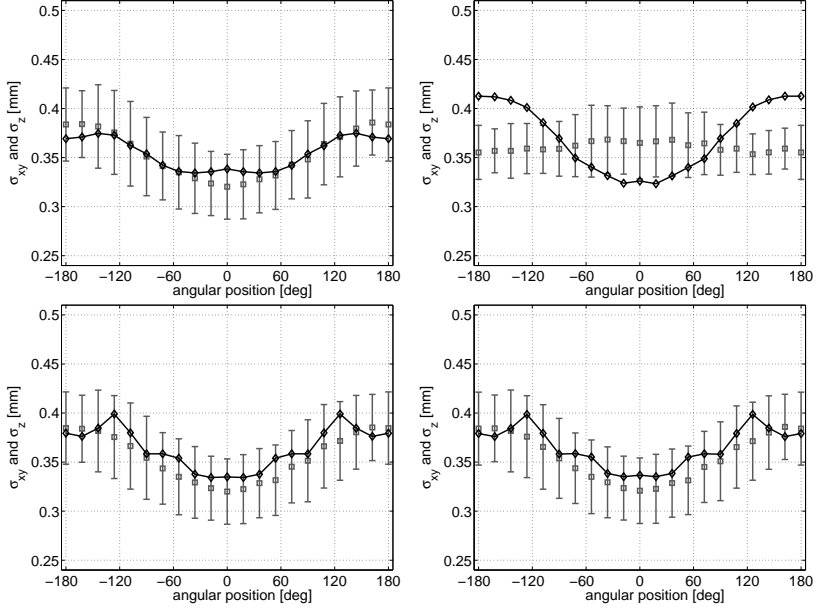
Figure 6.6: Evaluation of the spatial resolution using the inserts at $z = 0$ mm, which are located on the ring of radius 160 mm, for a short-scan with parameters $\lambda_c = 0°$ and $\lambda_s = 210°$. The four figures show for each reconstruction method the spatial resolution in $x - y$ and in z as a function of the angular position of the insert. The mean (x,y)-resolution and its anisotropy are indicated with gray squares and gray errorbars, respectively. The black curve shows the mean resolution in z. (Top left) Short-scan FDK method, (top right) ACE method, (bottom left) virtual PI-line BPF method, (bottom right) virtual PI-line BPF method with Parker weighting.

nicely homogeneous and almost invariant with respect to the angular position of the insert. However, its z-resolution noticeably varies throughout the image volume and appears to be slightly lower in average compared to that achievable with the other three methods.

6.6.2   Evaluation of Contrast-to-Noise Ratio

To investigate noise propagation, we evaluated the contrast-to-noise ratio (CNR) in the reconstruction results. For this evaluation, we first added noise to the CB data which was used in the previous subsection and reconstructed the density of the CB performance phantom throughout the entire region Ω_f, using again an isotropic sampling of 0.5 mm. Note that noise was added according to the Poisson noise model, as described in [89], and assuming an emission of $250,000$ photons per ray.

The CNR at an insert location $\underline{r} = (x_r, y_r, z_r)^{\mathrm{T}}$ was determined by defining two 3D regions in a neighborhood of $\underline{r}$, namely region $\mathcal{S}_A$ that is entirely located inside the insert and region $\mathcal{S}_B$, located in the phantom background and surrounding the insert. More specifically, region $\mathcal{S}_A$ consists of the points

$$\mathcal{S}_A = \left\{ \underline{x} \,\middle|\, \sqrt{(x - x_r)^2 + (y - y_r)^2} \in [0, 5]\, \mathrm{mm}\,,\, z - z_r \in [-2, 2]\, \mathrm{mm} \right\} \tag{6.36}$$
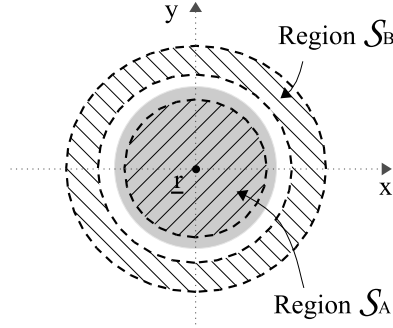
Figure 6.7: Top view of the insert at $\underline{r}$ in the CB performance phantom, illustrating the regions $\mathcal{S}_A$ (cylinder inside the insert) and $\mathcal{S}_B$ (torus around the insert) used for the CNR measurements.

and thus itself forms a cylinder with axis parallel to the z-axis, height $4\,\mathrm{mm}$ and circular base of radius $5\,\mathrm{mm}$. Region $\mathcal{S}_B$ is defined as

$$\mathcal{S}_B = \left\{\underline{x} \,|\, \sqrt{(x-x_r)^2 + (y-y_r)^2} \in [7,11]\,\mathrm{mm}\,, \; z - z_r \in [-2,2]\,\mathrm{mm}\right\} \tag{6.37}$$

and corresponds to a torus of thickness $4\,\mathrm{mm}$ around the insert cylinder; see Figure 6.7. Due to the noise in the CB data, the object density estimate f^e in these two regions is not homogeneous, but differs noticeably from the true density values. Let

$$\bar{f}_A = \frac{1}{|\mathcal{S}_A|} \sum_{\underline{x} \in \mathcal{S}_A} f^e(\underline{x}) \qquad \text{and} \qquad f_A^\sigma = \left(\frac{1}{|\mathcal{S}_A|-1} \sum_{\underline{x} \in \mathcal{S}_A} \left(f^e(\underline{x}) - \bar{f}_A\right)^2\right)^{1/2} \tag{6.38}$$

denote the mean and the standard deviation of the reconstructed values in region $\mathcal{S}_A$, respectively. Similarly, let

$$\bar{f}_B = \frac{1}{|\mathcal{S}_B|} \sum_{\underline{x} \in \mathcal{S}_B} f^e(\underline{x}) \qquad \text{and} \qquad f_B^\sigma = \left(\frac{1}{|\mathcal{S}_B|-1} \sum_{\underline{x} \in \mathcal{S}_B} \left(f^e(\underline{x}) - \bar{f}_B\right)^2\right)^{1/2} \tag{6.39}$$

denote this mean and standard deviation for region $\mathcal{S}_B$. The CNR at $\underline{r}$ in the reconstruction from a single noisy CB data set is estimated as

$$\frac{\bar{f}_A - \bar{f}_B}{\sqrt{\frac{1}{2}(f_A^\sigma)^2 + \frac{1}{2}(f_B^\sigma)^2}}. \tag{6.40}$$

This estimation is carried out using 10 distinct noise realizations, which yields 10 values of the FOM defined in (6.40). The mean and the standard deviation of these 10 values are then used to characterize the CNR of a given reconstruction method at the considered location $\underline{r}$.

Figure 6.8 shows 5 square regions from the average of 9 reconstructed slices between $z = -2\,\mathrm{mm}$ and $z = 2\,\mathrm{mm}$. Four of these five presented regions show the inserts on the ring with radius $160\,\mathrm{mm}$ and at polar angles $0°$, $90°$, $180°$ and $270°$. The fifth region shows the insert centered at the origin. Figure 6.9 shows the quantitative results of the CNR
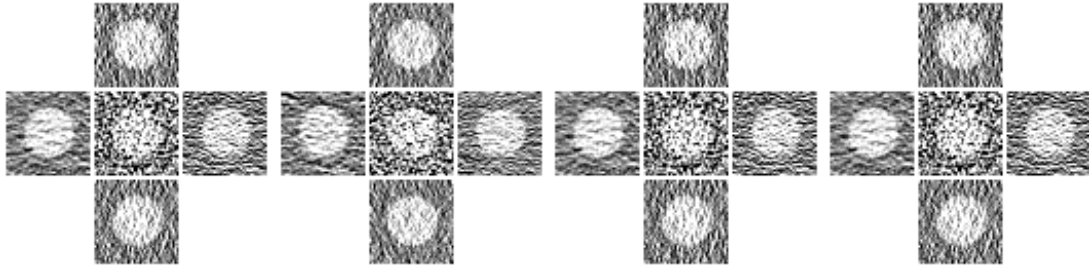
Figure 6.8: Illustration of five ROIs, obtained from the slice $z = 0\,\mathrm{mm}$ of thickness $4\,\mathrm{mm}$, in the grayscale window $[-150\,\mathrm{HU}, 150\,\mathrm{HU}]$; the ROIs show the inserts at (left) $\underline{r} = (-160, 0, 0)^{\mathrm{T}}\,\mathrm{mm}$, (top) $\underline{r} = (0, 160, 0)^{\mathrm{T}}\,\mathrm{mm}$, (right) $\underline{r} = (160, 0, 0)^{\mathrm{T}}\,\mathrm{mm}$, (bottom) $\underline{r} = (0, -160, 0)^{\mathrm{T}}\,\mathrm{mm}$, (center) $\underline{r} = (0, 0, 0)^{\mathrm{T}}\,\mathrm{mm}$. From (left) to (right): the short-scan FDK method, the ACE method, the virtual PI-line BPF method, the virtual PI-line BPF method with Parker weighting.
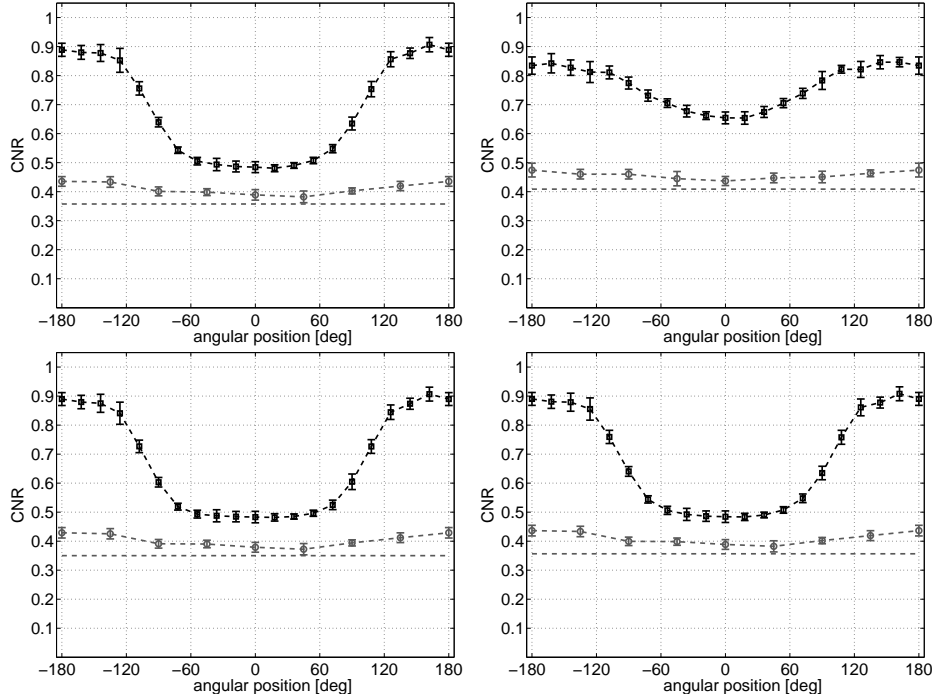

Figure 6.9: CNR in the plane $z = 0\,\mathrm{mm}$ for a short-scan with parameters $\lambda_c = 0°$ and $\lambda_s = 210°$, determined along the rings with radius $160\,\mathrm{mm}$ (black) and $50\,\mathrm{mm}$ (gray) and presented as a function of the angular position of the insert. The CNR obtained at the origin is displayed as a horizontal, dashed line. (Top-left) the short-scan FDK method, (top-right) the ACE method, (bottom-left) the virtual PI-line BPF method, (bottom-right) for the virtual PI- line BPF method with Parker weighting.

measurements at $z = 0\,\mathrm{mm}$ as a function of the angular position of the insert, separate for the two insert rings. It also shows the mean CNR value obtained at the origin.

These results illustrate that the CNR in each method is fairly symmetric with respect to the x-axis and also increases in regions further away from the short-scan center, as expected. Deviations from a perfectly symmetric behavior are caused by statistical uncer-
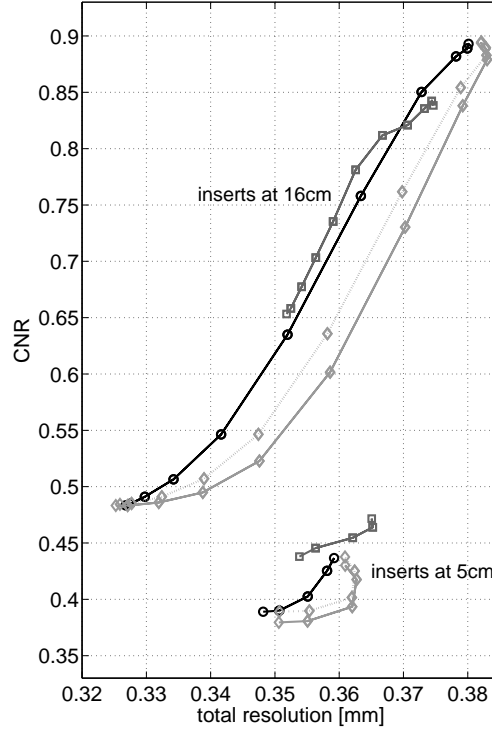
Figure 6.10: Interdependence between total resolution and CNR inside the plane of the scan. The short-scan FDK results are indicated with black circles, the ACE results with dark gray squares and the virtual PI-Line BPF results with gray diamonds (the approach using Parker weighting corresponds to the dashed curve). For each method, two curves are shown, indicating the properties on the ring with radius 16 cm or 5 cm, respectively.

tainties that break the symmetry of the reconstruction problem. Another phenomena that can be investigated is related to the fact that the average attenuation that the rays through a certain point $\underline{x}$ experience during the scan (and thus the uncertainties with which the corresponding line integrals are known) is higher close to the phantom center than close to the phantom boundaries. This is due to the shape of the performance phantom and makes us expect a decrease in the noise level in the reconstructions with increasing distance from the object center. Indeed, this effect could be nicely observed for each reconstruction method, as shown in Figure 6.9. Despite all these described similarities between the methods under comparison, we note that the ACE method comes with the most homogeneous distribution of the CNR across the investigated region among the four methods.

Figure 6.10 shows, in a compact form, the interdependence between CNR and total spatial resolution in the plane of the scan for all considered reconstruction methods. Total spatial resolution was here defined as the geometric mean of the average resolution in $x - y$ and the resolution in z, i.e., as the quantity $\left(\sigma_{xy}^2 \times \sigma_z\right)^{1/3}$. Note that different positions in the diagram of Figure 6.10 correspond to different locations in the image volume: the curves on the top-left in this diagram show the results on the ring with radius 160 mm while those on the bottom-right indicate the results obtained at distance 50 mm from the

origin. Note also that curves presented in the diagram were determined by fitting a smooth function into the samples of CNR and total resolution.

We observe again that in the ACE results, total resolution and CNR are more homogeneous over the reconstructed region. We can also see the differences between the two realizations of the virtual PI-Line BPF methods. The approach using Parker weighting yields improvements in terms of CNR over the approach that uses for reconstruction only a subset of the acquired CB projections. These improvements are however small, since the CB data used for this study was simulated for a scan interval of $\lambda_s = 210°$ only, and therefore did not contain a lot of redundancy.

Figure 6.11 presents for each method separately the range of values of the CNR on the rings of radius 160 mm and 50 mm, and the CNR obtained at the origin. It shows these quantities for the inserts at $z = 0$ mm and also for the inserts at $z = 50$ mm. From these results, we notice that with the performance phantom, the distribution of the CNR over the imaged region becomes somewhat more homogeneous in regions away from the plane of the circular scan; this general effect is identical in each reconstruction method.
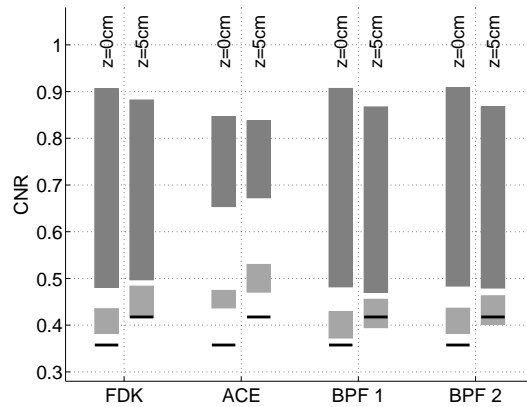

Figure 6.11: Illustration of the spatial homogeneity and of the z-dependency of the CNR. The bars show the range of values obtained on the ring with radius 50 mm (gray) and 160 mm (dark gray), and the value determined at the origin is shown using a black horizontal line. For each method, these ranges are given for the inserts centered on $z = 0$ mm and at $z = 50$ mm. BPF 1 and BPF 2 here refer to the virtual PI-line method without and with Parker weighting, respectively.

6.6.3   Evaluation of CB Artifacts

This section provides a quantitative measurement of CB artifacts that is based on investigating reconstructions of the FORBILD head phantom [3] from its noise-free CB data. In this study, the head phantom was centered on the slice $z = 40$ mm so that structures in the phantom that have high gradient in the z-direction are located more remotely from the plane of the scan. Reconstruction of these structures is therefore expected to suffer stronger from the effects of missing data, compared to the case of using a non-shifted phantom, and thus to reveal clearer the differences between the reconstruction methods under comparison.

CB data of the head phantom was simulated according to the general geometry parameters summarized in table 6.1 and using a detector that is large enough to avoid any

truncation in the CB projections. Furthermore, the presented evaluation considers 12 different realizations of the source trajectory with varying short-scan center λ_c and/or varying scan interval λ_s, as will be explained below.

From each CB data set, the estimate f^e of the object density was obtained throughout the entire region Ω_f on a Cartesian sampling grid with $\Delta x = \Delta y = \Delta z = 0.5\,\text{mm}$. We compare the reconstruction result to the true object density by computing a relative reconstruction error

$$\epsilon(\underline{x}) = \frac{f^e(\underline{x}) - f(\underline{x})}{f(\underline{x})} \tag{6.41}$$

at all points $\underline{x}$ where $f(\underline{x}) \neq 0$.

Evaluation of CB artifacts was carried out on a slice by slice basis, using slices that are orthogonal to the z-axis. Within each slice, a region $\mathcal{S}_z$ was defined that consists of all points at which the true density f takes values between $30\,\text{HU}$ and $80\,\text{HU}$ and which are at least $0.5\,\text{mm}$ away from the discontinuities in the object. CB artifacts were quantified by investigating the distribution of the relative reconstruction error $\epsilon(\underline{x})$ for $\underline{x} \in \mathcal{S}_z$; we represent this distribution from now on by its mean $\bar{\epsilon}_z$ and its standard deviation ϵ_z^σ, which are obtained respectively as

$$\bar{\epsilon}_z = \frac{1}{|\mathcal{S}_z|} \sum_{\underline{x} \in \mathcal{S}_z} \epsilon(\underline{x}) \qquad \text{and} \qquad \epsilon_z^\sigma = \left(\frac{1}{|\mathcal{S}_z| - 1} \sum_{\underline{x} \in \mathcal{S}_z} \left(\epsilon(\underline{x}) - \bar{\epsilon}_z \right)^2 \right)^{1/2} \tag{6.42}$$

Note that a mean value different from $\bar{\epsilon}_z = 0$ indicates a bias in the reconstruction of the considered region within slice z. Increasing ϵ_z^σ, on the other hand, indicates that the structure of CB artifacts gets more and more heterogeneous.

Figure 6.12 presents the results of the CB artifact measurement for the short-scan with parameters $\lambda_c = 0°$ and $\lambda_s = 210°$ and within the slice at $z = 52.5\,\text{mm}$. The left two columns in this figure show the corresponding reconstruction results, obtained from noise-free data, but also from noisy CB data assuming an emission of $300\,000$ photons per ray. The distribution of ϵ within $\mathcal{S}_z$, obtained from the noise-free reconstructions, is presented in the histogram in the right column of Figure 6.12. The two FOMs defined in (6.42) are indicated with a black circle and a black horizontal line in each histogram, respectively.

Measurement of the CB artifact level was then carried out for 6 different short-scan realizations with $\lambda_s = 210°$ and $\lambda_c = \{0°, 60°, 120°, 180°, 240°, 300°\}$, yielding 6 values for the artifact FOMs. The 6 values for $\bar{\epsilon}_z$ that measure the reconstruction bias in one z-slice are summarized by their mean and standard deviation. The top of Figure 6.14 shows these two quantities as a function of z. The artifact heterogeneity is quantified in a similar way, using the mean and standard deviation of ϵ_z^σ across the 6 experiments; see the bottom of Figure 6.14 for an illustration of the artifact heterogeneity FOM, as a function of z.

As expected, all methods yield accurate reconstruction in the plane of the scan and perform very well for $0\,\text{mm} < z < 10\,\text{mm}$. Further away from that plane, in particular in regions where object density varies significantly in z, the strength of CB artifacts increases noticeably. We observe that in those regions, the short-scan FDK method yields strong reconstruction bias with a magnitude of up to 1.2% and strong artifact heterogeneity of almost 3%. Its artifact level furthermore strongly depends on the center of the considered short-scan. The ACE method yields a reconstruction bias comparable to that of short-scan FDK, but comes with significant improvements in artifact heterogeneity, which is always below 1.25%, and in robustness of image quality with respect to the actual short-scan realization. The performance of the virtual PI-line BPF methods, on the other hand, is
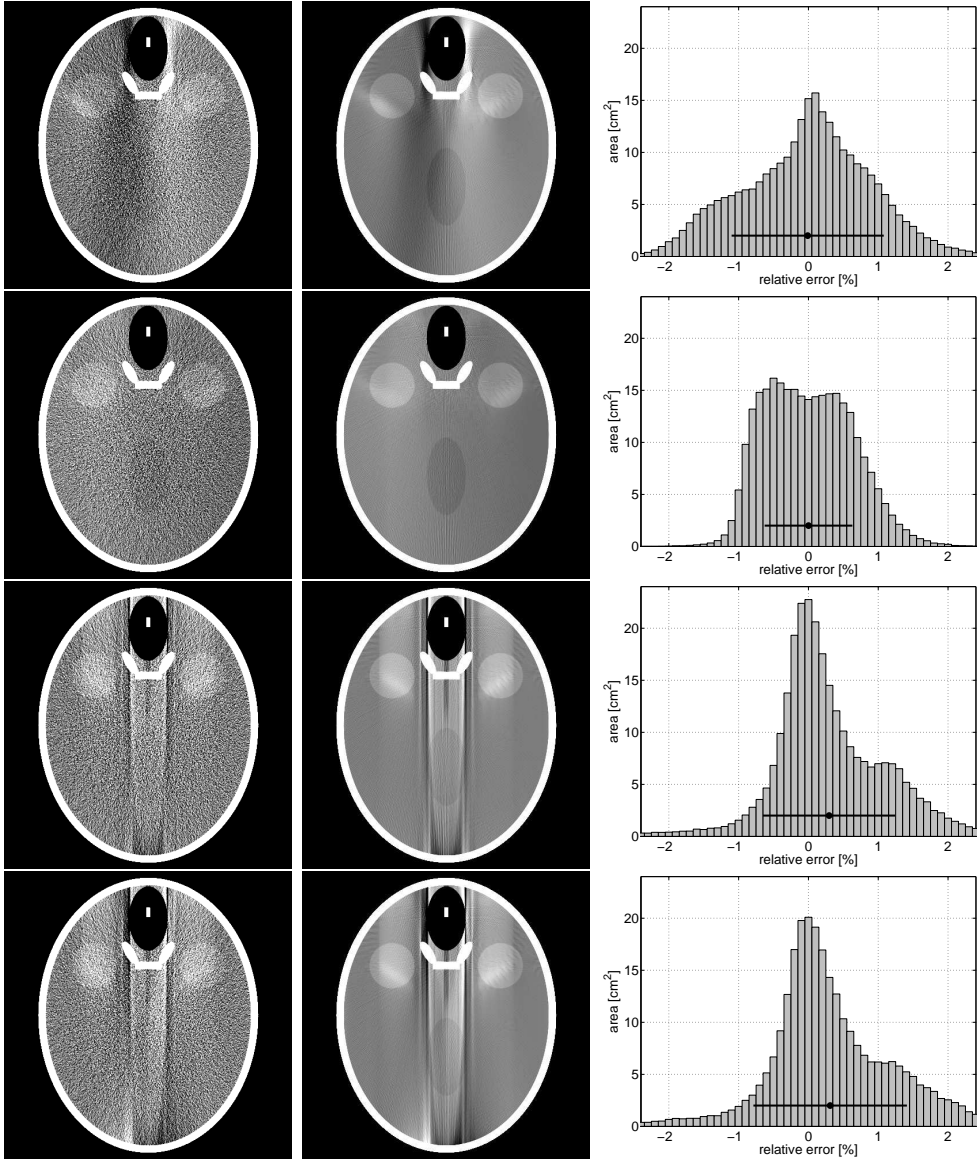
Figure 6.12: The slice $z = 52.5\,\text{mm}$ through the reconstructions of the FORBILD head phantom using a short-scan defined with $\lambda_c = 0°$, $\lambda_s = 210°$ and obtained using from (top) to (bottom): the short-scan FDK method, the ACE method, the virtual PI-line BPF method and the virtual PI-line BPF method with Parker weighting. (Left) reconstructions from noisy data assuming $300\,000$ photons per ray in the gray-scale window $[0\,\text{HU}, 100\,\text{HU}]$, (center row) reconstructions from noise-free CB data in the gray-scale window $[0\,\text{HU}, 100\,\text{HU}]$ and (right) histograms of the relative reconstruction error for the values in the region $\mathcal{S}_z$. The horizontal bar in each histogram shows the first moment (circle) and second moment (half-width of the bar) of the histogram.

superior to that of the other evaluated methods considering reconstruction bias (which is less than 0.75%), but shows like short-scan FDK disadvantages in terms of artifact
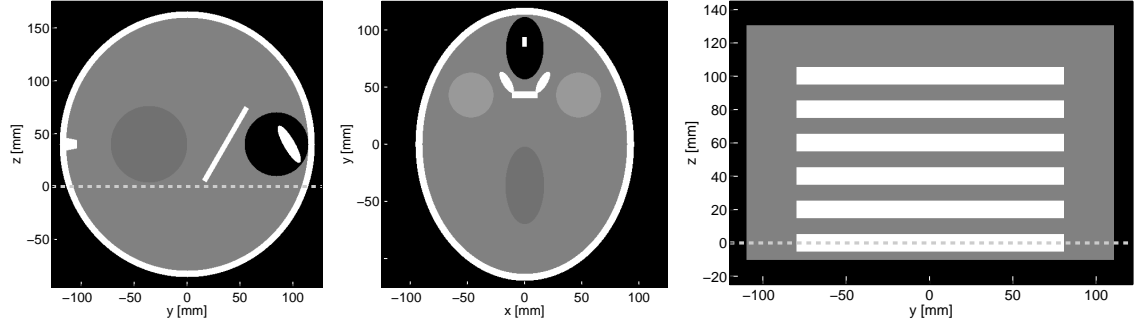
Figure 6.13: True density values of investigated phantoms. (Left) the slice $x = 0\,\text{mm}$ through the FORBILD head phantom, (Center) the slice $z = 52.5\,\text{mm}$ through the FORBILD head phantom, both using the grayscale window $[0\,\text{HU}, 100\,\text{HU}]$. (Right) the slice $x = 0\,\text{mm}$ through the disk phantom in the grayscale window $[-500\,\text{HU}, 500\,\text{HU}]$. The horizontal, dashed lines in the left and the right image indicate the location of the plane of the scan, at $z = 0\,\text{mm}$.

heterogeneity. Note also that the use of Parker weighting for the BPF based reconstruction seems to slightly increase the level of CB artifacts throughout the image volume.

In the presented evaluation, CB artifacts were measured globally over a considered z-slice; this evaluation does therefore not allow statements about the spatial distribution of the CB artifacts at fixed z. Visual assessment of reconstruction results, in Figure 6.12, shows that data insufficiency may in fact have very different impact on image quality. Compared to the true object density displayed in Figure 6.13, the results of short-scan FDK and ACE show CB artifacts that are distributed over the entire object slice and appear as a gradient in the reconstructions. The virtual PI-line BPF methods, on the other hand, yields CB artifacts that are spatially more compact and that appear in form of streaks in the reconstruction results. Furthermore, the Parker weighting seems to break symmetry in artifact behavior; see the bottom region in Figure 6.12.

Note that the CB artifact evaluation presented so far used short-scans of fixed scan-range $\lambda_s = 210°$. We now investigate potential improvements in image quality when progressively increasing this short-scan length towards $360°$. More specifically, CB data of the head phantom were simulated using 6 short-scans and increasing from one data set to the other the scan range from $210°$ to $360°$ in steps of $25°$. The center of these short scans was set to $\lambda_c = 120°$. For a fixed algorithm, each selection of λ_s yields in general different values of $\bar{\epsilon}_z$ and ϵ_z^σ and for each such selection the global level of CB artifacts is now represented by only two values, namely by the average of $\bar{\epsilon}_z$ over $z \in [0, 90]\,\text{mm}$ (the overall bias) and by the average in ϵ_z^σ over $z \in [0, 90]\,\text{mm}$ (the overall heterogeneity). Figure 6.15 displays these two quantities as a function of λ_s, individually for 3 of the investigated reconstruction methods[4]. For comparison, Figure 6.15 also indicates the corresponding FOMs obtained with the full-scan FDK approach using a horizontal, dashed line. Obviously, the short-scan FDK method does not show convergence behavior for increasing λ_s; its overall reconstruction bias is in general noticeably worse than that of the full-scan method, except for $\lambda_s = 360°$ and its overall artifact heterogeneity is always inferior to that of the full-scan algorithm. The

---

[4]The results of the virtual PI-Line BPF method without Parker weighting has been omitted, since an increase in λ_s does not affect this method that each time uses only the same subset of the known CB projections for reconstruction.
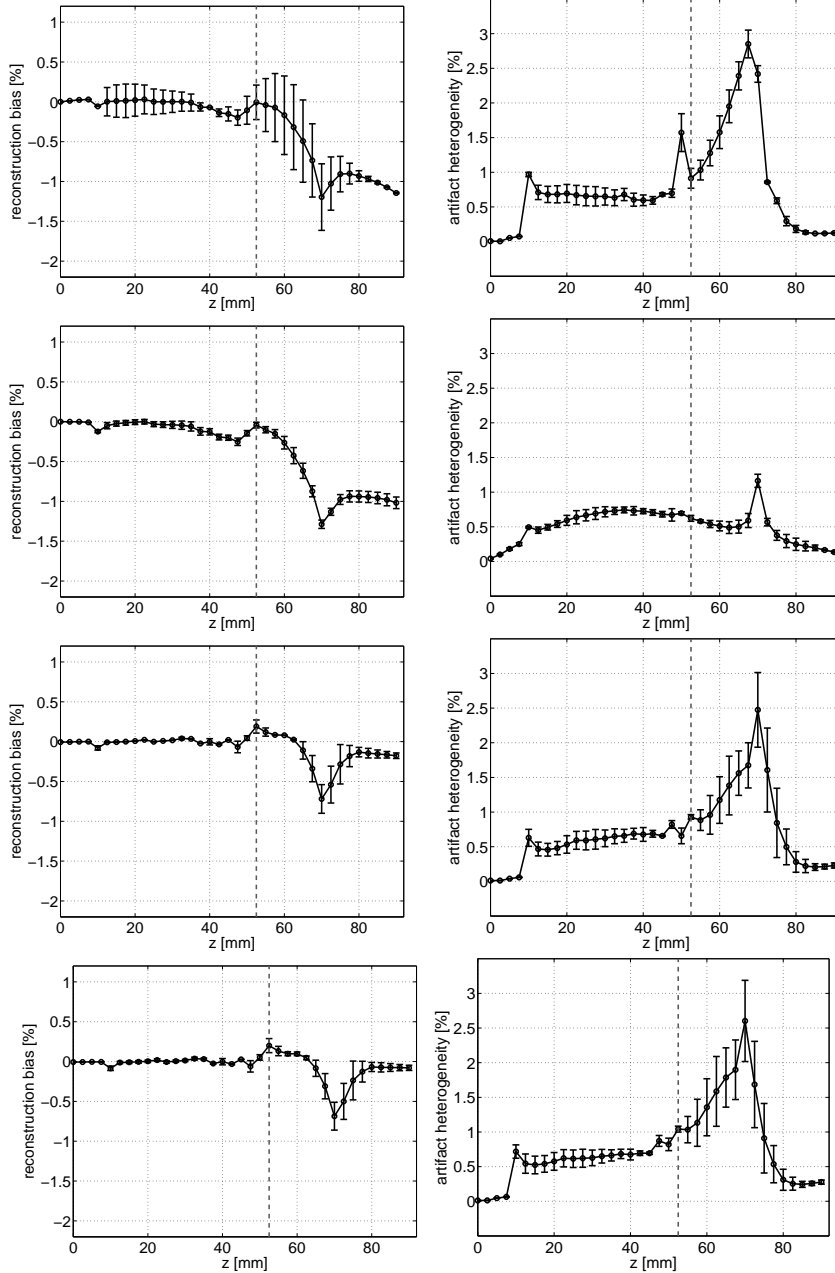
Figure 6.14: The CB artifact FOMs (left) reconstruction bias and (right) artifact heterogeneity, as a function of z. The black circles indicate the mean of these FOMs across 6 CB data sets with different short-scan center λ_c, while the errorbars illustrate the FOM standard deviations across these 6 different data sets. From (top) to (bottom): the short-scan FDK method, the ACE method, the virtual PI-line BPF method and the virtual PI-line BPF method with Parker weighting.

virtual PI-Line BPF method with Parker weighting has, for all choices of λ_s, an overall bias which is noticeably superior but also an overall artifact heterogeneity which is inferior to that of full-scan FDK; its image quality seems to be best for small λ_s.
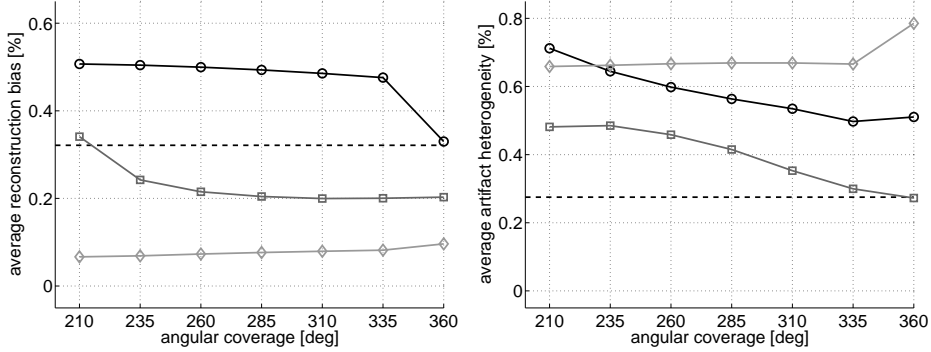
Figure 6.15: Dependency of the reconstruction bias and the artifact heterogeneity on the angular coverage of the scan interval λ_s for fixed short-scan center $\lambda_c = 120°$. The samples in the left diagram indicate for each method the average reconstruction bias across the slices $z \in [0 \text{ mm}, 90 \text{ mm}]$ and similarly, the right diagram presents the average artifact heterogeneity for $z \in [0 \text{ mm}, 90 \text{ mm}]$. In each diagram, the circles correspond to the short-scan FDK method, the squares to the ACE method and the diamonds to the virtual PI-line BPF method with Parker weighting. The dashed horizontal line indicates in each figure the FOM value obtained from CB data corresponding to a full circular scan using the full-scan FDK reconstruction method.

We realize that for the ACE method, the average reconstruction bias converges to a level that is superior to that achievable with the full-scan FDK approach for λ_s approaching 360°, while artifact heterogeneity seems to converge to the level of full-scan FDK. This convergence behavior is not unexpected, since the ACE algorithm converges by construction towards the full-scan FDK algorithm with Hu's correction term for λ_s approaching 360° [44].

CB artifacts were furthermore studied on the reconstructions of a disk phantom. The main body of this phantom consists of a cylinder of radius 110 mm and height 120 mm. Its axis coincides with the z-axis and the lower edge of the cylinder is at $z = -10$ mm. The interior of the phantom contains a stack of 6 cylindrical disks. Each disk has density 500 HU and a radius of 80 mm and a height of 10 mm. The disks are centered on the z-axis, the distance between the centers of two adjacent disks measures 20 mm and the center of the lowest disk is at $z = 0$ mm; see Figure 6.13 for an illustration of the true phantom values. Reconstructions of the disk phantom from circular CB data typically show a high level of CB artifacts, since the 3D Radon transform of this phantom contains significant information in the region that cannot be measured with the circular scan.

CB data was simulated using again parameters given in table 6.1 and using a short-scan of scan interval $\lambda_s = 200°$ (the actual value of λ_c is irrelevant due to the symmetry of the object). Reconstruction was carried out on an isotropic sampling grid using sampling distance of 0.5 mm; the left column in Figure 6.16 shows the slice $x = 0$ mm through these reconstructions. CB artifacts were evaluated by considering the relative reconstruction error ϵ, defined in (6.41), for the points inside each disk that are at least 2 mm away from the disk edges. The distribution of this error for the 3D region corresponding to the topmost disk of the phantom is presented in the histograms in the center of Figure 6.16. Again, each distribution is represented compactly by its mean and standard deviation, yielding two FOMs similar to those defined in (6.42), namely the reconstruction bias and the artifact

heterogeneity. These two FOMs are displayed in the right of Figure 6.16, as a function of the disk center.
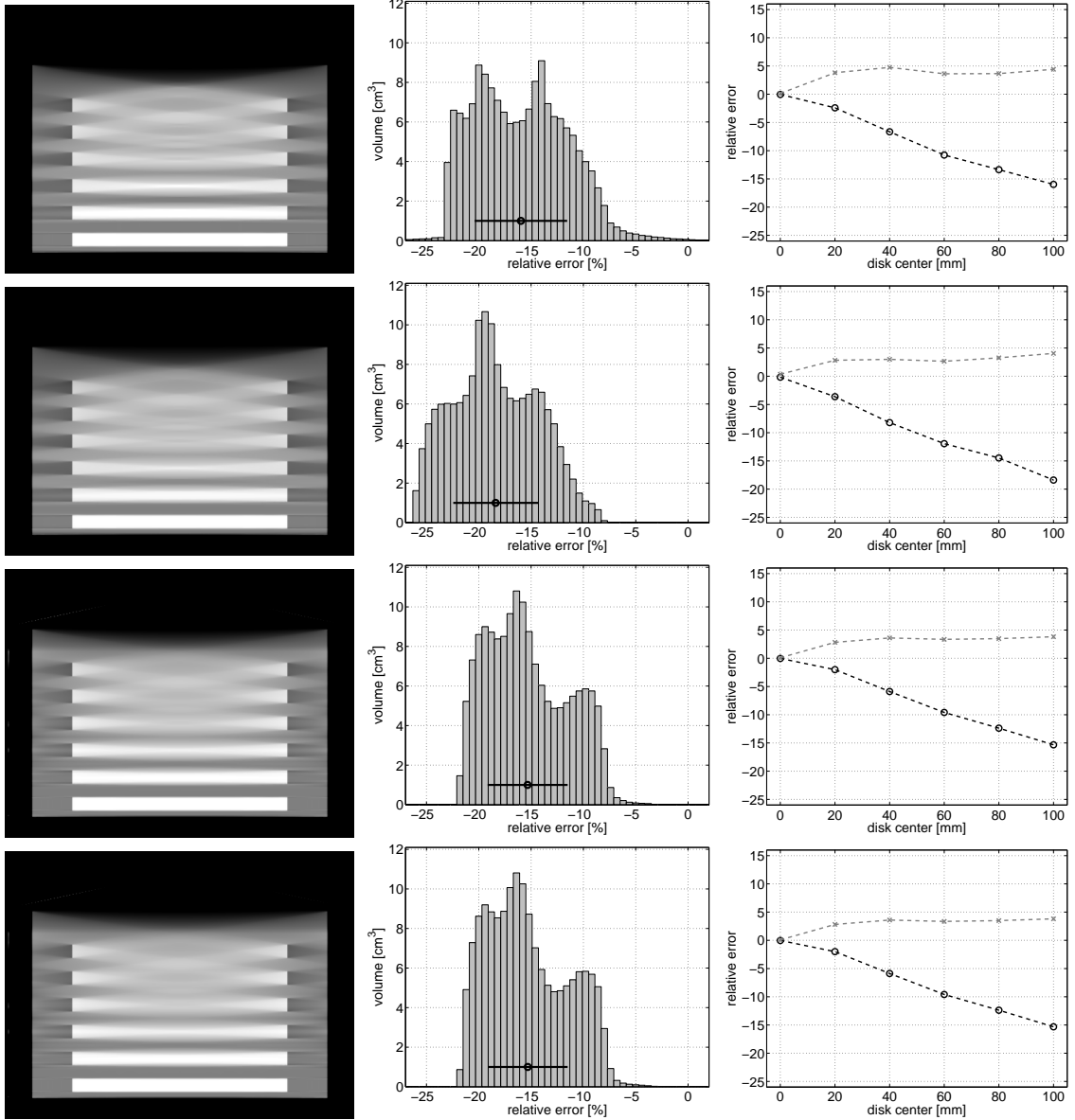
Figure 6.16: CB artifacts in the disk phantom reconstruction. (Top) to (bottom): the short-scan FDK method, the ACE method, the virtual PI-line BPF method without Parker weighting and the virtual PI-line BPF method with Parker weighting. (Left) Visualization of the vertical slice $x = 0\,\mathrm{mm}$ through the reconstruction result in the grayscale window $[-500\,\mathrm{HU}, 500\,\mathrm{HU}]$. (Center) Histogram of the relative reconstruction error for the points within the topmost disk of the phantom. The black circle indicates the reconstruction bias and the black horizontal line the artifact heterogeneity. (Right) The bias (black circles) and artifact heterogeneity (gray crosses) for each of the 6 disks of the phantom, as a function of the disk center.

While the reconstruction of the disk centered on the PCS is fairly accurate in each reconstruction method, the level of CB artifacts rapidly increases with increasing distance to the PCS. The reconstruction bias seems to be worst with the ACE method, reaching almost 19% for the topmost disk, whereas the other methods yield values of about 15%. The results of the virtual PI-Line BPF methods seem to be visually of best quality, since, for instance, the strength of the shading artifact enclosing each disk is reduced.

6.6.4 Evaluation of Impact of Axial Truncation

To study the impact of axial truncation on image quality, we simulated CB data of the FORBILD thorax phantom [3] in the C-arm geometry and using a short-scan of $\lambda_c = 0°$ and $\lambda_s = 224°$. It is assumed that CB data is known for the intervals $u \in [-440, 440]$ mm and $v \in [0, 220]$ mm during the entire scan. This selected detector size is sufficient to capture the entire horizontal extent of the phantom. However, the detector height is insufficient to allow the entire phantom extent in z to be measured. Therefore, all CB projections suffer from axial truncation and this truncation occurs close to the region where the top end of the lungs project to; see the right side of Figure 6.17 for an illustration of the degree of truncation[5].

Reconstruction from these truncated CB projections was carried out for the entire object support region Ω_f, using again isotropic sampling of 0.5 mm along each dimension. Image quality in the reconstructed f^e is degraded by several effect at the same time. Regions away from $z = 0$ mm, for instance, show strong CB artifacts, mainly caused by the significant z-gradient of the density values in the vertebrae. In order to identify the impact of truncation on image quality, reconstruction was performed a second time, now using non-truncated CB data as illustrated in the left of Figure 6.17.

The first and the second column in Figure 6.18 show the vertical slice $x = 0$ mm through the reconstructions of the thorax phantom from non-truncated CB data and from CB data with axial truncation, respectively. To investigate axial truncation impact on image quality, we compute the difference between these two results in the specific region $\mathcal{S}_{trunc}$ that consists of points $\underline{x}$ that project onto the measured detector area (in the truncation scenario) for each λ; this difference is shown in the third column of Figure 6.18.

Axial truncation in the CB data has no effect on the performance of the short-scan FDK method in the region $\mathcal{S}_{trunc}$ at all, as expected, because data filtering uses lines that are parallel to the u-axis and is therefore not impacted by truncation in v direction. Truncation artifacts occurring in the results of the virtual PI-line BPF methods are constricted in the small triangular region at the top of $\mathcal{S}_{trunc}$, but do not affect the results throughout other regions of $\mathcal{S}_{trunc}$. The ACE method, however, yields axial truncation artifacts that are distributed in general throughout the entire reconstructed region $\mathcal{S}_{trunc}$, except for the points that belong to the plane of the source trajectory. On the other hand, these artifacts are smooth and their magnitude drops rapidly with increasing distance from the top of the reconstructed region.

---

[5]Note that in this evaluation, we did not involve any heuristic correction algorithms that aim at approximately extrapolating the CB data beyond the edges of truncation.
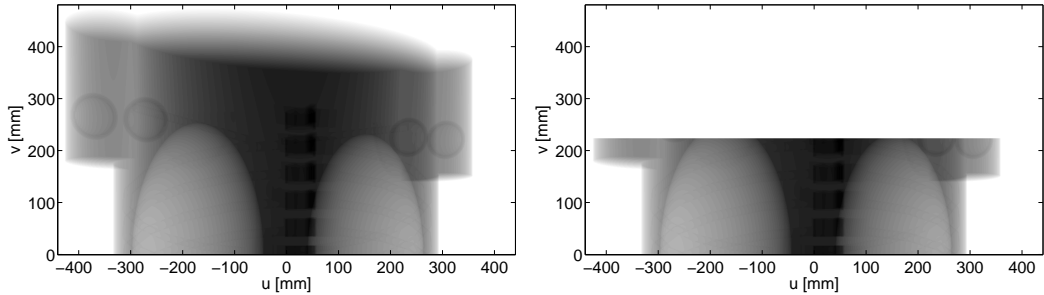
Figure 6.17: Single example CB projection of the FORBILD thorax phantom in (left) the scenario without axial truncation across the top detector border and (right) the scenario with axial truncation of CB data, occurring at $v_{max} = 220$ mm. The gray-value in these two figures encodes the number of photons measured on the detector plane.

6.7   Discussion and Conclusions

In this chapter, we focussed on the problem of image reconstruction from CB data acquired along a short-scan circular trajectory. First, we presented four state-of-the art approaches that have been suggested in literature to accomplish this reconstruction task, namely the short-scan FDK method, the ACE method and the virtual PI-Line BPF methods without and with Parker weighting. We then carried out a detailed comparative evaluation of these methods using simulated CB data and assuming geometry parameters that are representative of clinical C-arm systems.

We quantified spatial resolution and CNR achievable with the considered algorithms. The differences we observed were fairly small, but were overall in favor of the ACE method, which was determined to yield less noise in the reconstructions, better resolution in (x,y)-direction and also the most homogeneous distribution of these algorithmic properties over the investigated region. However, some of these advantages of the ACE method seem to be at the cost of its z-resolution, which is in average lower than that of the other methods and which noticeably varies inside the region Ω_f.

Another important focus of our comparative evaluation was on the issue of CB artifacts, i.e., the impact of theoretical data insufficiencies on the 3D reconstruction result. As expected, non of the considered methods is in general able to yield accurate results throughout the entire 3D image volume. However, strength and structure of artifacts vary noticeable among the considered methods. We note that the overall level of CB artifacts appeared to be highest in the results of the short-scan FDK method, where low-frequency artifacts affect reconstruction throughout large parts of the image volume. The ACE results also suffer in general from low-frequency, gradient-like artifacts that may affect quantitative accuracy almost everywhere in the 3D image volume. However, these artifacts are of significantly reduced strength, compared to that of short-scan FDK, so that they are not as disturbing to the human observer. The two realizations of the virtual PI-Line BPF method, in contrast, yield high-frequency CB artifacts. These artifacts introduce artificial structure to the estimated object density function and may thus distract the observer from actual structures, especially during visual interpretation of image content. However, outside these localized, streak-like artifact regions, the BPF-based reconstructions are quantitatively very accurate and thus closer to the true object density than the reconstructions obtained with both, short-scan FDK and ACE.
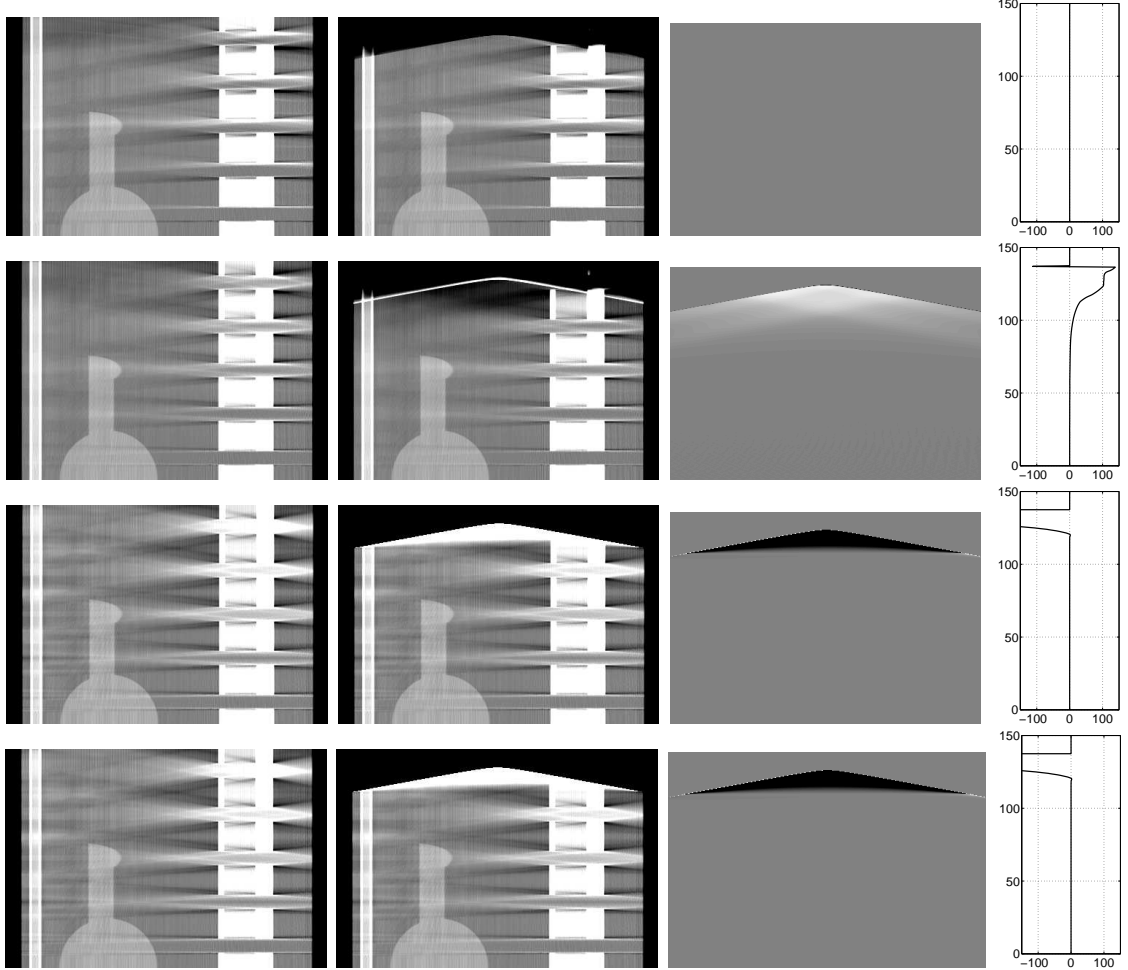
Figure 6.18: Impact of axial truncation on image quality for (top to bottom) short-scan FDK, ACE, virtual PI-Line BPF and virtual PI-Line BPF with Parker weighting. The left two columns illustrate the slice $x = 0\,\mathrm{mm}$ through the reconstruction obtained from (left) non-truncated and (center) truncated CB data, both in the grayscale window $[-150\,\mathrm{HU}, 150\,\mathrm{HU}]$. (Right) Pointwise differences between the two results in the region $\mathcal{S}_{trunc}$, using a window of width 300 units on the Hounsfield scale, and profile of these difference images along the central vertical line.

The investigated methods come with a different behavior in presence of truncation in the CB data. It is known that by construction, the BPF methods provide some flexibility with respect to truncation along the u-axis, unlike short-scan FDK and ACE. Here, however, we quantified the impact of axial truncation on image quality, i.e., of truncation along the v-axis. We note that there is a large region of interest $\mathcal{S}_{trunc}$ in which the short-scan FDK method is not affected at all by this truncation scenario. The other methods under investigation, however, suffer from artifacts attached to the edge of truncation and spreading into $\mathcal{S}_{trunc}$; the region affected by truncation is largest in the ACE method.

In conclusion, each of the four investigated approaches for short-scan circular CB reconstruction, which are either currently in use or which have been recently suggested in literature, has its pros and cons. The decision of which of these algorithm should be favored

for practical purposes thus highly depends on the imaging application and also on the class of investigated objects. Short-scan FDK, for instance, is computationally very efficient and comes with low (axial) detector requirements. The ACE method has advantages in image noise and CB artifacts only appear as low-contrast, low-frequency image defects. The BPF methods, on the other hand, are quantitatively most accurate and can deal with some scenarios of transaxial truncation, but at the cost of occasional streak artifacts. Finding an efficacious analytical circular short-scan reconstruction algorithm that brings advantages in every aspect of image quality is a highly complex issue and an overall satisfying solution may not exist due to the data incompleteness.

Chapter 7

A Factorization Method for Circular Short-Scan CB Reconstruction

7.1   Introduction

In this chapter, we present a novel, original method for CB image reconstruction in the short scan circular acquisition geometry. Our method is based on a theoretically-exact factorization of the 3D short-scan CB reconstruction problem into a set of independent 2D inversion problems, each of which corresponds to finding the object density on one plane. Reconstruction involves an iterative algorithm to numerically solve these 2D inversion problems on a one-by-one basis. Reconstruction of the entire 3D image volume is achieved by combining the results from each 2D inversion problem. The fundamental property of our factorization approach, which distinguishes it from the reconstruction methods compared in chapter 6, are its ability to perform reconstruction without involving geometric approximations and to enforce all reconstructed values to be positive. These properties make the factorization approach similar to 3D iterative reconstruction approaches; see for instance [35]. The latter, however, achieve reconstruction using 3D iterations, which is computationally demanding; our factorization approach, in contrast, involves only a set of 2D iterations and is thus more efficient.

7.2   Reconstruction Theory

This section presents the theoretical background underlying our reconstruction approach. We describe, in particular, how the factorization of the circular CB reconstruction problem is established and describe its usefulness for reconstruction of a 3D volume of interest.

7.2.1   The Plane of Interest $\mathcal{P}$

Our method targets reconstruction within planes that are parallel to the z-axis and that intersect the source trajectory at two locations. Let $\mathcal{P}$ be such a plane of interest and let λ_1 and λ_2 with $\lambda_{min} \leq \lambda_1 < \lambda_2 \leq \lambda_{max}$ denote the source polar angles where $\mathcal{P}$ hits the source trajectory. By construction, the source positions $\underline{a}(\lambda_1)$ and $\underline{a}(\lambda_2)$ both belong to $\mathcal{P}$.
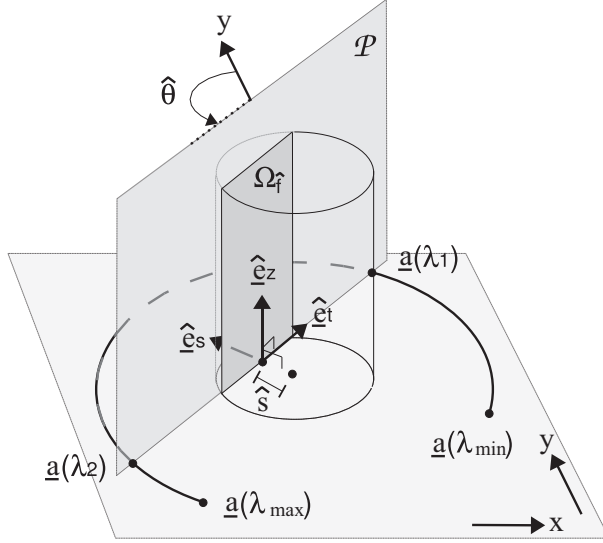
Figure 7.1: Illustration of geometric entities on the plane of interest $\mathcal{P}$, which is orthogonal to the plane of the circular scan (PCS) and intersects the source trajectory at $\underline{a}(\lambda_1)$ and $\underline{a}(\lambda_2)$.

In the following, several entities will be introduced that are closely related to $\mathcal{P}$. Some of these entities correspond to geometric parameters that provide further description on $\mathcal{P}$. Others correspond to functions which are defined on $\mathcal{P}$ and take an essential role in the reconstruction algorithm. To keep the notation clear, all these entities will be described from now on with symbols that contain a hat.

A selection of $\mathcal{P}$ implicitly imposes another coordinate system for the image volume. This new system is described with the orthonormal system of vectors

$$\underline{\hat{e}}_s = (\cos\hat{\theta}, \sin\hat{\theta}, 0)^{\mathrm{T}}, \qquad \underline{\hat{e}}_t = (\sin\hat{\theta}, -\cos\hat{\theta}, 0)^{\mathrm{T}} \qquad \text{and} \qquad \underline{\hat{e}}_z = (0,0,1)^{\mathrm{T}}, \qquad (7.1)$$

where $\hat{\theta} = \lambda_c = (\lambda_1 + \lambda_2)/2$; see Figure 7.1. By definition, $\hat{\theta}$ is the angle between the y-axis and $\mathcal{P}$, measured in the counterclockwise direction, and $\underline{\hat{e}}_s$ is normal to $\mathcal{P}$. We use $\hat{s}$ to denote the (signed) distance of $\mathcal{P}$ from the origin $(0,0,0)^{\mathrm{T}}$ of the image volume; $\hat{s}$ is measured in the direction of $\underline{\hat{e}}_s$ and is such that $\hat{s} = \underline{\hat{e}}_s \cdot \underline{a}(\lambda_1)$ (or, equivalently, $\hat{s} = \underline{\hat{e}}_s \cdot \underline{a}(\lambda_2)$). Hence, a point $\underline{x}$ belongs to $\mathcal{P}$ if $\underline{x} \cdot \underline{\hat{e}}_s = \hat{s}$.

To specify locations on $\mathcal{P}$, we use Cartesian coordinates t and z, measured along the directions $\underline{\hat{e}}_t$ and $\underline{\hat{e}}_z$, respectively. The point $(t, z)^{\mathrm{T}} = (0,0)^{\mathrm{T}}$ is at the orthogonal projection of the point $(0,0,0)^{\mathrm{T}}$ onto $\mathcal{P}$, and t increases when moving towards $\underline{a}(\lambda_1)$. The quadruple $(\lambda_1, \lambda_2, t, z)^{\mathrm{T}}$ then refers to a point of the image volume, the Cartesian coordinates of which are provided by the function

$$\underline{\hat{x}}(t, z) = \hat{s}\,\underline{\hat{e}}_s + t\,\underline{\hat{e}}_t + z\,\underline{\hat{e}}_z = \begin{pmatrix} \hat{s}\cos\hat{\theta} + t\sin\hat{\theta} \\ \hat{s}\sin\hat{\theta} - t\cos\hat{\theta} \\ z \end{pmatrix}. \qquad (7.2)$$

7.2.2 Image Reconstruction on $\mathcal{P}$

The object density on $\mathcal{P}$, i.e. the 2D function

$$\hat{f}(t, z) = f(\hat{\underline{x}}(t, z)) \tag{7.3}$$

is now recovered using a two-step scheme. In step one, an intermediate function $\hat{b}(t, z)$ is calculated for all points on $\mathcal{P}$, by first differentiating CB data with respect to the parameter of the source trajectory at fixed ray direction (thus applying an operation already used for the ACE method, as described in the previous chapter):

$$g_F(\lambda, u, v) = \lim_{\varepsilon \to 0} \frac{g(\lambda + \varepsilon, \underline{\alpha}(\lambda, u, v)) - g(\lambda - \varepsilon, \underline{\alpha}(\lambda, u, v))}{2\varepsilon} \tag{7.4}$$

The differentiation result is then backprojected onto $\mathcal{P}$ while using only the data over $\lambda \in [\lambda_1, \lambda_2]$, to obtain

$$\hat{b}(t, z) = \int_{\lambda_1}^{\lambda_2} \frac{1}{\|\hat{\underline{x}}(t, z) - \underline{a}(\lambda)\|} g_F(\lambda, u^*(\hat{\underline{x}}(t, z)), v^*(\hat{\underline{x}}(t, z))) \, d\lambda, \tag{7.5}$$

where $u^*(\hat{\underline{x}}(t, z))$ and $v^*(\hat{\underline{x}}(t, z))$ denote the detector coordinates of the CB projection of $\hat{\underline{x}}(t, z)$ at the given λ; see (6.8) on page 61 for the definition of the two functions u^* and v^*.

The algorithmic steps to compute the intermediate function resemble those of classical FBP methods. However, an important difference lies in the filtering step, which, according to (7.4), corresponds to a local operation. Consequently, to accurately obtain $\hat{b}$ at coordinates $(t, z)^{\mathrm{T}}$, it is sufficient to know, for each $\lambda \in [\lambda_1, \lambda_2]$, the function g on the rays that pass through a neighborhood of $\hat{\underline{x}}(t, z)$. The union of all points $(t, z)^{\mathrm{T}}$ for which g satisfies this sufficiency condition defines a region, which we call $\Omega_{\hat{b}}$.

Actual image reconstruction is achieved in step two, by making use of a fundamental relation linking the intermediate function to the wanted object density function [72]. This fundamental relation, which has been briefly explained in section 5.2.5, is expressed in its general form, following the notation in [72], as

$$\frac{1}{\pi} b(\underline{x}) = K^*(\underline{\omega}(\lambda_2, \underline{x}), \underline{x}) - K^*(\underline{\omega}(\lambda_1, \underline{x}), \underline{x}) \tag{7.6}$$

using the short-hand expression

$$K^*(\underline{\omega}, \underline{x}) = K(l, \underline{\omega}, \underline{s}) \big|_{l = (\underline{x} - \underline{s}) \cdot \underline{\omega}} \tag{7.7}$$

with the unit vector pointing from the source point at λ towards $\underline{x}$

$$\underline{\omega}(\lambda, \underline{x}) = \frac{\underline{x} - \underline{a}(\lambda)}{\|\underline{x} - \underline{a}(\lambda)\|} \tag{7.8}$$

and the 1D convolution

$$K(l, \underline{\omega}, \underline{s}) = \int_{-\infty}^{\infty} \frac{1}{\pi(l - l')} f(\underline{s} + l'\underline{\omega}) \, dl'. \tag{7.9}$$

Before explaining the involved equations, we first try to express this relation in terms of the geometry assumed in this chapter and using the coordinate system introduced on
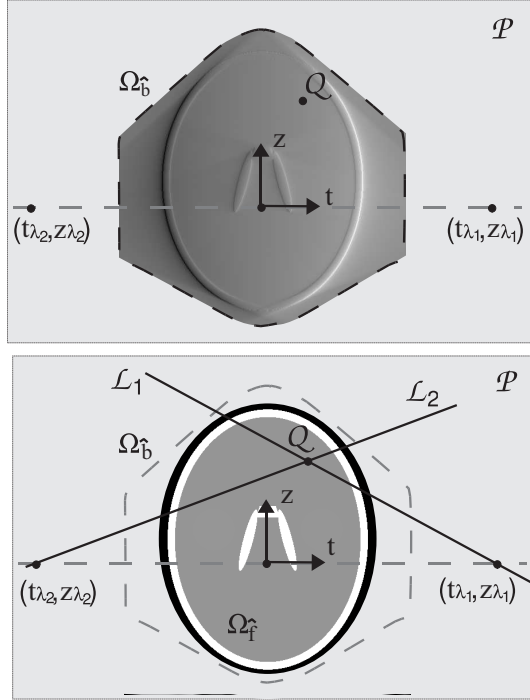
Figure 7.2: Illustration of functions $\hat{f}$ and $\hat{b}$ on $\mathcal{P}$. (Top) An example realization of the 2D intermediate function $\hat{b}$ in the region $\Omega_{\hat{b}}$ (delineated with a dashed line). (Bottom) The corresponding object density function $\hat{f}$, in its support $\Omega_{\hat{f}}$. The value of $\hat{b}$ at $\mathcal{Q}$, as indicated in the top figure, is related according to (7.14) to the values of $\hat{f}$ along the lines $\mathcal{L}_1$ and $\mathcal{L}_2$ illustrated in the bottom figure. Here, $(t_{\lambda_1}, z_{\lambda_1})$ and $(t_{\lambda_2}, z_{\lambda_2})$ define, respectively, the points $\underline{a}(\lambda_1)$ and $\underline{a}(\lambda_2)$ using the coordinates on $\mathcal{P}$.

$\mathcal{P}$. Since reconstruction is focussed on the points in $\mathcal{P}$ only, we may substitute $\underline{x} = \hat{\underline{x}}(t, z)$. We now consider only the first term on the right hand side (RHS) of (7.6), for which we will use the short-hand notation $\hat{K}_2 = K^*(\underline{\omega}(\lambda_2, \hat{\underline{x}}(t, z)), \hat{\underline{x}}(t, z))$. Selecting $\underline{s} = \underline{a}(\lambda_2)$ yields $l = \|\hat{\underline{x}}(t, z) - \underline{a}(\lambda_2)\|$ and therefore

$$\hat{K}_2 = \int\limits_{-\infty}^{\infty} \frac{1}{\pi(\|\hat{\underline{x}}(t, z) - \underline{a}(\lambda_2)\| - l')} f\left(\underline{a}(\lambda_2) + l' \frac{\hat{\underline{x}}(t, z) - \underline{a}(\lambda_2)}{\|\hat{\underline{x}}(t, z) - \underline{a}(\lambda_2)\|}\right) dl'. \tag{7.10}$$

For the argument of f in (7.10), we have

$$\left(\underline{a}(\lambda_2) + l' \frac{\hat{\underline{x}}(t, z) - \underline{a}(\lambda_2)}{\|\hat{\underline{x}}(t, z) - \underline{a}(\lambda_2)\|}\right) \cdot \hat{\underline{e}}_s = \hat{s} + l' \frac{\hat{s} - \hat{s}}{\|\hat{\underline{x}}(t, z) - \underline{a}(\lambda)\|} = \hat{s} \tag{7.11}$$

which shows that the function f in (7.10) is only evaluated on $\mathcal{P}$. Introducing coordinates $z_{\lambda_2} = \underline{a}(\lambda_2) \cdot \hat{\underline{e}}_z$ and $t_{\lambda_2} = \underline{a}(\lambda_2) \cdot \hat{\underline{e}}_t$ allows the notation

$$\hat{K}_2 = \int\limits_{-\infty}^{\infty} \frac{1}{\pi(\|\hat{\underline{x}}(t, z) - \underline{a}(\lambda_2)\| - l')}$$
$$\times \hat{f}\left(t_{\lambda_2} + l' \frac{t - t_{\lambda_2}}{\|\hat{\underline{x}}(t, z) - \underline{a}(\lambda_2)\|}, z_{\lambda_2} + l' \frac{z - z_{\lambda_2}}{\|\hat{\underline{x}}(t, z) - \underline{a}(\lambda_2)\|}\right) dl' \tag{7.12}$$

The change of variable $\tilde{l} = l'(t-t_{\lambda_2})/\|\hat{\underline{x}}(t,z)-\underline{a}(\lambda_2)\|$ with Jacobian $\|\hat{\underline{x}}(t,z)-\underline{a}(\lambda_2)\|/\,|t-t_{\lambda_2}|$ develops (7.12) into

$$
\begin{aligned}
\hat{K}_2 &= \int_{-\infty}^{\infty} d\tilde{l}\, \frac{\mathrm{sign}(t-t_{\lambda_2})}{\pi(t-t_{\lambda_2}-\tilde{l})}\, \hat{f}\left(t_{\lambda_2}+\tilde{l}, z_{\lambda_2}+\tilde{l}\frac{z-z_{\lambda_2}}{t-t_{\lambda_2}}\right)\\
&= \int_{-\infty}^{\infty} d\tau\, \frac{\mathrm{sign}(t-t_{\lambda_2})}{\pi(t-\tau)}\, \hat{f}\left(\tau, z_{\lambda_2}+(\tau-t_{\lambda_2})\frac{z-z_{\lambda_2}}{t-t_{\lambda_2}}\right),
\end{aligned}
\tag{7.13}
$$

where $\tau = t_{\lambda_2} + \tilde{l}$.

Similar calculations for the second term in the RHS of (7.6) can be performed. From there, the relation between the intermediate function $\hat{b}$ and the object density $\hat{f}$ may be expressed as

$$
\frac{1}{\pi}\hat{b}(t,z) = \int_{-\infty}^{\infty} h_{hilb}(t-\tau)\left(\hat{f}\left(\tau, z_1(\tau)\right) + \hat{f}\left(\tau, z_2(\tau)\right)\right) d\tau
\tag{7.14}
$$

since, by definition, $t_{\lambda_2} < t < t_{\lambda_1}$. In this equation, h_{hilb} denotes the kernel of the Hilbert transform; see (4.4) on page 4.4 for details about this kernel. The functions

$$
z_1(\tau) = z_{\lambda_1} + (\tau-t_{\lambda_1})\frac{z-z_{\lambda_1}}{t-t_{\lambda_1}} \qquad \text{and} \qquad z_2(\tau) = z_{\lambda_2} + (\tau-t_{\lambda_2})\frac{z-z_{\lambda_2}}{t-t_{\lambda_2}}
\tag{7.15}
$$

describe two oblique filtering lines on $\mathcal{P}$. These lines are defined such that the points $\hat{\underline{x}}(\tau, z_1(\tau))$ are on the line $\mathcal{L}_1$ connecting $\underline{a}(\lambda_1)$ to $\hat{\underline{x}}(t,z)$, while the points $\hat{\underline{x}}(\tau, z_2(\tau))$ are on the line $\mathcal{L}_2$ connecting $\underline{a}(\lambda_2)$ to $\hat{\underline{x}}(t,z)$, as depicted in Figure 7.2.

To understand (7.14), picture its left hand side (LHS) as the value of $\hat{b}$ at one fixed point $\mathcal{Q}$ in the plane $\mathcal{P}$. Then, draw the two lines, $\mathcal{L}_1$ and $\mathcal{L}_2$, that connect this point to the source positions $\underline{a}(\lambda_1)$ and $\underline{a}(\lambda_2)$. These lines are within $\mathcal{P}$ as shown in Figure 7.2. The RHS of (7.14) is the addition of the outcome at $\mathcal{Q}$ of the convolutions of $\hat{f}$ with the kernel h_{hilb} along these two lines. Altogether, (7.14) thus corresponds to an integral equation that relates one value of $\hat{b}$ to many values of $\hat{f}$. Both, $\hat{b}$ and $\hat{f}$ are 2D functions and consequently, image reconstruction on $\mathcal{P}$ corresponds to a 2D problem, namely to solving integral equation (7.14) for $\hat{f}$.

We note that the feasibility of finding this solution depends on the support of $\hat{f}$, which we denote as $\Omega_{\hat{f}}$, and on the region $\Omega_{\hat{b}}$ in which the intermediate function is known. Here, $\Omega_{\hat{f}}$ is defined by the intersection of the object support region Ω_f and the plane $\mathcal{P}$. If Ω_f is restricted to the plane of the scan so that $\Omega_{\hat{f}}$ contains only points with $z = 0$, the theory of finite Hilbert inversion states that reconstruction is possible if $\hat{b}$ is known over the support of $\hat{f}$ [65]. We hypothesize in this paper that this condition can be extended to a general $\Omega_{\hat{f}}$: i.e., that a recovery of $\hat{f}$ is possible if $\hat{b}$ is known over the entire support of $\hat{f}$, which requires $\Omega_{\hat{f}} \subset \Omega_{\hat{b}}$. Note in this context that the CB data g_m does not have to be non-truncated . As long as the CB projection of region $\Omega_{\hat{f}}$ onto the detector plane is contained within the measured area $[u_{min}, u_{max}] \times [v_{min}, v_{max}]$ for each $\lambda \in [\lambda_1, \lambda_2]$, there is enough information to compute $\hat{b}$ over the support of $\hat{f}$ – and therefore, following our hypothesis, there is enough information to reconstruct $\hat{f}$. See Figure 7.3 for an illustration.

7.2.3 Volume Reconstruction

The previous section described how to recover the object density in one plane of interest. From there, reconstruction in 3D can be accomplished in a straight-forward manner, by
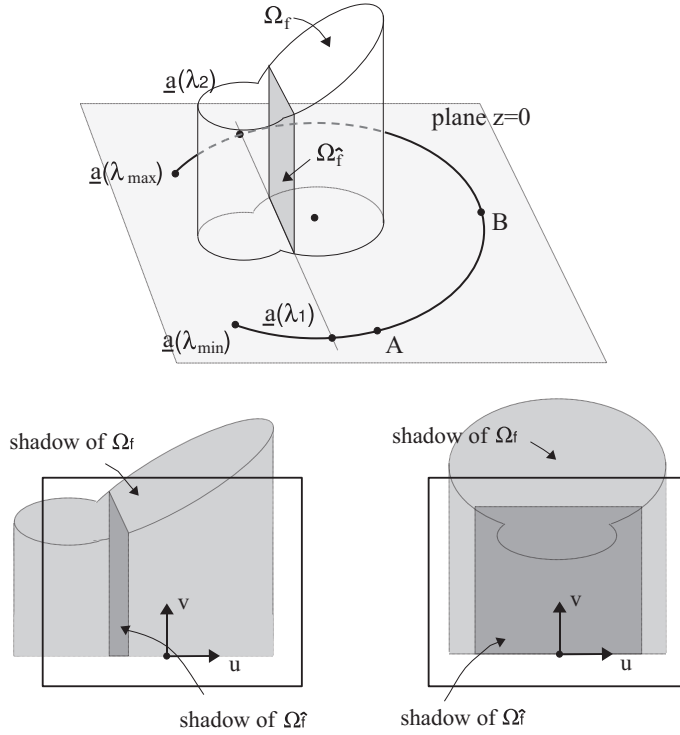
Figure 7.3: CB data truncation and its impact on the reconstruction on the planar reconstruction: (Top) 3D illustration of a specific data acquisition scenario (PCS stands for the plane of the circular scan). (Bottom) CB projection of the object support region with the source at (left) points A and (right) point B. The detector is indicated as a black delineated rectangle. The projection of $\Omega_{\hat{f}}$, i.e., of the object support in the plane of interest, is shown as a dark region. Although the entire object Ω_f is truncated, the projection of $\Omega_{\hat{f}}$ is covered by the detector for each $\lambda \in [\lambda_1, \lambda_2]$. Therefore, the intermediate function $\hat{b}$ can be computed over the region $\Omega_{\hat{f}}$.

considering all planes on which reconstruction is possible according to section 7.2.2 and by carrying out the required algorithmic steps to obtain $\hat{f}$ on each such plane. Combination of these planar results using interpolation schemes simply yields the object density for any 3D image volume that lies in the union of the considered planes. Hence, 3D reconstruction is accomplished by finding solutions to a set of 2D problems on a one-by-one basis.

From a practical viewpoint, however, the consideration of all possible planes is not feasible nor attractive since a lot of redundant information could be obtained. Furthermore, the issue of combining the planar results can be handled more efficiently if the considered planes do not intersect each other in the object region. For these reasons, we focus here on planes that are parallel to each other. We note that this choice may not be optimal in terms of noise, but it highly simplifies the numerical implementation. Since each planar reconstruction is achieved using Cartesian coordinates t and z, and since the considered planes are parallel to each other, a direct assembling of the planar reconstructions immediately yields the object density function f on a 3D Cartesian grid, as typically desired in 3D image reconstruction. More specifically, from now on, we focus on a one-parametric family of planes with normal vector $\underline{\hat{e}}_s = (\cos\hat{\theta}, \sin\hat{\theta}, 0)^{\mathrm{T}}$, where $\hat{\theta} = \lambda_c = (\lambda_{min} + \lambda_{max})/2$, and

use as plane parameter the signed distance from the origin $(0,0,0)^{\mathrm{T}}$, measured along the vector $\underline{\hat{e}}_s$. Volume reconstruction thus uses the set of planes

$$\mathcal{P}_p = \{\underline{x} \,|\, \underline{x} \cdot \underline{\hat{e}}_s = s_{start} + p\Delta s, \, p = 0, 1, \ldots, N_p\}, \tag{7.16}$$

where N_p gives the number of considered planes, while integer $p \geq 0$ is the plane index and Δs defines the distance between two adjacent planes. The quantity s_{start} denotes the signed distance of the first considered plane, $\mathcal{P}_0$, from the image volume origin. In order to have sufficient data for reconstruction on any $\mathcal{P}_p$ according to section 7.2.2, we require $s_{start} \geq s_{min}$ with $s_{min} = \underline{a}(\lambda_{min}) \cdot \underline{\hat{e}}_s = \underline{a}(\lambda_{max}) \cdot \underline{\hat{e}}_s$.

7.3 Numerical Algorithm

This section suggests a numerical algorithm to achieve image reconstruction on a plane $\mathcal{P}$ according to the theory of section 7.2. The basic principle of this algorithm is to first compute a discrete representation of $\hat{b}$ and to accurately transfer the initial, continuous 2D inversion problem (7.14) into a discrete setting. Next, an iterative scheme is used to compute an estimate $\hat{f}^e$ for the planar object density $\hat{f}$ in (7.14).

7.3.1 Computation of the Intermediate Function

The suggested algorithm achieves CB data differentiation according to (7.4) using the ray-interpolation method suggested in [68], which has already been utilized in the implementation scheme presented in section 6.4. As described before, this differentiation method involves a parameter ε, which controls the trade-off between resolution and noise in the results [68]. For all evaluations presented throughout this chapter, ϵ was fixed to the value $\varepsilon = 0.01$ which was determined to yield $\hat{b}$ in high spatial resolution [68]. The integration in λ in the backprojection equation (7.5) is approximated by a summation of the differentiated data g_F at the known samples in λ according to the trapezoidal rule. For increased computational efficiency, the intermediate function is immediately computed for the entire set of planes $\mathcal{P}_p$ at once. This computation yields for each of these planes an approximation $\hat{b}^e$ of the true function $\hat{b}$ and the accuracy of $\hat{b}^e$ depends on the noise in the acquired CB data and the discretization effects occurring during computation. For simplicity, the remainder of section 7.3 is focussed again on just one single plane of interest $\mathcal{P}$.

7.3.2 Discretization of the 2D Inversion Problem

The functions $\hat{f}$ and $\hat{b}$ on the considered plane $\mathcal{P}$ are both discretized, over their respective regions $\Omega_{\hat{f}}$ and $\Omega_{\hat{b}}$, using a Cartesian sampling pattern in t and z. The sampling density for both functions is assumed to be identical, with the distance between two adjacent samples specified by Δt in t and by Δz in z. However, the sampling grids used for $\hat{f}$ and $\hat{b}$ are shifted with respect to each other along the t-axis by $\Delta t/2$. More precisely, the function $\hat{f}$ is sampled at coordinates $(i\Delta t, j\Delta z)^{\mathrm{T}}$ with $i \in \mathbb{Z}$ and $j \in \mathbb{Z}$, while $\hat{b}$ is sampled at interleaved coordinates $(i\Delta t + \Delta t/2, j\Delta z)^{\mathrm{T}}$. This shift allows an improved realization of the required 1D convolutions in the discrete setting, as will be explained below. Furthermore, to better emphasize the discrete character of the resulting entities, the index notation

$$\hat{f}_{i,j} = \hat{f}(i\Delta t, j\Delta z) \qquad \text{and} \qquad \hat{b}_{i,j} = \hat{b}(i\Delta t + \Delta t/2, j\Delta z) \tag{7.17}$$

will be used from now on. The 2D relation (7.14) is then discretized in the form

$$\hat{b}_{i,j}^{\sigma} = \pi \Delta t \sum_{k=i_{min}}^{i_{max}} h_{hilb}^{\sigma} \left(\left(i - k + \frac{1}{2} \right) \Delta t \right) \left(\hat{f} \left(k\Delta t, z_1(k\Delta t) \right) + \hat{f} \left(k\Delta t, z_2(k\Delta t) \right) \right). \quad (7.18)$$

The quantity $k \in \mathbb{Z}$ covers the interval $[i_{min}, i_{max}]$ that is bounded by the minimum and maximum value of index i among all samples $\hat{f}_{i,j}$ in $\Omega_{\hat{f}}$. The restriction of the bounds of summation in (7.18) became possible since we assume as an a priori knowledge that $\hat{f}_{i,j} = 0$ everywhere outside the region $\Omega_{\hat{f}}$. The superscript σ in (7.18) denotes a free parameter that allows us to modify the smoothness of the applied discretization scheme. More precisely, the LHS of (7.18) corresponds to a discrete 1D convolution of the known samples of $\hat{b}$, namely

$$\hat{b}_{i,j}^{\sigma} = U(\sigma) \sum_{c=-2}^{2} \exp \left(\frac{-c^2}{2\sigma^2} \right) \hat{b}_{i-c,j}. \quad (7.19)$$

Hence, $\hat{b}_{i,j}^{\sigma}$ is a smooth version of $\hat{b}_{i,j}$, obtained with a Gaussian kernel of standard deviation $\sigma \Delta t$ that has been discretized at the 5 sampling positions $-2\Delta t$, $-\Delta t$, 0, Δt and $2\Delta t$. The factor $U(\sigma)$ allows for a correct normalization of the discrete kernel and is given as

$$U(\sigma) = \left(\sum_{c=-2}^{2} \exp \left(\frac{-c^2}{2\sigma^2} \right) \right)^{-1}. \quad (7.20)$$

Low-pass filtering of the function $\hat{b}_{i,j}$ is used to decrease discretization errors in the 2D intermediate function, and thereby provide improved input data for the planar reconstructions. While reducing discretization errors, we note that this low-pass filtering also reduces resolution. We counteract this resolution issue by including a similar Gaussian filtering in the RHS of (7.18). More precisely, the convolution kernel, h_{hilb}^{σ}, in (7.18) is defined as

$$h_{hilb}^{\sigma}(t) = U(\sigma) \sum_{c=-2}^{2} \exp \left(\frac{-c^2}{2\sigma^2} \right) h_{hilb}^{b}(t - c\Delta t) \quad (7.21)$$

with $U(\sigma)$ given by (7.20). This means that $h_{hilb}^{\sigma}(t)$ is a Gaussian-smoothed version of the band-limited Hilbert kernel $h_{hilb}^{b}(t)$ that is based on rectangular apodization and a cut-off frequency of $1/(2\Delta t)$. The expression of $h_{hilb}^{b}(t)$ is given as

$$h_{hilb}^{b}(t) = \frac{1}{\pi t} \left(1 - \cos \frac{\pi t}{\Delta t} \right), \quad (7.22)$$

see section 4.4.1, and we note that according to (7.18) and (7.21), this function is only evaluated at coordinates for which the cosine term vanishes. This suggested sampling scheme avoids oscillations in the discretized filter kernel and contributes to an overall improvement in numerical precision and to less aliasing artifacts in the reconstruction results [69, 32]; see also section 4.4.1 for a discussion about this issue.

Going back to relation (7.18), we finally note that the function $\hat{f}$ on its RHS is in general evaluated at points that are not on the sampling grid for $\hat{f}$, as illustrated in Figure 7.4. In order to obtain for example the value $\hat{f}(k\Delta t, z_1(k\Delta t))$, we use a linear interpolation in z between the two samples $\hat{f}_{k,j}$ and $\hat{f}_{k,j+1}$ that are closest to this location.

From now on, the discretized 2D functions $\hat{f}_{i,j}$ and $\hat{b}_{i,j}^{\sigma}$ will be represented using the vectors $\underline{\hat{f}} \in \mathbb{R}^{N_{\hat{f}}}$ and $\underline{\hat{b}}^{\sigma} \in \mathbb{R}^{N_{\hat{b}}}$, respectively. This 1D representation is easily achieved by
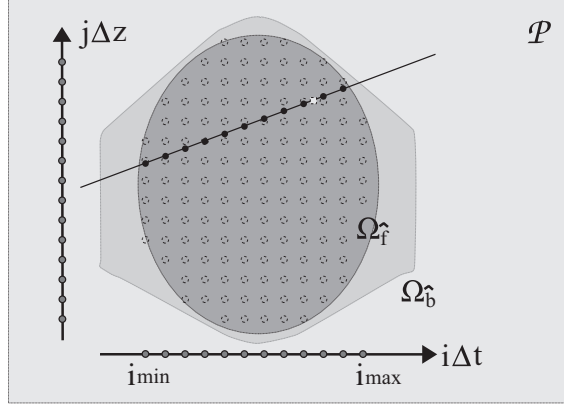
Figure 7.4: The applied discretization scheme on $\mathcal{P}$: Δz and Δt define the density of the sampling pattern. The small, dashed circles show all $N_{\hat{f}}$ sampling positions considered for $\hat{f}_{i,j}$, while the indices i_{min} and i_{max} describe, respectively, the leftmost and rightmost sampling points of $\hat{f}_{i,j}$ along coordinate t. We illustrate one filtering line, which passes through a sampling position for $\hat{b}$ (bright square). In order to obtain, from the sampled $\hat{f}$, data at the positions of the black solid circles on this filtering line, we use a linear interpolation in z between the two adjacent samples in $\hat{f}_{i,j}$.

defining a function $(i,j) \mapsto r$ that maps a sample (i,j) of the 2D Cartesian grid to an element r of the corresponding vector. In this notation, $N_{\hat{b}}$ is the total number of samples for $\hat{b}^{\sigma}$ in i and j together and similarly, $N_{\hat{f}}$ is the total number of samples used for $\hat{f}$. Then, for each sample of $\hat{b}^{\sigma}$, relation (7.18) may be expressed in the form

$$\hat{b}_r^{\sigma} = \underline{m}_r^{\sigma} \underline{\hat{f}} \tag{7.23}$$

where $\hat{b}_r^{\sigma}$ denotes element r of the vector $\underline{\hat{b}}^{\sigma}$ and $\underline{m}_r^{\sigma}$ denotes the row r of a matrix $\mathbf{M}^{\sigma} \in \mathbb{R}^{N_{\hat{b}} \times N_{\hat{f}}}$. The components of $\underline{m}_r^{\sigma}$ include both, the values of the filter kernel $h_{hilb}^{\sigma}(t)$ and the interpolation weights for $\hat{f}$, as occurring in (7.18). A finite dimensional approximation of the relation between all samples of $\hat{b}^{\sigma}$ and $\hat{f}$ on $\mathcal{P}$ is thus given by the linear system of equations

$$\underline{\hat{b}}^{\sigma} = \mathbf{M}^{\sigma} \underline{\hat{f}}. \tag{7.24}$$

Image reconstruction on $\mathcal{P}$ can now be accomplished by solving (7.24) for $\underline{\hat{f}}$.

In the rest of this chapter, emphasis on the smoothing parameter σ is again dropped to simplify the notation. So, from now on, the symbol $\underline{\hat{b}}$ will be used to describe $\underline{\hat{b}}^{\sigma}$, while $\mathbf{M}$ will be used for $\mathbf{M}^{\sigma}$.

7.3.3 Stability and Numerical Inversion Scheme

The numerical stability of the reconstruction problem on $\mathcal{P}$ can be investigated by studying the singular values of the system matrix $\mathbf{M}$ in (7.24), in a similar fashion as presented in [26]. Using $\sigma = 0$ and the CB geometry parameters summarized in Table 6.1, we composed the matrix $\mathbf{M}$ for the plane $\mathcal{P}$ defined by $p = 0$ and $s_{start} = 0\,\mathrm{mm}$ and then computed its singular values; see Figure 7.5. Note that we used the same number of samples, namely

7528, for both $\hat{b}$ and $\hat{f}$. Hence, $\mathbf{M}$ was square. Note also that the samples were distributed in a region of shape similar to that of $\Omega_{\hat{b}}$ in Figure 7.4, that we discretized this plane using $\Delta t = \Delta z = 2\,\text{mm}$, and that the maximum half cone-angle in $\mathcal{P}$ was about $11.3°$.
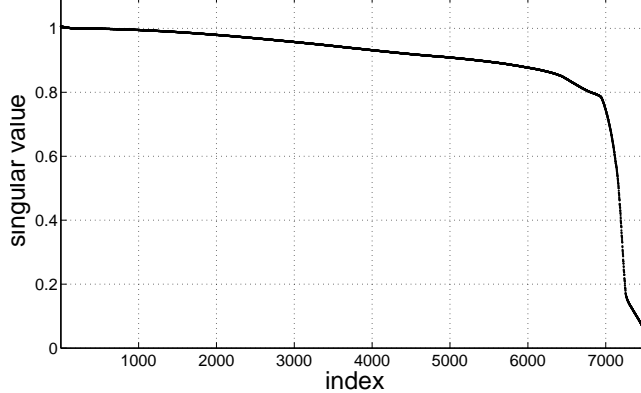

Figure 7.5: The 7528 singular values of the example system matrix $\mathbf{M}$, ordered from the largest one (which has value 1) to the smallest one. The matrix $\mathbf{M}$ was obtained using the geometry parameters explained in the text and using a discretization of $\Delta t = \Delta z = 2\,\text{mm}$.

Figure 7.5 shows the singular values of matrix $\mathbf{M}$, ordered from the largest to the smallest value. We note that $\mathbf{M}$ is non-singular and that its condition number is approximately 33, and therefore unexpectedly small. We attribute this phenomena to the band-limitation intrinsically modeled in $\mathbf{M}$, which was introduced when discretizing the continuous problem. The fast decay of the singular values in the last 10% of the graph in Figure 7.5, however, is an indication that solving (7.24) for $\hat{f}$ truly corresponds to an ill-conditioned problem [9]. This ill-posedness is problematic in practical scenarios, where only an approximation $\hat{b}^e$ of the 2D intermediate function can be determined. To obtain a meaningful reconstruction from contaminated data, we focus on finding a regularized solution to a constrained least-square formulation of (7.24). Furthermore, we consider two constraints, namely

1. **CRAY:** Knowledge about integrals of $\hat{f}$ along rays that diverge from $\underline{a}(\lambda_1)$ and $\underline{a}(\lambda_2)$ and that are entirely contained in $\mathcal{P}$. These integrals are part of the acquired CB data g.

2. **CPOS:** Knowledge that $\hat{f}$ is a non-negative function, since it represents physical object density.

Hence, we set up the constrained optimization problem in the form

$$\text{minimize } Q(\hat{f}) := \|\mathbf{M}\hat{\underline{f}} - \hat{\underline{b}}^e\|^2 + \alpha^2\|\mathbf{C}\hat{\underline{f}} - \hat{\underline{c}}^e\|^2$$
$$\text{subject to } \hat{\underline{f}} \geq \underline{0}. \tag{7.25}$$

The first term of $Q(\hat{f})$ accounts for the congruence between the reconstruction and the given intermediate function according to the relation modeled in $\mathbf{M}$, while the second term is a penalizing term that incorporates the linear constraint CRAY. Each row of the matrix $\mathbf{C}$ contains an equation to compute a ray integral from the discrete $\hat{f}$, while the vector $\underline{\hat{c}}^e$ contains the corresponding integral values, i.e., samples of the function g. The impact of

CRAY may be adjusted using parameter α. We note that finding an appropriate value for α is a difficult problem, which will be addressed in more details in section 7.4.2.

To simplify the notation for the remainder of this section, the objective function in (7.25) may be expressed equivalently as

$$Q(\underline{\hat{f}}) = \|\mathbf{A}\underline{\hat{f}} - \underline{\hat{d}}^e\|^2$$
$$= \underline{\hat{f}}^{\mathrm{T}}\mathbf{A}^{\mathrm{T}}\mathbf{A}\underline{\hat{f}} - 2\underline{\hat{f}}^{\mathrm{T}}\mathbf{A}^{\mathrm{T}}\underline{\hat{d}}^e + \underline{\hat{d}}^{e\mathrm{T}}\underline{\hat{d}}^e, \tag{7.26}$$

where

$$\mathbf{A} = \begin{bmatrix} \mathbf{M} \\ \alpha\,\mathbf{C} \end{bmatrix} \quad \text{and} \quad \underline{\hat{d}}^e = \begin{bmatrix} \underline{\hat{b}}^e \\ \alpha\,\underline{\hat{c}}^e \end{bmatrix}. \tag{7.27}$$

The solution of (7.25) is estimated using a projected steepest descent iteration scheme [61, 16], during which a sequence of intermediate estimates $\underline{\hat{f}}^{(q)} \in \mathbb{R}^{N_{\hat{f}}}$ with integer iteration index $q \geq 0$ is computed. The initial estimate is set to $\underline{\hat{f}}^{(0)} = \underline{0}$ and the updating equation is

$$\underline{\hat{f}}^{(q+1)} = \mathcal{C}\left(\underline{\hat{f}}^{(q)} + w^{(q)}\underline{u}^{(q)}\right), \tag{7.28}$$

using the update direction

$$\underline{u}^{(q)} = -\nabla Q(\underline{\hat{f}}^{(q)}) \tag{7.29}$$

with the gradient of $Q(\underline{\hat{f}})$ given as

$$\nabla Q(\underline{\hat{f}}) = 2\mathbf{A}^{\mathrm{T}}(\mathbf{A}\underline{\hat{f}} - \underline{\hat{d}}^e) \tag{7.30}$$

and using the update step-width

$$w^{(q)} = \frac{1}{2}\frac{\|\underline{u}^{(q)}\|^2}{\|\mathbf{A}\underline{u}^{(q)}\|_2^2}. \tag{7.31}$$

To understand the scheme described by (7.28) to (7.31), note that in each iteration, $\underline{\hat{f}}^{(q)}$ is first updated in the direction of the steepest descent of the quadratic functional Q at point $\underline{\hat{f}}^{(q)}$, which is a natural selection when pursuing minimization. The update step-width according to (7.31) guarantees that $\underline{\hat{f}}^{(q)} + w^{(q)}\underline{u}^{(q)}$ minimizes Q on the line through $\underline{\hat{f}}^{(q)}$ with direction $\underline{u}^{(q)}$ [16]. The operator $\mathcal{C}$ in (7.28) describes the orthogonal projection onto the convex set of vectors with nonnegative entries. This projection assures that each intermediate estimate satisfies the nonlinear constraint CPOS.

It can be shown that the sequence $\underline{\hat{f}}^{(q)}$ converges towards the solution of (7.25) for increasing q [45]. However, at some point during the iterations, the intermediate estimate may start diverging from the true, desired, $\underline{\hat{f}}$ due to contaminations in the data vector $\underline{\hat{d}}^e$. We want to avoid this behavior and therefore suggest to stop iterations early, when either of the two following conditions is satisfied:

1. The iteration index q reaches a pre-defined maximum number γ_{max}.

2. The value $\left\|\underline{\hat{f}}^{(q)} - \underline{\hat{f}}^{(q-1)}\right\|_\infty$ (with $\|\cdot\|_\infty$ denoting the maximum norm) first becomes equal or less than a certain threshold. This threshold is here defined as $\gamma_{thres}\left\|\underline{\hat{f}}^{(q)}\right\|_\infty$, i.e., relative to the norm of the current intermediate estimate.

Thus, iteration continues up to the maximum index γ_{max} if at least one element of the intermediate estimate is still updated strongly enough, even if the update in all other elements is already below the introduced threshold. Note that there exists a number of indications that the early stopping rule applied to our steepest descent iteration scheme asymptotically defines a regularization process [63], as discussed in [9, 91].

Let N_q denote the iteration index at which the stopping criterion is satisfied. We define

$$\underline{\hat{f}}^e := \underline{\hat{f}}^{(N_q)} \tag{7.32}$$

as the nonnegative approximation to the solution of the constrained optimization problem (7.25) and consider $\underline{\hat{f}}^e$ as a good estimate for the vector $\underline{\hat{f}}$ that satisfies (7.24). The inverse of the mapping defined earlier in this section, $r \mapsto (i, j)$, yields $\hat{f}_{i,j}^e$ from $\underline{\hat{f}}^e$ and therefore a discrete 2D representation of the reconstructed object density on $\mathcal{P}$, as desired.

7.4 Numerical Studies

This section presents an evaluation of the factorization method, based on CB data simulated in the C-arm geometry (as defined previously in table 6.1). During data simulation, we made sure that the CB projection of the object support region Ω_f onto the detector plane was always entirely contained in the measured area $[u_{min}, u_{max}] \times [v_{min}, v_{max}]$.

7.4.1 Experimental Set-Up

The experiments in this section involve two mathematical phantoms. The first one is a high-contrast disk phantom that consists of six cylindrical disks embedded in a low-attenuating cylinder of radius $100\,\text{mm}$ and density $-900\,\text{HU}$. Each disk has a thickness of $10\,\text{mm}$, a radius of $80\,\text{mm}$ and the density of water (defined as $\mu_{water} = 0.01836\,\text{mm}^{-1}$). The disks are centered on the z-axis and stacked one above the other with a center-to-center distance of $20\,\text{mm}$ between any two adjacent disks. The first disk was centered on the plane of the source trajectory and therefore, all other disks were above that plane. The second phantom we use in this chapter is the FORBILD head phantom [3]. In the presented evaluations, the head phantom was positioned so that its center is $40\,\text{mm}$ above the plane of the circular scan.

As described in section 7.3, the iterative inversion algorithm that we use for each planar reconstruction involves the selection of 4 parameters: α, σ, γ_{thres} and γ_{max}. We here study in details the impacts of parameters α and σ on achievable reconstruction quality, by investigating the results obtained on a single plane of interest. Unless otherwise stated, a fixed stopping rule was used, and this rule was defined with $\gamma_{thres} = 0.002$ and $\gamma_{max} = 400$.

7.4.2 Impact of Parameter α on Image Quality

The effects of α on image quality are studied by reconstructing the disk phantom for a range of values of α while using the discretization $\Delta t = \Delta z = 0.5\,\text{mm}$. The plane $\mathcal{P}$ on which reconstruction was achieved was defined with $s_{start} = 0\,\text{mm}$, $p = 0$ and we set $\sigma = 0$.

The reconstruction results were evaluated quantitatively by computing as a FOM, i.e., as a figure of merit, the root-mean-squared error (RMSE) between reconstruction $\hat{f}^e$ and the true object density $\hat{f}$ within two different regions in $\mathcal{P}$. These regions, denoted as A and B, were rectangular with width $100\,\text{mm}$ and height $6\,\text{mm}$ and were entirely contained,
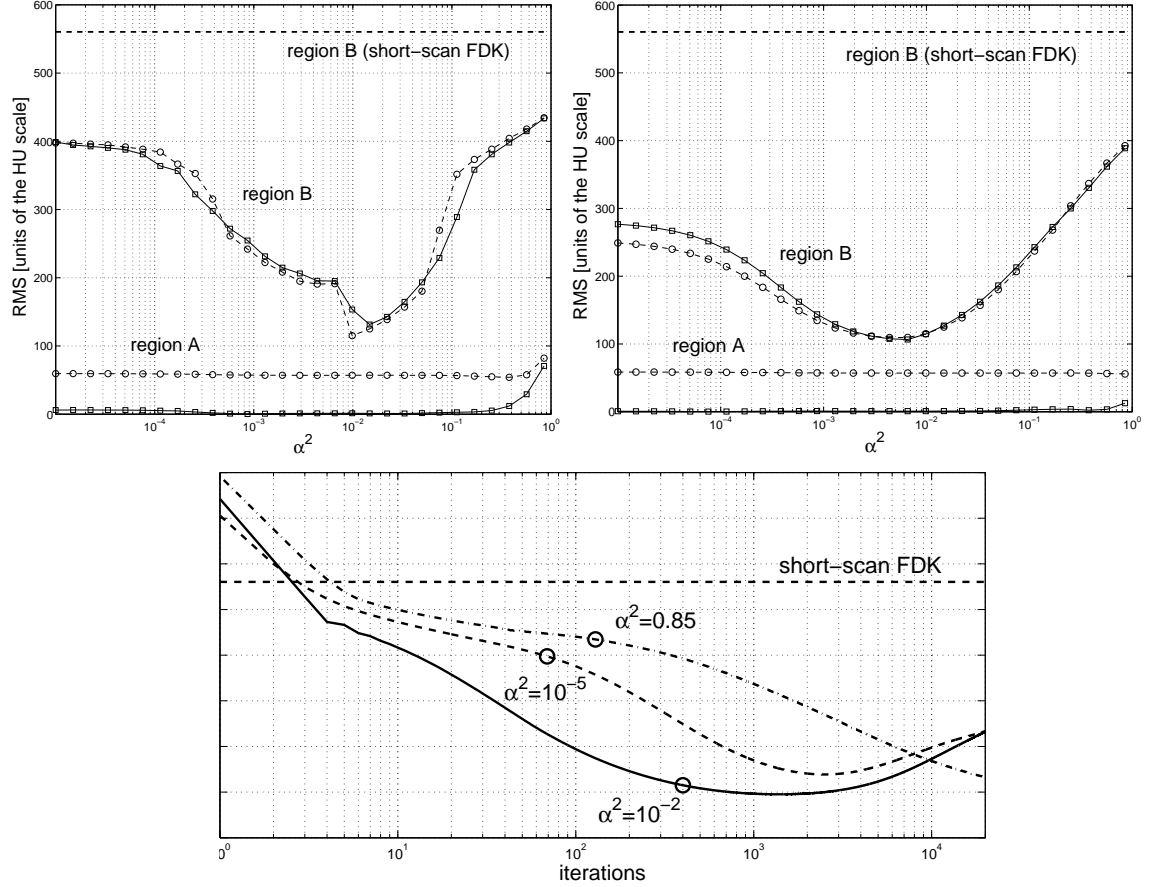
Figure 7.6: The impact of α on image quality: The two graphs at the top show the RMSE in regions A and B (see Figure 7.7) as a function of α^2, while using (left) the defined stopping rule and (right) a fixed number of 400 iterations. The dashed curves are achieved using CB data with Poisson noise and $25,000$ photons per ray, and the solid curves show results for non-noisy CB data. The graph at the bottom illustrates, for the noisy measurements, the convergence of the RMSE in region B for the three choices (dashed) $\alpha^2 = 10^{-5}$, (solid) $\alpha^2 = 10^{-2}$ and (dash-dotted) $\alpha^2 = 0.85$. The circle on each curve indicates the iteration at which the stopping criterion, which was used for the left diagram, is satisfied. The dashed horizontal line in each figure shows, for comparison, the RMSE obtained in region B with short-scan FDK and non-noisy data.

respectively, in the bottom disk and in the top disk of the phantom (see Figure 7.7). The two graphs in the top of Figure 7.6 display the RMSE as a function of α^2 in regions A and B, for both ideal and noisy CB data. Noisy CB data was simulated assuming the Poisson noise model and an emission of $25,000$ photons per measurement ray. For the first graph, we used the stopping criterion defined above ($\gamma_{thres} = 0.002$ and $\gamma_{max} = 400$), whereas the second graph was obtained using a fixed number of 400 iterations (thus without using the γ_{thres} rule). Figure 7.6 shows that α has in either case a strong impact on the reconstruction results. This impact is particularly significant in regions remote from $z = 0\,\text{mm}$ (top curves in the graphs). Selecting α too small or too large yields unbalancing
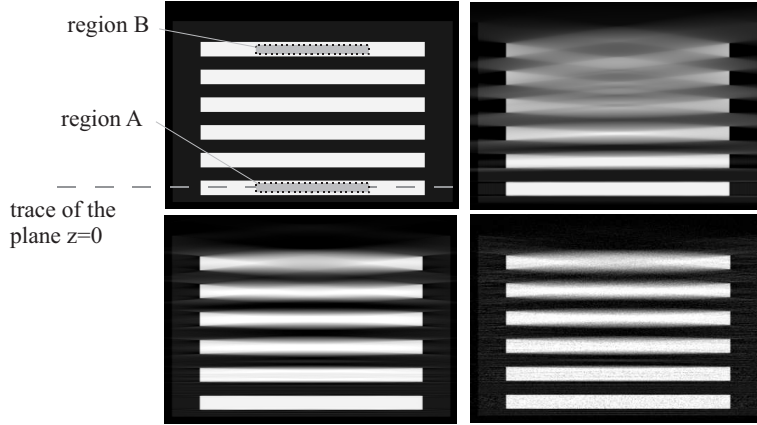
Figure 7.7: The plane $\mathcal{P}$ with $s_{start} = 0\,\mathrm{mm}$ and $p = 0$ through the disk phantom. (Top-left) Illustration of the true density values, of the phantom position relative to the plane of the circle and of regions A and B. (Top-right) Reconstruction using short-scan FDK. (Bottom) Reconstruction using the factorization approach and parameters $\alpha^2 = 10^{-2}$, $\sigma = 0$ from (left) non-noisy CB data and (right) CB data with Poisson noise assuming an emission of $25,000$ photons per measurement ray. Visualization in $[-1000\,\mathrm{HU}, 50\,\mathrm{HU}]$.

between the two terms of the objective function in (7.25) and this unbalancing affects convergence and achievable image quality, thus demonstrating that each term contains crucial information for reconstruction. Clearly, a careful selection of this parameter, such as $\alpha^2 = 10^{-2}$ in the considered experiment can improve image quality and convergence speed. These observations seem to apply as well to noisy data as to non-noisy data. Figure 7.7 shows that overall, noise is fairly robustly handled.

The diagram in the bottom of Figure 7.6 presents, for the noisy CB data, a closer investigation on the convergence properties of RMSE in region B for three particular choices of α^2: $\alpha^2 = 10^{-5}$, $\alpha^2 = 10^{-2}$ and $\alpha^2 = 0.85$. We realize that the general development of the RMSE during the iteration process is similar for various selections of this parameter: the intermediate estimates approach the true densities, reach a minimum distance to them at some iteration index and then start to diverge. Again, the superiority of $\alpha^2 = 10^{-2}$ becomes obvious, because this choice, compared to the other two, yields (i) better image quality for almost any fixed number of iterations and (ii) a minimum FOM-value indicating that the optimal reconstruction is closer to the true density and is reached after fewer iterations. We also note that the stopping criterion we applied for the top-left of Figure 7.6 is satisfied fairly early, before the minimum of either of the three curves is reached. On the other hand, the small improvements expected when continuing iterations, appear not very attractive considering that up to 10 times more iterations would have to be carried out. The selected values of γ_{max} and γ_{thres} thus achieve a practical trade-off between efficiency and image quality. Note, in this context, that the three investigated choices of α already yield improved CB artifact behavior, compared to short-scan FDK, after only 10 iterations, as depicted in the bottom of Figure 7.6.
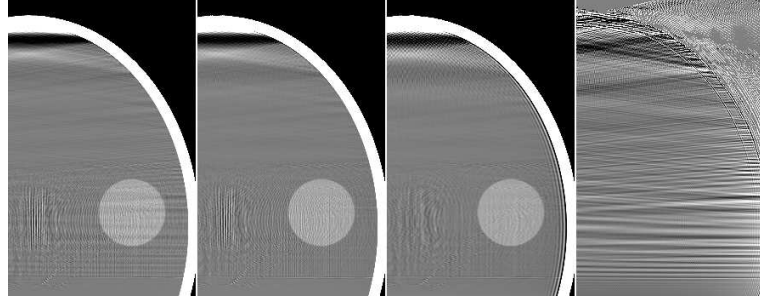
Figure 7.8: Reconstructions of the FORBILD head phantom on the plane $\mathcal{P}$ with $s_{start} = 10\,\text{mm}$ and $p = 0$ in the grayscale window $[20\,\text{HU}, 80\,\text{HU}]$. From (left) to (right): using parameters $\sigma = 0$, $\sigma = 0.7$ and $\sigma = 1.4$. Rightmost image: difference between reconstructions using $\sigma = 0$ and $\sigma = 0.7$ in a compressed window of width 10 units on the HU scale. The bottom edge in each of the presented images corresponds to $z = 0\,\text{mm}$.

7.4.3 Impact of Parameter σ on Image Quality

The effect of σ was studied using reconstructions of the FORBILD head phantom within the plane $\mathcal{P}$ that is given by $p = 0$ and $s_{start} = 10\,\text{mm}$. The plane $\mathcal{P}$ was again discretized using $\Delta t = \Delta z = 0.5\,\text{mm}$ and the reconstructions were obtained with fixed $\alpha^2 = 10^{-2}$, while using three different values of σ, namely $\sigma = 0$, $\sigma = 0.7$ and $\sigma = 1.4$. The results, displayed in Figure 7.8, show that an appropriate choice of the smoothing parameter, such as $\sigma = 0.7$, can lower the strength of horizontal, streak-like discretization artifacts. A large selection of σ should be avoided, since it would degrade high frequency contents in $\hat{b}_{i,j}$ too much. Then, a reconstruction of the object density $\hat{f}_{i,j}$ in its original resolution as pursued according to (7.18) would incorporate an additional deconvolution task. This issue will in general increase the ill-posedness of the problem so that the convergence property of the 2D optimization problem might be affected and so that additional artifacts might arise; see, e.g., the ringing in the third image of Figure 7.8 that occurs when selecting $\sigma = 1.4$.

7.5 Comparative Evaluation of the Factorization Method

This section presents a comparison of our factorization approach to the short-scan FDK method, the ACE method and the virtual PI-Line BPF methods, i.e., to the reconstruction approaches discussed in chapter 6. This evaluation is carried out in terms of spatial resolution, image noise and CB artifacts and also studies the impact of axial truncation.

During these comparative studies, the 2D iterations for the factorization approach were stopped according to the parameters $\gamma_{max} = 400$ and $\gamma_{thres} = 0.002$, and we used $\alpha^2 = 10^{-2}$ and $\sigma = 0.7$, which turned out to be efficacious parameter values in the investigations of section 7.4. In contrast to that section, however, reconstruction was now carried out not only a single plane of interest, but for the entire 3D image volume, by following the concepts described in section 7.2.3.

7.5.1   Comparison of Spatial Resolution and Image Noise

Spatial resolution was evaluated using the profile-matching method of section 6.6.1. Hence, we simulated CB data of the CB performance phantom using geometry parameters identical to those of table 6.1 on page 70 and using a short-scan with $\lambda_c = 0°$ and $\lambda_s = 210°$. Image reconstruction with the factorization approach was achieved using a set of 720 planes $\mathcal{P}_p$, all of which were orthogonal to the x-axis. We selected sampling parameters $\Delta s = \Delta t = \Delta z = 0.5\,\text{mm}$ and consequently, the object density function was recovered on an isotropic grid in the image volume with sampling distance $0.5\,\text{mm}$.
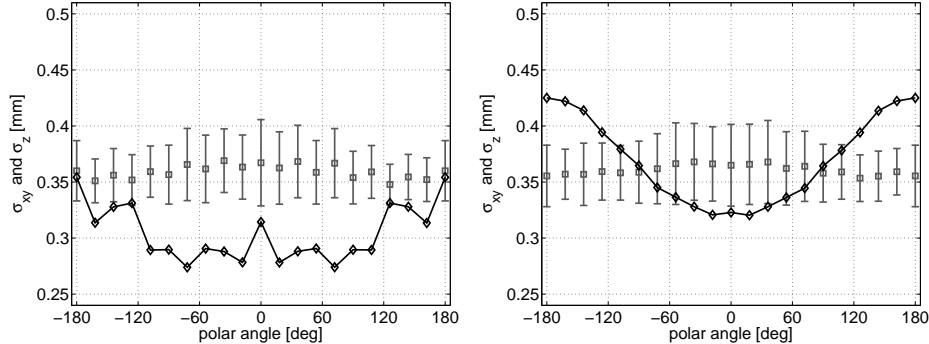
Figure 7.9: Estimate of spatial resolution in the plane of the circle for (left) the factorization approach and (right) the ACE method[2]. The black curve in each diagram shows the mean z-resolution at distance $160\,\text{mm}$ from the origin as a function of the polar angle. The gray rectangles show, for the same locations, the mean resolution in $x - y$; the bars attached to each such rectangle illustrate the anisotropy in this $x - y$ resolution.

The left side of Figure 7.9 presents, for the factorization approach, the estimated spatial resolution in $x-y$ and in z inside the plane of the circle, i.e., the plane of the circle scan, and on the ring with radius $160\,\text{mm}$ centered on the origin of the image volume. We observe that for the selected algorithmic parameters, the factorization approach yields an $x - y$ resolution that is almost identical to that of the ACE method, which was found to yield the most homogeneous overall resolution among the methods of chapter 6. It therefore outperforms the $x - y$ resolution property of the short-scan FDK as well as the virtual PI-line BPF method; see section 6.6.1. However, whereas the ACE method achieves this specific resolution advantage at the cost of lower z-resolution, the factorization approach seems to come along without this drawback; its z-resolution characteristic inside $z = 0\,\text{mm}$ is slightly superior to that of the other considered methods.

We also observe that the resolution curves determined for the factorization method are less smooth. We attribute this behavior to the fact that the resolution estimate at a specific location is based on the reconstruction results on several vertical planes. Each planar result was obtained using in general a different number of iterations (due to the stopping rule γ_{thres}) and therefore using a different regularization scheme, which obviously affects our measurements.

To evaluate the noise propagation, we simulated CB data of the FORBILD head phantom in the C-arm geometry and using a short-scan centered on the polar angle $\lambda_c = 0°$ and with scan range of $\lambda_s = 210°$. We then added noise to this data assuming an emission of $250,000$ photons per measurement ray. Image reconstruction was carried out over the
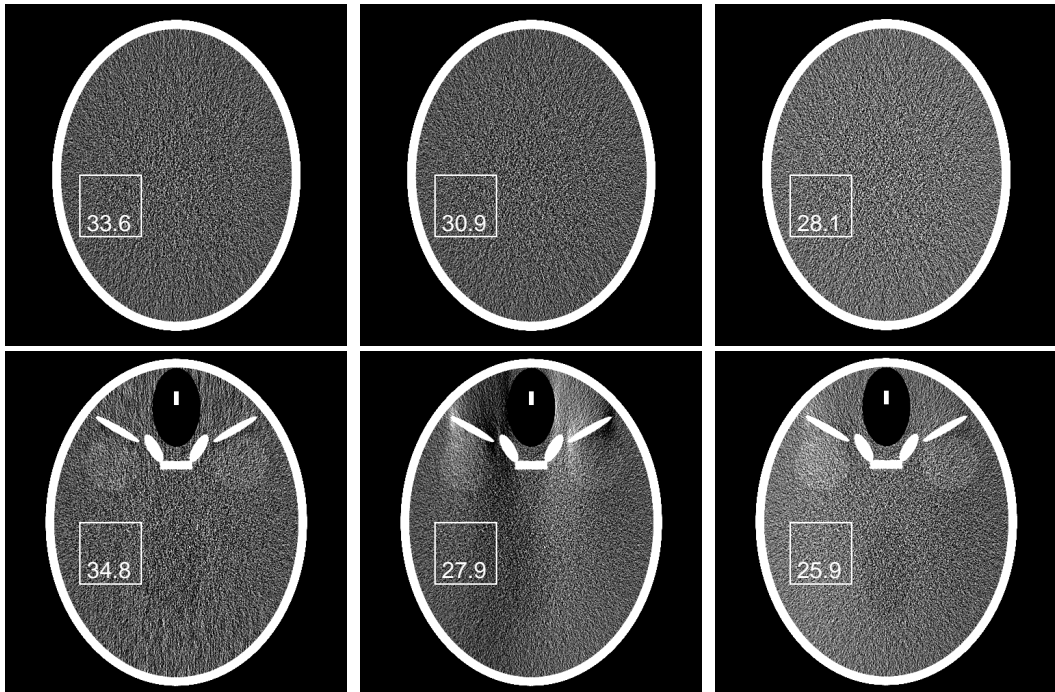
Figure 7.10: Investigation of noise propagation in the reconstruction of the FORBILD head phantom. Top and bottom rows present the slices $z = 0\,\mathrm{mm}$ and $z = 50\,\mathrm{mm}$ through these reconstructions, respectively, which were obtained using (left) the factorization approach, (center) the short-scan FDK method and (right) the ACE method. These images are presented in the grayscale window $[0\,\mathrm{HU}, 150\,\mathrm{HU}]$. The number in each image indicates the standard deviation (in units on the HU scale) of the reconstructed values inside the square ROI, which is marked with a white box.

entire region Ω_f using sampling parameters similar to that of the resolution study from above. Figure 7.10 presents the slices $z = 0\,\mathrm{mm}$ and $z = 50\,\mathrm{mm}$ through the factorization results, next to the corresponding results obtained with the short-scan FDK method and with the ACE method.

The noise level in each presented slice was quantified by computing the standard deviation of the reconstructed values within a square of side-length $45\,\mathrm{mm}$ that is entirely contained in the homogeneous phantom region that has density $50\,\mathrm{HU}$; see Figure 7.10 for an illustration of that region and for the determined standard deviations (measured in units on the HU scale). These results indicate that the factorization approach yields a somewhat increased level of noise compared to ACE inside the plane of the scan, with a difference of about 15%, while the noise performance of the short-scan FDK method lies between that of these two methods. Furthermore, comparison of the standard deviations determined at $z = 0\,\mathrm{mm}$ and $z = 50\,\mathrm{mm}$ indicates that the level of noise in the factorization results does not show the slight decrease outside the plane of the scan that can be observed in the short-scan FDK method and the ACE method.

These slightly different behaviors in image noise might be caused by the fact that each method comes with a distinct handling of the measured data: ACE and short-scan FDK involve all acquired CB projections for the computation of the density estimate (but use a different handling of redundant data), whereas the factorization method involves in general

only a subset of these projections, see section 7.2.3. Another source of these differences might be the degree of regularization imposed on the reconstruction problem. This degree correlates with the number of iterations carried out in the numerical 2D inversion algorithm; see section 7.3.3. The stopping rule used for the factorization method in this study yields a high number of iterations (between 100 and 400, depending on the plane) and yields therefore a less regularized estimate to the solution of the ill-posed reconstruction problem. Hence, we expect to observe a high spatial resolution and more accurate reconstructions from CB data that is consistent with the data model of section 2, but on the other hand also a stronger propagation of data noise.
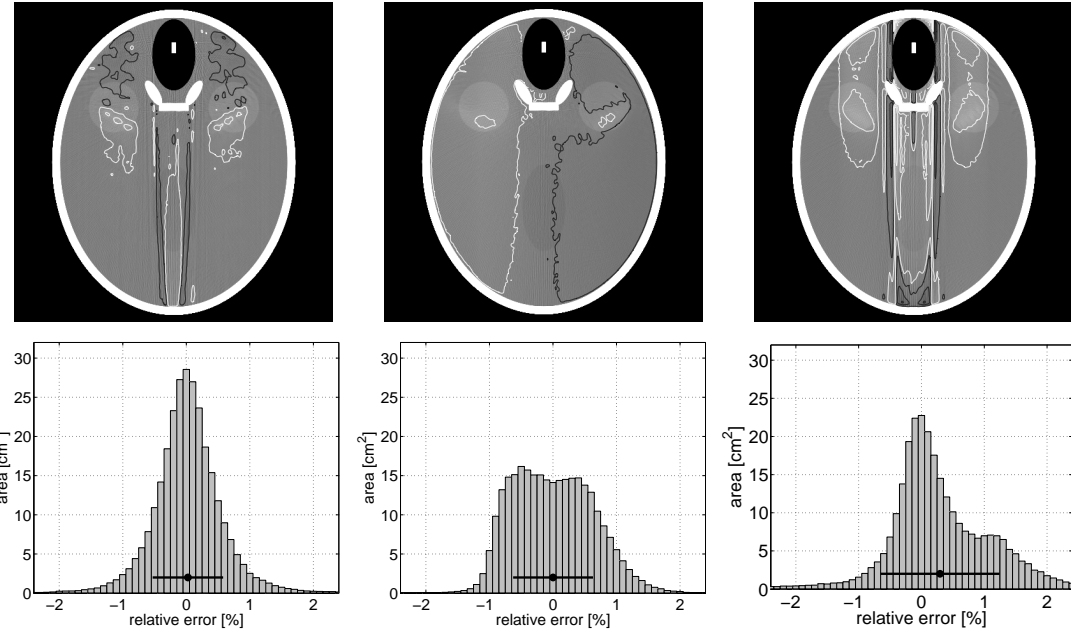
Figure 7.11: Investigation of CB artifacts in the slice $z = 52.5\,\mathrm{mm}$ through the FOR-BILD head phantom reconstructed using (left) the factorization approach, (center) the ACE method and (right) the virtual PI-line BPF method without Parker weighting. (Top) Reconstruction result in the grayscale window $[-50\,\mathrm{HU}, 150\,\mathrm{HU}]$. The nested contour lines indicate the locations at which the relative error reaches .25%, 1.25%, 2.25% and 3.25% (white contours) or -0.25%, -1.25%, -2.25% and -3.25% (black contours). (Bottom) Histogram of this relative reconstruction error in the slices presented at the top.

7.5.2 Comparison of CB Artifacts

The effects of missing 3D Radon data on image quality were investigated using the evaluation scheme presented in section 6.6.3. Consequently, we simulated noise-free CB data of the FORBILD head phantom for a short-scan with $\lambda_s = 210°$ and reconstructed its density function over the entire object support region Ω_f, while using an isotropic sampling of $0.5\,\mathrm{mm}$.

The slice $z = 52.5\,\mathrm{mm}$ through the reconstructions obtained with the factorization approach, with ACE and with the virtual PI-line BPF method without Parker weighting is presented in Figure 7.11, along with the histograms of the relative reconstruction error
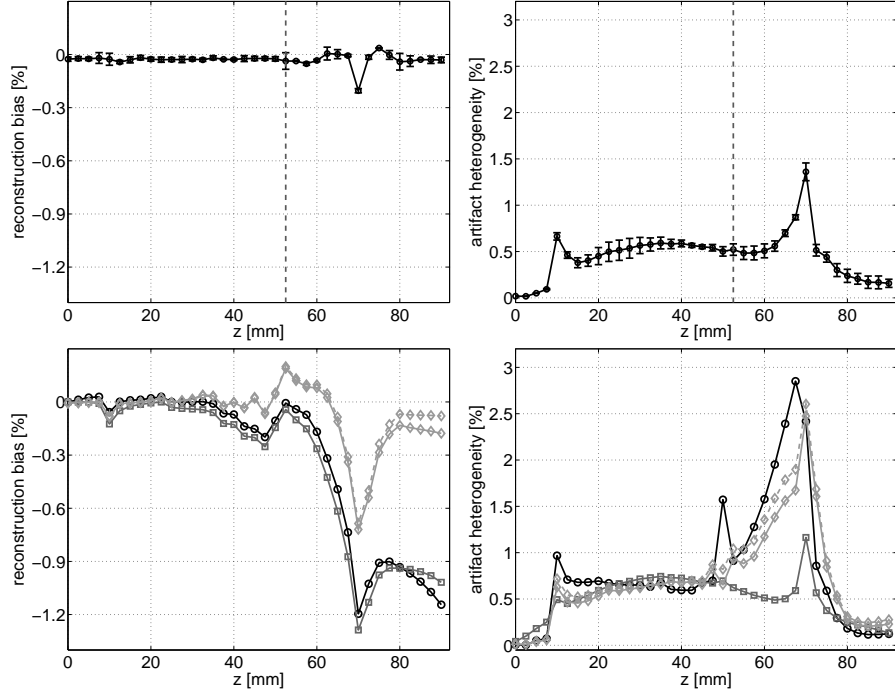
Figure 7.12: (Left) Reconstruction bias and (right) artifact uniformity, illustrated for the factorization approach (top row) and for the methods discussed in the previous chapter (bottom row). In the diagrams at the bottom, the black circles correspond to the short-scan FDK method, the dark gray squares to the ACE method and the light-gray diamonds to the virtual PI-line BPF methods (the method using Parker weighting is marked with a dashed line).

within this slice. These results were obtained using a short-scan with center $\lambda_c = 0°$ and they illustrate that in this specific slice, the factorization approach yields overall the smallest relative error; its error histogram is nicely compact and has a peak centered on 0%, in contrast to that of the other two considered methods.

The experiment was repeated for 6 different realizations of the short-scan, namely for scans with $\lambda_c = k \times 60°$ with $k = 0 \ldots 6$ and fixed $\lambda_s = 210°$. The diagrams in the top of Figure 7.12 show, for the factorization approach, the mean reconstruction bias and the mean artifact heterogeneity obtained across these 6 short-scans as a function of z; for a definition of these FOMs see section 6.6.3. These results indicate that our factorization approach yields image quality that is very robust with respect to the actual short-scan realization. A comparison to the corresponding curves of the four reconstruction methods discussed in chapter 6 shows that our method comes with a very low level of CB artifacts and overall quantitatively with the most accurate reconstruction results among the considered methods.

Similar observations can be made in the visual inspection of the slices $z = 50\,\text{mm}$ and $z = 60\,\text{mm}$ through the factorization results obtained for 4 different values of λ_c, presented in Figure 7.13 or in Figure 7.14, which shows the object density estimate on a vertical slice, obtained for the short-scan with $\lambda_c = 120°$. Our factorization approach can almost completely avoid the high-contrast gradient-like CB artifacts occurring with short-scan FDK, such as the dark shadows attached to the bones in the FORBILD head phantom or
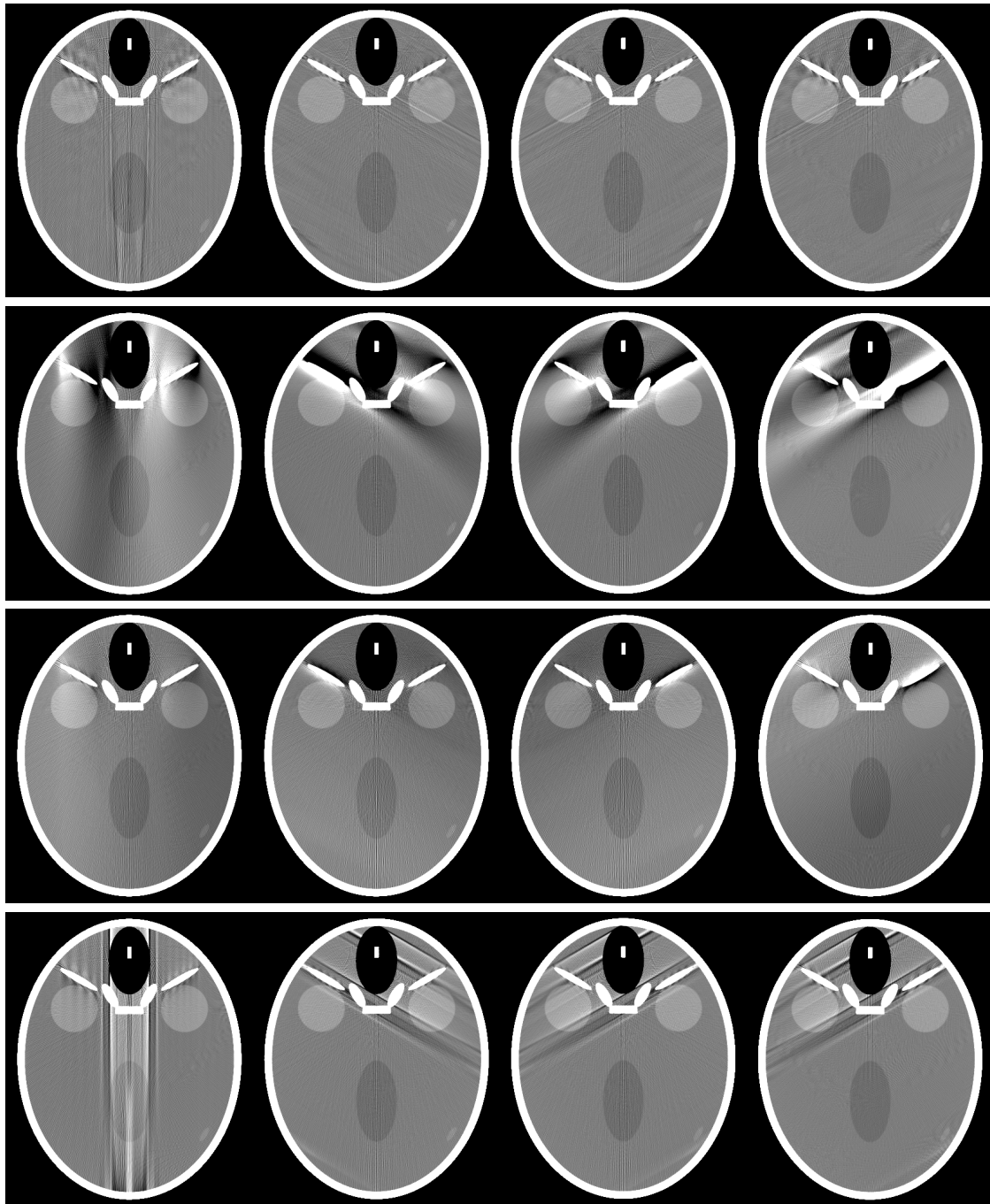
Figure 7.13: Impact of the short-scan center on image quality, demonstrated on the slice $z = 50\,\text{mm}$ through the reconstruction of the FORBILD head phantom. From (left) to (right), a short-scan with $\lambda_c = 0°$, $\lambda_c = 60°$, $\lambda_c = 120°$ and $\lambda_c = 300°$ was used. The results are obtained using (top) to (bottom): the factorization method, short-scan FDK, ACE and the virtual PI-line BPF method. All reconstructions are presented in the grayscale window $[10\,\text{HU}, 90\,\text{HU}]$.

the drop in reconstructed intensities in axial direction. Because the available CB data is insufficient for stable reconstruction, the issue of CB artifacts cannot be solved entirely,
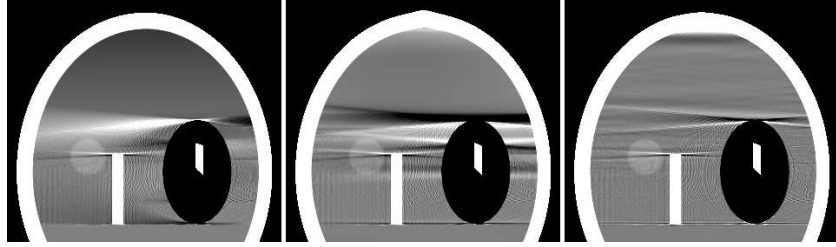
Figure 7.14: Reconstruction of the FORBILD head phantom within the plane defined by $p = 136$, $s_{start} = 10\,\text{mm}$ and $\Delta s = 0.5\,\text{mm}$, obtained with (left) short-scan FDK, (center) the virtual PI-line BPF method and (right) the factorization approach. Grayscale window: $[0\,\text{HU}, 100\,\text{HU}]$. The position $z = 0\,\text{mm}$ is at the bottom edge of each image.

but the effect of insufficient CB data can now only be seen in occasional spatially compact, streak-like (high frequency) artifacts, that are tangent to sharp discontinuities in the object; see, e.g., around the nose in Figures 7.13 and 7.14 or just below the skullcap in Figure 7.14.
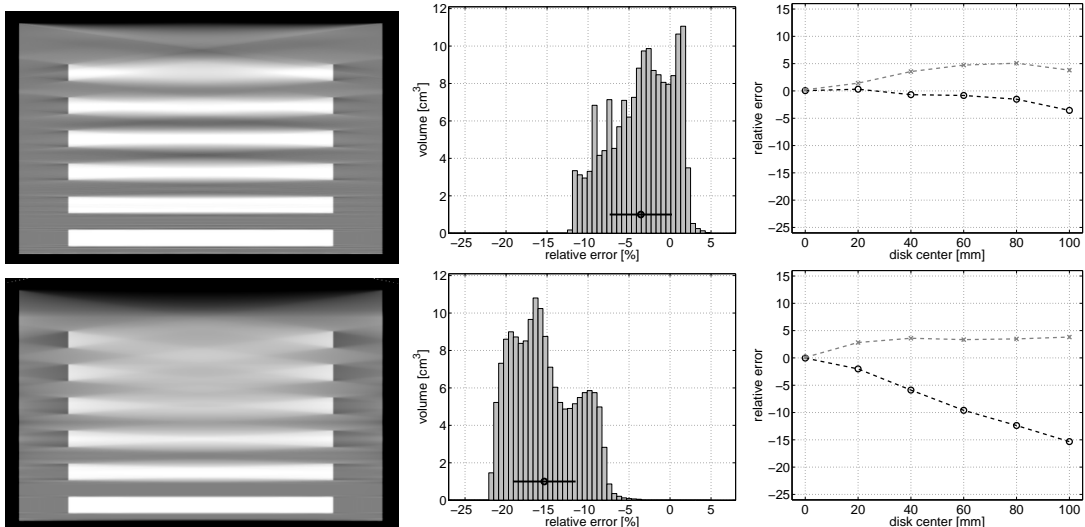
Figure 7.15: Evaluation of CB artifacts in the reconstruction of the disk phantom. Results are presented for (top) the factorization approach and (bottom) the the virtual PI-line BPF method without Parker weighting. The left image in each row shows the slice $x = 0\,\text{mm}$ through the reconstruction using the grayscale window $[-500\,\text{HU}, 500\,\text{HU}]$. The error histogram determined for the topmost disk is shown in the center. The black circle indicates reconstruction bias and the black line the artifact heterogeneity. The diagram on the right illustrated this bias (black circles) and this heterogeneity (gray crosses) for each of the 6 disks inside the phantom.

Following the scheme presented in section 6.6.3, CB artifacts were furthermore evaluated in the reconstruction of the disk phantom. The left image in Figure 7.15 shows the object density estimates on the vertical plane $x = 0\,\text{mm}$, obtained with the factorization method, but also with the virtual PI-Line BPF method, which performed best in the corresponding comparison presented on page 6.16. We observe a) that the shadow-like artifacts at the

left and right of each disk are noticeably reduced in the factorization results and (b) that the factorization results facilitate an easy distinction between the disks at the top of the phantom, especially close to the disk centers, whereas the high level of CB artifacts makes such a distinction very difficult in the BPF reconstruction. Figure 7.15 also presents the histogram of the relative reconstruction error inside the top disk of the phantom as well as the diagram presenting the reconstruction bias and artifact heterogeneity for each disk separately; these results confirm again the capability of the factorization method to yield the most quantitative results among all methods discussed in chapters 6 and 7.

7.5.3 Comparison of Axial Truncation Artifacts

The effects of axial truncation on image quality were evaluated analog to section 6.6.4: we reconstructed the vertical slice $x = 0$ mm through the FORBILD thorax phantom, first from CB data that is not truncated and then from CB data that suffers from axial truncation; see section 6.6.4 for details about the experimental set-up. Note that in the non-truncated case, the stopping criterion for the factorization method was satisfied after 48 iterations and that we made sure reconstruction from the truncated CB data involved the same number of iterations.
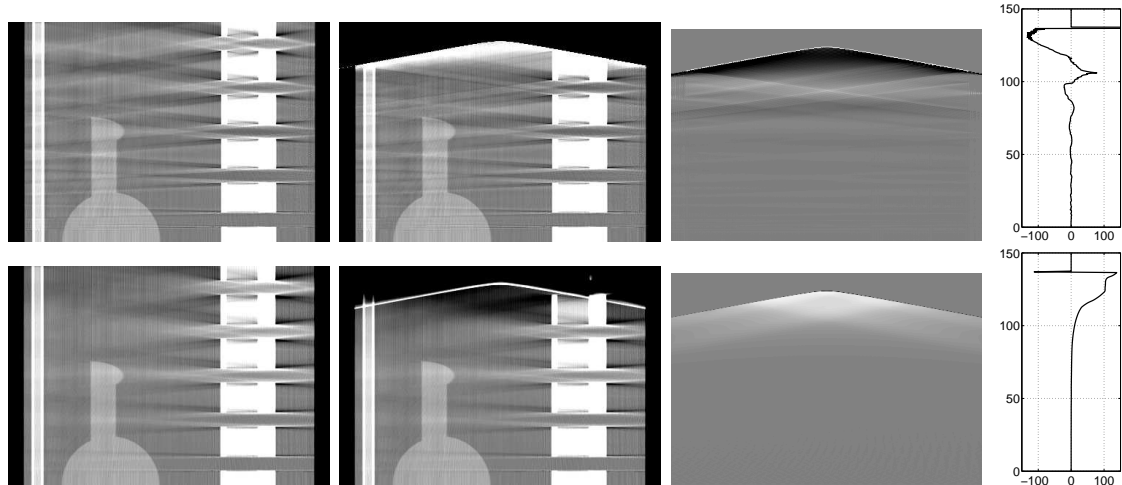

Figure 7.16: The effects of axial truncation within the slice $x = 0$ mm for (top) the factorization approach and (bottom) the ACE method [4]. From (left) to (right) reconstruction from non-truncated CB data, from truncated CB data (both using the grayscale window $[-150\,\text{HU}, 150\,\text{HU}]$), pointwise difference between these reconstructions in a window of width 300 units of the Hounsfield scale and central vertical profile of this difference.

The left two columns in Figure 7.16 show the reconstruction results, obtained with the factorization approach and – for comparison – with the ACE method. The third column in this figure shows the point-wise difference between the results illustrated on the left, which indicate numerical instabilities close to the edge of truncation, i.e., close to the top of region $\Omega_{\hat{b}}$, in the factorization results. Occurring truncation artifacts appear to impact image quality throughout almost the entire plane of interest, but their strength drops noticeably with the distance to the edge of truncation; see the top row of Figure 7.16. This property is

similar to that of the ACE method, where axial truncation in the CB data yields artifacts in almost comparable strength that appear, however, somewhat smoother.

7.6 Reconstruction from Real C-arm Data

The studies presented earlier in this chapter were based on simulated CB data, i.e., on data that is consistent with the ray-integral data model explained in chapter 2. We now evaluate how the factorization approach performs for image reconstruction from CB data collected with a commercially-available C-arm system, namely with the Siemens AXIOM Artis C-arm system [2]. On this system, we selected a scan protocol that delivers 543 CB projections, each of them consisting of 1240×960 square pixels of side-length $0.372969\,\text{mm}$. In this protocol, the X-ray source positions are approximately located on a circle of $750\,\text{mm}$ radius, which was centered on the origin of the image volume, and are distributed over a short-scan with scan-range of about $\lambda_s = 215°$. The detector was set to be $1200\,\text{mm}$ away from the source during the entire scan. The challenge with the task of image reconstructing on an existing C-arm system is that real CB data contains physical effects that are not considered in the data model on which the reconstruction algorithm relies, and this inconsistency is expected to have negative impacts on achievable image quality. These physical effects include for instance the impact of X-ray scatter and the effects related to detector dynamics, finite size focal spot and finite size detector elements, see e.g. [71].

Overall, the following evaluation appears similar to that of section 4.5, where we evaluated our original 2D fan-beam reconstruction method with no backprojection weight using data of a diagnostic CT scanner. However, one important difference between the two considerations lies in the degree of inconsistency between the assumptions of the data model and the real acquisition process. Note that diagnostic CT scanners have been designed primarily for imaging cross-sections through the human body [47]. Consequently, these scanners were targeted – from the very beginning – at yielding projection data that deviates as little as possible from the ideal data assumptions. Medical C-arm systems, on the other hand, were initially and primarily aimed at acquiring single 2D projections of the patient to support interventional procedures [71]. Consequently, these systems were designed for great mechanical flexibility rather than for yielding optimal input data for CT reconstruction method; in fact, the feature of 3D CT imaging was added only at a later moment [88]. Consequently, the inconsistency between the physical acquisition process and the ideal data assumptions that we have to deal with in this section are more significant than that occurring with diagnostic CT scanners; when pursuing good image quality, these deviations need to be considered during the reconstruction process.

7.6.1 Acquisition Geometry of a Real C-arm System

C-arm systems have a considerable mechanical degree of freedom, but the C-arm motion typically suffers from slight, but not negligible, instabilities during data acquisition. For instance, the X-ray source does in general not exactly describe a circular trajectory during the scan and the location and orientation of the detector might differ from the settings we selected on the scanner, see e.g. [23]. The accurate description of the acquisition geometry of existing C-arm systems using elementary analytic functions, as done in section 6.2, does not appear to be feasible nor practicable.

The geometry of the AXIOM Artis C-arm system that we considered for our real-data evaluation is thus described using the concept of projection matrices [38]. More specifically,

the C-arm system associates, to each measured CB projection, one projection matrix $P_i \in R^{3 \times 4}$ that describes, in homogeneous coordinates, the relation between a point $\underline{x}$ in the image volume and the coordinates of its CB projection on the detector plane [88, 41], where the integer i corresponds to the index of the projection image. The matrix P_i encodes complete information about the geometry parameters of the corresponding CB projection, such as the source position $\underline{a}_i$ or the vectors $\underline{e}_{u,i}$, $\underline{e}_{v,i}$ and $\underline{e}_{w,i}$. These parameters can be extracted from a given matrix P_i using the method described in [41].

Note that the sequence of projection matrices on the AXIOM Artis system are obtained in a calibration step. This step is based on acquiring CB data of a specific calibration phantom, the structure of which is precisely known, and on estimating for the CB projection i the matrix P_i that best describes the projection-relation between the known 3D structure of the calibration phantom and the acquired 2D image; for details see e.g. [41]. Fortunately, the deviations of the C-arm system from the ideal acquisition geometry are fairly reproducible so that for clinical use, the geometry information that is obtained in one calibration step may be used to geometrically describe the acquisition process of the subsequent scans.

7.6.2 Handling of Real C-arm CB Data

Recall that the factorization approach requires, as a first step, the partial differentiation of the CB data function $g(\lambda, \underline{\alpha})$ with respect to the curve parameter λ. This differentiation is a numerically delicate step, since (i) the sampling in λ of C-arm source trajectories is fairly coarse (compared the sampling of the trajectory for CT scanners) and (ii) the source trajectory does not describe a simple geometric curve, due to mechanical instabilities. Our algorithm therefore applies the differentiation scheme introduced in [68] that is numerically robust with respect to coarse sampling and to arbitrary source motions. In particular, this scheme was determined to yield an accurate differentiation results and to contribute to a good overall image quality in the context of C-arm reconstruction [40].

For the real-data reconstructions presented in the following (which are carried out using an isotropic sampling of $0.5\,\text{mm}$ in the image volume), the differentiated CB data is downsampled by a factor of 2 in u and in v, to reduce noise and to obtain a sampling in u and v that better matches the sampling grid defined for the image volume. The downsampled differentiated CB projection with index i is then backprojected according to the geometry parameters encoded in P_i. Note that the equations introduced on page 61 to compute u^* and v^*, i.e., the coordinates of the data samples required for reconstruction, involve simplifications that are based on the ideal geometry assumptions. Since the actual C-arm geometry does in general not satisfy these ideal assumptions, these equations are now replaced by a more general form, and we compute the quantities u^* and v^* for the CB projection i according to

$$u^*(\underline{x}) = -D \frac{(\underline{x} - \underline{a}_i) \cdot \underline{e}_{u,i}}{(\underline{x} - \underline{a}_i) \cdot \underline{e}_{w,i}} \tag{7.33}$$

and

$$v^*(\underline{x}) = -D \frac{(\underline{x} - \underline{a}_i) \cdot \underline{e}_{v,i}}{(\underline{x} - \underline{a}_i) \cdot \underline{e}_{w,i}} \tag{7.34}$$

respectively.

To determine the values λ_1 and λ_2 that describe the points of intersection between the source trajectory and the plane of interest $\mathcal{P}$, which is described by its normal $\underline{\hat{e}}_s$ and its

signed distance $\hat{s}$ from the image volume origin, we compute for each CB projection the quantity

$$\underline{a}_i \cdot \underline{\hat{e}}_s - \hat{s}, \tag{7.35}$$

where $\underline{a}_i$ is the source position extracted from the projection matrix P_i. Hence, (7.35) gives the signed distance of $\underline{a}_i$ from $\mathcal{P}$, measured along $\underline{\hat{e}}_s$. A positive value indicates that the source position for the CB projection with index i is between $\underline{a}(\lambda_1)$ and $\underline{a}(\lambda_2)$, so that according to (7.5) the corresponding filtered CB data is used for reconstruction on $\mathcal{P}$. The CB projections with indices that result in a negative value in (7.35), however, are disregarded for reconstruction on $\mathcal{P}$. CB projections at which (7.35) changes sign are considered partially for the final reconstruction, with a weight that depends on the trajectory discretization and the values computed in (7.35).

Finally, we make sure that the filtering lines involved in the 2D inversion process (for instance the two lines $\mathcal{L}_1$ and $\mathcal{L}_2$ in the example of Figure 7.2) are constructed accurately and consistent with the real acquisition geometry. This means that all these lines are constructed such that they pass through the actual intersection between the source trajectory and the plane $\mathcal{P}$, which e.g. does not necessarily need to have z-coordinate $z = 0\,\text{mm}$, as in the ideal short-scan geometry.

7.6.3 Reconstruction Results

In the following, we illustrate the performance of the factorization approach including the algorithmic modifications summarized in section 7.6.2 for reconstruction from real C-arm CB data. For comparison, we show also the results obtained with the short-scan FDK algorithm, i.e., the method used in state-of-the-art C-arm systems. Our short-scan FDK implementation follows the scheme presented in section 6.3 but also considers algorithmic modifications to handle the geometry deviations of C-arm systems. These modifications are similar to those explained in section 7.6.2 and are focussed on the accurate computation of the generalized Parker weighting function, of the backprojection weight and of the functions u^* and v^* in the context of non-ideal geometries. Moreover, the acquired CB data is downsampled by a factor of 2 in u and v before data filtering, as in the factorization method.
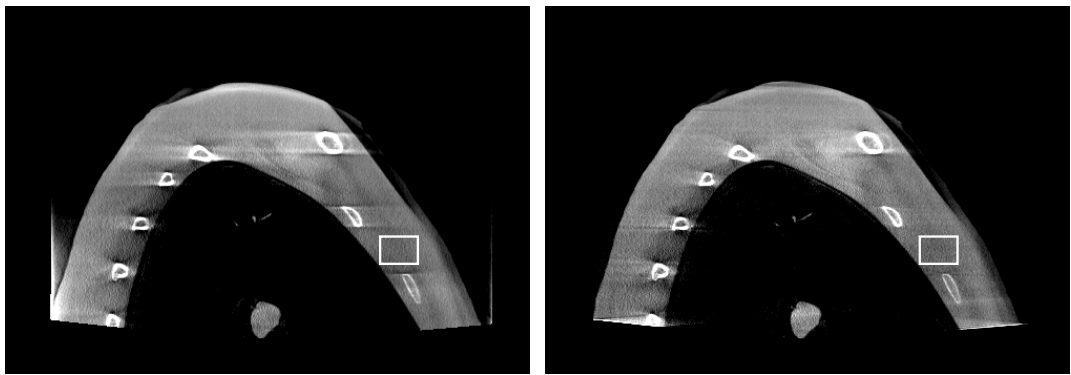

Figure 7.17: Reconstruction from the real C-arm data set A, obtained with (left) short-scan FDK and (right) the factorization approach. The results are presented using distinct grayscale-windows that were selected such that the mean of the reconstructed values in the small white rectangle has identical gray value in both images.

For our studies, we used a thorax phantom that is fairly wide such that its CB projection does not fit onto the detector from each viewing direction in the considered geometry. To evaluate the reconstruction in distinct scenarios of truncation, we collected two different sets of CB data[5]:

Set A: The thorax was placed such that its CB data was never truncated across the upper detector border (at v_{max}), but always truncated across the lower detector border (at v_{min}). Truncation in u only occurred at the ends of the short-scan, but not in the projections close to the short-scan center.

Set B: The placement of the phantom was such that its CB data was always truncated across the upper and lower detector border (along the v-coordinate). Truncation along the u-coordinate occurred in the projections in the center of the scan, but not at the ends of the short-scan.

Following the approach that is applied in the Siemens Axiom Artis C-arm system that we used for our evaluation, the acquired CB projection data was pre-processed prior to actual reconstruction. This pre-processing step aims at reducing the impact of X-ray scatter and beam-hardening on the data and therefore at improving overall image quality. Note, however, that this pre-processing requires the application of heuristic algorithms [95], and that these algorithms – while reducing the overall impact of physical effects – may also cause new inconsistencies in the CB data.

Image reconstruction was obtained from the pre-processed CB data and using the strategy described in this section on the set of vertical planes with $\hat{\theta} = -30°$. For the factorization method, we selected parameter $\alpha^2 = 0.01$ and we stopped the numerical inversion scheme after 20 iterations (set A) or 50 iterations (set B). We furthermore assumed that the inconsistencies in the CB data caused by physical effects dominate the achievable image quality so that the impact of the parameter σ on the result is not significant; we thus used $\sigma = 0$ for reconstruction.

Figure 7.17 presents the reconstruction result from data set A on one vertical plane, which was obtained by averaging 3 planar results obtained at $\hat{s} = 54.75\,\text{mm}$, $\hat{s} = 55.0\,\text{mm}$ and $\hat{s} = 55.25\,\text{mm}$. This averaging result contains less noise than each single planar reconstruction and therefore reveals clearer potential CB artifacts in the images. We furthermore realized that the short-scan FDK method and the factorization approach come with a different sensitivity to physical effects and to data truncation and that therefore, the reconstructed values slightly differ. To allow a meaningful comparison between the methods, we present the reconstruction results using grayscale windows selected to deliver similar image properties in all presented reconstructions. In Figure 7.17, for instance, we define a small rectangular region (see the figure) and scaled the reconstruction results individually on both sides so that the mean gray value in the regions is the same. Figure 7.18 shows two vertical slices through the reconstruction of CB data set B. These results were again obtained using averaging of 3 adjacent planar results and presented using approximate matching of image characteristics, as explained earlier in this paragraph.

From these results, we observe that the short-scan FDK approach yields strong, streak-like artifacts tangent to the bony structures in the thorax phantom and also some artifacts at the edges of the region $\Omega_{\hat{b}}$ caused by truncation effects. The factorization approach shows a clear reduction of these streak-like CB artifacts and of the impact of truncation on the results and thus a noticeable improvement of image quality.

---

[5]Our evaluation was carried out without using any extrapolation method to handle data truncation for the presented experiments
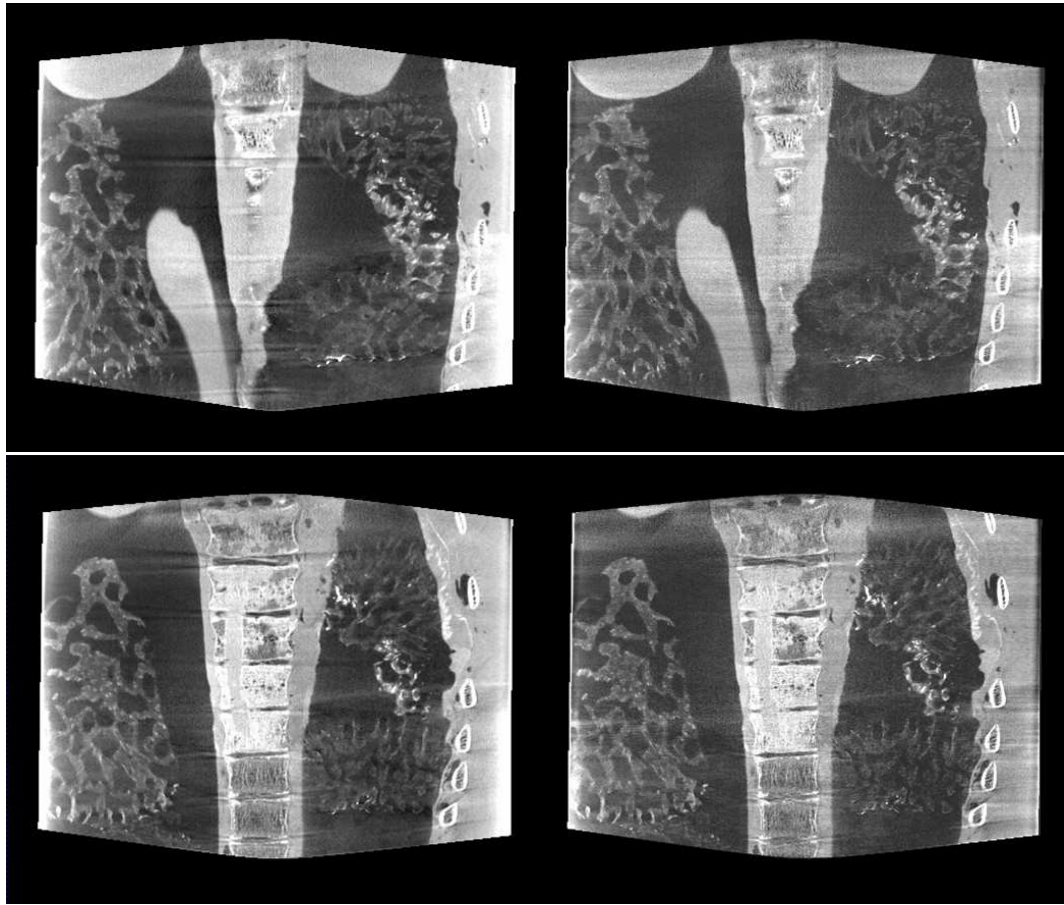
Figure 7.18: Reconstruction from the real C-arm data set B, obtained with (left) short-scan FDK and (right) the factorization approach.

7.7 Discussion and Conclusions

As discussed in chapter 6, the problem of 3D CB image reconstruction in the short-scan circular acquisition geometry is known to be theoretically very challenging. Analytical state-of-the-art algorithms suggested to solve this problem all come with advantages and disadvantages, as described before. For some imaging applications, one method may be more appropriate than the other, but for reconstruction of objects that contain significant information in the unmeasured region in 3D Radon space, such as the disk phantom, each state-of-the-art method that we investigated previously in this thesis yields results that severely suffer from CB artifacts.

This unsatisfactory conclusion stimulated us to derive, in this chapter, a novel factorization approach for 3D CB image reconstruction from a circular short-scan that aims at improving image quality at the cost of slightly higher algorithmic complexity. The main features of our algorithm are that it does not use any geometric approximations in its derivation and also does not involve assumptions about the unmeasured values of the 3D Radon space that would be required for a stable reconstruction. Furthermore, it enforces the reconstructed values to be positive, as desired. In these described points, our method differs from the reconstruction approaches presented in chapter 6.

We then evaluated achievable image quality of our factorization method and determined that its resolution and noise differs only slightly from that of other state-of-the-art approaches. For the selection of parameters used in this study, our method shows for instance more homogeneous image characteristics than short-scan FDK and better z-resolution than the ACE method, but also comes with an increase in image noise compared to these two. The strength of our method is that it allows a significant reduction of CB artifacts in the reconstruction results. This reduction becomes best visible in the reconstructions of the disk-phantom, where all other investigated state-of-the-art methods perform poorly. Our method, in contrast, yields an accurate estimate of the phantom structure and quantitatively very accurate results. Reconstruction of the head phantom confirmed this effect: the severe CB artifacts occurring with the short-scan FDK method, which is currently in use in many practically-available systems, can be nicely reduced. Remaining artifacts are restricted to only a few regions within the images and attached to the strong z-gradients of the object density. These improvements in image quality are relevant for applications in the medical arena, which we demonstrated on the reconstruction of a thorax phantom from real CB data, acquired with Siemens AXIOM Artis C-arm systems. These benefits for clinical applications were not obvious, since the real CB data contains various physical effects that are inconsistent with the data model that our algorithm strongly relies on. Despite these inconsistencies, the factorization method significantly reduces, using the same set of CB data, the streak-like CB artifacts close to the vertebrae that are present in the short-scan FDK results.

In addition to improvements in image quality, our factorization approach comes, by construction, with some flexibility with respect to transaxial data truncation. It can therefore naturally yield accurate reconstruction results in practically-relevant truncation scenarios without the need of heuristic data extrapolation methods [42]; see the results of the real data evaluations. Axial truncation, on the other hand, seems to impact image quality to some degree, especially close to the edge of truncation.

Chapter 8

Conclusions and Outlook

In this thesis, we discussed the issue of image reconstruction of static objects from projection data acquired in the geometries of medical X-ray imaging systems. We presented a review of the classical reconstruction theory and discussed various new CT reconstruction approaches, two of which are original.

The first part of this thesis was focussed on 2D reconstruction from full-scan fan-beam data, i.e., from data that can be acquired with diagnostic CT scanners. As described, an analytical FBP reconstruction formula for this acquisition geometry can be derived in a rather straightforward way from the 2D Radon transform theory. This formula, however, which we called the classical formula, is not necessarily the best choice for CT applications, partially because (i) it yields reconstruction results in which the noise characteristics depend noticeably on the distance to the axis of rotation and (ii) it requires the calculation and application of a spatially varying weighting factor during backprojection and is thus computationally demanding. New fan-beam inversion formulae were recently introduced in the literature, such as the formula of Noo *et al.*, see [67]. Noo's formula performs better in terms of image quality compared to the classical method and also simplifies the calculation of the weighting factor required during backprojection.

In this thesis, we went one step further and derived in the context of Noo's formula a novel FBP method for 2D full-scan fan-beam image reconstruction that completely avoids the spatially varying weighting factor during backprojection. Our method is thus computationally less complex and we were able to quantify a gain in computation speed of up to 47% in software implementation. In addition to a gain in efficiency, our novel reconstruction method comes with further improvements in image quality: it reduces the overall level of noise in the reconstructions without sacrificing spatial resolution. This effect was determined to be strongest at the edge of the imaged object region Ω_f, where noise could be reduced by up to 40%. These improvements in image quality were evaluated using simulated fan-beam data but could be verified in almost identical amount in the reconstructions from real fan-beam projection data collected with a commercially-available diagnostic CT scanner, making our new approach an attractive candidate for 2D image reconstruction in the clinical application.

Our FBP formula was derived exclusively for reconstruction from full-scan fan-beam data. It would be interesting to investigate if direct fan-beam FBP reconstruction without backprojection weight is possible when the data is measured on less than a full-scan. While the elimination of the weight for data associated to line integrals that are measured only once is not obvious, we note that at least a partial elimination of the backprojection weight may be readily achieved: the backprojection weight can be eliminated for each ray that

corresponds to a line integral that is measured twice, using the same redundancy weighting strategy as presented here.

Although the problem of analytic fan-beam reconstruction has been being studied for several decades, there is clear indication for further active research on specific topics in fan-beam reconstruction theory. Investigations in this context might be manifold; e.g., it would be interesting to see if it possible to develop fan-beam FBP reconstruction methods that optimize specific aspects of image quality, such as lesion detectability or the overall noise level at constant resolution. First developments in this direction are presented e.g. in [90, 89]. It is also likely to see further investigations in the context of reconstruction from a limited amount of fan-beam data, for instance, from data where most or even all projections suffer from truncation. A solution to this issue might be found in the context of DBP based reconstruction, initiated by the work in [65], and interesting results have been published recently [22, 55].

The second part of this thesis was focussed on 3D CB reconstruction with a circular short-scan, i.e., on CT imaging in the geometry of most clinical medical C-arm devices. We showed that the difficulty with this reconstruction task is that data acquisition delivers insufficient knowledge in 3D Radon space so that 3D reconstruction corresponds to an ill-posed problem almost everywhere throughout the image volume. Therefore, each method useful for practical application has to achieve a trade-off between numerical stability and accuracy. In FBP methods, this trade-off is often achieved by using geometric approximations or by making assumptions about the data in 3D Radon space that would be necessary for stable reconstruction, but is not acquired; the choices made by each method define the achievable image quality for this method.

We then presented a detailed comparative evaluation of four state-of-the-art methods, which either have been recently suggested in literature (ACE method, virtual PI-Line BPF method and virtual PI-Line BPF method with Parker weighting) or which are used in the clinical routine (short-scan FDK method). We realized that differences in noise and spatial resolution among these methods are rather small, but were overall in favor of the ACE method. A significant part of our study investigated the issue of CB artifacts and demonstrated that, while no method can achieve the impossible task of CB artifact-free reconstruction, the conventional short-scan FDK performs worst: it yields in general CB artifacts of high contrast, which are distributed over wide regions in the image volume and which significantly depend on the position of the short-scan relative to the object. The ACE method effectively reduces the contrast of artifacts, so that they are less disturbing to the human observer, whereas the virtual PI-Line BPF methods helps to reduce the spatial extent of the artifacts, so that they affect only parts of the image volume. All these improvements are, however, at the cost of increased computational complexity and of more sensitivity to axial truncation in the CB data. Hence, each of the reconstruction approaches we investigated has its pros and cons, so that a decision about which method is favorable for practical use depends on the imaging application and on the class of investigated objects. This is not a very satisfactory conclusion and stimulated us in developing a novel method for 3D circular short-scan CB reconstruction. Our new method is based on a theoretically-exact factorization of the initial 3D reconstruction problem into a set of 2D inversion problems. We suggested to solve each of these problems in a least-squares sense using a projected steepest descent 2D iterative algorithm; the solution to each 2D problem then directly delivers the object density on one vertical plane in the image volume. The main features of our factorization method are that it does not apply any geometric approximations or heuristic extrapolations during its derivation and that it can naturally

cope with certain scenarios of transaxial data truncation. It allows quantitatively very accurate reconstructions, compared to the other methods described above, and performs very well in terms of CB artifacts; these artifacts are now only visible as occasional, thin streaks in the reconstructions. Our method allows, for instance, an accurate recovery of the overall structure of the disk-phantom, whereas this recovery seems very difficult with the all the other state-of-the-art analytical methods we considered in this thesis. We furthermore collected CB data of a QRM thorax phantom on a commercially-available Siemens C-arm system and compared the reconstructions obained with the factorization method and with the short-scan FDK method against each other. This real-data evaluation showed that our novel method outperforms the reconstruction approach currently used in clinical systems, and thus also demonstrated that the artifact reduction we observed in the evaluations based on computer-simulated data is relevant for the practical application,

Note that the factorization method uses for reconstruction on any given plane only CB data on a limited interval along the source trajectory, so that it is not optimal in terms of noise. This algorithmic feature might furthermore be the source of occasional streak-artifacts in the reconstruction results. In order to improve on these two issues, it would thus be interesting to find a way to extend the factorization method so that all measured projections can be beneficially used for reconstruction in each plane.

An extension of the factorization reconstruction method to achieve reconstruction from CB data acquired along non-planar source trajectories can easily be achieved. In [28], e.g., we proposed such an extension for the circle-plus-orthogonal-line trajectory by using CB data from the line scan as additional constraints to the 2D inversion problems. Such an extension allows us to overcome the problem of insufficiencies in the CB data, and therefore to perform reconstructions that are free of CB artifacts. At the same time, this consideration of the additional CB data allows arbitrary (sparse) sampling on the additional linear scan segment, in contrast to methods that incorporate the line data using filtering and backprojection steps, such as the ones described in [51] or [23].

Going back to the field of volumetric CB imaging in general, we finally note that new generations of C-arm systems that allow even more flexible scanning motion are about to be getting installed in the clinical environment [6] and that several vendors recently released diagnostic CT scanners with an increased number of detector rows, e.g., in order to improve cardiac imaging applications [54]. It seems to be apparent that these new CT systems will raise even further the demand for efficient and theoretically well-justified CB reconstruction algorithms. We are convinced that within this thesis, we contributed to a better understanding of recent developments in circular CT and that the original methods we introduced are a step forward towards improved image quality in volumetric or slice-by-slice CT applications.

Summary

Examination of objects using X-rays is a technology that has been used for more than 100 years in various fields of application, in particular also in medical imaging, which is the focus of this thesis. Over the years, mechanical and electronic improvements contributed to a significant refinement of X-ray examination systems. Their natural capability, however, remains the same, namely to measure one or more transmission projection images of the investigated object. In order to achieve high-level imaging applications on these systems, projection data first need to be converted into a representation of object density using the concepts of computed tomography (CT). The reconstruction algorithm, which carries out this conversion, is clearly a key component of X-ray CT systems as it determines its imaging performance and therefore also its benefits for practical application.

This thesis is focussed on the development of algorithms useful for reconstruction of static objects from projection data acquired in the geometries of two medical imaging devices: the CT scanner, which is primarily used for diagnostic applications, and the medical C-arm device that is used to support interventional procedures. The standard CT data model introduces a formal link between X-ray measurements and object density: each X-ray measurement sample on these devices is interpreted to deliver the object density integral along the ray that connects the X-ray source with the X-ray detector element where the measurement is obtained. The problem of CT image reconstruction can thus be related to the task of finding a solution to a system of integral equations, for which methods can be derived. Our work is presented in two parts, which focus on 2D reconstruction from fan-beam data for a full-scan circular trajectory (the acquisition geometry of diagnostic CT scanners) and on CB reconstruction from a circular short-scan (the acquisition geometry of medical C-arm devices), respectively.

2D CT reconstruction from integral data associated to measurement rays that occur in parallel sets can be directly approached using the theory of the Radon integral transform, i.e., of a mathematical operator that describes the mapping of a function onto its integrals on hyperplanes. An analytical inversion formula for the 2D Radon transform can be derived in a rather straight-forward way using the 2D Fourier slice theorem; this classical formula follows the filtered- backprojection (FBP) structure, where the measured line-integral projection data are first high-pass filtered and subsequently backprojected into the image plane to yield an estimate of the object density function. Projection data that is measured using 2D CT scanners only differs from 2D parallel-beam data in the way the measurement rays are distributed during data acquisition: these rays then appear in groups of fans that diverge from a common ray source. CT reconstruction in the fan-beam geometry can thus be tackled by using the 2D Radon inversion formula together with some modifications that account for the distinct geometric set-up. An appropriate transfer of the resulting (classical) fan-beam inversion formula into the discrete setting then directly yields a numerical

algorithm for image reconstruction that may be readily applied in practical 2D CT imaging applications.

However, this fan-beam FBP reconstruction algorithm requires, in contrast to that for the 2D parallel-beam geometry, a weighted backprojection with the weighting factor depending on the point to be reconstructed and also on the source position. This back-projection weight implies an increase in computational effort and has also negative impact on noise properties of the reconstructed images. We suggest a new reconstruction formula that demonstrates that direct FBP reconstruction from full-scan fan-beam data is possible with no backprojection weight. Our novel approach is derived from the novel fan-beam inversion theory of Noo *et al.*, which allows, compared to the classical theory described in the previous paragraph, a more flexible handling of redundancies in the fan-beam data. This flexibility authorizes the use of a redundancy weighting function that cancels out the backprojection weight for the fan-beam FBP formula, yielding our novel method without backprojection weight. Using computer- simulated, realistic fan-beam data, we thoroughly compare our novel FBP formula with no backprojection weight to the use of a state-of-the-art FBP formula based on equal weighting of all data. Comparisons in terms of image noise, spatial resolution and computational efficiency are presented. These studies show that the formula we suggest yields images with a reduced noise level, at almost identical spatial resolution. This effect increases quickly with the distance from the origin of the image plane, from 0% at the origin to 20% less noise at 20 cm, and to 40% less noise at 25 cm. Furthermore, the new algorithm is computationally less demanding and reduces computation time with a gain that was found to vary between 12% and 43% on the computers used for evaluation. We furthermore demonstrate that our novel FBP formula can be readily applied for reconstruction from data acquired with a commercially-available CT scanner and that in this application we can expect improvements in image quality that are of almost identical quantity compared to those observed in the simulation studies.

Part two of this thesis focusses on CB reconstruction in the short-scan circular geometry. Although the 3D Radon transform and its analytic inversion formula are straight-forward generalizations of the corresponding concepts in 2D, the problem of 3D CB reconstruction cannot be directly related to the Radon transform theory. CB data acquisition does not yield direct access to 3D Radon values, as in the 2D scenario and CB image reconstruction techniques therefore rely on the theoretical findings of Grangeat and others that relate CB measurements to a partial derivative of 3D Radon data. These theories allow us to derive practical CB FBP reconstruction algorithms and also to define a criterion that indicates in which circumstances accurate and stable reconstruction from CB data can be achieved (Tuy's data sufficiency criterion).

Among the possible scenarios of CB tomography, the problem of image reconstruction from a circular short-scan using a 2D flat panel detector remains one of the most important ones, since it occurs with practically-available C-arm systems. The short-scan circular CB data, however, does not satisfy Tuy's data sufficiency criterion so that image reconstruction is an ill-posed problem almost everywhere in the image volume. Because of this, the development of an efficacious reconstruction method remains a challenging problem: the difficulty is to achieve an attractive trade-off between stability and accuracy. FBP-based CB reconstruction methods often use geometric approximations or assumptions about un-measured data samples during derivation, in order to allow for numerically stable results. The short-scan FDK method, for instance, which is commonly used for reconstruction in practical C-arm systems, is an heuristic generalization of the classical 2D fan-beam inversion formula. It is therefore computationally efficient and easy to implement, but also gener-

ally considered to be suboptimal in terms of image quality, due to its lack of theoretical foundation. Thus, various novel methods for CB reconstruction from a circular short-scan have been suggested in recent years. The ACE method, e.g., possesses FBP scheme but requires a more complex filtering step than short-scan FDK. The virtual PI- Line BPF methods (with and without Parker weighting), on the other hand, follow a slightly different structure: they first compute an intermediate function defined in the image volume and then use, in a second step, 1D filtering steps to reconstruct the wanted object density function from this intermediate result. We perform a detailed comparative evaluation of these described methods, which is based on CB data simulated in the C-arm geometry and which involves various mathematical phantoms. Our study investigates spatial resolution, contrast to noise ratio, CB artifacts and axial truncation artifacts. Noise propagation and resolution differ only slightly from one method to the other, but are overall in favor of the ACE method. The sensitivity with respect to CB artifacts, however, clearly reveals the algorithmic differences: Compared to short-scan FDK, the artifacts occurring with the novel approaches are either noticeably reduced in contrast (in the ACE method) or in size (for the virtual PI-Line BPF methods). These improvements in image quality are, however, achieved at the cost of higher algorithmic complexity and more sensitivity to axial CB data truncation. Hence, each investigated method has its pros and cons, and the issue which one is preferable for clinical application thus depends on the imaging task and on the investigated objects.

We then suggest a new, original method for CB reconstruction from a circular short-scan. Our method involves a novel factorization of the initial 3D reconstruction problem into a theoretically-equivalent set of independent 2D inversion problems, each of which corresponds to finding object density on one single plane in the image volume. This factorization is achieved analytically using the fact that backprojecting differentiated CB data onto this set of planes yields an intermediate function on each plane that is related to object density by some 2D filtering operations involving the kernel of the Hilbert transform. This factorization does not involve any geometric approximations or assumptions about the data that cannot be measured with the circular trajectory and can also cope with some scenarios of transaxial data truncation, in contrast to the methods discussed in the previous paragraph. Each 2D problem is then solved individually, in a second algorithmic step, by using a projected steepest-descent iteration scheme that yields a non-negative estimate of the object density function on the considered plane. This scheme requires the selection of a few discretization and iteration parameters, which affect the speed of convergence of the 2D iterations and also the achievable image quality. We determine in numerical studies a beneficial selection of these parameters and evaluate the resulting factorization algorithm against other competitive, state- of-the-art reconstruction methods. Numerical studies based on computer-simulated CB data of several mathematical phantoms demonstrate e.g. that the factorization method can significantly reduce the level of CB artifacts, especially when compared to the short-scan FDK method that is considered in practical C-arm devices. In particular, it allows an accurate recovery of the structure of a disk phantom from CB data – a task in which all other methods discussed in this thesis fail.

The application of our factorization method for reconstruction from real CB data acquired with medical C-arm systems requires special care, since the acquisition geometry of real-world C-arm systems slightly deviates from the ideal scenario assumed during the algorithmic derivation. Algorithmic steps that are numerically sensitive to these deviations, however, can be replaced by more robust implementations, thus allowing our algorithm to be evaluated using real CB data. The reconstruction results of a physical QRM thorax

phantom, scanned with a Siemens AXIOM Artis C-arm system, demonstrate that the improvements in image quality achieved over short-scan FDK are practically relevant: CB artifacts and truncation artifacts are noticeably reduced in the factorization results.

Although practical reconstruction formulae for 2D and 3D CT reconstruction have been known for many years, reconstruction theory remains to be a field of active research. The two methods we suggest in this thesis, for 2D fan-beam reconstruction without backprojection weight and 3D CB reconstruction by use of a novel factorization, effectively tackle specific limitations of classical approaches: they yield improvements in efficiency and image noise (fan-beam formula) or improvements in image quality at the cost of increased computational complexity (factorization appraoch). Future developments might focus on finding reconstruction formulae that optimize certain image characteristics, such as lesion detectability, from a given projection data set, or also at yielding accurate reconstructions in the context of limited data.

List of Symbols and Acronyms

Functions

μ	X-ray attenuation coefficient
f	object density function
f^e	object density estimate
b	intermediate DBP-function
w	redundancy weight (point-dependent)
m	redundancy weight (ray-dependent)
h	filter kernel function
g	fan-beam data (part 1), cone-beam data (part 2)
p	2D parallel beam data (part 1), density profile (part 2)
γ^*	fan-angle of the ray through $\underline{x}$
u^*	u-coordinate of intersection between detector and ray through $\underline{x}$
v^*	v-coordinate of intersection between detector and ray through $\underline{x}$

Operators

$\mathcal{R}$	Radon transform
$\mathcal{R}^{\#}$	2D Radon backprojection
$\mathcal{F}$	Fourier transform
$\lvert \cdot \rvert$	number of elements in a set
$\lVert \cdot \rVert$	Euclidean vector norm
T	transpose operator
¯	mean value
$\cdot$	inner vector product
$< \cdot, \cdot >$	scalar product

Scalars

R_o	radius of circular object support region
R	radius of source trajectory
D	distance between source and detector (part 2)
s	signed distance of hyperplane from origin
λ	source trajectory parameter
γ	ray fan-angle
u, v	coordinates of 2D detector

Geometric entities

$\mathcal{L}$	line in image domain
Π	plane in image domain
Ω_f	object support region in image domain
$\mathcal{S}$	set of points or vectors
$\mathcal{P}$	factorization plane
^	entities related to a factorization plane

Vectors

$\underline{x}$	coordinate vector denoting locations in image domain
$\underline{x}_\pi$	locations in image domain using BPF coordinate system
$\underline{\alpha}$	unit direction vector of measurement ray
$\underline{a}$	source position
$\underline{\theta}$	line normal vector (part 1), plane normal vector (part 2)
$\underline{e}_u, \underline{e}_v, \underline{e}_w$	axes of detector coordinate system
$\underline{e}_s, \underline{e}_t, \underline{e}_z$	axes of coordinate system associated to a factorization plane

Acronyms

CT	computed tomography (p.2)
HU	Hounsfield units (p.8)
FBP	filtered backprojection (p.18)
FFT	fast Fourier transform (p.21)
PSF	point spread function (p.36)
FWHM	full-width at half-maximum (p.37)
CB	cone-beam (p.53)
BPF	backprojection filtration (p.58)
DBP	differentiated backprojection (p.58)
FDK	algorithm of Feldkamp-Davis-Kress (p.59)
FOM	figure-of-merit (p.70)
CNR	contrast to noise ratio (p.74)
RHS	right hand side (p.92)
LHS	left hand side (p.93)
CPOS	positivity contraint (p.98)
CRAY	ray-integral contraint (p.98)
RMSE	root of mean square error (p.100)

List of Figures

List of Tables

Bibliography

[1] Antropomorphic Cardio CT Phantom, *Quality Assurance in Radiology and Medicine (QRM) GmbH, Moehrendorf, Germany*.

[2] AXIOM Artis dBA: Biplane C-arm system with flat detector for angiography, *Siemens AG, Medical Solutions*.

[3] Description of the FORBILD phantoms, online at: http://www.imp.uni-erlangen.de/forbild/english/results/index.htm.

[4] F. Noo. *Lecture notes in Computed Tomography*, Utah Center for Advanced Imaging Research (UCAIR), University of Utah, USA.

[5] Performance in CT: SOMATOM Sensation, Datasheet for 64-slice Configuration, *Siemens AG, Medical Solutions*.

[6] There's so much more to zee: Article from the customer magazine AXIOM Innovations, Nov. 2007, *Siemens AG, Medical Solutions*.

[7] I. Arai, H. Kudo, F. Noo, M. Defrise, and J. D. Pack. A new class of super-short-scan algorithms for fan-beam reconstruction. In *IEEE Nuclear Science Symposium Conference Record*, volume 4, pages 2296–2300, Puerto Rico, USA, 2005.

[8] A. Assmus. Early history of X rays. *Beam Line periodicals, Standford University, Summer 95*, pages 10–24, 1995.

[9] A. Bakushinsky and A. Goncharsky. *Ill-Posed Problems: Theory and Applications (Mathematics and Its Applications)*. Springer-Verlag, Kluwer Academic Publishers (New York), 1994.

[10] G. Besson. CT image reconstruction from fan-parallel data. *Med. Phys.*, 26(3):415–426, 1999.

[11] I. N. Bronstein and K. A. Semendjajew. *Taschenbuch der Mathematik, 25*. BG Teubner Verlagsgesellschaft und Verlag Nauka (Stuttgart Leipzig Moskau), 1991.

[12] T. M. Buzug. *Einfuehrung in die Computertomographie*. Springer (Berlin), 2004.

[13] G. H. Chen. An alternative derivation of Katsevich's cone-beam reconstruction formula. *Med. Phys.*, 30(12):3217–3226, 2003.

[14] G. H. Chen, R. Tokalkanahalli, T. Zhuang, B. E. Nett, and J. Hsieh. Development and evaluation of an exact fan-beam reconstruction algorithm using an equal weighting scheme via locally compensated filtered backprojection (LCFBP). *Med. Phys.*, 33(2):475–481, 2006.

[15] Z. Chen, R. Ning, D. L. Conover, and Y. Yu. Quantitative assessment of cone-beam CT system by 3D point-spread function. In *Proceedings of the SPIE*, volume 5368, pages 574–585, San Diego, CA, USA, 2004.

[16] E. K. P. Chong and S. H. Zak. *An Introduction to Optimization.* John Wiley and Sons, Inc., 1996.

[17] R. Clack and M. Defrise. Cone-beam reconstruction by the use of Radon transform intermediate functions. *J. Opt. Soc. Am. A*, 11(2):580–585, 1994.

[18] R. Clack and M. Defrise. Overview of reconstruction algorithms for exact cone-beam tomography. In *Proc. SPIE*, volume 2299, pages 230–241, San Diego, CA, USA, 1994.

[19] S. R. Deans. The Radon transform for higher dimensions. *Phys. Med. Biol.*, 23(6):1173–1175, 1978.

[20] M. Defrise and R. Clack. A cone-beam reconstruction algorithm using shift-variant filtering and cone-beam backprojection. *IEEE Trans. Med. Imag.*, 13(1):186–195, 1994.

[21] M. Defrise and G. T. Gullberg. Image reconstruction. *Phys. Med. Biol.*, 51(13):139–154, 2006.

[22] M. Defrise, F. Noo, R. Clackdoyle, and H. Kudo. Enlargement of the region of accurate reconstruction in computed tomography from truncated data. In *Proceedings Fully 3D Meeting and HPIR Workshop*, pages 46–50, Salt Lake City, UT, USA, 2005.

[23] F. Dennerlein, A. Katsevich, G. Lauritsch, and J. Hornegger. Exact and efficient cone-beam reconstruction algorithm for a short-scan circle combined with various lines. In *Proceedings of the SPIE*, volume 5747, pages 388–399, San Diego, CA, USA, 2005.

[24] F. Dennerlein, F. Noo, W. Haerer, J. Hornegger, and G. Lauritsch. Constriction of cone-beam artifacts by the z-smart reconstruction method. In *IEEE Nuclear Science Symposium Conference Record*, volume 6, pages 4090–4096, Honolulu, Hawaii, USA, 2007.

[25] F. Dennerlein, F. Noo, S. Hoppe, J. Hornegger, and G. Lauritsch. Cone-beam tomography with linearly distorted source trajectories. In *IEEE Nuclear Science Symposium Conference Record*, volume 4, pages 2311–2315, San Diego, USA, 2006.

[26] F. Dennerlein, F. Noo, J. Hornegger, and G. Lauritsch. Factorization of the reconstruction problem in circular cone-beam tomography and its use for stability analysis. In *IEEE Nuclear Science Symposium Conference Record*, volume 5, pages 2908–2912, San Diego, CA, USA, 2006.

[27] F. Dennerlein, F. Noo, G. Lauritsch, and J. Hornegger. Fan-beam filtered-backprojection reconstruction without backprojection weight. *Phys. Med. Biol.*, 52(11):3227–3240, 2007.

[28] F. Dennerlein, F. Noo, H. Schoendube, J. Hornegger, and G. Lauritsch. Cone-beam reconstruction on a circular short-scan using the factorization approach. In *Proceedings of the Fully3D*, pages 346–349, Lindau, Germany, 2007.

[29] F. Dennerlein, F. Noo, H. Schoendube, J. Hornegger, and G. Lauritsch. A factorization approach for cone-beam reconstruction on a circular short-scan. *IEEE Trans. Med. Imag.*, 27(7):887–896, 2008.

[30] K. Doi. Diagnostic imaging over the last 50 years: Research and development in medical imaging science and technology. *Phys. Med. Biol.*, 51(13):5–27, 2006.

[31] J. Eriksson. *Problems and experiments in cone-beam tomography*. Linkoeping studies in science and technology (Linkoeping University), 1998.

[32] A. Faridani, R. Hass, and D. C. Solmon. Numerical and theoretical explorations in helical and fan-beam tomography. *J. Phys.: Conf. Ser.*, 124(1):ID 012024, 2008.

[33] L. A. Feldkamp, L. C. Davis, and J. W. Kress. Practical cone-beam algorithm. *J. Opt. Soc. Am. A*, 1(6):612–619, 1984.

[34] D. V. Finch. Cone-beam reconstruction with sources on a curve. *SIAM J. Appl. Math.*, 45(4):665–673, 1985.

[35] R. Gordon, R. Bender, and G. T. Herman. Algebraic reconstruction techniques (ART) for three-dimensional electron microscopy and X-ray photography. *Journal of Theoretical Biology*, 29(3):471–481, 1970.

[36] P. Grangeat. Mathematical framework of cone-beam 3D reconstruction via the first derivative of the Radon transform. *Lecture Notes in Mathematics, G. T. Herman, A. K. Louis, F. Natterer, Eds.*, 1497:66–97, 1991.

[37] M. Grass, T. Koehler, and R. Proksa. 3D cone-beam CT reconstruction for circular trajectories. *Phys. Med. Biol.*, 45(2):329–347, 2000.

[38] R. I. Hartley and A. Zisserman. *Multiple View Geometry in Computer Vision*. Cambridge University Press, 2004.

[39] G. T. Herman. *Image Reconstruction from Projections - The Fundamentals of Computerized Tomography*. Academic Press, 1980.

[40] S. Hoppe, F. Dennerlein, G. Lauritsch, J. Hornegger, and F. Noo. Cone-beam tomography from short-scan circle-plus-arc data measured on a C-arm system. In *IEEE Nuclear Science Symposium Conference Record, 2006. IEEE*, volume 5, pages 2873 – 2877, San Diego, CA, USA, 2006.

[41] S. Hoppe, J. Hornegger, G. Lauritsch, F. Dennerlein, and F. Noo. Geometric calibration of the circle-plus-arc trajectory. *Phys. Med. Biol.*, 52(23):6943–6960, 2007.

[42] S. Hoppe, J. Hornegger, G. Lauritsch, F. Dennerlein, and F. Noo. Truncation correction for non-horizontal filter lines. In *Proceedings Fully 3D Meeting and HPIR Workshop*, volume 9, pages 209–212, Lindau, Germany, 2007.

[43] J. Hsieh and X. Tang. Conjugate backprojection approach for cone beam artifact reduction. In *Proceedings of the SPIE*, volume 6142, pages 758–764, San Diego, CA, USA, 2006.

[44] H. Hu. A new cone beam reconstruction algorithm for the circular orbit. In *IEEE Nuclear Science Symposium Conference Record*, volume 3, pages 1261–1265, 1994.

[45] A. N. Iusem. On the convergence properties of the projected gradient method for convex optimization. *Mat. apl. comput.*, 22(1):37–52, 2003.

[46] A. C. Kak and M. Slaney. *Principles of Computerized Tomographic Imaging.* IEEE Press, 1988.

[47] W. A. Kalender. *Computed Tomography - Fundamentals, System Technology, Image Quality, Applications, 2nd edition.* Publicis Corporate Publishing (Erlangen), 2005.

[48] W. A. Kalender. X-ray computed tomography. *Phys. Med. Biol.*, 51(13):29–43, 2006.

[49] A. Katsevich. Analysis of an exact inversion algorithm for spiral cone-beam CT. *Phys. Med. Biol.*, 47(15):2583–2597, 2002.

[50] A. Katsevich. A general scheme for constructing inversion algorithms for cone beam CT. *IEEE Trans. Med. Imag.*, 21:1305–1321, 2003.

[51] A. Katsevich. Image reconstruction for the circle and line trajectory. *Phys. Med. Biol.*, 49(22):5059–5072, 2004.

[52] A. Katsevich. Image reconstruction for the circle-and-arc trajectory. *Phys. Med. Biol.*, 50(10):2249–2265, 2005.

[53] A. Katsevich, K. Taguchi, and A. A. Zamyatin. Formulation of four Katsevich algorithms in native geometry. *IEEE Trans. Med. Imag.*, 25(7):855–868, 2006.

[54] T. Kido, A. Kurata, H. Higashino, Y. Sugawara, H. Okayama, J. Higaki, H. Anno, K. Katada, S. Mori, S. Tanada, M. Endo, and T. Mochizuki. Cardiac imaging using 256-detector row four-dimensional CT: preliminary clinical report. *Radiation Medicine*, 25(1):38–44, 2007.

[55] H. Kudo, M. Courdurier, F. Noo, and M. Defrise. Tiny a priori knowledge solves the interior problem in computed tomography. *Phys. Med. Biol.*, 53(9):2207–2231, 2008.

[56] H. Kudo, F. Noo, M. Defrise, and R. Clackdoyle. New super-short-scan algorithm for fan-beam and cone-beam reconstruction. In *IEEE Nuclear Science Symposium Conference Record*, volume 2, pages 902–906, Norfolk, VA, USA, 2002.

[57] H. Kudo and T. Saito. Derivation and implementation of a cone-beam reconstruction algorithm for non-planar orbits. *IEEE Trans. Med. Imag.*, 13(1):196–211, 1994.

[58] R. B. Marr, C. N. Chen, and P. C. Lauterbur. On two approaches to 3D reconstruction in NMR zeugmatography. *Proc. mathematical aspects of computerized tomography, Lecture notes in medical informatics*, 8:225–240, 1981.

[59] T. Moore and E. Rohm. *Application Protocol Book for AXIOM Artis 3D applications.* Siemens AG, Medical Solutions, Angiography, Fluoroscopic and Radiographic Systems (Forchheim), 2007.

[60] J. Moret. 3D rotational angiography: Clinical value in endovascular treatment. *Medica Mundi*, 42(3):8–14, 1998.

[61] O. Nakamura, S. Kawata, and S. Minami. Optical microscope tomography. II. Nonnegative constraint by a gradient-projection method. *J. Opt. Soc. Am. A*, 5(4):554–561, 1988.

[62] F. Natterer. *The Mathematics of Computerized Tomography.* John Wiley, Sons Inc, 1986.

[63] F. Natterer and F. Wuebbeling. *Mathematical Methods in Image Reconstruction.* Society for Industrial and Applied Mathematics (SIAM), 2001.

[64] B. E. Nett, T. L. Zhuang, S. Leng, and G. H. Chen. Arc-based cone-beam reconstruction algorithm using an equal weighting scheme. *J. of X-ray Sci. and Tech.*, 15(1):19–48, 2007.

[65] F. Noo, R. Clackdoyle, and J. D. Pack. A two-step hilbert transform method for 2D image reconstruction. *Phys. Med. Biol.*, 49(17):3903–3923, 2004.

[66] F. Noo, M. Defrise, R. Clackdoyle, and H. Kudo. Image reconstruction from fan-beam projections on less than a short scan. *Phys. Med. Biol.*, 47(14):2525–2546, 2002.

[67] F. Noo and D. J. Heuscher. Image reconstruction from cone-beam data on a circular short-scan. In *Proceedings of the SPIE*, volume 4684, pages 50–59, San Diego, CA, USA, 2002.

[68] F. Noo, S. Hoppe, F. Dennerlein, G. Lauritsch, and J. Hornegger. A new scheme for view-dependent data differentiation in fan-beam and cone-beam computed tomography. *Phys. Med. Biol.*, 52(17):5393–5414, 2007.

[69] F. Noo, J. D. Pack, and D. Heuscher. Exact helical reconstruction using native cone-beam geometries. *Phys. Med. Biol.*, 48(23):3787–3818, 2003.

[70] B. B. Ohnesorge, T. G. Flohr, C. R Becker, A. Knez, and M. F. Reiser. *Multi-slice and Dual-source CT in Cardiac Imaging.* Springer (Berlin), 2006.

[71] A. Oppelt. *Imaging Systems for Medical Diagnostics.* Publicis Corporate Publishing (Erlangen), 2005.

[72] J. D. Pack, F. Noo, and R. Clackdoyle. Cone-beam reconstruction using the backprojection of locally filtered projections. *IEEE Trans. Med. Imag.*, 24(1):70–85, 2005.

[73] X. Pan. Optimal noise control in and fast reconstruction of fan-beam computed tomography image. *Med. Phys.*, 26(5):689–697, 1999.

[74] X. Pan and L. Yu. Image reconstruction with shift-variant filtration and its implication for noise and resolution properties in fan-beam computed tomography. *Med. Phys.*, 30(4):590–600, 2003.

[75] D. L. Parker. Optimal short scan convolution reconstruction for fan-beam CT. *Med. Phys.*, 9(2):254–257, 1982.

[76] J. Radon. Ueber die Bestimmung von Funktionen durch ihre Integralwerte laengs gewisser Mannigfaltigkeit. *Berichte Saechs. Akad. Wiss., Math. Phys. Kl*, 69:262 – 277, 1917.

[77] W. C. Roentgen. Ueber eine neue Art von Strahlen. *Annalen der Physik*, 300(1):12– 17, 1898.

[78] S. Schaller, T. Flohr, and P. Steffen. An efficient Fourier method for 3-D Radon inversion in exact cone-beam CT reconstruction. *IEEE Trans. Med. Imag.*, 17(2):244–250, 1998.

[79] M. D. Silver. A method for including redundant data in computed tomography. *Med. Phys.*, 27:773–774, 2000.

[80] B. D. Smith. Image reconstruction from cone-beam projections: necessary and sufficient conditions and reconstruction methods. *IEEE Trans. Med. Imag.*, 4(1):14–25, 1985.

[81] B. D. Smith. Cone-beam tomography: Recent advances and a tutorial review. *Opt. Eng.*, 29(5):524–534, 1990.

[82] H. Turbell. *Cone-Beam Reconstruction Using Filtered Backprojection*. Linkoeping studies in science and technology (Linkoeping University), 2001.

[83] H. K. Tuy. An inversion formula for cone-beam reconstruction. *SIAM J. Appl. Math.*, 43(3):546–552, 1983.

[84] S. Valton, F. Peyrin, and D. Sappey-Marinier. Analysis of cone-beam artifacts in off-centered circular CT for four reconstruction methods. *Int. J. Biomed. Imag.*, 2006.

[85] R. VanTiggelen. In search for the third dimension: From radiostereoscopy to three-dimensional imaging. *JBR-BTR*, 85:266–270, 2002.

[86] G. Wang, Y. Liu, T. H. Lin, and P. C. Cheng. Half-scan cone-beam X-ray microtomography formula. *Scanning*, 16(4):216–220, 1994.

[87] G. Wang, S. Zhao, and P Cheng. Exact and approximate cone-beam X-ray microtomography. *Modern Microscopies (I) - Instrumentation and Image Processing, World Scientific, Singapore*, pages 1–14, 1998.

[88] K. Wiesent, K. Barth, N. Navab, P. Durlak, T. Brunner, O. Schuetz, and W. Seissler. Enhanced 3-D-reconstruction algorithm for C-arm systems suitable for interventional procedures. *IEEE Trans. Med. Imag.*, 19(5):391–403, 2000.

[89] A. Wunderlich and F. Noo. Image covariance and lesion detectability in direct fan-beam X-ray computed tomography. *Phys. Med. Biol.*, 53(10):2471–2493, 2008.

[90] D. Xia, L. Yu, E. Y. Sidky, Y. Zou, N. Zuo, and X. Pan. Noise properties of chord-image reconstruction. *IEEE Trans. Med. Imag.*, 26(10):1328–1344, 2007.

[91] Y. Yao, L. Rosasco, and A. Caponnetto. On early stopping in gradient descent learning. *Constructive Approximation*, 26(2):289–315, 2007.

[92] H. Yu and G. Wang. Feldkamp-type VOI reconstruction from super-short-scan cone-beam data. *Med. Phys.*, 31(6):1357–1362, 2004.

[93] L. Yu, Y. Zou, E. Y. Sidky, C. A. Pelizzari, P. Munro, and X. Pan. Region of interest reconstruction from truncated data in circular cone-beam CT. *IEEE Trans. Med. Imag.*, 25(7):869–881, 2006.

[94] A. A. Zamyatin, K. Taguchi, and M. D. Silver. Practical hybrid convolution algorithm for helical CT reconstruction. *IEEE Trans. Nucl. Sci.*, 53(1):167–174, 2006.

[95] M. Zellerhoff, B. Scholz, E. P. Ruehrnschopf, and T. Brunner. Low contrast 3D-reconstruction from C-arm data. In *Proceedings of the SPIE*, volume 5745, pages 646–655, San Diego, CA, USA, 2005.

[96] G. L. Zeng. Nonuniform noise propagation by using the ramp filter in fan-beam computed tomography. *IEEE Trans. Med. Imag.*, 23(6):690 – 695, 2004.

[97] K. Zeng, Z. Chen, L. Zhang, and G. Wang. A half-scan error reduction based algorithm for cone-beam CT. *J. of X-ray Sci. and Tech.*, 12:73–82, 2004.

[98] S. Zhao, H. Yu, and G. Wang. A unified framework for exact cone-beam reconstruction formulas. *Med. Phys.*, 32(6):1712–1721, 2005.

[99] T. Zhuang, S. Leng S, B. E. Nett, and G. H. Chen. Fan-beam and cone-beam image reconstruction via filtering the backprojection image of differentiated projection data. *Phys. Med. Biol.*, 49(24):5489–5503, 2004.

[100] Y. Zou and X. Pan. Exact image reconstruction on pi-lines from minimum data in helical cone-beam CT. *Phys. Med. Biol.*, 49(6):941–59, 2004.